MATERIALS RESEARCH SOCIETY
SYMPOSIUM PROCEEDINGS VOLUME 739

Three-Dimensional Nanoengineered Assemblies

Symposium held December 1–5, 2002, Boston, Massachusetts, U.S.A.

EDITORS:

Thomas M. Orlando
Georgia Institute of Technology
Atlanta, Georgia, U.S.A.

Lhadi Merhari
CERAMEC R&D
Limoges, France

David P. Taylor
Aerospace Corp.
El Segundo, California, U.S.A.

Koji Ikuta
Nagoya University
Nagoya, Japan

MRS
Materials Research Society
Warrendale, Pennsylvania

Effort sponsored by the Air Force Office of Scientific Research, Air Force Material Command, USAF, under F49620-03-1-0106. The U.S. Government is authorized to reproduce and distribute reprints for Governmental purposes notwithstanding any copyright notation thereon. The views and conclusions herein are those of the authors and should not be interpreted as necessarily representing the official policies or endorsements, either expressed or implied, of the Air Force Office of Scientific Research or the U.S. Government.

This work was supported in part by the Army Research Office under Grant Number DAAD19-02-1-0445. The views, opinions, and/or findings contained in this report are those of the author(s) and should not be construed as an official Department of the Army position, policy, or decision, unless so designated by other documentation.

This work was supported in part by the Office of Naval Research under Grant Number N00014-02-1-0775. The United States Government has a royalty-free license throughout the world in all copyrightable material contained herein.

This material is based upon work supported by the National Science Foundation under Grant No. DMI-0222694. Any opinions, findings, and conclusions or recommendations expressed in this material are those of the author(s) and do not necessarily reflect the views of the National Science Foundation.

Single article reprints from this publication are available through
University Microfilms Inc., 300 North Zeeb Road, Ann Arbor, Michigan 48106

CODEN: MRSPDH

Published by:

Materials Research Society
506 Keystone Drive
Warrendale, PA 15086
Telephone (724) 779-3003
Fax (724) 779-8313
Web site: http://www.mrs.org/

Manufactured in the United States of America

CONTENTS

*Invited Paper

PHYSICS, CHEMISTRY AND MODELING OF NANOSTRUCTURES

*Invited Paper

FABRICATION AND PROPERTIES OF 1D NANOSTRUCTURES

*Invited Paper

FABRICATION AND PROPERTIES OF 3D NANOSTRUCTURES

APPLICATIONS OF NANOSTRUCTURES AND DEVICES

*Invited Paper

PREFACE

Advances in nanoscale materials processing are taking place at a rapid pace via myriad paths, including lithography, production of nanoparticle assemblies, surface manipulation and many others. Several of the new techniques create structures that are three-dimensional or quasi three-dimensional. Even smaller structures intended to be two-dimensional have a "more" three-dimensional geometry as their two-dimensional feature size and layer thickness become similar. The properties of these denser assemblies are driving different applications in electronics (single electron devices), optics (photonic crystals and switches) and elsewhere. Since insights from one area of research can be crucial to the developments and advances in other areas, the symposium on "Three-Dimensional Nanoengineered Assemblies" provided the venue for a productive scientific and technical exchange.

Symposium H, "Three-Dimensional Nanoengineered Assemblies," held December 1-5 at the 2002 MRS Fall Meeting in Boston, Massachusetts, brought together researchers from a wide range of fields. The symposium included much work that was "not quite truly 3D" and "3D but not quite on the nanoscale," and the conference topic was not focused in a particular area of research, but on a goal that is being pursued by many groups approaching from diverse directions. The result was a symposium in which common overarching themes emerged from presentations in widely separated research areas. More than 100 abstracts were submitted and there were 29 invited talks covering work that spanned a remarkable number of topics. The symposium was generally well attended and there was good feedback about the overall quality of the presentations. The symposium addressed fundamental studies, technological advances and novel approaches to developing and processing three-dimensional nanoscale assemblies.

Lithographic methods can be either mask based or mask-less. Much of the time devoted to modern materials processing has been spent developing mask based lithographic techniques and as a consequence they are quite mature. Some of the speakers presented work that used conventional methods at high resolution to great advantage. An example of this sort of work was carried out at Cornell University. There were a variety of talks that presented variations on these methods, perhaps best exemplified by a speaker from Max Planck Institute (Halle, Germany). Work done at the University of New Mexico on laser based interference methods argues that the limits to optical methods have not been reached. This connects with lithographic processes because nonlinear response is important both for photoresist materials and for many of the direct write schemes for processing in three dimensions (work performed at Nagoya University, Japan).

The mask-less direct write processing community was well represented by electron and ion beam talks including works carried out at Lawrence Berkeley National Laboratory, at the company Ion Microfabrication Systems GmbH (Vienna, Austria), and at the National University of Singapore. There were also a variety of talks on soft lithographic methods, including presentations of work done at Lucent Technology and Princeton University. Non-lithographic and self-assembly techniques were also discussed in this meeting. Nanoparticle assemblies, nanotubes, nanowires and nanosprings were the topics of a number of talks. Research carried out at University of California-Irvine on electrochemical methods of producing nanowires, at Georgia Institute of Technology and at University of Idaho on nanosprings, is worth mentioning.

Two of the aspects of the biological model for materials processing that make it most appealing are the directed self-assembly and the bottom-up approach to processing. Together, these aspects of biological control of materials have become a prototype for an elegant approach to processing. If biological processes can be understood and controlled or mimicked, then there is potential to build structures starting on the nanoscale. This approach implicitly offers some level of 3D control from the nanoscale all the way to large structures. A significant part of this work has been directed at carbonates and this was highlighted in an

overview talk on work performed at University of California-Santa Barbara and excellent talks from several speakers including one from Lawrence Livermore National Laboratory and one from Ohio State University.

The case of non-thermal manipulation or coupling using plasmons was a theme which may couple the contact and non-contact modes together. Compelling examples of this sort of nanoscale phenomena exploit the collective electronic excitations (plasma oscillations or plasmons) in metal nanoparticles to manipulate energy and matter. This work was well represented by talks given by speakers from California Institute of Technology, University of Kassel (Germany), Georgia Institute of Technology, University of Canterbury (New Zealand) and Aerospace Corp. In particular, it was shown how plasmons in metal particles on a surface could be used to direct the flow of energy in a material analogous to more conventional electronic devices (CalTech). Other talks demonstrated the use of plasmons to control the size and shape of the metal nanoparticles both on a surface and in the bulk. This is a compelling set of applications for nanotechnology in general and 3D nanoengineered assemblies in particular.

Part of the success of the "Three-Dimensional Nanoengineered Assemblies" symposium is that it touches on a presently topical aspect of research. However, the real strength of this meeting was the multidisciplinary character of the entire symposium where works not only from Universities but also companies were presented. This symposium succeeded in presenting a snapshot of the current work on this topic to researchers, in keeping with the best traditions of the Materials Research Society Meetings.

Thomas M. Orlando
Lhadi Merhari
David P. Taylor
Koji Ikuta

March 2003

ACKNOWLEDGMENTS

The editors wish to thank the contributors to this volume and all the symposium chairs who directed and guided the discussions. Timely and conscientious efforts of the manuscript reviewers despite their heavy workload are greatly appreciated.

Finally, the success of the symposium is a direct result of the generous support received from the following organizations:

Army Research Office
Air Force Office of Scientific Research
National Science Foundation
Office of Naval Research

The organizers of this symposium are very grateful to these organizations.

MATERIALS RESEARCH SOCIETY SYMPOSIUM PROCEEDINGS

Volume 715— Amorphous and Heterogeneous Silicon-Based Films—2002, J.R. Abelson, J.B. Boyce, J.D. Cohen, H. Matsumura, J. Robertson, 2002, ISBN: 1-55899-651-6
Volume 716— Silicon Materials—Processing, Characterization and Reliability, J. Veteran, D.L. O'Meara, V. Misra, P. Ho, 2002, ISBN: 1-55899-652-4
Volume 717— Silicon Front-End Junction Formation Technologies, D.F. Downey, M.E. Law, A. Claverie, M.J. Rendon, 2002, ISBN: 1-55899-653-2
Volume 718— Perovskite Materials, K. Poeppelmeier, A. Navrotsky, R. Wentzcovitch, 2002, ISBN: 1-55899-654-0
Volume 719— Defect and Impurity Engineered Semiconductors and Devices III, S. Ashok, J. Chevallier, N.M. Johnson, B.L. Sopori, H. Okushi, 2002, ISBN: 1-55899-655-9
Volume 720— Materials Issues for Tunable RF and Microwave Devices III, S.C. Tidrow, J.S. Horwitz, J. Levy, X. Xi, 2002, ISBN: 1-55899-656-7
Volume 721— Magnetic and Electronic Films—Microstructure, Texture and Application to Data Storage, P.W. DeHaven, D.P. Field, S.D. Harkness IV, J.A. Sutliff, J.A. Szpunar, L. Tang, T. Thomson, M.D. Vaudin, 2002, ISBN: 1-55899-657-5
Volume 722— Materials and Devices for Optoelectronics and Microphotonics, R.B. Wehrspohn, S. Noda, C. Soukoulis, R. März, 2002, ISBN: 1-55899-658-3
Volume 723— Molecularly Imprinted Materials—Sensors and Other Devices, K.J. Shea, M.J. Roberts, M. Yan, 2002, ISBN: 1-55899-659-1
Volume 724— Biological and Biomimetic Materials—Properties to Function, J. McKittrick, J. Aizenberg, C. Orme, P. Vekilov, 2002, ISBN: 1-55899-660-5
Volume 725— Organic and Polymeric Materials and Devices—Optical, Electrical and Optoelectronic Properties, G.E. Jabbour, N.S. Sariciftci, S.T. Lee, S. Carter, J. Kido, 2002, ISBN: 1-55899-661-3
Volume 726— Organic/Inorganic Hybrid Materials—2002, R.M. Laine, C. Sanchez, S. Yang, C.J. Brinker, 2002, ISBN: 1-55899-662-1
Volume 727— Nanostructured Interfaces, G. Duscher, J.M. Plitzko, Y. Zhu, H. Ichinose, 2002, ISBN: 1-55899-663-X
Volume 728— Functional Nanostructured Materials through Multiscale Assembly and Novel Patterning Techniques, Steven C. Moss, 2002, ISBN: 1-55899-664-8
Volume 729— BioMEMS and Bionanotechnology, L.P. Lee, J.T. Borenstein, R.P. Manginell, M. Okandan, P.J. Hesketh, 2002, ISBN: 1-55899-665-6
Volume 730— Materials for Energy Storage, Generation and Transport, G. Ceder, S.A. Ringel, R.B. Schwarz, 2002, ISBN: 1-55899-666-4
Volume 731— Modeling and Numerical Simulation of Materials Behavior and Evolution, V. Tikare, E.A. Olevsky, A. Zavaliangos, 2002, ISBN: 1-55899-667-2
Volume 732E—Chemical-Mechanical Planarization, S.V. Babu, R. Singh, N. Hayasaka, M. Oliver, 2002, ISBN: 1-55899-668-0
Volume 733E—Polymer Nanocomposites, S. Nutt, R. Vaia, W. Rodgers, G.L. Hagnauer, G.W. Beall, 2002, ISBN: 1-55899-669-9
Volume 734— Polymer/Metal Interfaces and Defect Mediated Phenomena in Ordered Polymers, E.D. Manias, G.G. Malliaras, 2003, ISBN: 1-55899-671-0
Volume 735— Bioinspired Nanoscale Hybrid Systems, G. Schmid, U. Simon, S.J. Stranick, S.M. Arrivo, S. Hong, 2003, ISBN: 1-55899-672-9
Volume 736— Electronics on Unconventional Substrates—Electrotextiles and Giant-Area Flexible Circuits, M.S. Shur, P. Wilson, D. Urban, 2003, ISBN: 1-55899-673-7
Volume 737— Quantum Confined Semiconductor Nanostructures, J.M. Buriak, D.D.M. Wayner, F. Priolo, B. White, V. Klimov, L. Tsybeskov, 2003, ISBN: 1-55899-674-5
Volume 738— Spatially Resolved Characterization of Local Phenomena in Materials and Nanostructures, D.A. Bonnell, J. Piqueras, A.P. Shreve, F. Zypman, 2003, ISBN: 1-55899-675-3
Volume 739— Three-Dimensional Nanoengineered Assemblies, T.M. Orlando, L. Merhari, K. Ikuta, D.P. Taylor, 2003, ISBN: 1-55899-676-1
Volume 740— Nanomaterials for Structural Applications, C. Berndt, T.E. Fischer, I. Ovid'ko, G. Skandan, T. Tsakalakos, 2003, ISBN: 1-55899-677-X

MATERIALS RESEARCH SOCIETY SYMPOSIUM PROCEEDINGS

Volume 741— Nano- and Microelectromechanical Systems (NEMS and MEMS) and Molecular Machines, A.A. Ayon, T. Buchheit, D.A. LaVan, M. Madou, 2003, ISBN: 1-55899-678-8
Volume 742— Silicon Carbide 2002—Materials, Processing and Devices, S.E. Saddow, D.J. Larkin, N.S. Saks, A. Schoener, 2003, ISBN: 1-55899-679-6
Volume 743— GaN and Related Alloys—2002, E.T. Yu, C.M. Wetzel, J.S. Speck, A. Rizzi, Y. Arakawa, 2003, ISBN: 1-55899-680-X
Volume 744— Progress in Semiconductors II—Electronic and Optoelectronic Applications, B.D. Weaver, M.O. Manasreh, C.C. Jagadish, S. Zollner, 2003, ISBN: 1-55899-681-8
Volume 745— Novel Materials and Processes for Advanced CMOS, M.I. Gardner, J-P. Maria, S. Stemmer, S. De Gendt, 2003, ISBN: 1-55899-682-6
Volume 746— Magnetoelectronics and Magnetic Materials—Novel Phenomena and Advanced Characterization, S. Zhang, W. Kuch, G. Guentherodt, C. Broholm, A. Kent, M.R. Fitzsimmons, I. Schuller, J.B. Kortright, T. Shinjo, Y. Zhu, 2003, ISBN: 1-55899-683-4
Volume 747— Crystalline Oxide-Silicon Heterostructures and Oxide Optoelectronics, D.S. Ginley, S. Guha, S. Carter, S.A. Chambers, R. Droopad, H. Hosono, D.C. Paine, D.G. Schlom, J. Tate, 2003, ISBN: 1-55899-684-2
Volume 748— Ferroelectric Thin Films XI, D. Kaufman, S. Hoffmann-Eifert, S.R. Gilbert, S. Aggarwal, M. Shimizu, 2003, ISBN: 1-55899-685-0
Volume 749— Morphological and Compositional Evolution of Thin Films, N. Bartelt, M.J. Aziz, I. Berbezier, J.B. Hannon, S. Hearne, 2003, ISBN: 1-55899-686-9
Volume 750— Surface Engineering 2002—Synthesis, Characterization and Applications, A. Kumar, W.J. Meng, Y-T. Cheng, J. Zabinski, G.L. Doll, S. Veprek, 2003, ISBN: 1-55899-687-7
Volume 751— Structure-Property Relationships of Oxide Surfaces and Interfaces II, X. Pan, K.B. Alexander, C.B. Carter, R.W. Grimes, T. Wood, 2003, ISBN: 1-55899-688-5
Volume 752— Membranes—Preparation, Properties and Applications, V.N. Burganos, R.D. Noble, M. Asaeda, A. Ayral, J.D. LeRoux, 2003, ISBN: 1-55899-689-3
Volume 753— Defect Properties and Related Phenomena in Intermetallic Alloys, E.P. George, H. Inui, M.J. Mills, G. Eggeler, 2003, ISBN: 1-55899-690-7
Volume 754— Supercooled Liquids, Glass Transition and Bulk Metallic Glasses, A.L. Greer, T. Egami, A. Inoue, S. Ranganathan, 2003, ISBN: 1-55899-691-5
Volume 755— Solid-State Chemistry of Inorganic Materials IV, M. Greenblatt, M.A. Alario-Franco, M.S. Whittingham, G. Rohrer, 2003, ISBN: 1-55899-692-3
Volume 756— Solid-State Ionics—2002, P. Knauth, J-M. Tarascon, E. Traversa, H.L. Tuller, 2003, ISBN: 1-55899-693-1
Volume 757— Scientific Basis for Nuclear Waste Management XXVI, R.J. Finch, D.B. Bullen, 2003, ISBN: 1-55899-694-X
Volume 758— Rapid Prototyping Technologies, A.S. Holmes, A. Piqué, D.B. Dimos, 2003, ISBN: 1-55899-695-8
Volume 759— Granular Material-Based Technologies, S. Sen, M.L. Hunt, A.J. Hurd, 2003, ISBN: 1-55899-696-6
Volume 760E—The Undergraduate Curriculum in Materials Science and Engineering, E.P. Douglas, O.D. Dubón Jr., J.A. Isaacs, W.B. Knowlton, M. Stanley Whittingham, 2003, ISBN: 1-55899-697-4
Volume 761E—Molecular Electronics, M-I. Baraton, E.L. Garfunkel, D.C. Martin, S.S.P. Parkin, 2003, ISBN: 1-55899-698-2

Prior Materials Research Society Symposium Proceedings available by contacting Materials Research Society

Nanofabrication Via Lithographic Techniques

Mat. Res. Soc. Symp. Proc. Vol. 739 © 2003 Materials Research Society

Ion Projection Direct-Structuring For Nanotechnology Applications

Hans Loeschner[a]*, Ernest J. Fantner[a], Regina Korntner[a], Elmar Platzgummer[a], Gerhard Stengl[a], Michaela Zeininger[a], J.E.E. Baglin[b], Ruediger Berger[c], Wilhelm H. Brünger[d], Andreas Dietzel[c], Marie-Isabelle Baraton[e,f], and Lhadi Merhari[f]

[a] IMS Nanofabrication GmbH, A-1020 Vienna, Austria

[b] IBM Almaden Research Center, San Jose, California, USA

[c] IBM Storage Technology Division, Mainz, Germany

[d] Fraunhofer Institute for Silicon Technology (ISiT), Itzehoe, Germany

[e] UMR6638 CNRS, University of Limoges, France

[f] CERAMEC, Limoges, France

ABSTRACT

Large-field ion-optics has been developed for reduction printing. Sub-100nm ion projection direct-structuring (IPDS) of patterned magnetic media discs has been demonstrated, extending over 17mm diameter exposure fields, in a single exposure. First results of IPDS patterning of nanocomposite resist material are presented. Information about a novel 200x reduction projection focused ion multi-beam (PROFIB) tool development is provided. Further IPDS nanotechnology applications are discussed.

INTRODUCTION

In recent years (1997 – 2001), intense efforts have been conducted by International SEMATECH to find the best option for sub-100nm lithography. The ISMT target for NGL (Next Generation Lithography), initially set at 100nm, has steadily been pushed to smaller dimensions due to the continued success of optical lithography. With 193nm water immersion lithography there seems to be the possibility to push device production to the 65nm level and possibly even below, by implementing sophisticated resolution enhancement techniques. Beyond these photolithographic limits, mask-less lithography (ML2) becomes an important option for low and medium volume device fabrication. ML2 finds increased interest of the semiconductor industry facing first production year mask costs for critical levels of 150k$ (50nm-node), with anticipated mask delivery times of >100 days. The first production year is most significant with device design and shrinking being more and more accelerated.

For devices with sub-50nm features, NEMS (nano-electro-mechanical systems), nano-photonics, nano-magnetics, molecular nanotechnology devices, etc., novel and even revolutionary fabrication methods will turn out to be mandatory. Traditional lithography is only a fraction of a large variety of nanostructuring possibilities. Ideally, a new paradigm is required, to overcome the interference limitations inherent in optical lithography, and the impracticability of

* phone: +43-1-2144894-24, fax +43-1-2144894-99, e-mail: hans.loeschner@ims.co.at

serial e-beam writing as a production tool. The target of this paper is to point out that ion projection direct-structuring (IPDS) is a promising technique to fulfill these ambitious goals, being inherently free from limitations of optical interference. In section 2 IPDS principles will be described, while the functioning 4x-reduction, 17.5mmØ-field IPDS prototype system is shown in section 3. IPDS application fields are demonstrated with two examples: IPDS for patterned magnetic media data storage in section 4, and IPDS for patterning of nanocomposite materials in section 5, respectively.

Using the experience and expertise obtained with 4x, 5x and 10x reduction ion projection systems, a novel concept has been developed by IMS Nanofabrication GmbH: A projection focused ion multi-beam tool (PROFIB) will be produced with 200x ion-optical reduction, offering interesting applications for micro systems technology ("Micro-PROFIB") and for nanotechnology ("Nano-PROFIB"): section 6. Finally, an outlook for the PROFIB application fields is given in section 7.

PRINCIPLES OF ION PROJECTION DIRECT-STRUCTURING (IPDS)

The principles of ion projection direct-structuring (IPDS) are shown in Figure 1 [1]: Argon gas is fed to a multicusp ion source coupled with a proper extraction system, and ExB mass filter. An electrostatic condenser optical system generates a homogeneous broad ion beam, illuminating a stencil mask membrane which constitutes an objective plane for the following electrostatic reduction optics. As the stencil mask is part of the electrostatic reduction optical system, a diverging electrostatic lens effect can be achieved which greatly reduces the field curvature near the substrate plane. There is a cross-over within the multi-electrode optics, which is enlarged using aberration, thus minimizing stochastic Coulomb interactions.

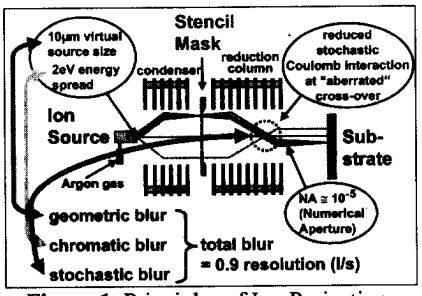

Figure 1 Principles of Ion Projection Direct-Structuring (IPDS).

The ion source extraction optics is properly shaped so that the virtual ion source has a diameter of ~10µm. Therefore a point in the stencil mask is irradiated from ion beam cone of very small angle which leads to a numerical aperture (NA) of the IPDS optics as small as NA≅10^{-5} (10µrad, Figure 2).

Whereas an IPDS operated with 100keV electrons at this small NA would have a diffraction limited resolution of several 100nm, the operation with ions has decisive advantages. The particle wavelength of 50 keV Ar^+ ions is $\lambda_{50keV\text{-}Ar\text{-}ions} \cong 2x10^{-5}$ nm, and thus the diffraction limited resolution is ~ ½ ($\lambda_{50keV\text{-}Ar\text{-}ions}$ / NA) ≅ 1nm. Therefore IPDS optics can be based on extremely small NA which is the key to achieving large exposure fields (Figure 2).

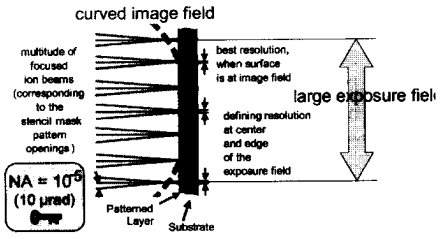

Figure 2 Principles of large field ion-optics.

system, 1.5nm pattern lock stabilization has been achieved. With resist exposures, 75nm lines/spaces have been obtained within a 12.5mm x 12.5mm exposure field (45keV He^+ ion beam exposure of Infineon CAR resist, $2\mu C/cm^2$ exposure dose); sub-50nm patterns have been obtained in parts of the field.

Resist-less direct-structuring was made possible with the IPDS prototype system by feeding argon instead of helium gas to the ion source and by selecting the desired Ar^+ ion species with the ExB mass filter. The ion energy at the stencil mask is about 5 keV, leading to substantial sputter erosion. Techniques to stabilize the stencil mask under these conditions are being studied and will be reported in future. In the IPDS prototype experiments the energy of the ion beam at the wafer was between 30 keV and 65 keV, with most experimental results obtained at 45 keV. The ion beam current density at the wafer was ~0.5 $\mu A/cm^2$, limited by total current which could be extracted from the multicusp ion source with a coaxial magnetic filter. The energy spread of this source with its extraction system was measured at 1.7 eV (FWHM).

IPDS OF MAGNETIC MEDIA FOR HIGH DENSITY DATA STORAGE

Ion beam induced modification of magnetic material properties is one example which points out unique IPDS advantages of (i) resist-less, (ii) non-contact, (iii) single shot direct-structuring, (iv) capable of high throughput. As shown in previous work, magnetic Kerr microscopy was used to demonstrate the circumference of a 17mm diameter track made by IPDS 45keV He^+ ion beam exposure with a dosis of 2 x 10^{15} ions/cm^2 (325 $\mu C/cm^2$) [2]. Using Ar^+ or Xe^+ ions instead of He^+ ions the IPDS prototype system exposure time can be reduced by a factor of ~50 or ~100

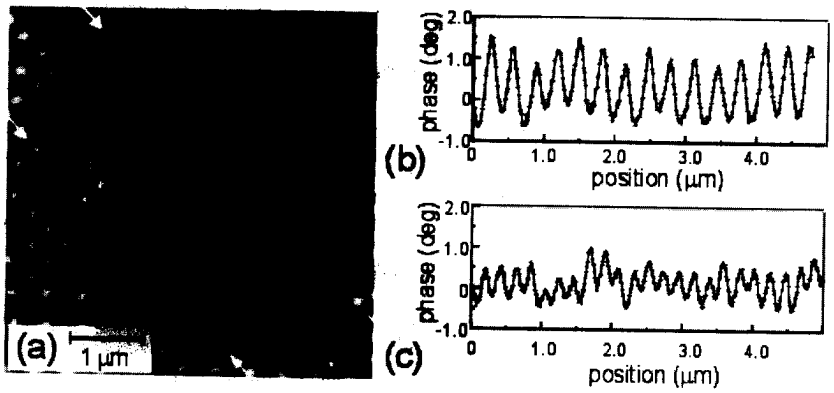

Figure 5 MFM analysis of a Co/Pt ML sample exposed through a stencil mask with cartesian dot configuration with 3 x 10^{14} Xe^+/cm^{-2} at 8.7x demagnification. Displayed is a) the micromagnetic structure which corresponds to 0.75 µm holes at 3 µm pitch (forming 86nm dots at 344nm pitch) in the lower left part and to 0.5 µm holes at 2 µm pitch (forming 57nm dots at 230nm pitch) in the upper right part of the image. Line scans from lower left and upper right part along rows of dost as indicated by white arrows are given in b) and c) respectively (more details in Ref. [2].

IPDS PROTOTYPE SYSTEM

The schematics and a photo of the IPDS prototype system are shown in Figure 3. In this system an ion beam with 115mm diameter at the stencil mask has been constructed. With 4x reduction the pattern field at the wafer is 17.5mm in diameter (a part of the outer beam is used for the so called "pattern lock" system, see below).

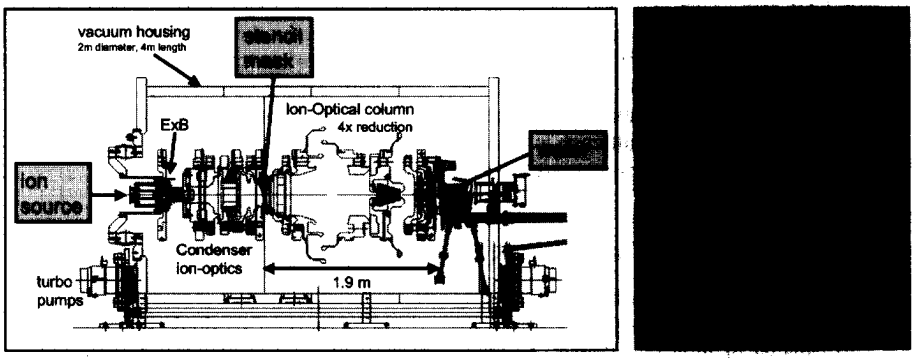

Figure 3 Schematics and photo of IPDS prototype system.

Figure 4 shows the pattern lock schematics. Parallel to the "die beam" – containing the ion beam pattern to be printed to the substrate – there are 12 "reference beams" which enter slits in a "scanner block" between ion-optics and the substrate surface. Within these scanner block slits there are deflection plates so that the reference beams are scanned over grooves in Si platelets bonded to a Zerodur "reference plate" in proximity to the substrate. There are 4 Si platelets at 7 mm distance and 12 Si platelets at 2 mm distance from the substrate plane. Secondary electrons generated by the ion beam are detected. The corresponding signals provide information about the status of the ion beam pattern in X, Y, rotation, X-Y-scale, X-Y-trapezoid as well as beam divergence. The signal information is used to stabilize the ion beam pattern in these functions by appropriate control of the multipole lens electrodes, solenoids and lens electrode voltages. In the IPDS prototype

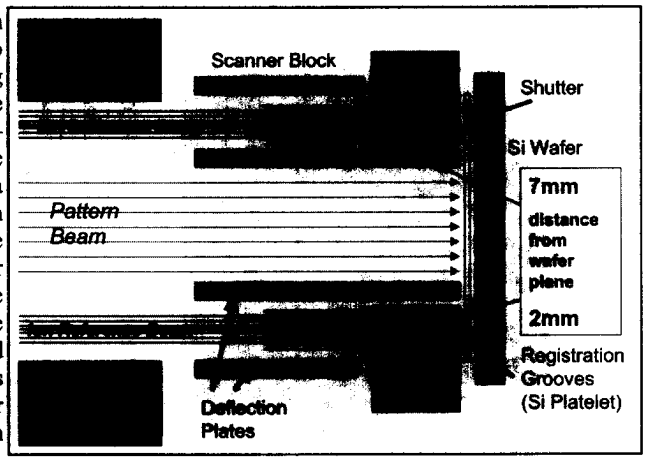

Figure 4 Schematics of IPDS Pattern Lock system.

respectively, which corresponds to IPDS prototype disc exposure times below 20 s. Figure 5 shows an MFM analysis of the magnetic contrast achieved by 73 keV Xe^+ irradiation of a Co/Pt multilayer (ML) sample with initial structure $[Co(0.3nm)/Pt(1nm)]_{10}$. The IPDS magnetic contrast is a result of localized modifications of the magnetic anisotropy obtained by ion beam mixing of Co/Pt ML of the initial structure.

Recent IPDS patterning experiments performed with 45 keV Ar^+ on a microdrive™ show excellent resolution (these results are being published in Ref. [3]). In an IPDS production stepper the exposure field could readily be enhanced to 25mm diameter to fit one inch diameter microdrive™ format. A preliminary study shows that with an IPDS production stepper a throughput of >200 discs/hour could be obtained [1], suitable to meet requirements of low production costs (~1$/disc).

A different approach for ion beam patterned magnetic media is also being studied, in which a continuous coating of self-assembled FePt nanoparticles of 4 nm diameter, dispersed in a soft organic binder [4] is selectively irradiated with a patterned ion beam. Patterned areas of the coating are thus converted into single-bit "rafts" of FePt particles captured in a diamondlike carbon binder; a solvent wash then removes the non-irradiated material. Annealing at 650°C to form the magnetic phase of FePt is then possible without spontaneous agglomeration of the particles. The removal of magnetic material between bits will solve the problem of domain leakage during switching observed by Kusinski et al. [5] for magnetic patterns in continuous media – evidently an important attribute for Tbit/in^2 storage media.

IPDS FOR PATTERNING OF NANOCOMPOSITE MATERIALS

Whatever the micro- or nano-fabrication approach, lithographic technologies for mass-producing devices with sub-100nm resolution not only require more sophisticated machines but also new paradigms for resists. One problem with current commercial resists is that collapse of high-density patterns often occurs. Moreover line edge roughness (LER) becomes of acute concern [6]. To tackle these resist shortcomings at sub-100nm resolution, the concept of nanocomposite resist has been successfully introduced [7-9]. Nanocomposites represent the current trend in novel nanostructured materials and can be defined as a combination of two or more phases containing different compositions or structures, where at least one of the phases is in the nanoscale regime (<100nm). The critical issues for preparing nanocomposites with a homogeneous dispersion of the phases involved lie in the tailoring of the interface/surface chemistry of the components. This requires a fundamental knowledge of the surface chemistry of the inorganic nanoparticles [6-13] to homogeneously disperse them in the radiation-sensitive polymer matrix. In all these approaches, a higher softening transition temperature (T_g) and increased rigidity due to the increased density of the film are anticipated to enhance resist performance for nanometer pattern fabrication. These also include improved mechanical properties that will prevent the collapse of dense high-aspect-ratio nanometer patterns. Increased etch resistance is also implicitly expected.

This approach has been first successfully demonstrated in the field of electron beam lithography, where functionalized 1-2nm silica clusters of polyhedral oligosilsesquioxane (POSS) [14] were homogeneously dispersed in two positive-tone commercial resists: one

respectively, which corresponds to IPDS prototype disc exposure times below 20 s. Figure 5 shows an MFM analysis of the magnetic contrast achieved by 73 keV Xe^+ irradiation of a Co/Pt multilayer (ML) sample with initial structure $[Co(0.3nm)/Pt(1nm)]_{10}$. The IPDS magnetic contrast is a result of localized modifications of the magnetic anisotropy obtained by ion beam mixing of Co/Pt ML of the initial structure.

Recent IPDS patterning experiments performed with 45 keV Ar^+ on a microdrive™ show excellent resolution (these results are being published in Ref. [3]). In an IPDS production stepper the exposure field could readily be enhanced to 25mm diameter to fit one inch diameter microdrive™ format. A preliminary study shows that with an IPDS production stepper a throughput of >200 discs/hour could be obtained [1], suitable to meet requirements of low production costs (~1$/disc).

A different approach for ion beam patterned magnetic media is also being studied, in which a continuous coating of self-assembled FePt nanoparticles of 4 nm diameter, dispersed in a soft organic binder [4] is selectively irradiated with a patterned ion beam. Patterned areas of the coating are thus converted into single-bit "rafts" of FePt particles captured in a diamondlike carbon binder; a solvent wash then removes the non-irradiated material. Annealing at 650°C to form the magnetic phase of FePt is then possible without spontaneous agglomeration of the particles. The removal of magnetic material between bits will solve the problem of domain leakage during switching observed by Kusinski et al. [5] for magnetic patterns in continuous media – evidently an important attribute for Tbit/in^2 storage media.

IPDS FOR PATTERNING OF NANOCOMPOSITE MATERIALS

Whatever the micro- or nano-fabrication approach, lithographic technologies for mass-producing devices with sub-100nm resolution not only require more sophisticated machines but also new paradigms for resists. One problem with current commercial resists is that collapse of high-density patterns often occurs. Moreover line edge roughness (LER) becomes of acute concern [6]. To tackle these resist shortcomings at sub-100nm resolution, the concept of nanocomposite resist has been successfully introduced [7-9]. Nanocomposites represent the current trend in novel nanostructured materials and can be defined as a combination of two or more phases containing different compositions or structures, where at least one of the phases is in the nanoscale regime (<100nm). The critical issues for preparing nanocomposites with a homogeneous dispersion of the phases involved lie in the tailoring of the interface/surface chemistry of the components. This requires a fundamental knowledge of the surface chemistry of the inorganic nanoparticles [6-13] to homogeneously disperse them in the radiation-sensitive polymer matrix. In all these approaches, a higher softening transition temperature (T_g) and increased rigidity due to the increased density of the film are anticipated to enhance resist performance for nanometer pattern fabrication. These also include improved mechanical properties that will prevent the collapse of dense high-aspect-ratio nanometer patterns. Increased etch resistance is also implicitly expected.

This approach has been first successfully demonstrated in the field of electron beam lithography, where functionalized 1-2nm silica clusters of polyhedral oligosilsesquioxane (POSS) [14] were homogeneously dispersed in two positive-tone commercial resists: one

undergoing main-chain scissions (ZEP520® developed by Nippon Zeon, Japan) and the other being a chemically amplified system (KRS-XE® developed by IBM, USA). Not only resolution (down to sub-50nm), mechanical resistance of the nanopattern, and resistance to reactive ion etching (RIE) in O_2 (up to a factor of 20) were improved, but also electron proximity effects were reduced [15].

Knowing that polymers can be several orders of magnitude more sensitive to ion irradiation than to electron irradiation, (and that lateral straggling of ions in the target may, in general, be much less than that of electrons), it is of obvious interest to investigate the behavior of nanocomposite resists subjected to ion beams. In the following silica cages consisting of cyclohexenyl-POSS $Si_8O_{12}R_8$ where R= $OSiMe_2CH_2CH_2C_6H_9$ (Tal Materials, Ann Arbor, MI, USA) were dispersed in an Infineon chemically amplified resist (CAR). The choice of R in POSS depends on the characteristics (e.g. hydrophobicity, hydrophilicity) of the host polymer matrix for optimum dispersion. Figure 6 compares preliminary results obtained with the Infineon resist and its nanocomposite counterpart both irradiated by a 75 keV He^+ beam at $4\mu C/cm^2$ through the 175nm-wide apertures of a stencil mask. The 200nm-thick film of nanocomposite CAR exhibits finer lines (width ~100nm instead of ~180nm) with straight walls and comparatively higher aspect ratio. These preliminary results show the promise of IPDS for nanocomposite resists in the field of nanolithography and justify further exploration and LER evaluations, which are already planned.

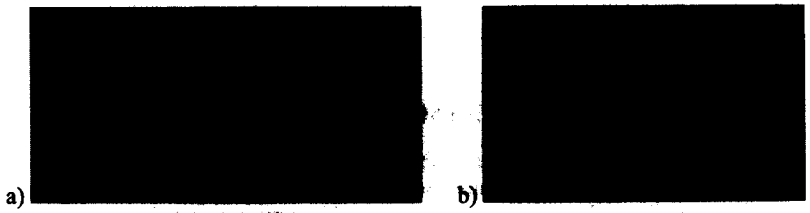

Figure 6 75keV He^+ ion beam, $4\mu C/cm^2$ exposure dose, conventional development, of: a) Infineon chemically amplified resist with addition of ~10% SiO_2 nanoparticles of 1-2 nm diameter, b) without nanoparticle addition (showing less stability during SEM examination).

In fact, nanocomposite materials are key in a large number of emerging nanotechnology fields. Hybrid organic-inorganic nanocomposites can already be synthesized so that they exhibit useful magnetic, optical, and biological properties by carefully selecting the host matrix and the inorganic phase. The added value here will be to fabricate sub-100nm structures in these nanocomposite films in a reproducible manner and at high speed. Photonic band gap crystals, intelligent substrates for cell engineering, magnetic nanopatterns, molecular electronics and quantum devices can already be envisaged on a large scale thanks to the promises of the versatile IPDS nanofabrication technique.

PROJECTION FOCUSED ION MULTI-BEAM TOOL (PROFIB) WITH 200x REDUCTION ION-OPTICS

In the following a novel concept for a 200x reduction projection focused ion multi-beam tool ("PROFIB"), as recently developed by IMS Nanofabrication, is presented. Initial validation of the possibilities offered by PROFIB ion projection direct-structuring will be performed in the fields of micro- and nano-electronics, MEMS and NEMS, functionalized nano-materials, sensor and actuator systems and biomedical nanotechnology. The PROFIB tool principles are shown in Figure 7.

The core of the ion-optical system is based on two demagnifying projection steps, transforming an incident telecentric (highly parallel) beam into a 200x reduced telecentric ion beam, where the incident beam is patterned by means of a stencil mask. The telecentricity of the ion image is a key issue for 3-dimensional fabrication, as the projection using a highly parallel ion beam implies a large depth of focus, and allows a large vertical aspect ratio during structuring.

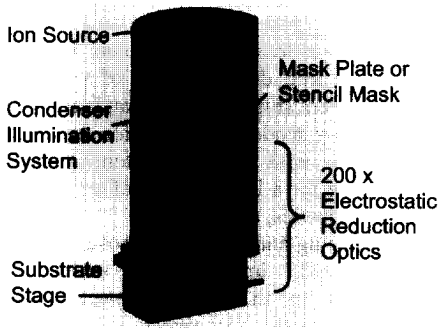

Figure 7 PROFIB principles

We will distinguish between Micro-PROFIB for applications in micro-systems technology, and Nano-PROFIB for applications in nanotechnology, but the basic principles are the same. Micro-PROFIB will be operated in the maximum current mode, whereas Nano-PROFIB will be operated in the maximum resolution mode, see Table 1.

Table I Main specifications of Micro- and Nano-PROFIB

	Micro-PROFIB high current mode	Nano-PROFIB high resolution mode
resolution	1 μm	< 10 nm
ion beam current density	40 mA/cm²	5 mA/cm²
beam current	1 μA	10 nA

Using an ion-optical system with 200x reduction offers the possibility to achieve high ion beam current densities at the substrate to be modified, with respect to topographical, morphological, chemical or electronic contrast. To achieve 1μm resolution at writing currents typically required for MEMS fabrication *(~1 μA mode)*, 200μm openings in a stencil mask plate (e.g. 50μm stainless steel plate) are used, which can be simply fabricated with e.g. micro-erosion techniques.

On the other side, the same optical setup is able to resolve <10 nm features *(~10 nA mode)* with stencil mask openings of ~1μm at comparably lower current through the column. Masks with 1 μm openings can be fabricated with silicon technology as used in any conventional semiconductor fabline. Due to the high reduction factor, mask damage is effectively reduced (40,000x). To extend stencil mask life time protection coatings are used to further reduce the sputter and implantation damage.

The aim of the Micro-PROFIB tool concept is the closing of the presently existing „machining gap" between the classical micro machining technologies and semiconductor patterning technologies. Micro-PROFIB will be a machinery especially developed for the micro machining of feature sizes in the range between 1 µm and 10 µm, focused on rapid prototyping and substrate materials, where no conventional fabrication is available. Typical applications will include micromachining, cutting and surface structuring of various solid materials such as steel, metal alloys and ceramics. Micro-PROFIB can also be applied to insulator materials by providing proper means to avoid electrostatic charging of the sample, such as a low energy electron shower.

Concerning the Nano-PROFIB tool concept, the target is to obtain <10nm resolution within a 20µm□ exposure field. This means that there will be the possibility to expose e.g. 1 million 10nm dots in less than 0.5 seconds for dose of 10^{16} ions/cm² in a single shot. The pattern will be distortion free, due to the use of a pre-contoured stencil mask. The already described "pattern lock" system (Fig. 4) will be implemented to stabilize the ion beam. The tool can be used in the lithography mode as well as for direct-structuring. In particular the combination of top-down structuring with selective bottom-up self-assembly techniques is the key to implement novel patterning for a large variety of emerging nanotechnology products in the field of nano-optics, nano-magnetics, etc.

Stepping and scanning exposure modes will be realized. Implementing multipole lens electrodes in the column, electrostatic step exposure (ESE) techniques will add to the versatility for rapid prototyping. This enables the realization of arbitrary patterns (including "doughnut structures") with one single stencil mask, thus eliminating the need of complementary stencil mask overlay. ESE is achieved by four-fold exposure, through electrostatic shifts of the image with ~0.1nm precision (Fig. 8). The machining strategy for a certain application will be adjusted to the particular structures to be transferred.

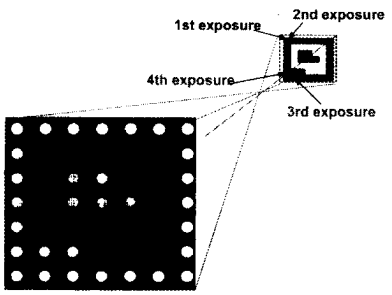

Figure 8 Electrostatic step exposure (ESE)

IPDS NANOTECHNOLOGY APPLICATION FIELDS WITH PROFIB

Ion projection direct-structuring (IPDS) performed with PROFIB offers a plurality of interesting applications in micro and nanotechnology, including ion beam erosion, ion beam assisted deposition, implantation and other ion beam modifications of matter (Figure 9).

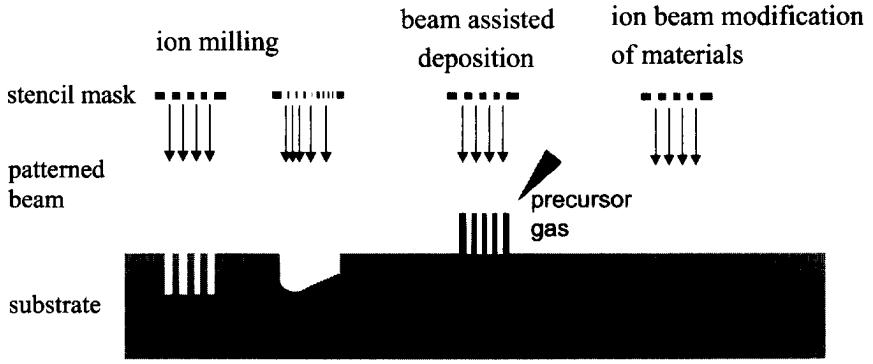

Figure 9 Ion Projection Direct-Structuring application schematics as becoming possible with PROFIB (Projection Focused Ion multi-Beam tool).

As the total beam current acting parallel on the substrate is targeted to 1μA / 1μm resolution and 10nA / <10nm resolution, respectively, the potential throughput of PROFIB is 2-3 orders higher than for present (single beam) FIB technology. This high productivity (despite the relatively low source brightness compared to a liquid metal ion source) [16]) is based on the novel large field 200x reduction optical system, which allows efficient use of the current density extracted from a multi-cusp ion source, resulting in an enhanced productivity on an exposure area of up to 100 μm image field size.

CONCLUSION

Ion projection direct structuring (IPDS) is based on large field ion optics with 4x (IPDS prototype) up to 200x (PROFIB) reduction factors, and offers novel fabrication techniques to micro- and nano- technology. The main advantage of IPDS is the possibility of resist-less, non-contact, single shot direct-structuring, combined with the capability of mass production. Concerning direct structuring, the flexibility to adjust ion species, energies and ion current densities (ion doses) within a wide parameter range enables an effective use of ion beam modification techniques, such as in ion erosion, in ion implantation or ion assisted growth etc.

Beyond existing IPDS technology demonstrated by the IPDS prototype tool, which is applicable for high volume patterning magnetic media, a novel tool generation with 200x reduction is in development (PROFIB). The new tool is expected to achieve better than 10nm resolution on a 20μm□ image field, and is aiming for bringing the unique ion optics advantages into the labs and into prototype production.

ACKNOWLEDGMENTS

The results as achieved with the ion projection direct-structuring tool are due to the dedicated work of the IMS team. As part of a 1997-2001 MEDEA project the work on ion projection lithography was supported by the Austrian government organizations FFF (Forschungs-foerderungsfonds fuer die Gewerbliche Wirtschaft) and FGG (Finanzierungs Garantie Gesellschaft) and by the Austrian and German federal ministries for science and technology. ASM Lithography and Infineon Technologies AG have also contributed to the MEDEA IPL project. The work on ion projection magnetic media has been supported by the German federal ministry of education, science, research, and technology under grant number 13N7837.

REFERENCES

1. H. Loeschner, G. Stengl, et.al., Proc. SPIE Vol. **4688**, 595 (2002); an updated version t.b.p. in JM3 (Jan2003).
2. A. Dietzel, R. Berger, H. Grimm, W.H. Bruenger, C. Dzionk, F. Letzkus, R. Springer, H. Loeschner, E. Platzgummer, G. Stengl, Z.Z. Bandić, and B.D. Terris, IEEE Transactions on Magnetics, Vol. **38**, 1952 (2002).
3. A. Dietzel, R. Berger, H. Loeschner, E. Platzgummer, G. Stengl, W. H. Bruenger, F. Letzkus, "Nanopatterning of *Magnetic Discs by Large Field, Single Exposure Ar+-Ion Projection Step*", t.b.p.
4. S. Sun, C.B. Murray, D. Weller, L. Folks and A. Moser, Science **287**, 1989 (2000).
5. G.J. Kusinski, K.M. Krishnan, G. Denbeaux, G. Thomas, B. Terris and D. Weller, Appl. Phys. Lett. **79**, 2211 (2001).
6. H. Namatsu, T. Yamaguchi, and K. Kurihara, Mat. Res. Soc. Symp. Proc. Vol. **584**, 135 (2000).
7. T. Ishii, A. Yokoo, Y. Murata, and K. Shigehara, Mat. Res. Soc. Symp. Proc. Vol. **636**, D6.4.1 (2001).
8. L. Merhari, H.H. Li, and K.E. Gonsalves, Mat. Res. Soc. Symp. Proc. Vol. **584**, 97 (2000).
9. K.E. Gonsalves, L. Merhari, H. Wu, and Y. Hu, Adv. Mater. **13**, 703 (2001), and references therein.
10. M.-I. Baraton, in *Handbook of Nanostructured Materials and Nanotechnology*, Ed. H.S. Nalwa, Academic Press, San Diego (CA, USA), 1999, pp. 89-153.
11. M.-I. Baraton, in *Functional Gradient Materials and Surface Layers Prepared by Fine Particles Technology*, Edited by M.-I. Baraton and I. Uvarova, NATO Science Series, Kluwer Academic Publishers, Dordrecht, 2001, pp. 45-60.
12. K.E. Gonsalves, S. Jin and M.-I. Baraton, Mat. Res. Soc. Symp. Proc. Vol. **501**, 233 (1998).
13. M.-I. Baraton, Mat. Res. Soc. Symp. Proc. Vol. **705**, 159 (2002).
14. Frank J. Feher, http://www.gelest.com/Library/05Pol.pdf
15. L. Merhari, K.E. Gonsalves, Y. Hu, W. He, W.-S. Huang, M. Angelopoulos, W.H. Bruenger, C. Dzionk, and M. Torkler, Microelectronic Engineering **63**, 391 (2002).
16. L. Scipioni, D. Stewart, D. Ferranti, A. Saxonis, J. Vac. Sci. Technol. **B18**, 3194 (2000).

Mat. Res. Soc. Symp. Proc. Vol. 739 © 2003 Materials Research Society H2.8

Proton Induced Structuring of a Photostructurable Glass

Meg Abraham[1], Inmaculada Gomez-Morilla[1], Mike Marsh[1], Geoff Grime[2]
[1] Oxford University, Material Department, Parks Rd. Oxford UK
[2] University of Surrey, Physics Department, Guilford, UK

ABSTRACT

The use of photons to create intricate three-dimensional and buried structures [1] in photo-structurable glass has been well demonstrated at several institutions [2]. In these instances the glass used whether it be Foturan™, made by the Schott Group or a similar product made by Corning Glass, forms a silver nucleation sites on exposure to intense UV laser light via a two-photon process. Subsequent annealing causes a localized crystal growth to form a meta-silicate phase which can be etched in dilute hydrofluoric acid at rates of 20 to 50 times that of the unprocessed glass. The same formulation of glass can be "exposed" using a particle beam to create the nucleation site. In the case of particle beam exposure, experiments have shown that the mechanisms that cause this initial nucleation and eventual stochiometric transformation, after annealing, depend largely on the beam energy.

INTRODUCTION

New materials processing methods are leading to a revolution in the types of micro-machines that are currently being developed. The size and dimensionality as well as the types of materials are expanding every year greatly enhancing the number of device types that can be made. One of the more interesting approaches to these types of new three-dimensional processes is the combination of photo-structurable glass with laser direct write patterning to create truly three dimensional micro-machines in glass. In this instance UV photons initiate a sequence where silver ions are reduced, crystals are formed under annealing conditions, and a meta-silicate crystalline phase nucleates. In this crystalline phase, the silicate etches much faster than the glass and it is possible to create very high aspect ratios. Due to the interesting nonlinear properties involved in the initial exposure step, it has been demonstrated that it is possible to create embedded structures in the glass [3] as well as structures with very high aspect ratios by simply varying the laser power, wavelength or focus [4].

The Scanning Proton Microprobe is a tool which has been developed largely to aid in the analysis of the chemical composition or crystal state of materials using techniques such as Rutherford backscattering, X-ray emission, and proton channeling. More recently the tool has been shown to be of value in the area of micro-machining [5] of polymers and related materials. This is accomplished by using the long range and low lateral spread of MeV protons to expose thick photoresists to fabricate high aspect ratio structures (e.g. 1 μm grooves 60 μm deep).

By using focused protons, we have shown that it is also possible to create embedded structures as well as surface features in photostructurable glass. We have begun to work with developing and understanding this alternative ion beam method for exposing glass. We have found that the physical process by which the nucleation sites are formed are dependent on the beam energy with three distinct physical possibilities emerging for the mechanism used to create the exposure.

EXPERIMENTAL SETUP

Sections of Foturan glass were exposed in the Oxford Scanning Proton Microprobe (SPM) [6] using a beam of 2 MeV protons focused to a diameter of less than 1 μm FWHM using the 'Oxford' triplet configuration of quadrupole lenses (Oxford Microbeams Ltd., Oxford, UK). The beam currents used were in the range of .7 to 1.5 pA. The beam was incident normal to the sample. Characteristic x-rays (PIXE) were detected using a lithium-drifted silicon detector with an active area of 70 mm^2 and an energy resolution of 140 eV (Oxford Analytical Ltd., High Wycombe, Bucks, UK) at an angle of 45° to the beam. The distance from the detector to the sample could be adjusted from 17 mm to 90 mm, giving a maximum solid angle of 240 msr. Recoiling protons (RBS) were detected using a surface barrier detector of active area 250 mm^2 mounted at an angle of 25° to the incident beam direction. A grating was created by scanning the beam up and back then stepping the beam over 20 μm. The beam was scanned over the sample up to a maximum area of 2500 μm × 2500 μm with the maximum speed such that the total scan time was less then one second for the grating. Signals from the detectors were recorded together with the instantaneous beam position using the OM_DAQ data acquisition system (Oxford Microbeams Ltd.) [7], which also controls the beam scanning in a raster mode and allows the accumulation of elemental maps, during the line scans.

After exposure to the proton beam the samples were annealed at 500 degrees C for 30 min and 610 degrees C for one hour. The samples were then etched in a 5% solution of hydrofluoric acid to clear out the meta-silicate phase of the glass.

RESULTS

The scans were run over the edge of the glass sections to create lines of exposure. Three sets of exposures were done at beam currents of .7 pA, 1 pA and 1.5 pA. In each case a distinct set of results were seen. A slight hysteresis in the beam on its return scan was seen in some cases. This is evidenced by overlapping etch channels.

In the case of the lowest flux of protons (.7 pA) a single embedded channel was created by the proton beam during each pass up and back (fig.1). At first we believed this to be consistent with the fact that almost all the proton beam energy is deposited at the end of the range of the implantation. On closer inspection we noted that the channels were not sufficiently deep into the glass to be at end of range (approximately 100 μm in glass). We also noted a slight ghost of a second channel appearing below the main one which is about 100 μm into the sample (fig 2.). While we are not sure of the cause of the single channel we noted that it is possible to make a single embedded channel by limiting the beam flux such that there is only sufficient energy to nucleate a silver ion at the end of the protons travel. We speculate that the exposure may be due to an oxygen resonance induced in the glass at that depth by the proton beam. In any case, the resulting channels are on the order of 5 μm in diameter. Finally, there is clear structuring of the edge of the sample as the beam ran over the side of the glass section.

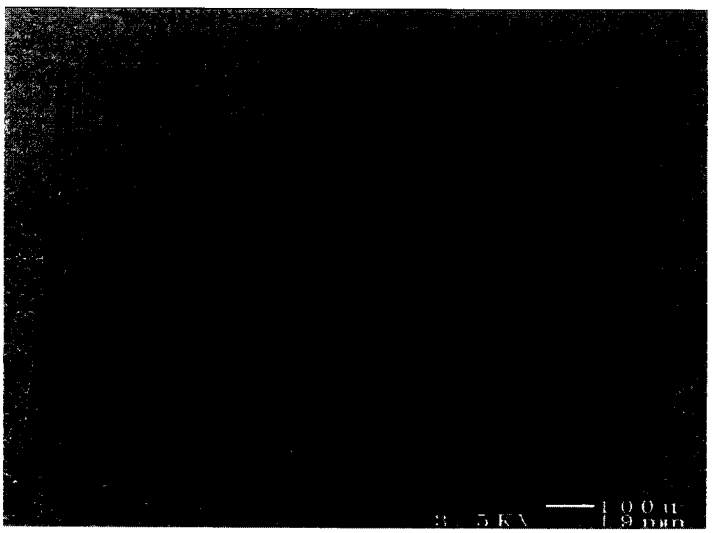

Figure 1. Embedded channels in glass and some edge structuring as the beam ran off the sample.

Figure 2. Same as above at higher magnification, the ghost of a second set of channels can be seen below the first. A slight hysteresis in the beam scan can be noted in this sample.

In the case of the highest flux of protons (1.5 pA) a single channel was created through the bulk of the glass by the proton beam during each pass up and back (fig. 3 and 4). We believe this is consistent with the observed fluorescing of the glass at the higher proton flux. In this case, the proton beam is causing the glass to fluoresce in a narrow region as the beam passes through the sample and the resulting photons expose the glass.

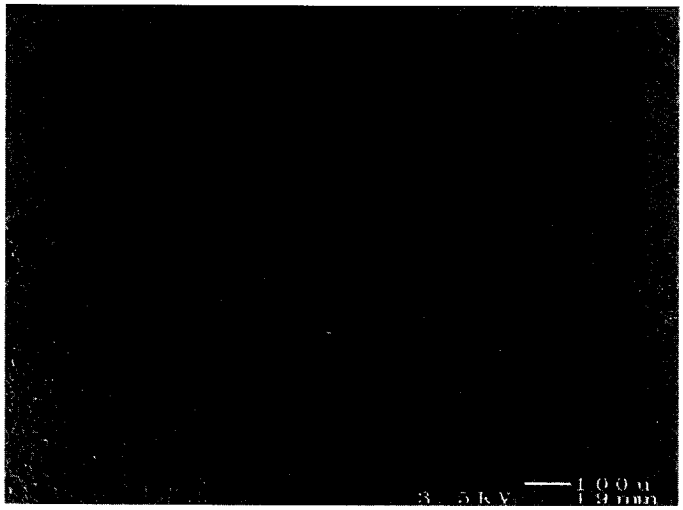

Figure 3. Channels in the glass formed by higher proton flux (damage to sample occurred during handling)

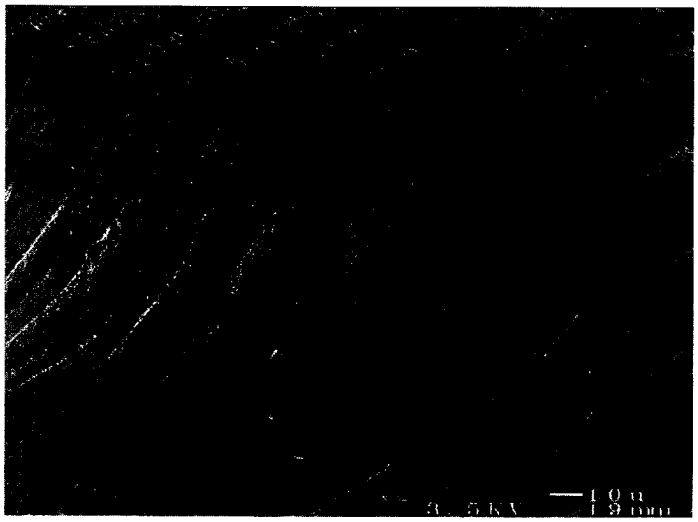

Figure 4. Same as above at higher magnification.

Perhaps the most intriguing result was that of the section of glass exposed to the proton beam at 1 pA. In this case the flux of protons created two embedded channels, one stacked on the other. While we are still investigating the potential cause of this "double" exposure, we believe that the top channel is the result of an oxygen resonance partway into the implantation depth that causes the formation of a nucleation site. The end of range energy deposited by the proton beam then forms the bottom channel.

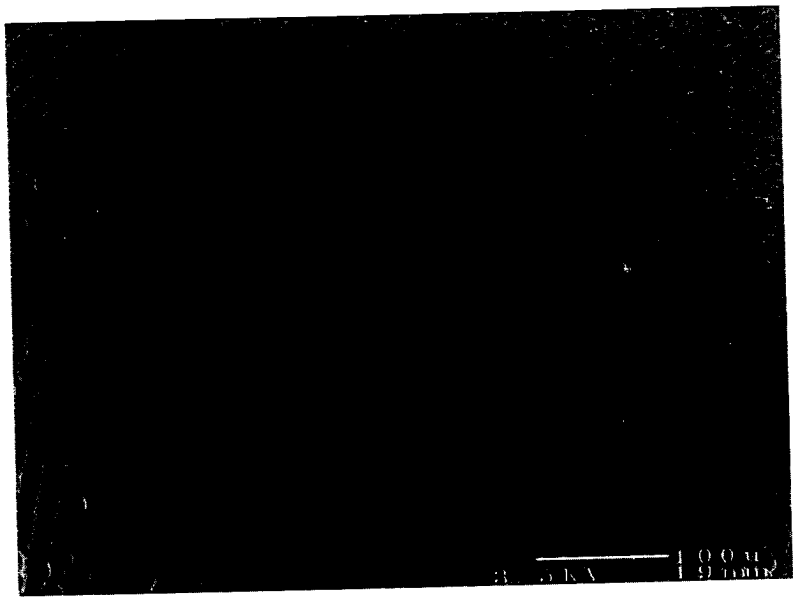

Figure. 5 Two sets of channels formed by the rastering of a single beam of protons across the glass

CONCLUSION

It is possible to make embedded channels and other structures in photostructurable glass using focused ion beams. There are a number of mechanisms identified for the formation of the silver ions that result in a nucleation site where meta-silicate forms after annealing. While there is more work needs to fully understand these mechanisms we believe that this technology offers the potential to expand the usefulness of this material

ACKNOWLEDGMENTS

We would like to thank the British National Space Agency for their support of this work.

REFERENCES

1. W. W. Hansen, P. Fuqua, F. Livingston, A. Huang, M. H. Abraham, D. P. Taylor, S. Janson, and H. Helvajian, *The Industrial physicist*, **June/July**, 18, (2002).
2. S. D. Stookey, G. H. Beall, and J. E. Pierson. *J. Appl. Phys.*, **49,** 5114, (1978).
3. P. D. Fuqua, D. P. Taylor, H. Helvajian; W. W. Hansen, M. H. Abraham in *Materials Development for Direct Write Technologies,* edited by D. Christy, D. Ginley, H. Helvajian and D. P. Taylor (Mater. Res. Soc. Proc. **624**, Warrendale, PA, 2000) pp. 79-87.
4. J. C. Cheang-Wong, A Oliver, J. Roiz, L. Rodriguez-Fernandez, J. M. Hernandez, and A. Crespo-Sosa, *J. Phys.: Cond. Mat.*, **13**, 10207, (2001).
5. A. A. Bettiol, I. Rajta, E. J. Teo, J. A. van Kan, and F. Watt, *Nucl. Instrum. Meth.*, **B 190**, 154 (2002).
6. G. W. Grime, M. Dawson, M. Marsh, I. C. McArthur, and F. Watt, *Nucl. Instrum. Meth.*, **B 54**, 52 (1991).
7. G. W. Grime and M. Dawson, *Nucl. Instrum. Meth.*, **B 104**, 107 (1995).

Mat. Res. Soc. Symp. Proc. Vol. 739 © 2003 Materials Research Society

Resist Requirements and Limitations for Nanoscale Electron-Beam Patterning

J. Alexander Liddle,[1] Gregg M. Gallatin[2] and Leonidas E. Ocola[3]
[1]Materials Sciences Division, Lawrence Berkeley National Laboratory
Berkeley, CA 94720, USA
[2]IBM T.J. Watson Research Center
Yorktown Heights, N.Y. 10598, USA
[3]Advanced Photon Source, Argonne National Laboratory
Argonne, IL 60439, USA

ABSTRACT

Electron beam lithography still represents the most effective way to pattern materials at the nanoscale, especially in the case of structures, which are not indefinitely repeating a simple motif. The success of e-beam lithography depends on the availability of suitable resists. There is a substantial variety of resist materials, from PMMA to calixarenes, to choose from to achieve high resolution in electron-beam lithography. However, these materials suffer from the limitation of poor sensitivity and poor contrast.

In both direct-write and projection e-beam systems the maximum beam current for a given resolution is limited by space-charge effects. In order to make the most efficient use of the available current, the resist must be as sensitive as possible. This leads, naturally, to the use of chemically amplified (CA) systems. Unfortunately, in the quest for ever smaller feature sizes and higher throughputs, even chemically amplified materials are limited: ultimately, sensitivity and resolution are not independent. Current resists already operate in the regime of < 1 electron/nm^2. In this situation detailed models are the only way to understand material performance and limits.

Resist requirements, including sensitivity, etch selectivity, environmental stability, outgassing, and line-edge roughness as they pertain to, high-voltage (100 kV) direct write and projection electron-beam exposure systems are described. Experimental results obtained on CA resists in the SCALPEL® exposure system are presented and the fundamental sensitivity limits of CA and conventional materials in terms of shot-noise and resolution limits in terms of electron-beam solid interactions are discussed.

INTRODUCTION

Some years ago it was still possible to treat the resist requirements for high sensitivity and high resolution as two separate cases, divided between commercial applications, such as mask making, and small scale patterning for research. More recently, however, the separation between these two domains has all but disappeared. This has been driven primarily by the continuing reduction in feature size accompanying the progress of the semiconductor industry (Figure 1). The concomitant demands on mask fabrication have become rigorous, particularly with the introduction of sub-resolution elements for optical proximity effect correction [1]. In addition, as optical lithography becomes more difficult and costly, there is a strong possibility that electron-beam systems will be used directly [2, 3] for the mass production of integrated circuits (IC's). These factors mean that electron-beam resists are now required to provide high resolution and high speed simultaneously.

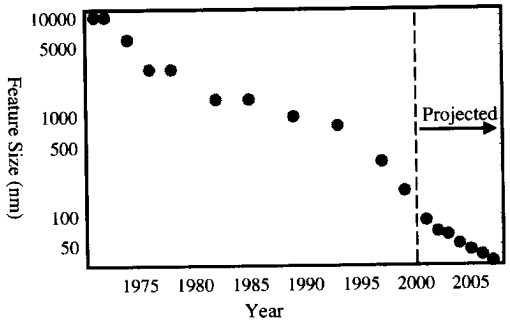

Figure 1. Minimum integrated circuit feature size as a function of time.

In this paper we will discuss the detailed requirements for advanced electron-beam resists, review the basic mechanisms governing resist exposure and development with particular attention to the statistics of the processes involved, and, finally, consider what the fundamental limitations to the resolution of electron-beam lithography might be.

RESIST REQUIREMENTS

Process stability

Process stability covers a number of specific factors related to variations in the printed feature size or critical dimension (CD). The overall CD tolerance is usually given as ±10%, with process related effects allowed to contribute only ±3%.

Table I. Values of process sensitive parameters for electron-beam resists.

Process Sensitive Parameter	Value
Post Exposure Delay (PED) Time	> 3 hrs
Development Time	< 5% CD/minute
Etch Resistance	= Polyhydroxystyrene
Post Exposure Bake (PEB)	< 1% CD/°C
Developer	0.26N TMAH
Vacuum Compatibility	Zero outgassing

The requirements in Table I are generic for all lithographic technologies, apart from the need for vacuum compatibility. The evolution of volatile organic compounds from the resist while it is in the electron-beam system is highly undesirable because of the potential for contamination of the electron-optical column with material that can charge and degrade the system performance. In addition, the loss of material from the resist can adversely affect the resist performance.

In a single component material, such as PMMA, solvent can escape from the film, but this can be addressed using a suitable pre-exposure bake protocol. However, particularly in view of the indiscriminate nature of the radiolysis induced by electron-beam exposure, there is always the potential for the production of volatile moieties – in the case of PMMA substantial amounts of MMA monomer are evolved.

Chemically amplified materials contain a base resin with pendant protecting groups (positive tone), or a cross-linker (negative tone), in addition to a base, a photoacid generator (PAG), residual solvent, as well as additives to promote adhesion and film formation. During exposure a latent image of acid is formed in the film. The acid then goes on to catalyze a number of deprotection or cross-linking reactions (Figure 2).

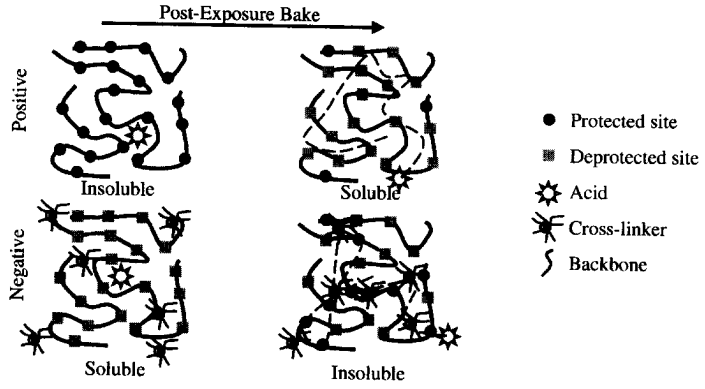

Figure 2. a) Schematic of the exposure mechanism for a CA resist [7]. Note that the crosslinker functions to protect soluble sites, rather than link polymer chains.

Loss of the PAG from the film, which could be exacerbated by the vacuum environment, will obviously degrade the lithographic performance of the resist, which suggests that large molecules that can associate with the polar functionalities of the resist are required. Ideally the acid formation process should not occur through a reaction involving leaving groups, and the acid molecule itself should be large enough to be non-volatile. It is also important that either the kinetics of the acid catalyzed reaction is minimal at the maximum temperature the resist experiences in the exposure system, which requires that it be a high activation energy (E_a) process, or that the volatility of the products is zero. Current experience suggests that the high E_a materials are most suitable.

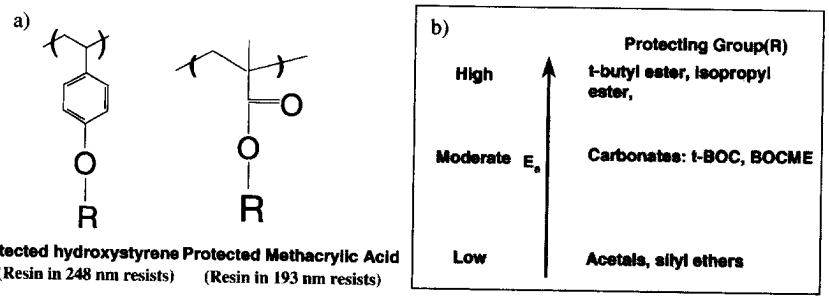

Figure 3. a) Typical resist structures for 248 nm and 193 nm resists, which are also suitable for electron-beam systems. b) Influence of protecting group, R, on activation energy for deprotection reaction.

It is important to note that the absorption or optical density is not an issue for electron-beam resists. This imposes a major constraint on the design of optical resists because the transparency of the materials needs to be adjusted so that the absorption through the film thickness does not lead to excessive resist sidewall angles due to depth variation of the deposited energy profile [4]. This is becoming harder to realize as the exposure wavelengths used decrease from 248 nm to 193 nm and below as fewer and fewer polymer systems are available with acceptable absorption characteristics. Limitations on the choice of polymer components can also affect the etch resistance of the material, which is influenced by its fractional carbon content, and by the relative proportion of carbon atoms contained within a ring structure [5,6].

Contrast

The resist contrast is a measure of how non-linear the response of the development process is to the chemical contrast produced in the material after exposure and is essential in determining how small an image modulation can be successfully converted into an actual developed resist image. A typical requirement for conventional IC manufacture is that the contrast should exceed 5, but there is no upper limit, greater values leading to steeper sidewall angles. Note, however, that if topographic control of a resist surface is desired, as in the production of diffractive optical elements, then low contrast values are useful.

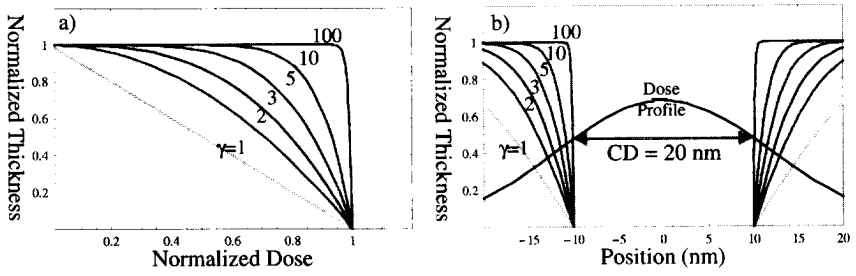

Figure 4. a) Normalized film-thickness remaining versus normalized dose for a positive resist material for different values of the dissolution rate contrast, γ, defined as $\gamma = \frac{d \ln r}{d \ln E}$, where r is the dissolution rate from an exposure dose E. b) Normalized film-thickness remaining versus position for a 20 nm feature printed with a 10 nm σ Gaussian blur (Dose Profile) for different values of the contrast, γ, assuming uniform energy deposition through the film thickness.

The contrast is determined by the nature of the development process. In a non-chemically amplified material, such as PMMA, the effect of exposure is to cause scissioning of the main polymer chain. The developer used is a minimal solvent for the material, and it extracts the lower molecular weight polymer chains from the exposed regions more rapidly than the high molecular weight chains from the unexposed regions leading to a variation in dissolution rate with dose. This is a process that is strongly

dependent on kinetics, and, since it is essentially sorting material on the basis of molecular weight differences, it is fundamentally a low contrast process.

Certain measures can be taken to improve the contrast, such as reducing the polydispersivity (the ratio of the weight average to number average molecular weight) of the starting polymer. If the polydispersivity is small, then it is easy to establish a clear separation in weight distribution between exposed and unexposed areas. This also has the effect of reducing the dose necessary to achieve that separation.

In a chemically amplified material, there is a change in polarity between the exposed and unexposed areas. In a positive tone material, exposure results in the conversion of an insoluble non-polar material into a highly soluble polar material. The change in solubility occurs when the density of deprotected sites exceeds a critical value and is relatively abrupt [7]. Aside from the change in solubility, this process converts the material from hydrophobic to hydrophilic, which further encourages the attack of the developer on the exposed regions. These factors lead to CA resists having typically very high contrasts.

Sensitivity

Reductions in exposure dose have been essential in making technologies such as 248nm and 193nm optical lithography and electron-beam mask making systems viable, in terms of throughput, because of limitations in the sources. Mask making has, until recently, relied on simple post-processing of the resist image – wet Cr etching – and so the demands on the resist have been minimal in terms of its process robustness. These demands have been satisfied with single component materials such as PBS [8] and COP [9], which were optimized primarily for sensitivity. Optical resists have had to meet all the demands of IC fabrication and so have developed as complex systems with a number of components that offer the ability to optimize sensitivity as well as features such as etch resistance and process stability independently [10]. These considerations have naturally led to the chemically amplified (CA) resist systems developed for optical lithography finding application in electron-beam systems.

In electron beam systems for IC manufacture, low doses are critical for a number of reasons. Resolution in electron-beam systems is linked to the beam current through the space-charge effect: electron-electron interactions in the beam cause blurring of the image, which increases as the beam current is increased [11, 12]. The development of a more sensitive material can therefore be of benefit in two ways: for a fixed beam current the throughput can be increased, or, for a given throughput, the beam current can be decreased and the resolution improved. In addition to the tradeoff between resolution and throughput, heating, both of the wafer and the mask, is reduced as the sensitivity improves. High-throughput systems typically operate at 100 kV and at beam currents as high as 30 μA; a heat load of 3 W deposited deep in the wafer. For example, a 10 $\mu C/cm^2$ dose requirement will lead to an overall wafer temperature increase of about 8 K: the heating process is of course localized to the beam and thus leads to dynamic wafer distortions that can be a significant contributor to the total overlay error [13,14].

Fortunately there is some relief from the requirement to continue endlessly reducing the sensitivity. The system throughput depends on other factors such as stage speed, alignment time and wafer load/unload overhead, which means that there is little to be gained in throughput once the exposure time becomes much less than the system

overhead time. Similarly, the resolution is ultimately limited by electron-optical aberrations, and there is a point at which further reductions in beam current will not improve resolution. These factors mean that there is a practical lower limit on the minimum sensitivity required, which will vary with the system design details, however, values as challenging as 1 $\mu C/cm^2$ [15] have been specified.

It should be noted that similar considerations apply in direct write systems, particularly mask making tools. In such systems the minimum useful sensitivity is determined by the beam current and the deflection speed. For example, in a raster scanning mask maker with a deflection speed of 320 MHz, a maximum beam current of 720 nA and a pixel size of 120 nm, the minimum useful resist sensitivity is 16 $\mu C/cm^2$ [1]. A typical vector beam tool for nanolithographic applications [16] operating at 25 MHz with a beam current of 500 pA and a pixel size of 8 nm would be able to employ a resist with a sensitivity as low as 31 $\mu C/cm^2$, while very high resolution work, which might need a pixel size of 2 nm, would increase this value to 500 $\mu C/cm^2$.

IC Manufacture vs Nanofabrication

Although the feature sizes involved in IC manufacture are starting to approach the nanoscale domain, there are a number important differences between the respective resist requirements. First, sensitivity: this is not, within reason, a major concern for the nanofabrication community, where the resolution is the dominant performance metric, whereas for IC production where overall manufacturing costs are very strongly weighted by throughput, it is critical. Second, the evolution of volatile products from the resist film can be tolerated to a limited extent in nanofabrication, because the very low typical throughputs mean that the total volume of material released into the vacuum system is small. Third, the requirement for compatibility with a TMAH developer can be relaxed since the use of different developers, including organic solvents, is only an issue in the context of the large quantities needed in a production environment.

Resolution

So far we have not discussed the resolution requirement, since this is intimately linked to both the contrast and sensitivity through the details of the image formation process. We now consider those details in the context of their effect on the ultimate resolution attainable. Note that we judge the resolution limit to be defined by the smallest equal lines and spaces that can printed. Smaller isolated features are always possible, but are more representative of the process than the resist.

Aerial Image

Calculation of the aerial image in an electron-beam system is relatively straightforward because diffraction effects are negligible at the short (3.7 pm at 100 keV) wavelengths used. This means that the convolution of a suitable point-spread function (PSF) with the desired features is sufficient [17].

In a high-throughput system, such as a mask-writer or projection tool, the PSF is comparable in size to the features being printed, in order to maximize the beam current, which means it has a substantial impact on the ultimate resolution and process latitude.

The situation is somewhat different for nanofabrication systems where the PSF can be much smaller than the feature ranging from a Gaussian with a σ of 5 nm for commercial tools to 0.5 nm in systems based upon scanning transmission electron microscopes.

Figure 5 shows the aerial image for 20 nm features at several different Gaussian blur values.

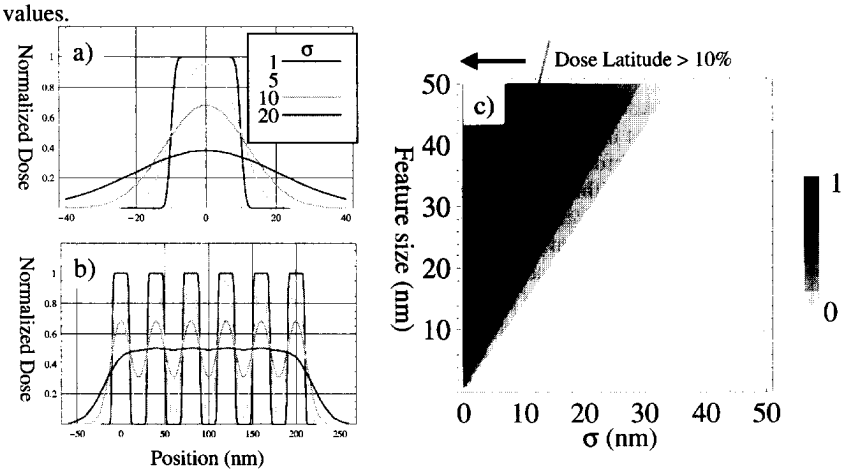

Figure 5. Aerial image intensity profiles for isolated and dense features as a function of Gaussian beam blur width, σ. a) 20 nm isolated feature, b) 20 nm lines and spaces, c) Normalized modulation transfer function as a function of feature size and blur.

Once the blur reaches roughly $\sqrt{2Ln2}$ of the feature size the aerial image contrast becomes negligible, hence, in the ideal case of infinite resist contrast and no other sources of blur, the resolution attainable is determined solely by the beam blur. It is necessary, however, to provide some latitude in the process. If we define an acceptable variation in dose as one that causes less than a 10% change in the feature size, then the blur should be less than 20% of the feature size.

Statistics

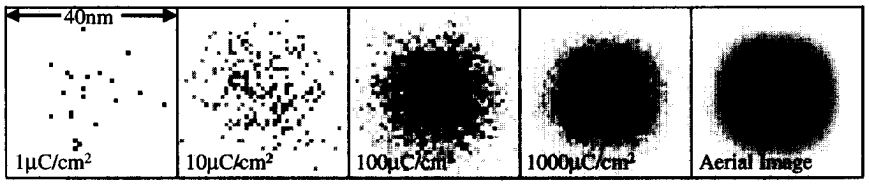

Figure 6. Arrival statistics for a 20 nm square feature printed with a Gaussian blur of 5 nm σ at doses of 1, 10, 100 and 1000 μC/cm² respectively. 1000 μC/cm² corresponds to an average of 62.5 electrons/nm². The gray level in each pixel corresponds to the number of electrons arriving in a 1 nm square.

Unfortunately the aerial images shown above really only represent the probability of finding an electron at a particular location. The low doses demanded for high throughput mean that the number of electrons delivered is small enough that the arrival statistics can cause dose variations (Figure 6) that could, in principle, lead to significant feature size variations [18, 19].

The most basic limit to the resolution from a statistical perspective is given by the mean separation between the electrons, and corresponds to $4\ nm/\sqrt{S}$, where S is the sensitivity in $\mu C/cm^2$, leading to dose of 16 $\mu C/cm^2$ or 1 e^-/nm^2 for 1 nm resolution. Note that this approach does not include the three dimensional nature of the exposure. A more realistic value is obtained through making a signal to noise argument and requiring that the uncertainty in the dose within a resolution element be less than 10%, for example, giving a dose value of 1600 $\mu C/cm^2$ for the same resolution. Exactly what the limit is will be controlled by what constitutes a meaningful resolution element. Clearly the molecular size of the resist is one such limit, while the maximum tolerable value of the line edge roughness, typically 10% of CD, is another. We could also choose the CD, and, bearing in mind that for an isolated feature the dose to print on size is twice the threshold dose for development, calculate the probability that the dose falls below threshold so that the feature fails to print. If we choose an error threshold of 1 in 10^{15}, the minimum dose is approximately 200 particles per feature, corresponding to a dose of 32 $\mu C/cm^2$ for a 10 nm square feature. As Figure 7 shows, the most sensitive resists are operating well at 5 – 6 $\mu C/cm^2$ for 100 nm features, so the simple square law scaling derived from any of the above criteria would indicate that the worst case required sensitivity at 20 nm should be no more than 125 - 150 $\mu C/cm^2$.

We should note at this point, that the arrival statistics do not constitute the whole story. In a 100 nm thick resist film each 100 keV electron is on average responsible for an average of one ionization event. As we will discuss shortly, these events are not localized, and naturally lead to some smoothing out of the arrival statistics.

In the case of CA resists, the simple statistical picture would seem to be rather damning in terms of the likely resolution because of the small volume fraction that the photoacid generator molecules occupy. This would lead one to imagine that the number of electrons necessary would have to be increased to account for the reduced probability of a "hit" on a PAG molecule.

80 nm, 5.8 $\mu C/cm^2$ 80 nm, 5.8 $\mu C/cm^2$ 100 nm, 5.4 $\mu C/cm^2$

Figure 7. Results obtained from chemically amplified resist (TOK EP004, positive, and EN009, negative) exposed on the SCALPEL® system.

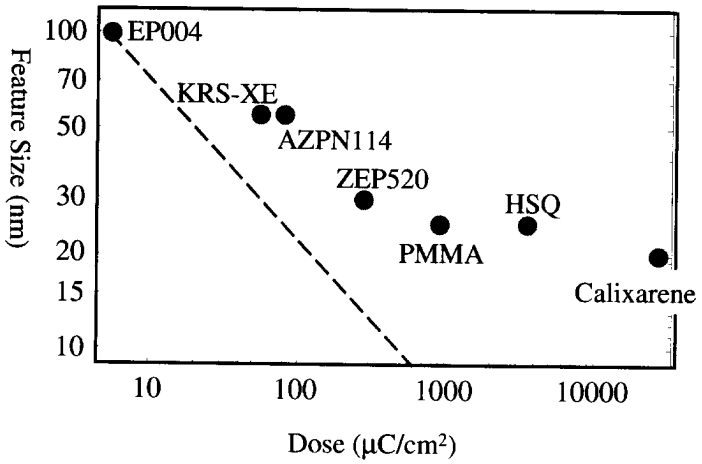

Figure 8. Resolution versus process dose for a range of resists for equal lines and spaces. The dashed line represents the $Dose^{-1/2}$ dependency that we would expect to observe, scaled to EP004 at 5.8 $\mu C/cm^2$.

Recent work [20, 21], however, has suggested that ionization events in the base polymer can also result in acid generation through an electron "scavenging" process, substantially increasing the efficiency with which incident electrons are converted into acid species.

The situation in CA materials increases in complexity when one considers the role of acid diffusion and its effect on the developed image. Image formation in CA materials can be thought of as a concatenation of statistics - dose – acid formation – PEB chemistry – dissolution rate – surface evolution – and can be modeled as such [22]. The net result is that the initial dose statistics are washed out [22]. Detailed models have been produced of the processes occurring during acid diffusion and acidolysis [23, 24, 25], incorporating effects such as the sharp decrease in acid diffusion that occurs when the acid is diffusing in a deprotected as opposed to protected area and the evolution of deprotected site density during post-exposure bake. Current estimates [26] put the acid diffusion range at 5 nm during a typical post exposure bake, indicating that it is the highly efficient acidolysis process that is a major cause of image blur during PEB at large feature sizes, while the two are equally important in the 40 – 50 nm range, with acid diffusion dominating at the smallest feature sizes.

Energy deposition distribution

We can see from Figure 8 that the resolution that can be obtained ceases to improve as the dose continues to increase: at this juncture it is appropriate to consider how the energy of the incident electron beam is actually distributed through the resist. If we confine ourselves to a discussion of high-energy (> 50 keV) electrons, then forward scattering is a negligible factor in controlling the form of the deposited energy profile [27,28], as expected. 90% of a 100 keV beam is contained within a diameter of 8 nm at the base of a 100 nm thick resist [28]. The bond-breaking that accompanies the passage

of the incident electron is controlled by the distribution of ionization events, plasmons and the trajectories of electrons generated within the resist [29]. We note that the peak in the secondary electron energy distribution is approximately 10 eV [25], and that such low energy electrons can have mean free paths of several nanometers [30]: these factors, combined with the "scavenging" picture [21], requires that these low energy electrons be accounted for carefully in CA materials. We note that it has been suggested that the PAG, through the scavenging effect, limits the range of thermalized electrons [20, 21]. Figure 9 shows the results of a simulation that does so, and indicates that the beam broadening in the resist as a consequence of these processes is approximately 10 nm. This result suggests that there is little to be gained by reducing the incident beam blur much beyond 5 nm.

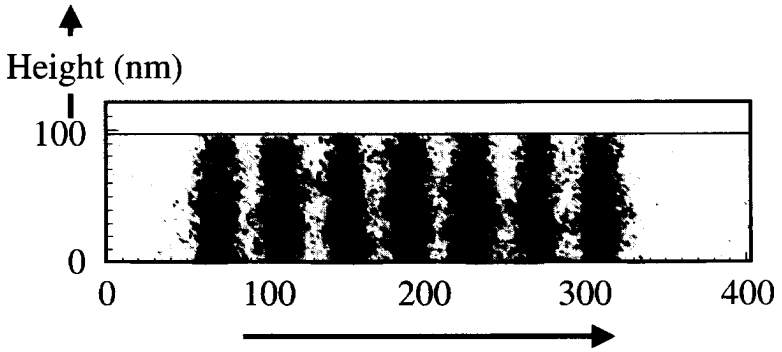

Figure 9. Deposited energy distribution in a 100 nm thick resist for a square-wave function (20 nm lines and spaces) incident beam generated using a Monte-Carlo simulation of a 20 $\mu C/cm^2$ dose.

PERFORMANCE LIMITS

From the preceding discussion it is clear that the minimum feature size is ultimately controlled by the energy deposition profile. It should be noted that there are instances where higher resolution has been achieved using electron-beam systems and inorganic resists such as SiO_2 [31] and Al_2O_3 [32, 33]. The exposure mechanism in these cases involves high energy-loss events, which therefore tend to be highly localized. In the case of SiO_2 radiation damage occurs by knock-on, while in Al_2O_3 feature formation proceeds through lattice defect production at very high rates in a process that relies upon the excitation of core electrons, necessitating the use of very high current densities and doses in the C/cm^2 range. Though interesting, such methods cannot form the basis of a viable nanofabrication technology.

CONCLUSIONS

The resolution that can be obtained in an electron-beam resist is limited by the modulation in the deposited energy profile that can be generated. This means that features below about 20 nm (lines and spaces) cannot be resolved in conventional organic resist materials – indicated by the fact that the smallest features produced have not been

bettered in almost three decades [34, 35]. However, the ease of producing those features can be greatly enhanced by the increasing the resist contrast to take full advantage of whatever dose latitude may be available. In addition, if dose is not a constraining requirement, then we might expect that the feature quality (i.e. LER) would improve [36] based upon signal-to-noise arguments. These considerations suggest that CA materials with their high-contrast development mechanisms will become increasingly useful for high resolution work, especially if the formulations are changed to benefit from relaxations in, for example, the amount of PAG that can be incorporated or the absence of a need for optical transparency [37], and to reduce diffusion lengths and catalytic chain lengths to match the lower required sensitivities. Recently, novel resists based on hybrid organic/inorganic nanocomposites have been developed and show some indications of improved resolution, possibly through a reduction in the fast secondary range [38].

ACKNOWLEDGEMENTS

The authors would like to acknowledge F.A. Houle, W.D. Hinsberg, J.M.M. Macaulay and A.E. Novembre for helpful discussions. This work was supported in part by DARPA under contract number MDA972-98-C-0007 and by the Director, Office of Science, Office of Basic Energy Sciences, Materials Science and Engineering Division, U.S. Department of Energy under Contract Nos. DE-AC03-76SF00098 and W-31-109-ENG-38.

REFERENCES

1. F. Abboud , Ki-Ho Baik, V. Chakarian, D. Cole, J. Daniel, R. Dean, M. Gesley, Maiying Lu, R. Naber, T. Newman, F. Raymond, D. Trost, M. Wiltse, W. DeVore, Proc. SPIE **4562**, 1 (2002).
2. J.A. Liddle, L.R. Harriott and W.K. Waskiewicz, Microlithography World, **6**, 15 (1997).
3. S. D. Golladay, H. C. Pfeiffer, J. D. Rockrohr, and W. Stickel, J. Vac. Sci. Technol., **B18**, 3072 (2000).
4. R.L. Brainard, G.G. Barclay, E.H. Anderson, L.E. Ocola, Microelectronic Engineering, **61-62**, 707 (2002)
5. Y. Ohnishi, M. Mizuko, H. Gokan and S. Fujiwara, J. Vac. Sci. Technol., **19**, 1141 (1981).
6. R. Kunz et al., Proc. SPIE **2724**, 365 (1996).
7. L.E. Ocola, to appear in J. Vac. Sci. Technol., Proceedings of the 46th EIPBN meeting.
8. M.J. Bowden, L.F. Thompson and J.P. Ballantyne, J. Vac. Sci. Technol., **12**, 1294 (1975).
9. L.F. Thompson, J.P. Ballantyne and E.D. Feit, M.J. Bowden, L.F. Thompson and J.P. Ballantyne, J. Vac. Sci. Technol., **12**, 1280 (1975).
10. R.D. Allen, W.E. Conley and R.R. Kunz, in *Microlithography, Micromachining and Microfabrication*, edited by P. Rai-Choudhury (SPIE Optical Engineering Press, Bellingahm, 1997), p. 321.
11. M. M. Mkrtchyan, J. A. Liddle, S. D. Berger, L. R. Harriott, J. M. Gibson and A. M. Schwartz, J. of Appl. Phys., **78**, 6888 (1995).

12. M. M. Mkrtchyan, J. A. Liddle, S. T. Stanton, E. Munro, W. K. Waskiewicz, Microelectronic Engineering, **53**, 299 (2000).
13. N. Fares, S. Stanton, J. Liddle and G. Gallatin, J. Vac. Sci. Technol., **B18**, 3115 (2000).
14. S.T. Stanton, Proc. SPIE, **4343**, 138 (2001).
15. K. Okamato, K. Suzuki, H. Pfeiffer and M. Sogard, Solid State Technol., **May**, 118 (2000)
16. B.H. Koek, T. Chisholm, A.J. van Run, J. Romijn, J.P. Davey, Microelectronic Engineering, **23**, 81 (1994).
17. M. Mkrtchyan, G. Gallatin, A. Liddle, X. Zhu, E. Munro, W. Waskiewicz, D. Muller, Microelectronic Engineering, **57-58**, 277 (2001).
18. H.I. Smith, J. Vac. Sci. Technol., **B4**, 148 (1986).
19. G.M. Gallatin and J.A. Liddle, Microelecronic Engineering., 46 **365** (1999)
20. S. Tagawa, S. Nagahara, Y. Yamamoto, D. Werst and A.D. Trifunac, Proc. SPIE **3999**, 204 (2000).
21. A. Saeki, T. Kozawa, Y. Yoshida and S. Tagawa, Jpn. J. Appl. Phys. **41**, 4213 (2002)
22. G.M. Gallatin, Proc. SPIE, **4404**, 123 (2001).
23. F.A. Houle, W.D. Hinsberg, M.I. Sanchez and J.A. Hoffnagle, J. Vac. Sci. Technol., **B20**, 924 (2002).
24. W.D. Hinsberg, F.A. Houle, M.I. Sanchez and G.M. Wallraff, IBM J. Res. & Dev. **45**, 667 (2001).
25. L.E. Ocola, Mat. Res. Soc. Symp. Proc., **705**, Y.1.1.1 (2002)
26. F. A. Houle, W. D. Hinsberg, M. Morrison, M. I. Sanchez, G. Wallraff, C. Larson, and J. Hoffnagle, J. Vac. Sci. Technol., **B18**, 1874 (2000).
27. E.H. Anderson, D.L. Olynick, W. Chao, B. Harteneck and E. Veklerov, J. Vac. Sci. Technol., **B18**, 2970 (2000).
28. D.C. Joy, Microelectronic Engineering, **1**, 103 (1983).
29. L.E. Ocola, Microelectronic Engineering, **53**, 433 (2000).
30. D.C. Joy, http://web.utk.edu/~srcutk/htm/interact.htm
31. D.R. Allee, C.P. Umbach and A.N. Broers, J. Vac. Sci. Technol., **B9**, 2838 (1991).
32. J.M. Macaulay "The production of nanometre structures in inorganic materials by electron beams of high current density", Ph.D. dissertation, University of Cambridge (1989).
33. J.M. Macaulay, R.M. Allen, L.M. Brown, S.D. Berger, Microelectronic Engineering, **9**, 57 (1989)
34. A.N. Broers, Proc. R. Soc. Lond. A, **416**, 1 (1988).
35. A.N. Broers, Phil. Trans. R. Soc. Lond. A, **353**, 291 (1995).
36. M. Williamson, A. Neureuther, Proc. SPIE, **3999**, 1189 (2000).
37. M. Sato, L.E. Ocola, A.E. Novembre, K. Ohmori, K. Ishikawa, K. Katsumata and T. Nakayama, J. Vac. Sci. Technol., **B17**, 2873 (1999).
38. K.E. Gonsalves, L. Merhari, H. Wu, and Y. Hu, Advanced Materials, **13**, 703 (2001).

Mat. Res. Soc. Symp. Proc. Vol. 739 © 2003 Materials Research Society H1.2

Techniques and Applications for Non-Planar Lithography

John A. Rogers
Bell Laboratories, Lucent Technologies, Murray Hill, NJ 07974, U.S.A.

ABSTRACT

Certain classes of three dimensional nanostructures can be fabricated by contact printing patterns onto curved or non-flat surfaces. This paper reviews some of our work that demonstrates this approach by using microcontact printing to form a range of three dimensional structures with feature sizes as small as 1-2 microns and it demonstrates their use in a variety of functional devices. We also describe a nanotransfer printing technique with operational characteristics that are similar to those of microcontact printing but which enables nanometer resolution. High resolution replica molding techniques provide a method for producing copies of some of these printed structures.

INTRODUCTION

General techniques for fabricating complex, three dimensional nanostructures are important to the future of nanoscience and technology. Historically, research and development in the area of micro/nanofabrication has been driven mainly by the needs of the microelectronics industry. The spectacularly successful techniques that have emerged from those efforts – photolithography, electron beam lithography, etc. – are extremely well suited to the tasks for which they were principally designed: forming structures of radiation sensitive materials (e.g. photoresists or electron beam resists) on ultraflat glass or semiconductor surfaces. Significant challenges exist in adapting these methods for three dimensional structures since the limited depth of focus restricts their use to patterning on flat surfaces. As a result, complex objects formed with these techniques must be generated using layer-by-layer strategies that can be slow and difficult to implement.

Some of the oldest and conceptually simplest forms of lithography – embossing, molding, stamping, writing, etc. – are now being re-examined for their potential to serve as the basis for nanofabrication techniques that are capable of producing complex three dimensional shapes [1]. Considerable progress has been made in the last few years, mainly by combining these approaches or variants of them with new materials, chemistries and processing techniques. This paper summarizes some of our past efforts to develop and apply to curved surfaces high resolution printing methods, in which a 'stamp' forms a pattern of 'ink' on a surface that it contacts. It briefly describes the techniques and presents some examples of their use in building functional three dimensional micro and nanostructures. It also shows that molding approaches which incorporate flexible, elastomeric molds can be used to replicate certain structures of this type.

EXPERIMENT

Figure 1 schematically illustrates approaches for building high resolution stamps and molds as pattern transfer elements. In this example, photolithography patterns a thin layer of resist on a silicon wafer. Stamps and molds are generated from this structure in one of two ways: by casting against this master or by etching the substrate with the patterned resist as a mask. In the first approach, the master itself can be used multiple times to produce many elements, typically using a light or heat-curable prepolymer. In the second, the etched substrate serves as the stamp or mold; additional elements can be generated either by repeating the lithography and etching, or by using the original stamp to print replica stamps. For minimum lateral feature sizes greater than ~1-2 microns, contact or proximity mode photolithography with a mask produced by direct write photolithography represents a convenient method to fabricate the master. For features smaller than ~2 microns, techniques such as projection mode photolithography or direct write electron beam (or focused ion beam) lithography can be used.

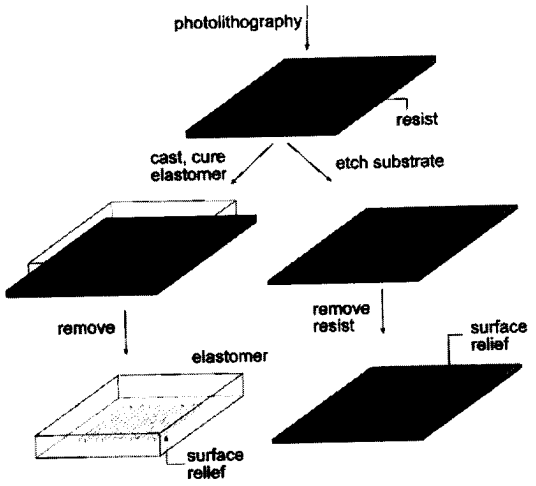

Figure 1. Procedures for building high resolution stamps and molds.

Microcontact printing (μCP) [2] provides one approach for printing with stamps formed out of the elastomer poly(dimethylsiloxane) (PDMS) according to the procedures shown on the left part of Figure 1. μCP was mainly developed for use with elastomeric stamps and inks that form self-assembled monolayers (SAMs) of alkanethiolates on gold and silver. The patterned SAM can be used, for example, as a resist in selective wet etching or as a template in selective deposition to form structures of a variety of materials. An attractive feature of μCP and other contact printing techniques is their ability to pattern features with high resolution on highly curved or rough surfaces [3,4,5]. Figure 2 shows, as an example, a

straightforward approach for high resolution printing on the highly curved surfaces of optical fibers. Here, simply rolling the fiber over an inked stamp prints a pattern on the entire outer surface of the fiber. Simple staging systems allow alignment of features to the fiber axis; they also ensure registration of the pattern from one side of the fiber to the other [6].

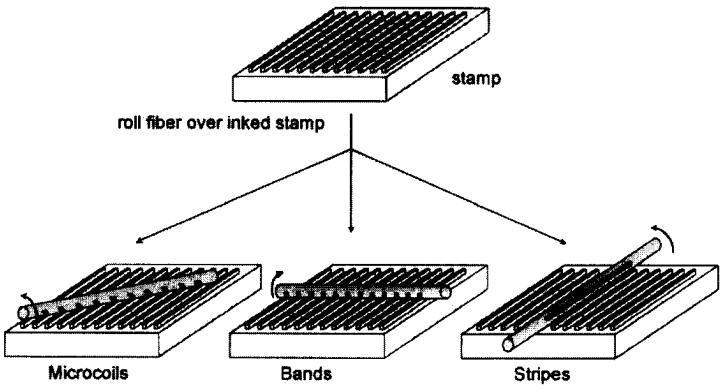

Figure 2. Procedures for printing coils, bands and stripes onto fibers.

Nanotransfer printing (nTP) is a more recent high resolution printing technique which uses surface chemistries as interfacial 'glues' and 'release' layers (rather than 'inks' as in μCP) to control the transfer of solid material layers from relief features on a stamp to a substrate [7,8,9]. This approach is purely additive (i.e. material is only deposited in locations where it is needed) and it can generate complex patterns of single or multiple layers of materials with nanometer resolution over large areas in a single process step. Unlike μCP, it does not suffer from surface diffusion or edge disorder in the patterned 'inks' nor does it require post-printing etching or deposition steps to produce structures of functional materials. Figure 3 presents procedures for using nTP to pattern a thin metal bilayer of Au/Ti with a surface transfer chemistry that relies on a condensation reaction [7]. Electron beam evaporation of Au (20 nm; 1 nm/s) and Ti (5 nm; 0.3 nm/s) generates uniform metal bilayers on the surface of a rigid or elastomeric stamp. A vertical, collimated flux of metal from the source ensures uniform deposition only on the raised and recessed regions of relief. The gold adheres poorly to the surfaces of stamps made of GaAs, PDMS, glass or Si. A fluorinated silane monolayer can reduce further the adhesion when, for example, a Si stamp (with native oxide) is used. The Ti layer serves two purposes: (i) it promotes adhesion between the Au layer and the substrate after pattern transfer, and (ii) it readily forms a ~3 nm oxide layer at ambient conditions which provides a surface where the dehydration reaction can take place. Exposing the titanium oxide (TiO_x) surface to an oxygen plasma breaks bridging oxygen bonds, thus creating defect sites where water molecules can adsorb. The result is a titanium oxide surface with some fractional coverage of hydroxyl (-OH) groups (titanol). Other surface chemistries, such as those based on self-assembled monolayers can also be used to control the transfer [8,9].

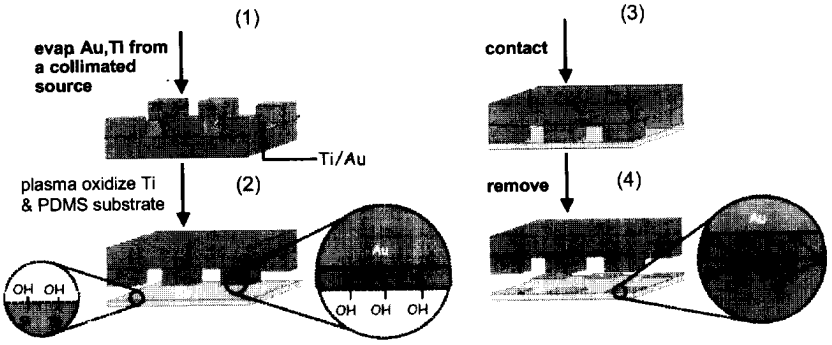

Figure 3. Procedures for nanotransfer printing.

RESULTS

Figure 4 shows scanning electron micrographs of patterns of gold and silver (Au: 20 nm thick, thermally evaporated with a 2.5 nm layer of Ti as an adhesion promoter; Ag: 100 nm thick formed by electroless plating) fabricated by μCP and wet etching on Si wafers. The

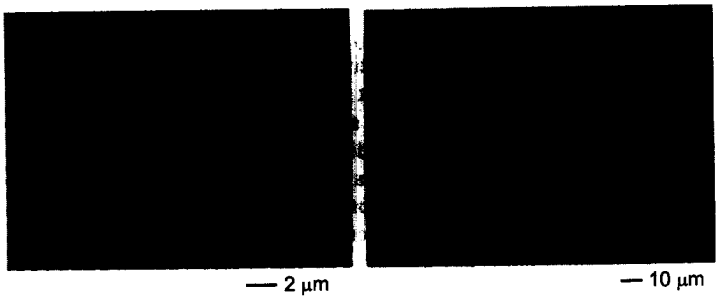

Figure 4. Patterns of Au and Ag formed by μCP

results indicate that patterns with edge resolution of ~100 nm are possible with μCP. Figure 5 shows a typical pattern formed with nTP [8]. The edge resolution in this case is 5-15 nm. Printing using the approaches illustrated in Figure 2 yields three dimensional micro/nanostructures on curved or non-flat surfaces. Figure 6 shows, as examples, 3 micron wide lines and spaces formed on the surface of a single mode optical fiber and a free standing metallic structure with the geometry and mechanical properties of an intravascular stent, which is a biomedical device that is commonly used in balloon angioplasty procedures. For the stent, μCP followed by electroplating generated the Ag microstructure on a sacrificial glass cylinder that was subsequently etched away with concentrated hydrofluoric acid [10].

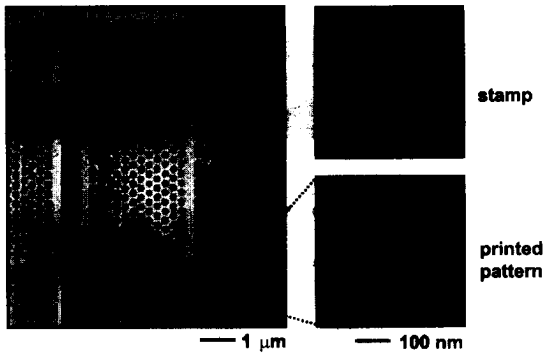

Figure 5. Patterns of Au with sub-micron features formed by nTP

These classes of three dimensional microstructures have many applications in unconventional optoelectronic and analytical systems. Figure 7 shows, as an example, a conducting microcoil printed, with μCP using the approach illustrated in Figure 4, on a microcapillary tube. The coil serves as the excitation and detection element for high resolution proton nuclear magnetic resonance of nanoliter volumes of fluid that are housed in the bore of the microcapillary [11]. The high fill factor and other considerations lead to extremely high sensivitity with such printed coils. The bottom frame of Figure 7 shows the spectrum of an ~8 nL volume of ethylbenzene [11]. Similar microcoils can be used as magnets [12], springs [10], electrical transformers [13] and inductors [12]. Examples of other optoelectronic components appear in fiber optics where microfabricated on-fiber structures serve as integrated photomasks [6] and distributed thermal actuators [4].

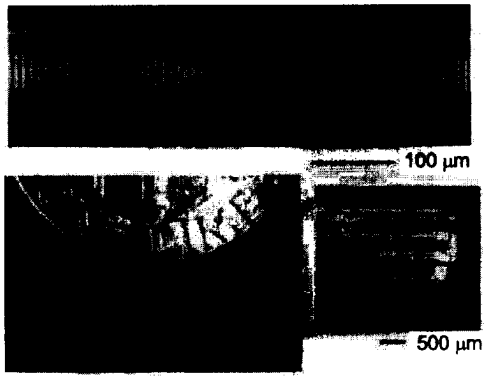

Figure 6. 3D structures formed by printing on cylindrical supports

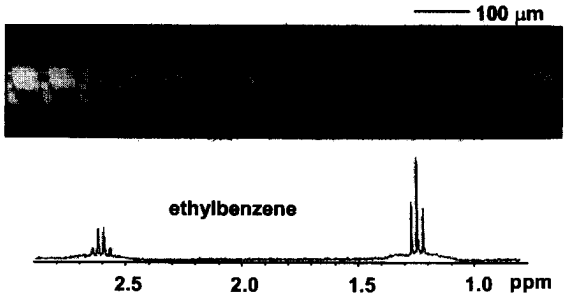

Figure 7. High resolution NMR on nanoliter volumes using printed microcoils.

Printing can also be used to form micro and nanopatterns on surfaces that are not continuously curved but which are non-flat. For example, μCP can be used to form distributed feedback (DFB) resonators directly on the top surfaces ridge waveguides [14]. Figure 8 illustrates the procedures; the bottom left frame shows an optical micrograph of the printed gold lines. Sublimation of a ~200 nm film of tris(8-hydroxyquinoline) aluminum (Alq) doped with 0.5-5.0 weight percent of the laser dye DCMII onto the resonators produces

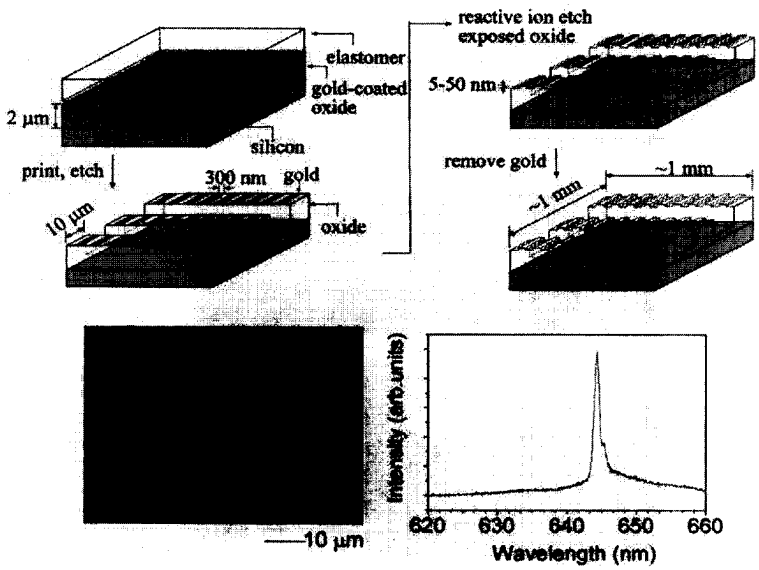

Figure 8. Fabrication procedures and performance of printed DFB waveguide lasers.

waveguide DFB lasers. The layer of gain material itself provides a planar waveguide with air and polymer as the cladding layers. The relief waveguide provides lateral confinement of the light. Photopumping these devices with the output of a pulsed nitrogen laser (~2 ns, 337 nm) causes lasing due to Bragg reflections induced by the DFB structures on the top surfaces of the ridge waveguides. Some of the laser emission scatters out of the plane of the waveguide at an angle allowed by phase matching conditions. The grating thus also functions as an output coupler and offers a convenient way to characterize the laser emission. The bottom right frame of Figure 8 shows the emission profile [14].

Once built, this type of structure can be used as a master to produce an elastomeric mold that can then be used for replication. Figure 9 shows procedures and results for the DFB waveguide structures of Figure 8 [15].

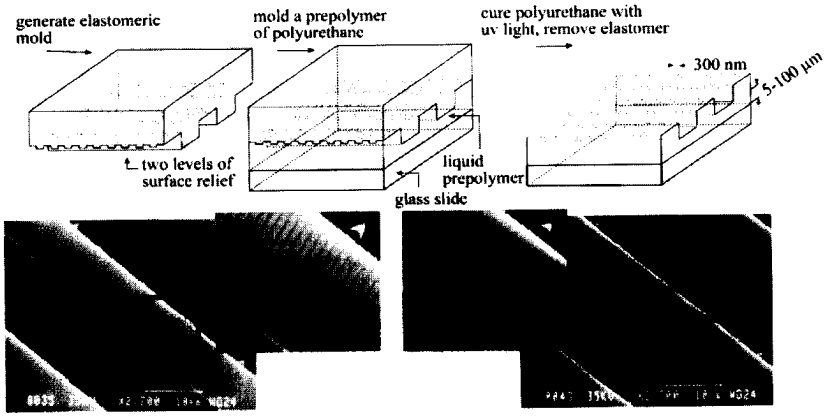

Figure 9. Nanostructures with three dimensional features of relief formed by molding.

The elastomeric nature of the molds allows not only replication of structures with multiple levels of relief but also elements that have re-entrant profiles. Figure 10 shows molding results which use an anisotropically etched piece of silicon as a master. The reentrant profile and the sharp edges are remarkable features of the molded polymer structure shown on the right.

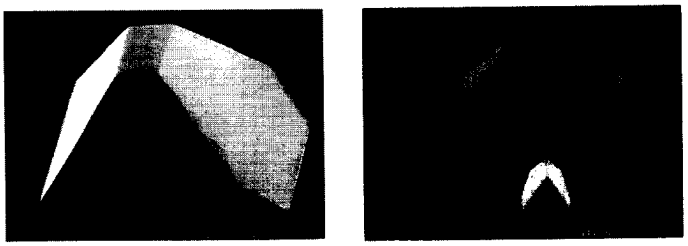

Figure 10. 3D re-entrant structures formed with an elastomeric mold.

CONCLUSIONS

This paper provides a brief overview of some of our past and current work in the area of printing and molding techniques for three dimensional micro and nanofabrication. While the approaches are promising, they do not represent, of course, truly general approaches to 3D. Nevertheless, they have important niche applications and they serve as valuable complements to other existing and emerging nanofabrication techniques that have three dimensional capabilities.

ACKNOWLEDGEMENTS

The author expresses thanks to all of his collaborators whose work appears in this paper.

REFERENCES

1. C.A. Mirkin and J.A. Rogers, *MRS Bull.* **26**, 506 (2001).
2. A. Kumar and G.M. Whitesides, *Appl. Phys. Lett.* **63**, 2002 (1993).
3. R.J. Jackman, J. Wilbur and G.M. Whitesides, *Science* **269**, 664 (1995).
4. J.A. Rogers, *MRS Bull.* **26**, 530 (2001).
5. R.J. Jackman, S.T. Brittain, A. Adams, M.G. Prentiss and G.M. Whitesides, *Science* **280**, 2089 (1998).
6. J.A. Rogers, R.J. Jackman, J.L. Wagener, A.M. Vengsarkar and G.M. Whitesides, *Appl. Phys. Lett.* **70**, 7 (1997).
7. Y.-L. Loo, R.L. Willett, K. Baldwin and J.A. Rogers, *Appl. Phys. Lett.* **81**, 562 (2002).
8. Y.-L. Loo, R.L. Willett, K. Baldwin and J.A. Rogers, *J. Am. Chem. Soc.* **124**, 7654 (2002).
9. Y.-L. Loo, J.W.P. Hsu, R.L. Willett, K.W. Baldwin, K.W. West and J.A. Rogers, *J. Vac. Sci. Techn. B.*, in press.
10. J.A. Rogers, R.J. Jackman and G.M. Whitesides, *Adv. Mater.* **9**, 475 (1997).
11. J.A. Rogers, R.J. Jackman, G.M. Whitesides, D.L. Olson and J.V. Sweedler, *Appl. Phys. Lett.* **70**, 2464 (1997).
12. J.A. Rogers, R.J. Jackman and G.M. Whitesides, *J. Microelectromech. Syst. (JMEMS)* **6**, 184 (1997).
13. R.J. Jackman, J.A. Rogers and G.M. Whitesides, *IEEE Trans. Magn.* **33**, 2501 (1997).
14. J.A. Rogers, M. Meier and A. Dodabalapur, *Appl. Phys. Lett.* **74**, 3257 (1999).
15. J.A. Rogers, Z. Bao, A. Dodabalapur, O.J.A. Schueller and G.M. Whitesides, *Synth. Met.*, **115**, 5 (2000).

Unconventional Fabrication Methods of Nanostructures

Mat. Res. Soc. Symp. Proc. Vol. 739 © 2003 Materials Research Society

Optical Nanolithography Using Evanescent Fields

Richard J. Blaikie, Sharee J. McNab[1] and Maan M. Alkaisi
MacDiarmid Institute for Advanced Materials and Nanotechnology,
Department of Electrical and Computer Engineering, University of Canterbury,
Christchurch, NEW ZEALAND
[1]Present address. IBM Thomas J Watson Research Center, PO Box 218,
Yorktown Heights, NY 10598, USA

ABSTRACT

In the optical near field region the well understood resolution limits for projection optical lithography can be overcome. This offers the possibility of performing optical nanolithography without the need to use expensive, deep ultraviolet light sources. For exposures that utilise evanescent fields close to metallic amplitude masks sub-diffraction-limited resolution has been achieved experimentally, and the theoretical resolution limits have been explored using vector electromagnetic near field simulations. Resolution down to 20nm using exposure wavelengths greater than 400nm is predicted. It is also found that the exposure wavelength is of secondary importance in this regime, and that the properties of the mask are much more significant. Scaling to smaller feature sizes requires better resolution and control during mask manufacture, rather than the conventional (and costly) approach of driving the exposure wavelength deeper and deeper into the ultraviolet. Near field interference effects have also been explored, and the characteristics of spatial frequency doubling using Evanescent Interferometric Lithography (EIL) have been determined by simulation. Sub-diffraction-limited resolution can be achieved with increased exposure intensity compared with conventional interferometric lithography. The trade-off is against the depth of field in the resultant interference pattern. Finally, the use of negative refraction and surface plasmons have been investigated to improve further the resolution in the evanescent near field, and to produce novel, three dimensional near field patterns.

INTRODUCTION

The resolution of conventional projection optical lithography is limited by diffraction, making it extremely challenging to fabricate sub-100 nm structures even using deep UV light sources and advanced wavefront engineering. However, by working in the optical near field the conventional diffraction limit can be overcome and nanopatterning can be achieved. Whilst this idea is not new [1,2], it is only relatively recently that detailed studies have been performed. The first demonstrations of sub-wavelength resolution near field nanolithography used serial scanning techniques [3,4], however for the rest of this review paper we will concentrate on parallel-exposure techniques.

Two near field lithography techniques have been developed using waveguiding or interference effects in transparent masks. Light-coupling masks (LCM) [5], using a conformal elastomeric material, consist of a surface relief pattern on a transparent mask. Flood exposure through this relief pattern induces near-field optical modes, and this waveguiding action amplifies the intensity in the protruding mask regions, resulting in contrast in the underlying resist. Structures with 240 nm periods have been exposed using a 248 nm wavelength source [5].

In a closely related near-field phase shifting mask (PSM) technique a conformal mask with a surface relief pattern that gives rise to a π phase shift at the step edge is used. In this case destructive interference close to this step edge can be used to pattern sub-wavelength features, and sub-100 nm structures have been demonstrated [6].

Near field exposure through amplitude masks has also been the subject of a number of studies, mostly variants on Smith's original Conformal Contact Lithography (CCL) technique [7]. Goodberlet has modified this technique to embed the absorber pattern into the mask substrate [8,9]. His embedded amplitude mask (EAM) consists of a thin, flexible fused silica mask with embedded Cr absorber patterns. There are a number of advantages of the having the absorber embedded: a flat mask would be expected to reduce local deformations around the absorber areas, the narrow regions between the absorber also improve waveguiding with their higher refractive index (akin to the LCM technique), and the planarity of the mask will protect the absorber and minimise particle contamination. Most recently the EAM technique has been used to reproduce sub-50 nm features using near-field interference effects from larger mask patterns [10]. Such resolution is difficult to achieve using other nanolithography techniques, and this represents the state of the art for experimental demonstrations of near field optical nanolithography.

An alternative to using a conformable mask with a rigid substrate is to use a rigid mask with a conformable substrate. Ono et al. [11] have replicated 500 nm period structures with such an arrangement. They formed substrates from 1 μm silicon diaphragms and performed a contact exposure with a standard chrome on glass mask using vacuum pressure and a mercury arc lamp source. However, the use of conformable substrates limits the range of devices that can be fabricated.

We have undertaken a series of extensive experimental and simulation studies of near field photolithography [12,13,14,15], and it is a review of this work that is the subject of the remainder of this paper. We have concentrated on the role of evanescent fields in the process, and our technique has been named Evanescent Near Field Optical Lithography (ENFOL) to emphasise this point. By utilising exposure from evanescent fields sub-diffraction-limited resolution has been demonstrated [12], and our simulation studies indicate that resolution below $\lambda/20$ should be possible [14]. In addition, the role of interference between evanescent fields [16], and the possible exploitation of near field plasmonic effects [17] have been investigated, and these simulation studies are also reviewed here.

In all of the above techniques the details of the contact lithography mask geometry and mask material are critical, as the evanescent fields around the mask play a large role in the exposure. There have been simulation studies reported on the effects of the mask geometry, with a recent comparative study [18] showing that an EAM gives superior transmission and contrast to a conventional metal-protruding mask, with further improvement possible using a LCM.

The remainder of the paper is structured as follows: in the next section the ENFOL experimental technique is described, and the best experimental results to date are presented; techniques for simulating the process are then given, and simulations are used to determine the ultimate resolution of the process; extensions of the ENFOL technique using near field interference and/or near field surface plasmon effects are the subjects of the final two main sections, pointing to directions for future work in this area.

EXPERIMENTAL TECHNIQUES AND RESULTS

The principle of our ENFOL technique is illustrated in Fig. 1. A conformable membrane mask is held in intimate contact with a photoresist-coated substrate, such that the mask-substrate gap g (including the photoresist thickness) is much less than the wavelength of the exposing light source. Under these conditions the optical field in the thin resist contains high spatial frequency evanescent components together with propagating diffracted components. The presence of these high frequency components makes resolution beyond the diffraction limit of projection lithography possible.

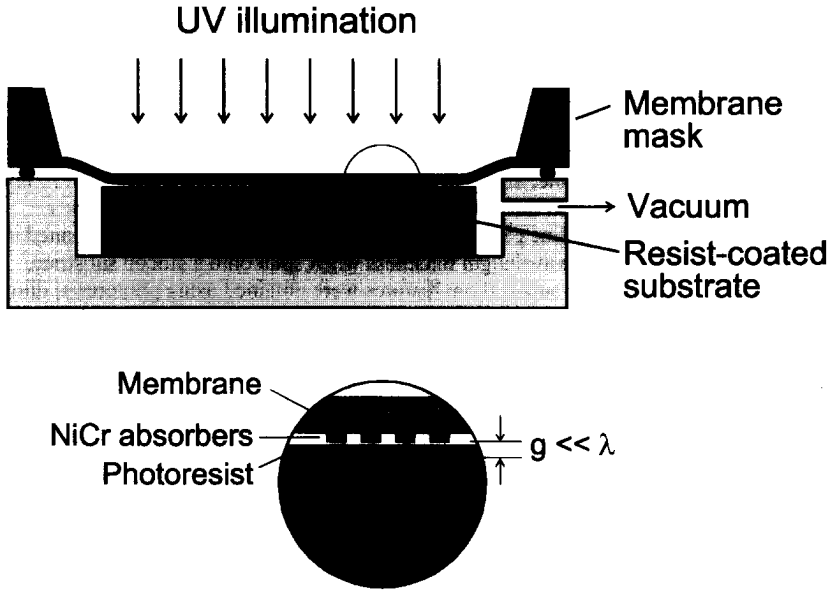

Figure 1. Schematic diagram illustrating the experimental ENFOL technique. Exposure is performed through a conformable mask held in intimate contact with a resist layer that is much thinner than the illuminating wavelength.

As can be seen from Fig. 1, the two main requirements for ENFOL are intimate mask-substrate contact over a large area, and ultra-thin (sub-100 nm) resists. Using a conformable mask held in contact with the resist by external pressure or the use of a vacuum can achieve the former, however the exact requirements for the resist thickness are not easy to determine. Trade-offs exist between the required resolution and the ease of performing pattern transfer with the resist after exposure and development. The process latitude for the exposure can also be severely degraded if the resist becomes too thin.

To achieve conformability our ENFOL masks are fabricated on 2 μm thick low stress silicon nitride Si_xN_y membranes. Typically, a 5×5 mm^2 square membrane is formed in the centre of a

larger silicon supporting substrate, and this is subsequently patterned with the ENFOL mask pattern using electron beam lithography (EBL). A polymethyl-methacrylate (PMMA) resist bilayer is used for the EBL: the bottom layer is spin coated using a 4% (by weight) solution of low molecular weight (120k) PMMA dissolved in chlorobenzene, and the top layer is spin coated using a 2.5% concentration of high molecular weight (996k) PMMA dissolved in xylene. A 30-minute pre-exposure bake at 185°C is performed following application of each layer. The bilayer resist was used to obtain an undercut profile desirable for the lift off metallisation process that was used to form the mask patterns. Arrays of 30 nm thick NiCr metal gratings of varying duty cycle have been used to define the opaque regions on the mask. The linewidths in the gratings vary from 2 μm down to 60 nm. The minimum grating period used to date is 140 nm (70 nm lines with 70 nm spaces), close to the resolution limits of our EBL machine.

ENFOL exposures were performed using a conventional mask aligner with mercury arc lamp having broadband illumination with dominant wavelengths between 313 and 600 nm. Exposures from the deep ultraviolet (UV) lines (313 and 334 nm) can be discounted due to absorption in the silicon nitride membranes, which transmit less than 2% of the incident light at these wavelengths. The most intense exposing wavelength is 436 nm (*g* line), with 61% transmission through the membrane, although there is significant exposure at 405 nm (*h* line) and 365 nm (*i* line) where transmission through the membrane is 29% and 9%, respectively.

A commercially available *g*-line photoresist (Shipley S-1805) has been used, thinned using PGMEA solvent to provide sub-wavelength thickness when spun onto a silicon substrate. Optimum results for reproducing sub-100 nm features were obtained using photoresist diluted 1:4 in PGMEA (60 nm thickness after spin coating) and an exposure time of 70 s. It should be noted that no strong feature-size dependent exposure times have been observed in our experimental work. This has been demonstrated by the ability to pattern micron-scale and nanometre-scale features at the same time and from the same mask.

Scanning electron microscope (SEM) images of the highest-resolution ENFOL-defined patterns obtained to date are shown in Fig. 2. The patterns have been dry etched approximately 100 nm deep into silicon to facilitate imaging. Figure 2(a) shows a 280 nm period grating formed by exposure through a mask with 70 nm isolated lines. After exposure, development and dry etching, the line width has been reduced to less than 50 nm, and there is some line edge roughness (LER) evident. It should be noted that the width of these lines is less than $\lambda_{min}/7$, where λ_{min} is the minimum exposing wavelength (365 nm). The period is approximately 0.77 λ_{min}. The pattern fidelity is uniform over the 20×20 μm^2 area of each grating on the mask, and uniform between gratings distributed over the 5×5 mm^2 mask. Figure 2(b) shows a 280 nm period grating formed by exposure through a mask with 70 nm apertures, the negative of the mask pattern used for Fig. 2(a). These 70 nm apertures are less than $\lambda_{min}/5$ wide, however, the exposure time for this pattern is the same as for patterns with large features. This indicates that there is no significant attenuation of the incident light through these sub-wavelength apertures. High transmission through sub wavelength sized circular aperture arrays has been previously reported [19], and was attributed to plasmon resonances. In our case, we have rectangular aperture that are long with respect to the wavelength, so high transmission of one polarisation will always be possible.

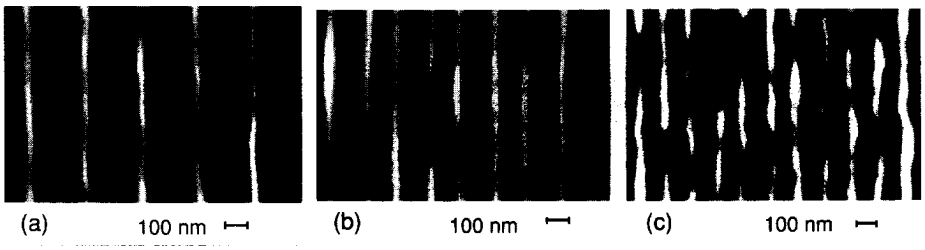

Figure 2. Scanning electron microscope images of patterns produced using ENFOL and subsequent reactive ion etching: (a) 280 nm period grating exposed through a mask with 70 nm lines, (b) 280 nm period grating exposed through a mask with 70 nm apertures, and (c) 140 nm period grating exposed through a mask with 70 nm lines and 70 nm apertures.

Figure 2(c) shows a 140 nm period grating, the smallest period structure that has been patterned to date. The lines in this pattern are discontinuous in places due to LER, however continuous lines are obtained for all patterns with periods greater than 200 nm. The 140 nm grating period is well below the diffraction limit for an equivalent projection lithography system. For normal incidence coherent illumination at wavelength λ the minimum resolvable period p_{min} in a projection optical lithography system is [20]

$$p_{\min} = \frac{\lambda}{NA}, \qquad (1)$$

where NA is the numerical aperture of the system . The maximum ***possible*** NA is equal to the refractive index of the imaging medium, n, which is 1.6 for the photoresist we are using. Therefore, the best result that projection lithography into this photoresist could achieve would be p_{min} = 228 nm for the shortest available exposure wavelength in our source (λ = 365 nm). The structure in Fig. 2(c) has a period 40% smaller than this. Index-matched projection lenses are not generally used so in practice a projection optical lithography system is limited to $NA < 1$. If, together with this, we consider the peak exposing wavelength transmitted through our masks (λ = 436 nm) then p_{min} = 436 nm and our experimentally demonstrated resolution is less than 1/3 of the diffraction limit for the equivalent projection system.

ENFOL's ability to pattern nanometre-scale and micron-scale features at the same time using the same exposure conditions is illustrated in Fig. 3. This figure shows a SEM micrograph for a grating structure of 2 μm lines with 1 μm spaces exposed and processed simultaneously with gratings that have periods down to 140 nm. These patterns show no pinhole defects and are uniform over the 40 × 40 μm^2 area of each grating on the substrate, and are uniform between fields distributed over the 5 × 5 mm^2 patterned area. This ability to simultaneously pattern large and small features is one of the benefits of ENFOL over other low-cost nanolithography techniques such as nano-imprint lithography [21].

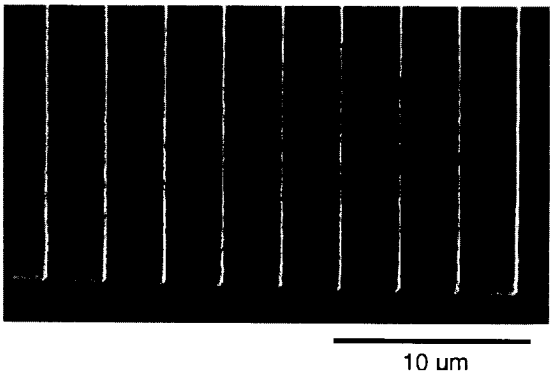

Figure 3. Scanning electron microscope image of 2 µm lines and 1 µm spaces produced using ENFOL. Patterns with feature sizes down to 70 nm have also been exposed and produced from the same mask in the same exposure.

Further experimental exploration of the resolution limits of ENFOL have proved difficult due to the challenges of fabricating sub-140 nm pitch gratings on the mask with EBL, and the inherent LER of the photoresists we have been employing (e.g. Fig. 2(c)). Whilst efforts are underway to overcome these experimental issues, much insight into the ENFOL process has been gained by performing simulation studies.

SIMULATION MODEL AND METHOD

The resolution achievements of scanning near field optical microscopy of better than $\lambda/40$ [22] suggest the potential for equivalent resolutions in near field lithography. An understanding of the near field mechanisms responsible for evanescent exposure are required to guide future ENFOL studies and to explore its potential as a nanolithography technique. To aid this, simulations have been undertaken using a rigorous electromagnetic technique to study the near field region behind conducting gratings.

The system that has been studied is shown in Fig. 4. A grating of period p (50% duty cycle) and thickness $t = 40$ nm is illuminated from above with either transverse magnetic (TM) or transverse electric (TE) polarised light of vacuum wavelength λ. The mask is embedded in a dielectric medium with refractive index n_1 and the underlying photoresist is assumed to have the same index, $n_2 = n_1$. This represents EAM lithography with an index-matched substrate. The grating fingers have a radius of curvature of 5 nm in the model to limit the field strength at the sharp corners.

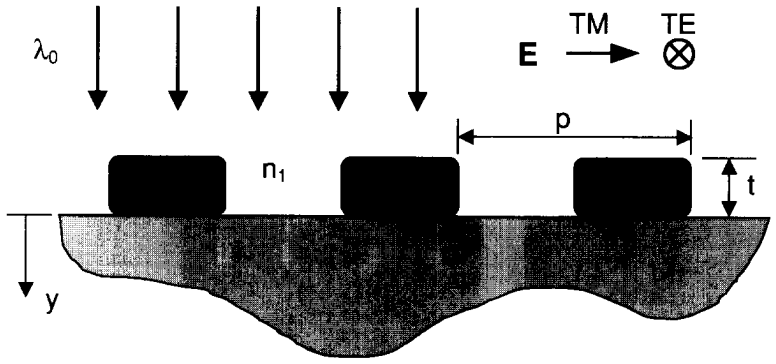

Figure 4. Schematic view of the simulated geometry. A grating with permittivity ε is embedded in a material of refractive index n_1 and brought into contact with a photoresist of refractive index n_2. This is exposed with light of vacuum wavelength λ_0.

The multiple multipole program (MMP) [23] has been used to calculate the electromagnetic fields throughout the system. A unit cell consisting of one period of the grating is computed while specialised periodic boundaries take into account the effects of surrounding conductors to obtain a solution for effectively an infinitely long grating. From this the normalised electric field intensity is determined, $I = |E|^2/|E_0|^2$, where $|E_0|^2$ is the incident intensity. This is used rather than the Poynting vector, as it is the electric field intensity that will be responsible for exposure of a photoresist.

Figure 5 shows the 2D normalised intensity $|E|^2/|E_{in}|^2$, where E_{in} is the incident electric field, for an ENFOL exposure of a 140 nm pitch Cr grating (ε = -13.24 + j14.62) into a 60 nm thick photoresist (n = 1.6) on silicon. The grating is illuminated at normal incidence by light with a wavelength λ = 436nm. For TE polarisation the light is blocked by the polarising nature of the sub-wavelength grating, but for TM polarisation a high contrast image of the grating is transferred into the photoresist. Two of the important characteristics of an ENFOL exposure are illustrated in this TM exposure simulation: the decaying amplitude of the intensity as we move further below the grating, and strong edge enhancements that are evident close to the exit aperture of the grating. In this case the intensity close to the 5 nm radius curves of the mask conductors is greater than twice the incident intensity. Such intensity enhancement is characteristic of evanescent fields close to metal-dielectric interfaces, and could be used to provide significantly reduced exposure times for near-field photolithography. This is one of the counter-intuitive findings of our simulations studies, as one might expect exposure times to increase for sub-wavelength structures due to the possible reduction in light transmission through them.

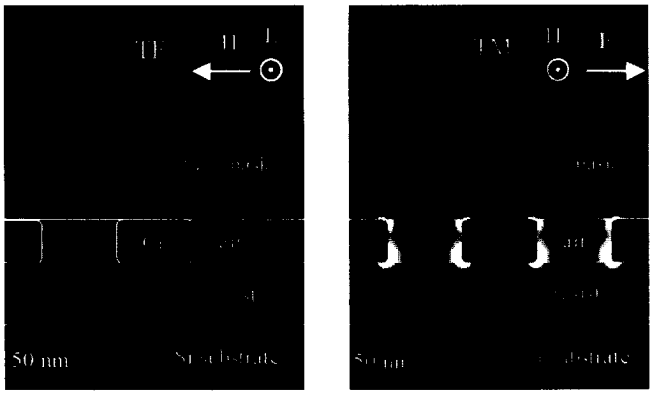

Figure 5. Normalised intensity distribution for ENFOL exposure through a 140 nm pitch, 40 nm thick Cr grating into a 60 nm thick resist layer on silicon. The grating is illuminated from above at 436 nm for both TE and TM polarisations. Contour plots of the normalised electric field intensity are shown $|E|^2/|E_{in}|^2$, where E_{in} is the incident electric field. The scale varies linearly from 0 (black) to 2.0 (white) in 10 linear steps.

The ultimate resolution of the ENFOL technique has also been explored by performing simulations of gratings with smaller and smaller periods [14]. Two main observations have been noted from these studies. Firstly, the depth of field of the resultant exposure pattern reduces linearly with the grating period, as illustrated in Fig. 6(a). Here the depth of field (DOF) is plotted as a function of grating period for a range of values of the resist contrast factor k (see [14] for full definitions of DOF and k). Secondly, in the deep-sub-wavelength regime these curves are found to be only weakly dependent upon the exposure wavelength; this has the important implication that the exposure wavelength can be chosen to best suit the resist to be patterned, rather than the usual requirement that exposure wavelength must be reduced in order to obtain improved resolution. From Fig. 6(a) we also highlight the fact that for ENFOL contrast is predicted in the first 5 nm of a resist even for grating periods as small as 20 nm. The intensity profile 5 nm below a 20 nm period grating is shown in Fig. 6(b). This period is less than $1/20^{th}$ of the exposure wavelength, and is also considerably less than the skin depth of the metal (Cr) used for the mask material. This predicted resolution ties in well with the ultimate resolution of near-field microscopy techniques [22], however experimentally achieving such resolution will be difficult.

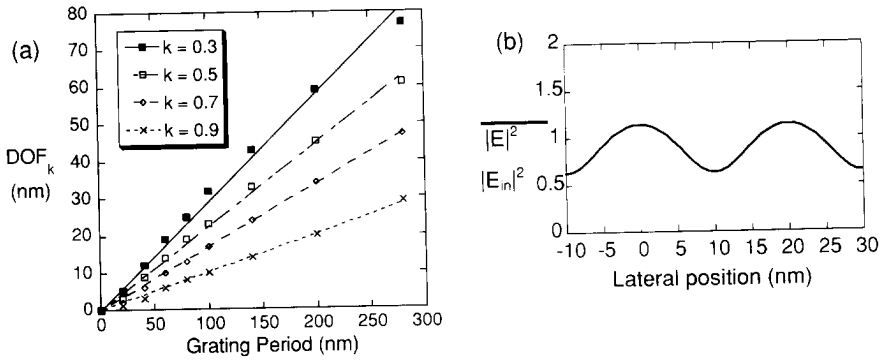

Figure 6. (a) Depth of Field (DOF_k) versus pitch p for simulated gratings plotted for values of the contrast factor, k, of 0.3, 0.5, 0.7, and 0.9. (b) Line plot of the intensity profile 5 nm beneath a 20 nm period grating exposed at 436 nm wavelength.

EVANESCENT INTERFEROMETRIC LITHOGRAPHY

The transition between the deep-sub-wavelength regime and that of conventional contact lithography (feature sizes larger than the wavelength) is also very interesting in the optical near field. When gratings that are close to being resonant with the illumination wavelength are exposed, strong near field interference patterns result. In particular, we have studied the case where all the diffracting orders are just beyond cutoff, and have called this the Evanescent Interferometric Lithography (EIL) regime [16].

Figures 7 and 8 show simulation of two cases that may be of particular interest for using near field exposures for three-dimensional patterning. In Fig. 7 the near field exposure pattern for a 1 μm period grating exposed at 436 nm is shown. A rich near field interference pattern is observed in both the TE and TM polarisations, which extends into the underlying resist with infinite depth of field (for a weakly absorbing resist), so could be used to pattern structures such as those required for making three-dimensional photonic crystals in a single exposure.

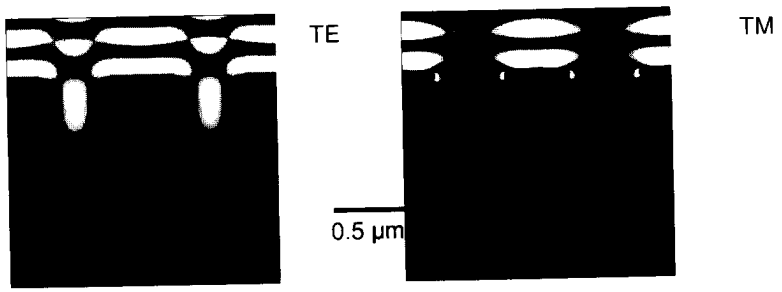

Figure 7. Near field interference patterns for a 1 micron period Cr grating embedded in air ($n = 1$) and exposed at 436 nm. Both TE and TM polarisation cases are shown.

Figure 8 shows the EIL effect, with a comparison between an exposure performed at cutoff of all propagating diffracted orders (Fig. 8(a)), and one performed at a slightly larger wavelength where all diffracted orders are evanescent (Fig. 8(b)). Remarkably, the intensity in the second case is enhanced by a factor of five compared with the first case (conventional interferometric lithography), which would result in considerably shortened exposure times. The trade off is with the depth of field of the exposure, which reduces as the exposure wavelength increases beyond cutoff. However this may also be advantageous for three-dimensional patterning in cases in which a shallow periodic structure was required to be superimposed upon an underlying layer without disrupting it.

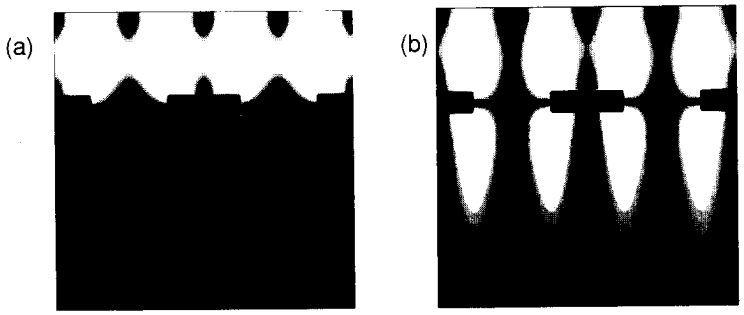

Figure 8. Near field TM interference patterns for a 270 nm period Cr grating embedded in a material with $n = 1.6$ for exposure wavelengths of (a) 432 nm and (b) 438 nm. Both TE and TM polarisation cases are shown. The normalized intensity scale varies linearly from 0 (black) to 2.0 (white) in 10 linear steps.

PERFECT LENSING EFFECTS

Following a recent proposal that suggests [24] that sub-diffraction-limited optical resolution can be achieved with a 'perfect lens' – a planar slab of material with a negative refractive index – we have investigated the implications this might have for near field photolithography [17]. Whilst not appearing in nature, negative-refractive-index materials can be engineered [25], although not yet at optical wavelengths. It is also predicted that perfect lensing is possible in the optical near field using a planar slab of metal illuminated near the plasma frequency, where the real part of the permittivity is negative [24] – we will call this a near field perfect lens (NFPL). By adding a NFPL layer to an ENFOL exposure stack it may be possible to perform *proximity* optical lithography whilst maintaining sub-diffraction-limited resolution. This is an attractive prospect, as it offers a path to non-contact, sub-50 nm optical lithography using conventional light sources.

Figure 9 shows a comparison of the simulated near field exposure profiles expected with and without a silver NFPL layer. Exposures are at $\lambda = 341$nm for a mask with period $p = 140$ nm, which is sub-diffraction limited. In Fig. 9(a), where a Ag NFPL ($\varepsilon = -1.0 + j0.4$) is included beneath the mask, two sub-diffraction-limited images of the mask are observed, the first in the

centre of the NFPL layer, and approximately 20 nm below it. This second image could be used for nanolithography by placing a photoresist in this plane. The intensity distribution for the non-NFPL case shown in Fig. 9(b) shows no similar lensing effects, but rather the intensity and visibility of this image decays smoothly with distance from the mask.

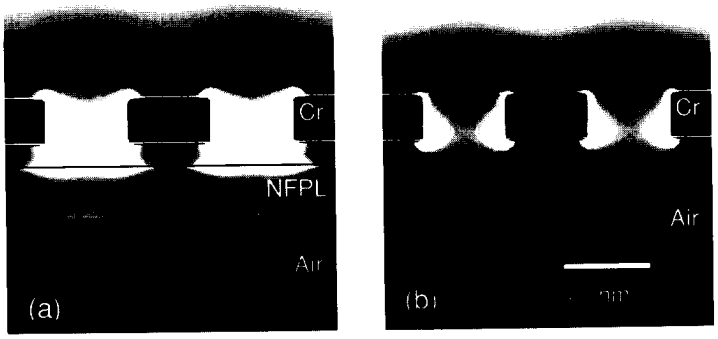

Figure 9. Near field intensity profiles for a 140nm pitch grating illuminated at 341nm, (a) with a near field perfect lens (NFPL) and (b) without a silver NFPL layer. The normalised intensity is plotted from 0 (black) to 2 (white) in linear steps of 0.1.

The ultimate resolution of this technique has also been explored in the simulation domain, and it is found that gratings with periods down to 40nm can be imaged using a NFPL. However, what is found from these simulation studies is that the focal position of the image beneath the NFPL varies strongly with both the period of the structure and the loss in the NFPL layer, as shown in Fig. 10. This is not expected from the simple description of a 'perfect lens' [24], but arises from the fact that the phenomenon is associated with the generation and coupling between surface plasmon polaritons on both sides of the NFPL. Such resonant couplings will be strongly dependent on the details of the local electromagnetic environment, as Fig. 10 suggests.

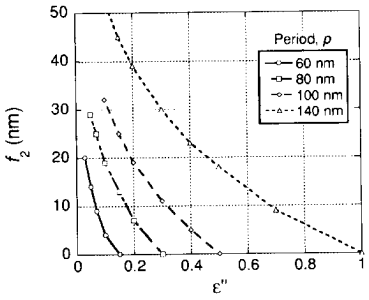

Figure 10. Variation in the second focal position f_2 for NFPL lithography through a grating with period p, using an NFPL with dielectric constant $\varepsilon = -1 + j\varepsilon''$. Exposure is at 341 nm and the 40 nm thick NFPL is positioned 20 nm below a Cr grating.

CONCLUSION

We have reviewed here the extensive work that has been performed on ENFOL and its related techniques. Sub-diffraction-limited resolution has been achieved experimentally and simulations point to resolution below 20 nm being achievable. Recent work has shown that the role of near field interference and surface plasmons is important in ENFOL; for example, the use of a thin silver 'perfect lens' may make non-contact (proximity) sub-100 nm optical lithography possible using low cost UV sources. This is an attractive and exciting prospect.

We acknowledge the assistance of the staff and students of the Nanostructure Engineering, Science and Technology group in performing this work, and are grateful to the Marsden Fund and the New Economy Research Fund for providing financial support.

REFERENCES

1 H. I. Smith , N. Efremow and P. L. Kelly, *J. Electrochem. Soc.* **121**, 1503 (1974).
2 U. C. Fischer and H. P. Zingsheim, *J. Vac. Sci. Technol.* **19**, 881 (1981).
3 S. Davy and M. Spajer, *Appl. Phys. Lett.* **69**, 3306 (1996).
4 V. Bouchiat and D. Esteve, *Appl. Phys. Lett.* **69**, 398 (1996).
5 H. Schmid, H. Biebuyck, B. Michel, O. J. F. Martin and N. B. Piller, *J. Vac. Sci. Technol B* **16**, 3422 (1998).
6 J. A. Rogers, K. E. Paul, R. J. Jackman and G. M. Whitesides, *Appl. Phys. Lett.* **70**, 2658 (1997).
7 H. I. Smith, *Rev. Sci. Instrum. B* **40**, 729 (1969).
8 J. G. Goodberlet, *Appl. Phys Lett.* **76**, 667 (2000).
9 J. G. Goodberlet and L. D. Bryan, *Microelectronic Engineering* **53**, 95 (2000).
10 J. G. Goodberlet and H. Kavak, *Appl. Phys. Lett.* **81**, 1315 (2002).
11 T. Ono and M. Esashi, *Jpn. J. Appl. Phys.* **37**, 6745 (1998).
12 R. J. Blaikie, M. M. Alkaisi, S. J. McNab, D. R. S. Cumming, R. Cheung, and D. G. Hasko, *Microelectronic Engineering* **46**, 85 (1999).
13 M. M. Alkaisi, R. J. Blaikie, S. J. McNab, R. Cheung, D. R. S. Cumming, *Appl. Phys. Lett.* **75**, 3560 (1999).
14 S. J. McNab and R. J. Blaikie, *Appl. Opt.* **39**, 20 (2000).
15 M. M. Alkaisi, R. J. Blaikie and S. J. McNab, *Adv. Mater.* **13**, 877 (2001).
16 R. J. Blaikie and S. J. McNab, *Appl. Opt.* **40**, 1692 (2001).
17 R. J. Blaikie and S. J. McNab, *Microelectron. Eng.* **61-62**, 97 (2002).
18 M. Paulus, H. Schmid, B. Michel and O.J.F. Martin, *Microelectron. Eng.* **57-58**, 109 (2001).
19 T. W. Ebbesen, H. J. Lezec, H. F. Ghaemi, T. Thio and P. A. Wolff, *Nature* **391**, 667 (1998).
20 P. Rai-Choudhury, (Ed.), *Microlithography, Micromachining, and Microfabrication. Volume 1: Microlithography*. SPIE Press, Washington, pp. 31-33 (1997).
21 S. Y. Chou, P. R. Krauss and P. J. Renstrom, *Appl. Phys. Lett.* **67**, 3114 (1995).
22 E. Betzig, J. K. Trautman, T. D. Harris, J. S. Weiner, and R. L. Kostelak, *Science*, **251**, 1468 (1991).
23 C. Hafner, *The Generalised Multipole Technique for Computational Electromagnetics* (Artech House, Boston, 1990).
24 J. B. Pendry, *Phys. Rev. Lett.* **85**, 3966 (2000).
25 R. A. Shelby, D. R. Smith and S. Schultz, *Science* **292**, 77 (2001).

Mat. Res. Soc. Symp. Proc. Vol. 739 © 2003 Materials Research Society

Fabrication of Ordered Metallic Nanocluster Arrays Using a Focused Ion Beam

Matthew D. McMahon, Anthony B. Hmelo, Rene Lopez, Wesley T. Ryle, Allen T. Newton, Richard F. Haglund, Jr., Leonard C. Feldman, Robert A. Weller[1], and Robert H. Magruder III[1,2]
Dept of Physics and Astronomy, Vanderbilt University,
Nashville, TN 37235, U.S.A.
[1]Dept of Electrical Engineering and Computer Science, Vanderbilt University,
Nashville, TN 37235, U.S.A.
[2]Dept of Chemistry and Physics, Belmont University,
Nashville, TN 37212-3757, U.S.A.

ABSTRACT

We have fabricated ordered arrays of gold nanocrystals on FIB-processed silicon substrates using electroless deposition. We have also fabricated ordered arrays of silver nanocrystals on silicon with diameters 40-60 nm separated by 180 nm center-to-center, using pulsed-laser deposition (PLD) to deposit silver on the substrate. The metal nanocrystal arrays are characterized using SEM as well as AFM and energy dispersive x-ray (EDX) analysis. AFM confirms particle sizes measured in SEM, and EDX analysis demonstrates that Ag preferentially clusters at sites that have been damaged by the ion beam. These results suggest that the FIB-PLD combination can be used to create ordered arrays of Ag nanocrystals with diameters of 10 nm or less.

INTRODUCTION

Ordered arrays of metal nanoclusters have potential applications as elements of nonlinear or near-field optical circuits, as sensitizers for fluorescence emitters and photodetectors, and as anchor points for arrays of biological molecules. Metal nanocrystals are strongly confined electronic systems with a band structure drastically altered by the small size of the system and the reduced population of conduction-band electrons. Their optical response is extremely sensitive to the size, size distribution and spatial arrangement of individual nanocrystals. This effort is focused on the fabrication of ordered metallic nanocrystal arrays for optical investigations. Our approach is to promote the formation of metal nanocrystals on a spatially arranged lattice of holes that has been prepared by focused ion beam (FIB) processing.

Periodic arrays of metal nanocrystals embedded in a dielectric have several interesting properties. The property we wish to exploit is the third-order nonlinear optical response of these arrays, which gives rise to such effects as intensity-dependent index of refraction. Ordered arrays using this property could be used in photonic circuits, particularly in interferometry schemes and all-optical switching. The purpose of the experiments described in this paper is to create ordered arrays of metal nanocrystals for such optical experiments.

EXPERIMENTAL

We use a FIB to create arrays of sites at which metal nanocrystals will nucleate and grow following the deposition of a heteroepitaxial metal layer. The principles of material removal via sputter erosion using the FIB are well known. [1, 2] Facilities at the Vanderbilt Nanofabrication Laboratory include the FEI FIB 200, which features a 30kV liquid Ga^{+} ion source. In the FIB, liquid gallium is drawn to a very small cone from which individual ions can be extracted. The ions are accelerated through 30kV and focused onto a substrate, where material is sputtered from the surface. The FIB is computer-controlled, and patterns of arbitrary complexity can be written to the substrate with user-defined pixel-addressable files. The smallest feature sizes that can be written with the FIB are 8 nm, according to manufacturer specifications. In practice, we have demonstrated 10 nm features. The experimental approach is to create ordered damage sites in Si and other substrates using the FIB, and to subsequently use deposition techniques to form nanoparticles, with the expectation that the particles will nucleate and grow at the selected sites.

We have experimented with two approaches to forming nanocrystals on the ordered sites: (a) electroless deposition of Au on Si through a thermal oxide mask which has been selectively prepared with FIB milling; and (b) pulsed-laser deposition (PLD). PLD is a versatile technique for depositing and growing nanoparticles and thin films of metals, semiconductors and insulators. In PLD, an excimer laser is used to ablate material from a target; the resulting ablation plume deposits the target material on a substrate. The laser parameters, deposition rate, and substrate temperature govern the nucleation and growth of nanocrystals.

RESULTS

Au nanoparticle arrays via electroless deposition

A heavily doped n-type (100) silicon wafer was cleaned in HF and thermally oxidized to produce a 20 nm layer of SiO_2. The FIB was used to mill an array of holes completely through the oxide layer, approximately 30 nm diameter on 200 nm centers. Following this step, gold was deposited in the holes by electroless deposition from solution (Alfa Aesar # 42307). SEM micrographs of typical array patterns are shown in Figures 1 and 2. Evident in the micrograph are gold nanoclusters, only some of which are congruent with array sites on the substrate. The lack of consistent deposition on the ordered sites is attributable to poor capillary wetting of the electroless reagents in the 30 nm holes. Both the Au nanocrystals and the array spacing are larger than are optimal for nonlinear optical applications; however, this result has laid the groundwork for future refinement of particle size and spacing.

Figure 1. SEM micrograph of an ordered array of gold nanoparticles created by FIB and electroless deposition. Note scale bar in lower right corner of all SEM images.

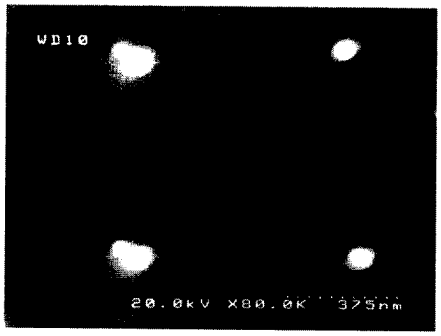

Figure 2. SEM micrograph of ~80 nm gold nanoparticles deposited by electroless deposition at ordered sites defined by the FIB.

Ag nanoparticle arrays via pulsed laser deposition (PLD)

The heteroepitaxial growth of Ag on Si has been of recent interest in the literature. [3, 4] We have successfully created two-dimensional ordered square arrays of Ag nanoparticles on Si using the combination of FIB milling and PLD. The FIB image Figure 3 displays a nanoscale hole array prepared in highly conductive (metallic) n-type silicon. The array was prepared at 80 kX magnification using a 1 pA Ga^+ ion beam with an effective spot diameter of 8 nm. The result was an array of 30 nm diameter holes on 120 nm centers. When FIB hole diameters are 30 nm or smaller, single Ag nanoparticles are observed on these selected sites as illustrated in Figure 4.

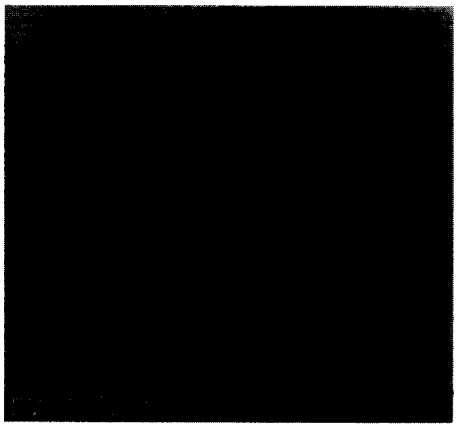

Figure 3. FIB-generated secondary electron image of FIB-milled hole array. The array has 27x27 holes and measures 2.5 μm on a side. Each hole is ~30 nm diameter.

Figure 4. SEM micrograph of 40-60 nm diameter Ag nanoparticles in ordered array created by FIB and PLD. The distance between adjacent particles is 180 nm.

DISCUSSION

It is generally accepted that surface and line defects such as surface steps and ledges act as preferred sites for the nucleation of metals on insulators and semiconductors. [5] Of interest in this investigation is the ability of the FIB to specify the location of specialized sites with nanoscale precision. By controlling the geometry of milled structures on silicon substrates we have been able to demonstrate that the specific nucleation sites are coincident with the location of a Si/SiO_2 interface.

When the FIB is used to prepare larger diameter holes (>80 nm), Ag particles are observed to assemble on the periphery of the hole structures, as illustrated in Figure 5.

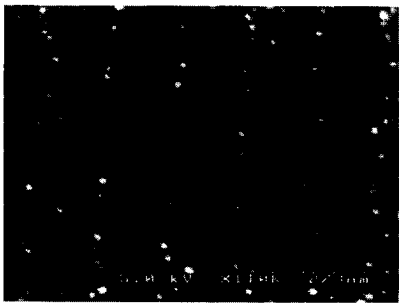

Figure 5. SEM micrograph of an ordered array of 150 nm diameter Ag "nano-bracelets" created with the FIB-PLD process. The individual particles making up the bracelets range from <10 nm to ~30 nm.

Here the oxide layer has been selectively thinned and removed in regions adjacent to milled array sites. This occurs because the Ga^+ ion beam has a Gaussian distribution of intensity that extends beyond the FWHM that defines the quoted spot diameter of 8 nm. The tails of the ion intensity distribution contribute additional sputtering on the periphery of the intended damage sites. Ag nanoclusters are observed to form on this periphery, presumably coincident with the location of the interface of the Si substrate and the oxide layer.

Ag particles have been observed to nucleate at FIB-damaged sites of arbitrary configuration, including straight line segments and right angles (Figure 6.) The observation that Ag particles will segregate to form linear arrays of discrete nanoparticles with a self-assembled diameter and spacing suggests the possibility of linear structures, such as plasmon waveguides.

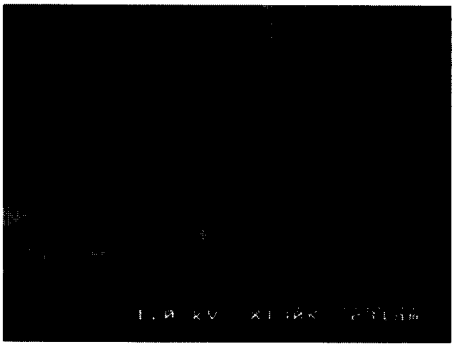

Figure 6. SEM micrograph of a linear array of Ag nanoparticles deposited via PLD around a right-angle bend milled with the FIB.

The demonstration of these structures gives an indication of the mechanisms responsible for nucleation. It is clear from these results that Ag, deposited via PLD, has a preferential nucleation site at or near the exposed interface of the silicon substrate and the overlying oxide. This conjecture is confirmed by experiments in which FIB holes were formed in bulk amorphous SiO_2 (glass). No preferential Ag accumulation was observed in that case. This observation rules out Ga-induced Ag clustering, simple SiO_2 defects or SiO_2 sidewall/surface interactions as mechanisms for the preferential nucleation. There appears to be unique stressor sites or other specialized interactions at the exposed interface.

CONCLUSIONS

We have demonstrated that Au and Ag deposited on oxidized Si via electroless deposition or PLD preferentially cluster at the sites we define with the FIB. In the case of Ag nanocluster formation possible nucleation mechanisms must involve the special sites associated with the Si/SiO_2 interface. Since the FIB is capable of creating feature sizes as small as 10 nm and Ag nanoparticles have been shown to form at FIB-defined features, we expect that arrays of particles as small as 10 nm diameter can be fabricated using the FIB-PLD method.

ACKNOWLEDGEMENTS

This research has been supported by the U.S. Department of Energy under grant DE-FG02-01ER45916, by the U.S. Army Research Office under grant DAAD 19-99-1-0283, and by the National Science Foundation through the Research Experience for Undergraduates (REU) program under grant DMR 9988030. The authors express thanks to Mr. Tim Miller for SEM work and training.

REFERENCES

1. C. Lehrer, L. Frey, S. Petersen and H. Ryssel, *J. Vac. Sci. Technol. B* **19**(6), 2533-2538 (2001).
2. S. Lipp, L. Frey, G. Franz, E. Demm, S. Petersen and H. Ryssel, *Nucl. Instr. and Meth. in Phys. Res. B* **106**, 630-635 (1995).
3. J.C. Glueckstein, M.M.R. Evans and J. Nogami, *Phys. Rev. B* **54**(16), R11 066 (1996).
4. M. Sakurai, C.Thirstrup and M. Aono, *Phys. Rev. B* **62**(23), 16 167 (2000).
5. J.A. Venables, *Surf. Sci.* **299/300**, 798-817 (1994).

Mat. Res. Soc. Symp. Proc. Vol. 739 © 2003 Materials Research Society H2.6

Construction of Spherical Assembly of Gold Nanoparticles Using Tetra[(methylthio)methyl]silane as Ligand

Mathew M. Maye, I-Im S. Lim, Jin Luo, Li Han, Daniel Rabinovich[a)], Sandy Chen, Michael P. Maye and Chuan-Jian Zhong*
Department of Chemistry, State University of New York at Binghamton, Binghamton, New York 13902; [a)] Department of Chemistry, The University of North Carolina at Charlotte, 9201 University City Boulevard, Charlotte, North Carolina 28223.

ABSTRACT

This paper reports a study on the assembly of gold nanoparticles via a tetradentate organosulfur ligand, tetra[(methylthio)methyl]silane. We have characterized the evolution of the assembly from individual nanoparticles to spheres (30 ~ 160 nm) of linked nanoparticles using UV-Visible, TEM, and AFM techniques. We have also demonstrated that the assemblies could be effectively disassembled via manipulating the ligand chemistry. Intriguing assembly-substrate interactions were observed, which could be related to interfacial hydrophobicity. Implications of these findings to the development of abilities in interfacial manipulation of the nanostructures are also discussed.

INTRODUCTION

The assembly of core-shell gold nanoparticles into functional thin films has a wide range of potential applications, including sensing, catalysis, drug delivery, microelectronics and medical diagnostics [1-2]. Many existing approaches have limited capabilities in manipulating the dimensionality of the assembly. While most synthetic approaches [3-4] explore the strong affinity of thiol groups to gold or silver surfaces, several recent reports involved the use of disulfides [5] or thioethers [6] as shell encapsulation. The thiolate-based chemistry is often exploited for nanoparticle assembly via crosslinking [7] such as stepwise assembling [8-10] and exchanging-crosslinking-precipitating [11]. The difference in metal-binding strength between thiols and thioethers, especially multidentate thioethers, may provide a new route for manipulating the dimensionality of the assembly and introduce chemical reversibility.

In this report, we focus on the results of a study of the assembly of monolayer-capped gold "core-shell" nanoparticles (Au_{nm}) using a tetradentate thioether, i.e., tetra[(methylthio)methyl]silane ($Si(CH_2SCH_3)_4$, (TTE). The chemistry of this assembly explores the TTE-mediated binding and interparticle linking of gold nanocrystals towards spherical assembly. We note that similar morphology has been reported recently using molecular recognition structures on polymers to mediate the assembly of gold nanoparticles [12]. The structural, morphological, dimensional and reversible properties of the assembly were characterized by UV-visible spectroscopy, transmission electron microscopy (TEM), and atomic force microscopy (AFM).

EXPERIMENTAL

Synthesis and Assembly: The core-shell nanoparticles utilized in this study were synthesized by the standard two-phased protocol [3] and were capped with monolayer shells of either tetraoctylammonium bromide (3.7 ±1.4 nm, TOA^+Br^--Au_{nm}) [3b] or decanethiolate monolayer (5.3 ±0.3 nm, DT-Au_{nm}) [13]. $Si(CH_2SMe)_4$ (TTE) was prepared similarly to the synthesis of $MeSi(CH_2SMe)_3$ [14], but starting from $SiCl_4$ and $LiCH_2SMe$. Both TTE, and TOA^+Br^--Au_{nm} were stored in toluene at room temperature and protected from light. Spherical Assemblies of TOA^+Br^--Au_{nm} were mediated by TTE ([TTE]= 10 μM, [Au_{nm}] = 1.0 μM) and soluble for 3-5 days. Spherical disassembly was performed with addition of 10 μM DT.

Instrumentation: UV-Visible spectra were acquired with a HP 8453 spectrophotometer. Reactions took place in a 1cm quartz cell.Transmission electron microscopy (TEM) was performed on Hitachi-H-7000 Microscope (100 kV). The samples were prepared by casting the nanoparticle solution onto a carbon-coated Cu-grid and followed by quick evaporation of the solvent. Atomic Force Microscopy (AFM) images were acquired using Digital Instrument's Nanoscope IIIa in "tapping mode." The nanoparticle solutions were drop-cast on freshly cleaved HOPG or MICA.

RESULTS AND DISCUSSION

1. UV-Visible Characterization. Upon addition of TTE into a TOA^+Br^--Au_{nm} solution, we observed an immediate color change from wine red to purple. The UV-Vis spectrum showed a red shift in the surface plasmon (SP) resonance band indicating a TTE mediated Au_{nm} assembly. The SP band is related to particle size, shape and particle-particle separation, and can be explained using Mie theory [15]. Figure 1 shows a typical set of UV-Vis spectra. The decrease in absorbance for the SP band at ~520 nm and a new peak at ~700 nm is evident. The spectral evolution was gradual, and was accompanied by a color change from red to purple after ~30 minutes. The purple solutions were stable for 3~5 days before precipitation of black powders was observed.

We found no colorimetric change when using DT-Au_{nm} with TTE. This observation can be understood on the basis that thiol has a much stronger interaction with gold than thioether, thus prohibiting the exchange between DT and TTE. In a control experiment no colorimetric change was detectable using a single-dentate thioether, e.g., butyrlsulfide (BS). The results demonstrate the difference in binding between TOA^+Br^-, TTE, and DT.

We also examined the possibility of dissassembly of TTE-Au_{nm} via alkanethiols. Upon addition of thiols (e.g., DT) into the solution of TTE-Au_{nm} we observed a reverse reaction, and subsequent purple to red color change. By monitoring the absorbance vs time for the evolution of the SP band for the starting solution of TOA^+Br^--Au_{nm} (521 nm) and the SP band for the TTE-Au_{nm} assembly (700 nm), we were able to follow the interparticle linking process. For example, when ~10 μM DT is added into the TTE-Au_{nm} solution, we observed a quick return of the SP band characteristic for isolated Au_{nm}. Both absorbance and wavelength of the SP band were largely reversed after ~15 minutes as shown by the nearly

identical position and intensity for the 520 nm band for individual particles. Interestingly the decrease of the ~700-nm shoulder band was complete in about the same amount of time for assembly, ~30 minutes. This observation demonstrated that the spherical TTE-Au_{nm} assembly could be disassembled via replacement of TTE by DT.

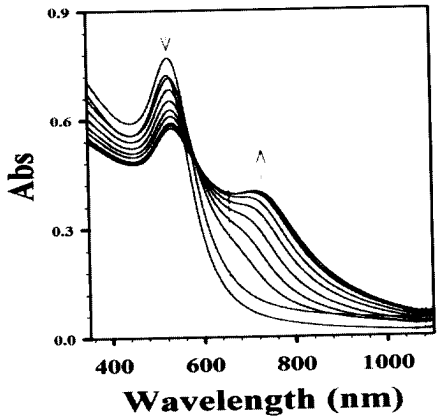

Figure 1. UV-Vis spectra of a toluene solution of TOA^+Br^--Au_{nm} upon the addition of TTE. The spectra were recorded in one minute intervals.

2. TEM Characterization. We examined the TTE-Au_{nm} product by sampling the reaction solution for characterization via TEM. Figure 2 shows a TEM micrograph from a typical sample.

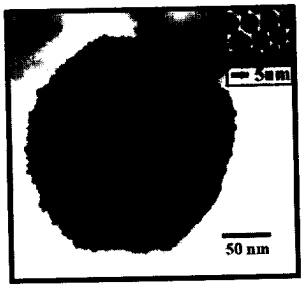

Figure 2. A representative TEM micrograph for a sample of a TTE-Au_{nm} assembly cast on carbon-coated Cu-grid. Insert: TOA^+Br^- capped Au_{nm} precursors.

The morphology of the TTE-Au_{nm} assembly is remarkable in terms of the shape. The nanoparticles form a 3D assembly with a spherical outline. The average diameter of the spherical assembly is ~160 nm based on multiple samples. The individual character of nanoparticles can clearly be seen on the periphery of the assembly. These individual

particles are similar to TOA^+Br^--Au_{nm} precursors (insert). This observation has demonstrated that the particles maintain their size within the spherical assemblies.

3. AFM Characterization. We further probed the morphology of the spherical assemblies on flat surfaces of a different hydrophobicity. Figure 3 shows a set of AFM images for the spherical assembly cast on two different substrates, HOPG (a) and Mica (b). Upon casting TTE-Au_{nm} onto HOPG we observed a unique wetting morphology. The spherical assembly showed an interesting melting-like phenomenon which appears to form a monolayer of Au_{nm} particles ~4-5nm. This phenomenon is perhaps best characterized by the deformation of the spherical assembly on the surface. This is most likely due to the highly hydrophobic nature of the HOPG surface. The hydrophobic spherical assembly is thus of a soft nature. Since the AFM imaging is performed in tapping mode, we believe that the tip had a relatively small effect on the morphology of the spherical assembly. We next imaged TTE-Au_{nm} on a Mica surface. On mica (B), the topographical feature is characterized by spherically-shaped islands of various sizes. In contrast to the HOPG surface, we observe no "melting" of the TTE-Au_{nm} spherical assemblies onto the surface, which again can be understood in terms of wetting properties. Since the x-y data are affected by tip-sample convolution for features smaller than ~ 50 nm [16], the spherical sizes for the such spheres may appear larger than the TEM-determined actual sizes. The z-scale data (i.e., height) for these spheres range from 30 nm to 80 nm, which reflect closely the TEM determined true size for the imaged sample. For the observed larger spheres (500-600 nm in the xy-plane), a likely scenario is the aggregation of the small spheres on the surface. An analogy to this phenomenon is the formation of large droplets of water from small droplets on surfaces. A further investigation of factors controlling this type of aggregation will be carried out by understanding the interfacial interaction properties of the hydrophobic spheres and the hydrophilic substrate.

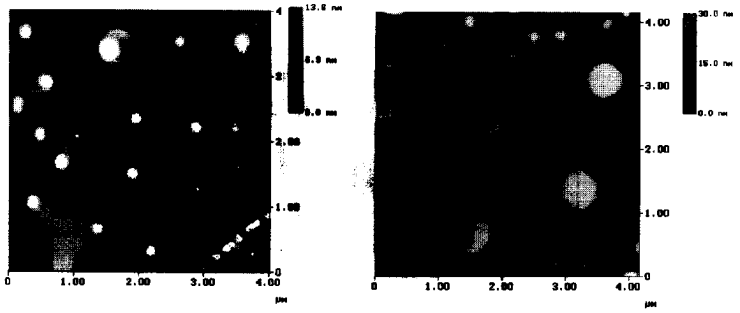

Figure 3: A set of AFM image of a TTE-Au_{nm} assembly ([TTE]= 20μM, [Au_{nm}] = 0.6 μM) cast on HOPG (A) and on MICA (B) surfaces.

These phenomenon can be understood by considering the difference of surface properties between mica and HOPG, and their interaction with the hydrophobic spherical assembly. The hydrophilic mica does not wet the spherical assembly and thus forms spherical islands.

In contrast, the hydrophobic HOPG surface wets the spherical assembly and consequently has the propensity of increasing the contact area and interaction between its surface and the spherical assembly. The fact that this interaction apparently led to the partial spreading of nanoparticles over the contacted surface of the spherical assembly is intriguing. We believe that this observation is indicative of the soft nature of the outmost layer of nanoparticles on the spherical assembly. This soft feature could form the basis of a new pathway for creating nanoscale linkage between individual 3D assemblies of nanoparticles.

We have also carried out infrared spectroscopic characterization for these nanoparticle assemblies. The displacement of the TOA^+Br^- shell on the gold nanoparticles by TTE was also confirmed by FTIR spectroscopic characterization of precipitation collected after two days of reaction. The data for the product after thorough cleaning revealed the disappearance of bands corresponding to the TOA^+Br^- structure and the appearance of bands corresponding to the TTE structure.

CONCLUSION

Based on the experimental observations, we concluded that the spherical assembly is mediated by the tetradentate ligand. We believe that the nanoparticles are linked by TTE at interfacial sites between neighboring nanoparticles. The spherical assembly process is likely to start with the encapsulation of one nanoparticle by TTE and followed by bonding to additional particles around the surface. This process likely repeats itself in a layer-by-layer fashion to grow into larger-sized spherical assemblies. While the spherical shape is comparable with those derived by thiolate or polymer chemistry [12,17,18], the fact that it can be disassembled by thiols and can be partially melted in its outmost layer into a monolayer on a hydrophobic surface has demonstrated a novel pathway for spherical assembly and engineering. An in-depth investigation of the structural effects and size or shape control of the ligand-mediated nanoparticle assembly is in progress, along with the manipulation of the spherical nanostructures on surfaces for technological applications.

ACKNOWLEDGEMENT

Financial support of this work is gratefully acknowledged from the ACS-PRF and the 3M grants. M.M.M. thanks the Department of Defense (Army Research Office) for support via the National Defense Science & Engineering Graduate Fellowship. D.R. also thanks Research Corporation for a Cottrell College Science Award.

REFERENCES

1 A.C. Templeton, W.P. Wuelfing, R.W. Murray, *Acc. Chem. Res.*, **33**, 27. (2000)

2 (a) J.J. Storhoff, C.A. Mirkin, *Chem. Rev.*, **99,** 1849 (1999). (b) X. Peng, M.C. Schlamp, A.V. Kadavanich, A.P. Alivisatos, *J. Am. Chem. Soc.*, **119**, 7019 (1997). (c) S. Mann, W. Shenton, M. Li, S. Connolly, D. Fitzmaurice, Adv. Mater., **12**, 147 (2000).

3 (a) M. Brust, M. Walker, D. Bethell, D.J. Schiffrin, R. Whyman, *J. C. S. Chem. Commun.*, 801, (1994). (b) J. Fink, C.J. Kiely, D. Bethell, D.J. Schiffrin. *Chem. Mater.*, **10**, 922 (1998).

4 M.J. Hostetler, J.E. Wingate, C.J. Zhong, J.E. Harris, R.W. Vachet, M.R. Clark, J.D. Londono, S.J. Green, J.J. Stokes, G.D. Wignall, G. L. Glish, M.D. Porter, N.D. Evans, R.W. Murray, *Langmuir*, **14**, 17. (1998).

5 Y.S. Shon, C. Mazzitelli, R.W. Murray, *Langmuir*, **17**, 7735, (2001).

6 (a) X.M. Li, M.R. de Jong, K. Inoue, S. Shinkai, J. Huskens D.N. Reinhoudt, *J. Mater. Chem.*, **11**, 1919 (2001). (b) L.J. Prins, D.N. Reinhoudt, P. Timmerman, *Angew. Chem. Intl. Ed.*, 2383 (2001).

7 (a) A.C. Templeton, M.J. Hostetler, C.T. Kraft, R.W. Murray, *J. Am. Chem. Soc.*, **120**, 1906 (1998). (b) R.S. Ingram, M.J. Hostetler, R.W. Murray, *J. Am. Chem. Soc.*, **119**, 9175 (1997). (c) M.J. Hostetler, A.C. Templeton, R.W. Murray, *Langmuir*, **15**, 3782 (1999). (d) A.C. Templeton, M.J. Hostetler, E.K. Warmoth, S. Chen, C.M. Hartshorn, V.M. Krishnamurthy, M.D.E. Forbes, R.W. Murray, *J. Am. Chem. Soc.* **120**, 4845, (1998).

8 (a) D. Bethell, M. Brust, D.J. Schiffrin, C. Kiely, *J. Electroanal. Chem.*, **409**, 137, (1996). (b) M. Brust, D. Bethell, C.J. Kiely, D.J. Schiffrin, *Langmuir*,**14,** 5425 (1998).

9 (a) M.D. Musick, C.D. Keating, L.A. Lyon, S.L. Botsko, D.J. Pena, W.D. Holliway, T.M. McEvoy, J.N. Richardson, M.J. Natan, *Chem. Mater.*, **12**, 2869, (2000). (c) F.P. Zamborini, J.F. Hicks, R.W. Murray, *J. Am. Chem. Soc.*, **122**, 4514, (2000).

10 (a) R. Elghanian, J.J. Storhoff, R.C. Mucic, R.L. Letsinger, C.A. Mirkin, *Science,* **277,** 1078, (1997). (b) J.K.N. Mbindyo, B.D. Reiss, B.R. Martin, C.D. Keating, M.J. Natan, T.E. Mallouk, *Adv. Mater.*,**13**, 249, (2001). (c) C.J. Loweth, W.B. Caldwell, X.G. Peng, A.P. Alivisatos, P.G. Schultz, *Angew. Chem. Intl. Ed.*, **38**, 1808, (1999).

11 (a) F.L. Leibowitz, W.X. Zheng, M.M. Maye, C.J. Zhong, *Anal. Chem.*,**71**, 5076, (1999). (b) W.X. Zheng, M.M. Maye, F.L. Leibowitz, C.J. Zhong, *Anal. Chem.*, **72**, 2190, (2000). (c) F.X. Zhang, W.X. Zheng, M.M. Maye, Y. Lou, L. Han, C.J. Zhong, *Langmuir,* **16**, 9639, (2000).

12 A.K. Boal, F. Ilhan, J.E. DeRouchey, T. Thurn-Albrecht, T.P. Russell, V.M. Rotello, *Nature,* **404**, 746, (2000).

13 M.M. Maye, W.X. Zheng, F.L. Leibowitz, N.K. Ly, C.J. Zhong, *Langmuir*,***16***, 490, (2000).

14 (a) H.W. Yim, L.M. Tran, E.D. Dobbin, D. Rabinovich, L.M. Liable-Sands, C.D. Incarvito, K.-C. Lam, A.L. Rheingold, *Inorg. Chem.*, **38**, 2211, (1999). (b) H.W. Yim, L.M. Tran, E.E. Pullen, D. Rabinovich, L.M. Liable-Sands, T.E. Concolino, A.L. Rheingold, *Inorg. Chem.*, **38**, 6234. (1999).

15 G.C. Papavassiliou, *Prog. Solid St. Chem,* **12,** 185-271 (1979).

16 M.M. Maye, J. Luo, L. Han, C.J. Zhong, *Nano Lett.*, **1**, 575, (2001).

17 E. Adachi, *Langmuir*, **16**, 6460, (2000).

18 J. Jian, I. Tomokazu, C. Changsheng S. Yanlin, J. Lei, J.L. Tie, B.Z. Dao, *Angew. Chem. Int. Ed.*, **40**, 2135, (2001).

Mat. Res. Soc. Symp. Proc. Vol. 739 © 2003 Materials Research Society

Application of a Focused Ion Beam System to Nanolithography

Richard M. Langford[1], Shamus O'Reilly and *Iain J. McEwen
Department of Materials, University of Oxford
Parks Road, Oxford, OX1 3PH, UK
*Chemistry Department, Heriot-Watt University,
Edinburgh, EH14 4AS, UK

ABSTRACT

Nano-imprint lithography (NIL) and micro-contact printing (MCP) are currently receiving considerable attention as techniques that can be used for low cost nanolithography. Here the application of a focused ion beam (FIB) system for the analysis of the elastomer stamps and imprinted patterns which are used in these nanolithography techniques is discussed. It is shown that the 'lift-out' technique can be used to prepare cross-sections of both the elastomer poly(dimethylsiloxane) (PDMS) stamps and the imprinted poly(methylmethacrylate) (PMMA) patterns. In addition, the use of the FIB system to prepare masters such as gratings and structures with curved shapes that would be difficult to fabricate using conventional processing techniques is discussed.

INTRODUCTION

Current optical based lithography is now reaching its limits of resolution, while focused electron beam (e-beam) lithography is a serial process and as such is inherently slow. Electron Projection Lithography (e.g. SCALPEL system developed by Lucent Technologies, USA) or Ion Projection Lithography (system developed by IMS GmbH, Vienna, Austria) offer sub-50nm resolution at a commercially viable wafer throughput but are not instruments readily available to researchers. Therefore, methods for nano-lithography, such as MCP and NIL, that offer low cost, high throughput processing are being developed. MCP involves making an elastomer stamp, normally by curing PDMS onto a master and using this to transfer and pattern an 'ink' for further processing. NIL involves imprinting a master, usually into PMMA and then using the patterned PMMA as a mask for subsequent processing. Using MCP, lines as narrow as 35 nm have been patterned [1], whilst using NIL holes 6 nm deep and 30 nm in diameter have been fabricated in PMMA [2]. These results are better than those achievable using optical lithography and are comparable to the line widths that can be obtained achieved using e-beam lithography. One tool which could have a considerable impact in the further development of these nanolithography techniques is a FIB system.

A FIB system is similar to a scanning electron microscope (SEM) except that a beam of ions is used instead of electrons. The system can be used to ion implant and sputter in areas as small as 10 – 20 nm^2 and to deposit metals and insulators in areas as small as 100 nm^2. In addition the secondary ions or electrons (SE) generated as the ion beam is scanned over the surface can be used for imaging enabling the milling or implantation to be made to within 50 nm of a feature of interest. As a result of these capabilities, FIB systems are now routinely used for the preparation of site-specific cross-sections of metals and semiconductors [3] and for the fabrication or modification of optoelectronic and magnetic devices [4,5]. Also, since the dwell time at a pixel

[1] Richard.Langford@materials.ox.ac.uk

can be varied while the ion beam is scanned over a sample, FIB milling has been used to micro-machine complicated 3-dimensional structures [6].

Here the use of a FIB beam system for the analysis of the MCP stamps and NIL imprinted patterns and the fabrication of masters for these nanolithography techniques is discussed. In the first part of the paper it is shown that TEM specimens through the stamps and imprinted patterns can be prepared using the external 'lift-out' technique. In the second part of this paper some of the results characterising FIB milling, such as the effect of different dwell times during milling are reported and some examples of FIB milled masters are given.

EXPERIMENTAL METHOD

The masters used to produce the MCP stamps and the imprinted patterns (to investigate the preparation of the cross-sections using the FIB system) were prepared in silicon using e-beam lithography and conventional processing. The sizes of the features in these masters ranged from 10 μm to 300 nm.

The thickness of the PMMA which was spun onto silicon for the NIL was 60 nm. The imprinting was done using a Dynamic Mechanical Thermal Analyser with forces up to 15 kN and at 160°C. The PDMS used was Slygard 182 (Dow Corning) and was poured over the masters and cured for 2 hours at 120 °C. The FIB system used was a FEI FIB 200 TEM, the TEM a JEOL 4000 EX and the SEM a JEOL 6300.

Application of the FIB system to the analysis of imprinted patterns and masters

A FIB system can be used to prepare cross-sections for both transmission electron microscopy (TEM) and SEM. For the preparation of TEM cross-sections two FIB techniques are routinely used: the 'lift-out' and the 'trench' technique. Detailed discussion of these techniques can be found in the literature [7]. Of the two, the 'lift-out' method involves milling away less material and as a result is much faster and is therefore used more often. Two staircase shaped boxes are milled on either side of the feature of interest and then the intervening region is milled until it is electron transparent. Next the base and sidewalls of the TEM specimen are cut to release it from the substrate and the TEM specimen is then lifted away from the substrate using a glass needle and micromanipulator and placed onto a carbon coated TEM support grid for

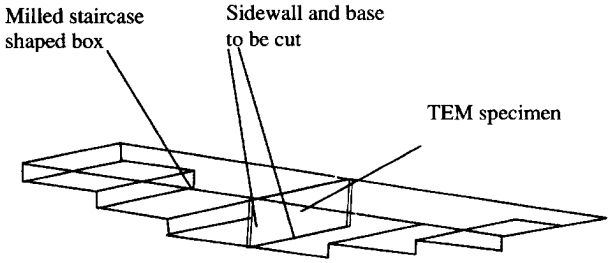

Figure 1. Schematic of FIB milled TEM specimen

subsequent TEM analysis. Figure 1 shows a schematic of a FIB prepared TEM specimen before its base and sidewalls have been cut. There were three concerns about using this technique for the preparation of specimens of the PDMS stamps and the imprinted PMMA. Firstly, that charging effects would cause the ion beam to drift so that it would not be possible to prepare the specimens at the feature of interest. Secondly, that sample beam interactions would result in the 'melting' of the polymer, making it difficult to thin the specimens in a controlled manner and thirdly, that after the specimens had been cut from the substrate it would be difficult to lift them

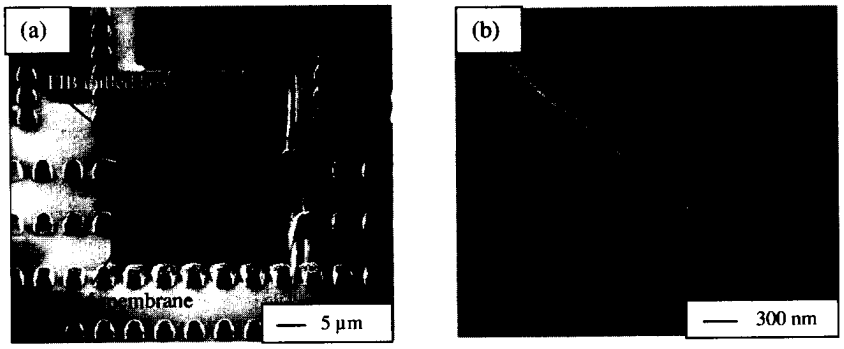

Figure 2. (a) SEM image of an array of PDMS 'buttons' viewed at 45° and (b) BF TEM image of a cross-sectioned 'button'.

out using the micro-manipulator and glass needle.

In the first experiments involving the MCP stamps and PMMA imprinted patterns it was observed that charging of the sample caused the ion beam to drift. In order to overcome this problem the samples were coated with a 100 nm thick carbon film by thermal evaporation. (Carbon was used in preference to gold as the gold would 'ball up' and form a discontinuous layer). As a result of coating with carbon it was subsequently possible to successfully mill the specimens to electron transparency. Having made the TEM specimens it was found that it was possible to lift them out using the glass needle and micromanipulator and to place them onto a TEM carbon support grid with a success yield of approximately 70%.

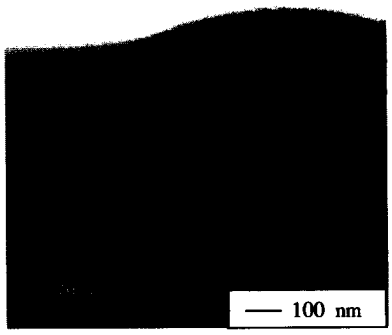

Figure 3. SEM image of a FIB cross-sectioned imprinted pattern.

Figure 2(a) shows a FIB SE image of a TEM specimen through an array of PDMS 'buttons' before it has been cut free from the specimen. The two staircase shaped FIB boxes milled on either side of the TEM specimen are clearly visible. Figure 2(b) shows a bright field (BF) TEM image of the cross-sectioned 'buttons'. The Pt layer, visible in the TEM image, was deposited using ion beam assisted breakdown to

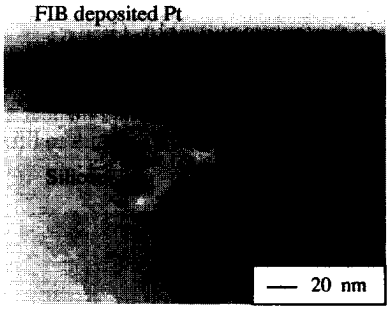

Figure 4. BF TEM image of a cross-section of a FIB milled line.

planarise the sample surface and to protect the top surface of the PDMS from being milled during ion imaging and the thinning of the specimen to electron transparency. The Si master used for this was coated in silicon nitride to reduce the sticking between it and the PDMS.

The procedure for making a cross-section for SEM or FIB analysis is very similar to that outlined above except that only one box is milled. Again for preparing the cross-sections of the stamps and the imprinted patterns it was necessary to coat them in a conductive carbon layer to prevent charging. Figure 3 shows a FIB SE image of a FIB cross-sectioned imprinted pattern. The Si master used consisted of a grating with a 3 µm periodicity and 1 µm depth. Important parameters, such as the imprinted depth into the PMMA and the accumulation of the displaced PMMA at the edge of the master can clearly be seen.

An advantage of using a FIB system to prepare the cross sections or TEM specimens is that the same regions on the masters, stamps and imprinted patterns can be cross-sectioned and thus directly compared. Using conventional sample preparation procedures, such as microtoming for

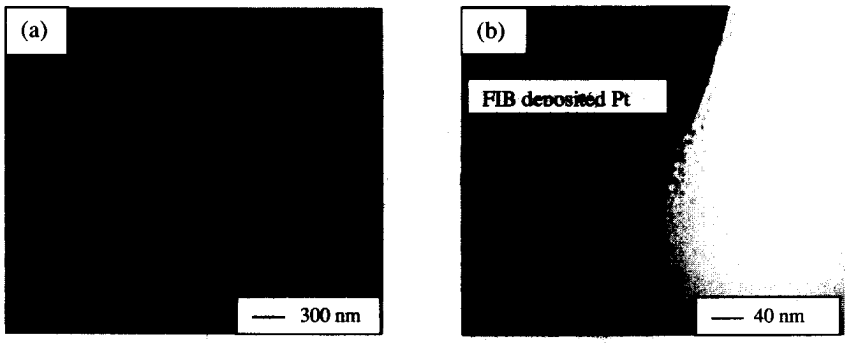

Figure 5. (a) SEM image of a grating in PDMS and (b) BF TEM image of a 50 nm ridge structure in PDMS.

the stamps and either broad ion beam milling or cleaving for the masters, it would almost be impossible to prepare cross-sections of the same region in each. We are currently using the FIB to assess the transfer reproduction of the master at different positions of the substrate and the effect of using masters with different geometries and feature densities.

Preparation of the masters using the ion lithography

This second section focuses on the use of FIB milling as a tool for preparing the masters rather than for analysing the stamps and imprinted patterns. In order to concentrate on this aspect the FIB milling of narrow lines in silicon and the effect of different milling conditions, such as the dwell times, are discussed. Figure 4 shows a BF TEM cross-section of a 30 μm long line milled into silicon using a 1 μs dwell time, a 1 pA beam and an ion dose of 2×10^{17} Ga cm^{-2}. The image shows that the milled line is grooved in cross-section and that its apex is 15 nm deep and it is 20 nm wide. This shape is a result of the ion beam profile and a dynamic interplay between re-deposition and sputter yield changes as the angle of incidence of the ion beam to the substrate varies. In figure 4 it can be seen that the groove is non-symmetrical. This can be attributed to the profile of the ion beam being non-symmetrical and mechanical drift of the stage during milling. For this ion dose, the depth and shape of the milled lines were found to be dependent on the milling conditions, such as the dwell time at the pixels and the percentage of beam overlap between adjacent pixels. For a dwell time of 100 μs the milled depth was found to be 30% less than when either a 1 μs or a 10 μs dwell time was used. It is possible that when milling with the 100 μs dwell time, a cone at the pixel is generated due to an increase in redeposition as the milled depth at the pixel increases. This eventually causes the milling at the pixel to become self-limiting in depth. For a dwell time of 1 μs and again a dose of 2×10^{17} Ga cm^{-2} the milled depth was found also to be dependent on the percentage of beam overlap between adjacent pixels. The maximum milled depth occurred when a 50% beam overlap was used. For both the 25% and 75% beam overlaps the milled depths were about 20% less. This is possibly due to the different beam overlaps resulting in different surface topographies. These cause different amounts of redeposition and result in different angles of incidence of the ion beam to the sample's surface and thus different sputter yields.

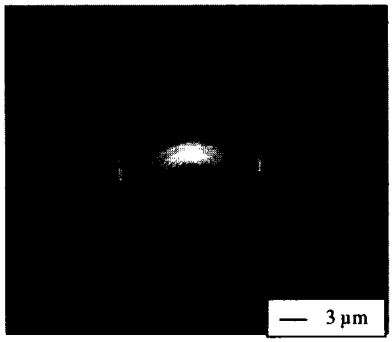

Figure 6. FIB SE image of 3-D structure milled into silicon.

The interplay between redeposition, the shape of the ion beam and changes in the sputter yield as a structure is milled was also found to affect the sidewall profiles of FIB milled gratings and vias. Generally, as the depth to width aspect ratio of a milled via or grating increases the solid angle over which the sputtered material can 'escape' decreases with the result that the amount of redeposition increases and the sidewalls of the vias or gratings become more tapered.

The minimum spacings and depths of gratings that can be transferred to PDMS and the suitability of these in terms of the mechanical properties required for printing are currently being assessed. Figure 5(a) shows an SEM image of a 300 nm period grating in PDMS which were 50 nm deep and Figure 5(b) shows a BF TEM image of a single 50 nm wide ridge in PDMS. The Si masters for both of these were milled using a beam current of 10 pA and a dwell time of 1 μs.

The milled structures in Figures 5(a) and (b) could have been prepared using conventional processing. However, FIB milling could be used to make masters with curved surfaces or varying step heights, as well as structures onto curved surfaces which are difficult to achieve

using conventional processing. Figure 6 shows a structure with curved surfaces which has been milled into silicon by making the dwell time at the pixels proportional to the milled depths. For either very deep or more complicated structures this simplistic approach results in large differences between the intended and final milled structures due to redeposition and changes in the sputter yield as the angle of incidence of the ion beam to the structure changes. More complicated milling procedures have been used which take these factors into account and which appear to achieve a good correlation between the intended and the actual milled structure [6]. The applicability of these more complicated milling procedures for the milling of vias and gratings with large depth to width aspect ratios and with near vertical sidewalls is currently being assessed.

DISCUSSION

The FIB system is a powerful tool which can be used to analyse the stamps and imprinted patterns and for preparing masters with structures that would be difficult to achieve using conventional processing. As the resultant cross-sections are site-specific to within 50 nm of a particular feature, preparing the cross-section with the FIB system enables the sidewall profiles of the stamps, imprinted patterns and masters to be assessed and compared at different regions of the substrates. In this work a FIB system with only an ion column was used. However, the latest FIB systems comprise of both an electron and an ion column. This combination will enable the stamps and imprinted patterns to be imaged with the electron beam and milled with the ion beam, thereby reducing the amount of milling due to ion imaging. The use of FIB systems with both electron and ion beam columns might also enable 3-D reconstruction [8] from a set of sequential cross-sections taken through the stamps and NIL patterns. This will enable slices to be then made through the stamps and patterns in directions other than that of the initial FIB milled cuts.

In conclusion it has been shown that a FIB system can have a considerable impact on the further development of both MCP and NIL in terms of analysing the patterns and preparing masters.

REFERENCES

1. H. A. Biebuyck, N. B. Larson, E. Delamarche and B. Micheal, IBM J. Res. Dev. **42**, 159 (1997).
2. S. Y. Chou, P. R. Krauss, W. Zhang, L. Guo and L. Zhang, J. Vac. Sci. Technol. B **15**, 2897 (1997).
3. L. A. Giannuzzi, J. L. Drown, S. R. Brown, R. B. Irwin and F. A. Stevie in *Specimen Preparation for Transmission Electron Microscopy of Materials IV,* edited by R.M.Anderson and S.D.Walck, (Mat. Res. Soc. Proc. **480**, 1997) pp. 19.
4. G. Pan, S. Takahashi, J. F. Walker, D. J. Mapps, K. Yamakawa, N. Honda and K. Ouchi, J. Magn. and Magn. Mater. **202**, 583 (1999).
5. A. Orth, J. P Reithmaier, J. Muller, A. Kieslich, A. Forchel, J. Weber, I. Gyuro and E. Zielinski, Microelectron. Eng., **27**, 347 (1995).
6. M. J. Vasilie, R. Nassar and J. J. Xie, Vac. Sci. Technol.B **16,** 2499 (1998).
7. R. M. Langford and A. K. Petford-Long, J. Vac. Sci. Technol. A **19,** 2186 (2001).
8. R. M. Langford, B. J. Inkson, G. Moebus and J. M. Titchmarsh, Inst. Phys. Conf. Ser. **168,** 135 (2000).

Mat. Res. Soc. Symp. Proc. Vol. 739 © 2003 Materials Research Society

Shape Variations and Control in Self-Assembled Metal Nanoclusters

M. Zubris[a], M. Solimando[a,b], E. P. Goldberg[b], S. Reich[c], and R. Tannenbaum[a]*

[a]School of Materials Science and Engineering, Georgia Institute of Technology, Atlanta, GA 30332, USA; [b]Department of Materials Science and Engineering, University of Florida, Gainesville, FL 32611, USA; [c]Department of Materials and Interfaces, Weizmann Institute of Science, Rehovot 76100, ISRAEL

ABSTRACT

The selective interaction of metal clusters with various polymers constitutes the basis for the self-assembly approach to the synthesis of organic-inorganic hybrid materials, that leads to the control of particle size, geometry and dispersion gradient. Metal particles were synthesized by the thermal decomposition of an organometallic precursor, in this case, iron pentacarbonyl, in the presence of a polymer matrix. Under the conditions utilized for these reactions, the aggregation of the metallic clusters competed with the interactions between the growing metal fragments and the polymer matrix. The dominance of one reaction route as compared to the other, ultimately determined the equilibrium particle shape, size and distribution for each metal-polymer system. In this work, we attempted to analyze the formation of iron oxide nanoclusters in several structurally-distinct polymers, and developed a general mechanistic view to explain the characteristics of the polymer-metal oxide hybrid materials that were obtained.

INTRODUCTION

Self–assembly represents a key approach to hierarchical ordering through length scales, where material properties at the molecular level determine the structure at the nanoscale, which further determines material characteristics at the mesoscale [1]. This results in unique materials properties, which cannot be achieved in disordered, or partially disordered systems. Such an approach has been applied to the synthesis of organic-inorganic nanocomposite structures, whereby metallic particles have been selectively incorporated into polymer matrices, and in turn, the polymer moiety has effectively controlled the size and shape of the particles. The ability to control particle size, size distribution, morphology, geometry and dispersion, directly translates to an ability to control the material properties of the polymer-metal nano-cluster composites [2-4]. Some studies have shown that metal nano-cluster formation is, indeed, sensitive to the presence of polymers during the synthesis process [5-7]. For example, Tang et al. [8] have shown that the size distribution of copper clusters formed in a polymer matrix host was narrow, centered on clusters of order 10 nm, while Pitcher et al. [9] produced novel morphologies of lead-sulfide in polyethylineoxide. Tannenbaum [10], Rotstein et al. [11] and Rotstein and Tannenbaum [12] have shown that both the mechanism of metal cluster formation and the equilibrium cluster size and cluster size distribution is a direct function of polymer concentration in the immediate environment of the cluster-forming process. However, little is known regarding the exact relationship between the characteristics of the polymer environment and the resulting metal cluster properties.

In this paper we will study the controlled synthesis of polymer/metal-cluster nanocomposites by self-assembly, that will enable the formation of metal clusters of precise geometries and dispersion gradients. The polymer molecules present in the system interact with the forming metal clusters [13-17], resulting in an adsorbed polymer layer on the surface of the metal cluster, or a "cap", thus preventing the cluster from undergoing further aggregation. The process of clusters formation is significantly influenced by the reactivity of the polymer chains and the effectiveness of the cluster-polymer interactions, the viscosity of the reactive medium, and the diffusion mechanism of small cluster fragments through this medium.

EXPERIMENTAL

Preparation of polymer composites

Ten (10.0) g polycarbonate pellets (LEXAN®, 131-111, $\overline{M}_W$ = *32,200* g/mol), or 10 g polysulfone (UDEL®, $\overline{M}_W$ = *30,100* g/mol), were dissolved in 43.9 mL or 41.5 mL methylene chloride (Fisher Reagent), respectively, and mixed 24 hours at room temperature in a 50 mL glass-stoppered Erlenmeyer flask. The methylene chloride solvent was dried using molecular sieve pellets (Matheson, Coleman and Bell). Iron pentacarbonyl (Alfa Products, Thiokol/Ventron Division) was filtered through filter paper circles (Whatman 7.0 cm, qualitative 4) into a foil-covered test tube. Then 1.0 mL was added dropwise to the above Erlenmeyer, now completely covered with aluminum foil. This solution of iron pentacarbonyl and polymer in methylene chloride was mixed for approximately five minutes and then film cast onto sheets of glass using a 0.005" or 0.020" steel doctor blade. All films were analyzed for iron content to determine actual $Fe(CO)_5$ retained.

Five (5.0) g polystyrene pellets (Polyscience, Inc., $\overline{M}_W$ = *159,400* g/mol), and 30.0 mL toluene (Fisher-Reagent) were mixed for 48 hours at 50 °C in an Erlenmeyer flask. The toluene was dried using molecular sieve pellets. When all polystyrene was dissolved, the solution was let to cool to room temperature, and the flask was covered with a foil. Filtered iron pentacarbonyl was added dropwise to the foil-covered flask of PS–toluene solution and mixed for five minutes. As before, all films are analyzed for iron content to determine the actual $Fe(CO)_5$ concentration retained.

Five (5.0) g PMMA pellets (Polyscience, Inc., $\overline{M}_W$ = *323,000*), and 32.2 mL chlorobenzene (Fisher-Reagent) were mixed for 48 hours at room temperature in an Erlenmeyer flask. The chlorobenzene was dried using molecular sieve pellets. Filtered iron pentacarbonyl was added dropwise to a foil-covered flask of PMMA–chlorobenzene solution and mixed for five minutes. The rest of the sample preparation was identical to the polycarbonate system.

Characterization of the polymers and iron oxide particles

Thermal decompositions were carried out in a temperature controlled vacuum oven with controlled atmosphere capability. Decomposition times and temperatures were varied for kinetic measurements. The infrared absorption band (measured on Nicolet MX-1 and

Nicolet Nexus 870 Fourier transform infrared spectrophotometers) at 1996 cm^{-1} was used to follow the kinetics of the thermal decomposition reactions in the composite films. An ethylbenzene reference solution of $Fe(CO)_5$ was used to determine the concentration of the carbonyl precursor using Noack's extinction coefficient of 8000 1 $mol^{-1}cm^{-1}$ [18].

Intrinsic viscosities ([η]) of polymers and composites were determined using a Brookfield viscometer (Brookfield Engineering Corp.). Solutions for PC and PS films were prepared in dioxane (Fisher Reagent) and then filtered through glass fiber filters just prior to viscosity measurements. Polystyrene and polymethyl methacrylate films were prepared from benzene solutions. Measurements were carried out at 25°C. The [η] was used to calculate viscosity-average molecular weights, $\overline{M}_W$, using the Mark-Houwink equation [19] and appropriate constants.

Particle size and shape were measured by transmission electron microscopy using both TEM (Hitachi HF-2000, JEOL 2010 and JEOL Model 200CX), and a high resolution TEM (JEOL 4000EX). The operating voltage was 200 keV for all three microscopes. Electron diffraction patterns from a TEM field emission gun were used to study the composition and morphology of metallic particles. Samples were prepared by placing a 0.1% solution of polymer and $Fe(CO)_5$ onto carbon coated (100 Å thick) TEM grids, removal of the solvent to form films, which were subsequently treated to decompose the $Fe(CO)_5$.

RESULTS AND DISCUSSION

Kinetics and mechanism of nanoparticle stabilization via polymer adsorption

The decomposition of $Fe(CO)_5$ in polymers of differing molecular structures is expected to lead to significant differences in polymer interactions and decomposition chemistry. As model systems for studying the preparation of metal-polymer composites with control of shape, size and size distribution, we selected $Fe(CO)_5$ as the organometallic precursor and the following polymers: polycarbonate (PC), polystyrene (PS), aromatic polysulfone (PSF) and polymethylmethacrylate (PMMA). These polymers were selected due to the different functional groups that they possess, resulting in various degrees of interaction with the growing metal particles.

The interactions between metallic iron fragments and the surrounding polymer may occur via two different mechanisms: (1) Bond formation between a coodinatively-unsaturated iron fragment and the functional groups of the polymer, resulting in a polymer-metal complex. This occurs due to the irreversible interaction of the functional groups on the polymer with the metallic species generated in the first stages of the decomposition reaction, and hence it directly competes with the metal-metal aggregation process; (2) Adsorption of polymer chains onto the surface of a large iron cluster via surface interactions. In this case, the surface interactions between the polymer and the metallic cluster are slower than the metal-metal aggregation process, and they take place upon the formation of a pseudo-stable metallic aggregate. In a given system, both mechanisms occur simultaneously, but the relative dominance of one or the other is a function of the polymer reactivity, polymer molecular weight, and type of metal precursor and its concentration [10,20-29].

The changes that occur in the polymer chains upon the thermal treatment in the presence of $Fe(CO)_5$ are summarized in Table I. Polycarbonate undergoes extensive chain scission during thermal decomposition with a reduction of ~85% in molecular weight. This is accompanied by the appearance of an infrared absorption band at 3510 cm^{-1}, corresponding to a hydroxyl group, and an infrared absorption band at 1675 cm^{-1}, corresponding to a COO^- group. The first step of the $Fe(CO)_5$ decomposition is most likely an attack by the iron carbonyl on the ester function of the polymer, followed by iron oxidation and scission of the polymer chain. The presence of water is supported by the formation of the OH and the COO^- groups and by the formation of δ-FeOOH particles, due to the reaction of water with Fe_2O_3. Since the scission of the polymer is extensive, it is most likely carried out by either $Fe(CO)_5$ itself, or by iron fragments in the early stages of aggregation. The bonding between the iron fragment and the polymer that is formed through this reaction is irreversible, and hence additional particle growth becomes suppressed.

For the PMMA composite, a reduction of ~15% in molecular weight was also noted upon decomposition of $Fe(CO)_5$. This was accompanied by the appearance of an infrared absorption band at 1672 cm^{-1}, corresponding to a COO^- group. The formation of this group suggests that the methoxy group of the PMMA was cleaved upon interaction with the iron oxide fragment, and removed from the interface. This was achieved by the hydrolysis of the ester bond at the interface, mediated by the iron oxide surface, to form a carboxylic acid whose hydroxyl group has an infrared absorption band at 2940 cm^{-1}, and subsequently the carboxylate ion. Since the ester group resides on the side chain of the polymer (unlike the PC system), the hydrolysis of the ester bond does not result in chain scission.

Table I: Summary of characteristic changes in the polymer matrices that occur upon the oxidative thermal in-situ decomposition of $Fe(CO)_5$. The wavenumbers in *italics* denote new infrared absorption bands that appear after the decomposition process is complete.

Polymer	**No Thermal Treatment**		**Thermal Treatment**	
	$\overline{M}_w \pm 1000$ g/mol	Characteristic Infrared Bands, cm^{-1}	$\overline{M}_w \pm 1000$ g/mol	Characteristic Infrared Bands, cm^{-1}
PS	159,400	1575	159,000	1575
PS + $Fe(CO)_5$	147,500	1996, 1575	127,800	1575
PC	32,200	1735	32,200	1735
PC + $Fe(CO)_5$	30,500	1996, 1735	4,400	***3510***, 1735, ***1675***
PSF	30,100	1362	31,600	1362
PSF + $Fe(CO)_5$	27,000	1996, 1362	21,250	1362, ***1235***
PMMA	321,200	1735	323,400	1735
PMMA + $Fe(CO)_5$	318,500	1996, 1735	291,800	***2940***, 1735, ***1672***

For the PSF composite, a reduction of ~30% in molecular weight was measured , and was accompanied by the decrease in the intensity of the 1362 cm^{-1} infrared absorption band, corresponding to the SO_2 group, and the appearance of the 1235 cm^{-1} infrared absorption band, corresponding to the SO_2^- group. This corresponds to a lower bonding order of the S=O bonds caused by the coordination to the surface of an iron oxide fragment. The coordination of the SO_2^- group to a metallic center does not necessitate chain cleavage, and hence this type of bonding can occur with both a discrete iron carbonyl complex and with the surface atoms of an iron oxide cluster. The various aspects of the metal-polymers interactions are shown in Figure 1.

The kinetics of aggregation of the iron oxide nanoclusters was based on the rate of decomposition of the iron carbonyl precursor, as evidenced by the decrease of the intensity of the carbonyl absorption bands of $Fe(CO)_5$ monitored by infrared spectroscopy. The progressions of the thermal decompositions of Fe(CO)5 in various polymeric matrices are shown in Figure 2a. The thermal decompositions were performed at 90°C, 118°C, 125°C, 132°C and 142°C. The rate constants were plotted as a function of temperature (Arrhenius plot) as shown in Figure 2b.

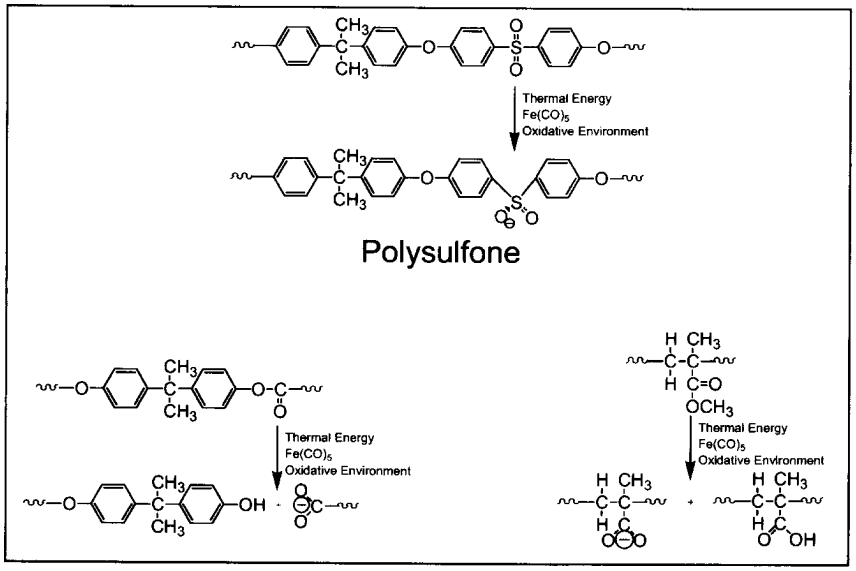

Figure 1: Schematic description of the reaction mechanisms of the various polymers with the iron moiety as detected by infrared spectroscopy.

The calculated rate constants and the activation energies for the thermal decompositions for each system are summarized in Table II. Note that the decomposition in a polymer matrix is *faster* than in solution. This observation has also been made in systems containing cobalt [10,27,30], where the decomposition and oxidation of $Co_2(CO)_8$ was two orders of magnitude faster in a solid polymeric matrix than in solution. PS and PC exhibit the higher rate constants among the various polymer systems.

The interactions between PS and the Fe fragments are expected to be weak, promoting metal-metal aggregation, while the interactions between PC and $Fe(CO)_5$ are expected to give rise to an extensive reaction, promoting metal-polymer complex formation. The activation energy of the PS system is lower than that of the other three polymer systems, suggesting that the oxidation and aggregation process in PS encounters a lower energetic barrier than in the other three polymer systems.

In view of the type of interactions observed between iron oxide fragments and the various polymers studied, it is possible to explain the results of the kinetic measurements and thermodynamic values. The overall reaction rate is evaluated through the decrease in the concentration of $Fe(CO)_5$ as a function of time, but it actually contains the contribution from the aggregation process and that from the discrete metal-polymer interaction process in a given system, as follows:

$$\left\{-\frac{d[Fe(CO)_5]}{dt}\right\}_{eff} = k_{agg}\cdot[Fe(CO)_5]_{agg} + k_{poly}\cdot[Fe(CO)_5]_{poly} \qquad (1)$$

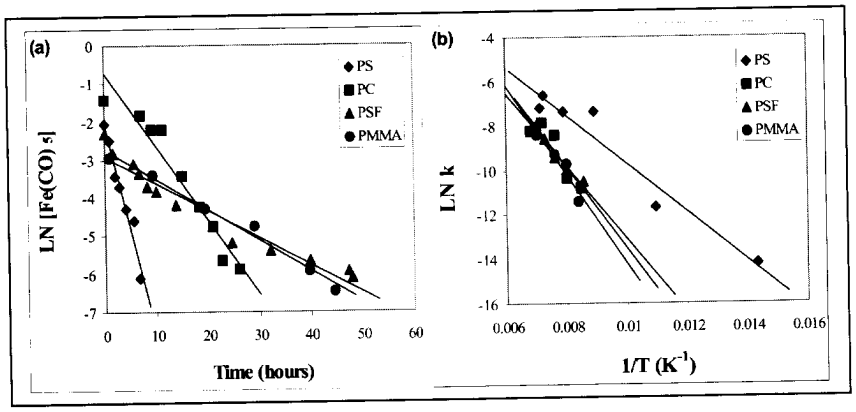

Figure 2: Kinetics of the thermal decomposition of $Fe(CO)_5$ in the presence of various polymers at ~90°C (2a) and the Arrhenius plot for the rate constant of the thermal decompositions at several temperatures.

Table II: Summary of the calculated rate constants and the activation energies for the thermal decompositions for each system

Polymer Composite System	Rate Constant at 132 °C (sec^{-1})	Activation Energy (kcal/mol)
$Fe(CO)_5$ - PS	$-5.59 \cdot 10^{-4}$	29.8
$Fe(CO)_5$ - PC	$-1.97 \cdot 10^{-4}$	33.6
$Fe(CO)_5$ - PSF	$-7.27 \cdot 10^{-5}$	31.2
$Fe(CO)_5$ - PMMA	$-7.65 \cdot 10^{-5}$	36.9
$Fe(CO)_5$ – Ethyl Benzene	$-8.69 \cdot 10^{-5}$	40.5

The effective reaction rate, and hence, the effective rate coefficient, will be that of the faster process. In the case of the PS system, the interactions between the iron oxide fragments and the polymer are limited, and hence the system is dominated by the aggregation process. On the other hand, in the case of the PC system, the metal-polymer interactions dominate. Both these systems exhibit comparable rate coefficients. In the case of PMMA and PSF, the interactions with polymer occur both at the molecular level and at the later stages of aggregations, between the polymers and the iron oxide clusters. Under these circumstances, small changes in the concentration of $Fe(CO)_5$ may result in large changes in reaction rates, and hence, since the overall rate is a combinations of both processes, the effective rate coefficients are smaller.

The thermal decomposition of $Fe(CO)_5$ in solid polymeric matrices produced heterophase metallic domains consisting of γ-Fe_2O_3 [31], based both on electron diffraction experiments and EDX data. The additional formation of β-FeOOH in some cases, indicates reaction with water present during decompositions in air as show below:

$$\gamma\text{-}Fe_2O_3 + H_2O \rightleftharpoons 2\,\beta\text{-}FeOOH \qquad (2)$$

Reaction of the passive γ-Fe_2O_3 particles with water is well known, and has been discussed by Griffith et. al. [32]. It should be noted, however, that it is the α-polymorph of FeOOH, which is normally formed. The β structure has been observed to form only during the breakdown of γ-Fe_2O_3 in the presence of chlorinated solvents. Thus, it is suggested that traces of CH_2Cl_2 present in the PC and PSF systems (supported by electron energy dispersive spectra) and atmospheric moisture are responsible for this reaction.

Characterization of iron oxide particles formed in various polymers

Transmission electron microscopy (TEM) images of the iron oxide particles formed in the polymeric media studied in this work exhibit interesting morphologies and distribution patterns, as shown in Figures 3 a-d. The γ-Fe_2O_3 particles formed in polystyrene (Fig. 3a) do not possess any particular geometric features, and are mainly

spherical in nature. This thermodynamically-favored morphology is expected in this case, since the metal-polymer interactions possible in this system cannot constitute a driving force for a kinetically-driven mechanism [33]. The same general pattern is also observed in the polysulfone system (Fig. 3b), but in this case, two different types of particles are formed: very small (~10nm) and very large (~200nm). This indicates the direct competition between the aggregation process and the metal-polymer interaction process, since the particles that experienced extensive interactions with the polymer remained small, while those that were able to aggregate, grew large. The fact that the TEM image reveals mainly two populations of particles, indicates that the adsorption of the polymer onto the surface of the cluster occurred early in the aggregation process, immediately upon the formation of irreversible nuclei, and that the kinetic of this adsorption was slower compared to the polymer-free aggregation process. This can be expected from the analysis of the type of interaction anticipated in this case, which involves conformational changes of the rigid backbone of the polymer.

In the case of polycarbonate (Fig. 3c) and PMMA (Fig. 3d), the metal-polymer interactions dominate the overall decomposition process, and hence the resulting particle morphology is largely driven by the kinetic details of the polymer adsorption. In the polycarbonate system, the reactive functional groups are an integral part of the main chain, and hence, the interaction with the iron oxide surface causes the scission of the chain in to small fragments. The particles attached to these fragmented domains come in closer proximity than otherwise possible in a larger chain, and additional aggregation becomes possible, as shown in the inset in Figure 3c. The resulting particles distribution shows "strings" of clusters aligned along the main chains of the polymer fragments. In the PMMA system, the reactive functional groups reside on the side chain, and hence, the interaction with the iron oxide surface does not cause a disruption of the main chain. In both these system, the polymers adsorb preferentially to specific crystallographic faces of the growing particles, giving rise to particle morphology that is kinetically driven rather than determined by equilibrium. The strong kinetic component in the determination of particle geometry has been shown with an iron oxide system in which the same polymer was used, but the thermal conditions of the reaction process were different, resulting in particles of different shapes [33].

SUMMARY

In this paper we used self-assembly techniques to develop a synthesis method that will enable the control of particle size, geometry and dispersion gradient. This was based on the selective interaction of the metal fragments with various functional groups in polymers. The metal clusters were therefore allowed to aggregate in-situ in the presence of a series of carefully chosen polymers. Hence, this led to the formation of distinct metallic phases within the polymer matrix.

The formation of the metal phases occurred via the thermal decomposition of an organometallic precursor in the presence of a polymer, creating a system in which the aggregation mechanism of the metallic clusters competed with the interactions between the growing metal fragments and the polymer matrix. The dominance of one reaction route as compared to the other, ultimately determined the equilibrium particle shape, size and distribution for each metal – polymer system.

The formation of uniform dispersions of iron oxides in a polymeric matrix, may give rise to a new class of composite materials with very interesting physical or electronic properties. By understanding the variables which govern decomposition chemistry, aggregation mechanism and polymer adsorption onto metal oxide nanoclusters, it is hoped to achieve the level of control regarding nanocomposite structure and properties that are currently only possible in naturally occurring self-assembled structures.

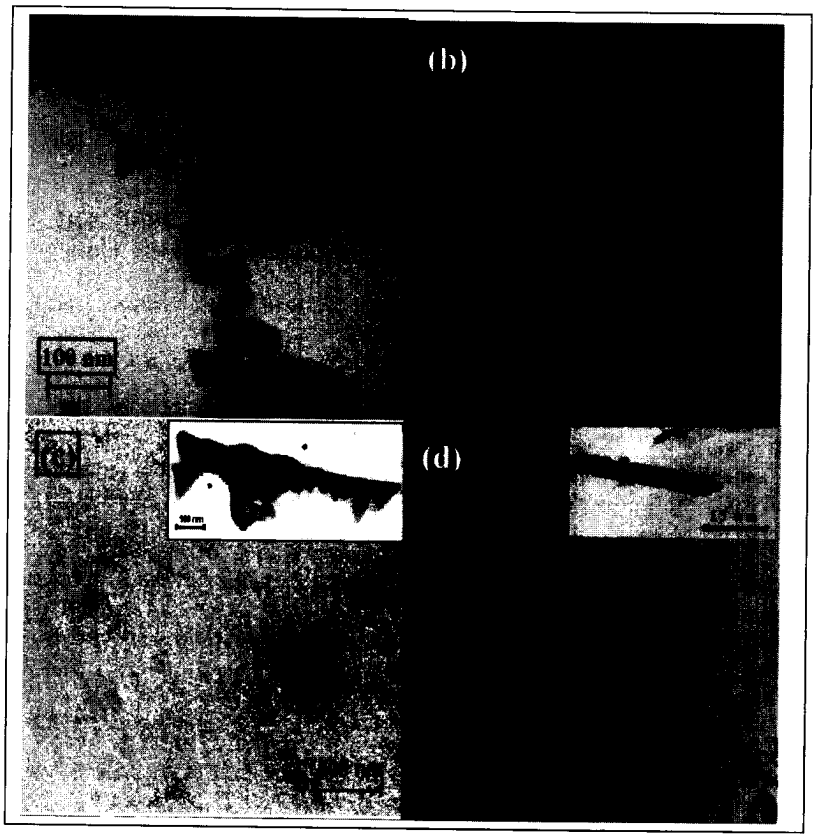

Figure 3: TEM images of the Fe_2O_3 particles formed in various polymeric matrices. (a) Iron oxide nanoclusters formed in PS with a magnification of 100,000; (b) Iron oxide nanoclusters formed in PSF with a magnification of 100,000; (c) Iron oxide nanoclusters formed in PC. The main image shows particles obtained with initial concentration of 10 wt. % $Fe(CO)_5$ and a magnification of 28,000. The inset image shows particles obtained with initial concentration of 30 wt. % $Fe(CO)_5$ and a magnification of 100,000; (d) Iron oxide nanoclusters formed in PMMA with a magnification of 100,000.

ACKNOWLEDGEMENTS

This work was funded by DARPA's "Metamaterials" program, the NSF-ERC (through the Packaging Research Center at Georgia Tech), the NSF-SURF program (to M. Solimando), The Georgia Tech Research Institute (GTRI), the Georgia Tech Foundation, the State of Florida Biomedical Engineering Center of Excellence, and the College of Engineering at Georgia Tech.

REFERENCES

1. A. M. Belcher, P. K. Hansma, G. D. Stucky, and D. E. Morse, *Acta Mater.* **46**, 733-736 (1998).
2. A. P. Alivisatos, A. L. Harris, N. J. Levinos, M. L. Steigerwald, and L. E. Brus, *J. Chem. Phys.* **89**, 4001 (1988).
3. C. F. Kernizan, K. J. Klabunde, C. M. Sorensen, and G. C. Hadjipanayis, *J. Appl. Phys.* **67(9)**, 5897 (1990).
4. L. E. Brus, *J. Phys. Chem.* **90**, 2555 (1986).
5. J. S. Bradley, J. M. Millar, and E. W. Hill, *J. Am. Chem. Soc.* **113**, 4016 (1991).
6. G. Schmid, B. Morun, and J.-O. Malm, *Angew. Chem.* **101**, 772 (1989); *Angew. Chem. Intl. Ed. Engl.* **28**, 778 (1989).
7. J. Kiwi, and M. Grätzel, *J. Am. Chem. Soc.* **101**, 7214 (1979); N. Toshima, and T. Takahashi, *Bull. Chem. Soc. Jpn.* **65**, 400 (1992).
8. J. G. Tang, K. Hu, H. Y. Liu, D. Guo, and R. J. Wu, *J. App. Pol. Sci.* **76**, 1857-1864 (2000).
9. M. W. Pitcher, E. Cates, L. Raboin, and P. A . Bianconi, *Chem. Mat.* **12**, 1738-1742 (2000).
10. R. Tannenbaum, *Langmuir* **13(19)**, 5056 (1997), and pertinent references therein.
11. H. G. Rotstein, A. Novick-Cohen, and R. Tannenbaum, *Stat. Phys.* **90(1/2)**, 119 (1998).
12. H. G. Rotstein, and R. Tannenbaum, *J. Phys. Chem. B* **106(1)**, 146 (2002).
13. L. M. Bronstein, D. M. Chernyshov, P. M. Valetsky, E. A. Wilder, and R. J. Spontak, *Langmuir* **16(22)**, 8221-8225 (2000).
14. D. Zanchet, B. D. Hall, and D. Ugarte, *J Phys Chem. B* **104(47)**, 11013-11018 (2000).
15. Z. Tang, and E. Wang, *J. Electroanal. Chem.* **496(1-2)**, 82-87 (2001).
16. H. Pardoe, W. Chua-Anusorn, T. G. St. Pierre, and J. Dobson, *J. Magn. Magn. Mater.* **25(1-2)**, 41-46 (2001).
17. J. P. Stevenson, M. Rutnakornpituk, M. Vadala, A. R. Esker, S. W. Charles, S. Wells, J. P. Dailey, and J. S. Riffle, *J. Magn. Magn. Mater.* **225(1-2)**, 47-58 (2001).
18. K. Noack, *Helv. Chim. Acta* **45**, 1987 (1962).
19. F. W. Billmeyer, "*Introduction to Polymer Science and Technology*," Eds. H. S. Kaufman, and T. T. Falcetta, Wiley-Interscience (1977), p. 186.
20. J. M. Ball, J. Carr, and O. Penrose, *Commun. Math. Phys.* **104**, 657 (1986).
21. P. J. Flory, and T. G. Fox, *J. Am. Chem. Soc.* **73**, 1904 (1951).
22. P. J. Flory, "*Principles of Polymer Chemistry*," Cornell University Press, Ithaca, New York (1953).
23. W. W. Graessley, *Adv. Polym. Sci.*, **16**, 1 (1974).

24. R. B. Bird, C. F. Curtis, O. Hassager, and R. C. Armstrong, "*Dynamics of Polymeric Liquids: Vol. 2, Kinetic Theory*," 2nd ed. (1st ed. 1976), Wiley, New York (1987).
25. P. G. deGennes, "*Scaling Concepts in Polymer Physics*," Cornell University Press, Ithaca, New York (1979).
26. M. T. Reetz, W. Helbig, S. A. Quaiser, U. Stimming, N. Breuer, and R. Vogel, *Science* **267**, 367 (1995).
27. E. Tadd, J. Bradley, and R. Tannenbaum, *Langmuir* **18(6)**, 2378 (2002).
28. R. Hariharan, and W. B. Russell, *Langmuir* **14(25)** , 7104 (1998).
29. N. Dan, *Langmuir* **16(8)**, 4045 (2000).
30. R. Tannenbaum, C. L. Flenniken, and E. P. Goldberg, *J. Polym. Sci., Polym. Phys. Ed.* **25**, 1341-1358 (1987), and pertinent references therein.
31. S. Reich, and E. P. Goldberg, *J. Polym. Sci. Polym. Phys. Ed.* **21(6)** , 869-879 (1983).
32. C. H. Griffiths, M. P. O'Horo, and T. W. Smith, *J. Appl. Phys.* **50(11)**, 7108-7115 (1979).
33. R. Tannenbaum, S. Reich, C. L. Flenniken, and E. P. Goldberg, *Adv. Mat.* **14(19)**, 1402-1405 (2002).

Mat. Res. Soc. Symp. Proc. Vol. 739 © 2003 Materials Research Society

Dendrimer Mediated 'Bricks and Mortar' Self-Assembly of Nanoparticles

Benjamin L. Frankamp, Andrew K. Boal, and Vincent M. Rotello
Department of Chemistry University of Massachusetts, Amherst
Amherst MA, 01301

ABSTRACT

Control of particle-particle spacing is a key determinant of optical, electronic, and magnetic properties of nanocomposite materials. We have used poly(amidoamine) (PAMAM) dendrimers to assemble carboxylic acid-functionalized mixed monolayer protected clusters (MMPCs) through acid/base chemistry between particle and polymer. IR spectroscopy and selective dendrimer staining, observed by Transmission Electron Microscopy (TEM), establish that the PAMAM dendrimers are the mortar in the assembly and act to space the MMPCs in the resulting aggregates. Small angle X-ray scattering (SAXS) was then used to establish average interparticle distances; five generations of PAMAM dendrimer (0, 1, 2, 4, 6) were investigated and monotonic increase in interparticle spacing from 4.1 nm to 6.1 nm was observed.

Initial studies involving the application of this methodology to control the magnetic properties of □-iron oxide nanoparticles have been completed. γ-Iron oxide nanoparticles (6.5 nm in diameter) have been assembled with PAMAM dendrimers generations 2.5, 4.5, and 6.5. The resulting aggregates were characterized with SAXS and magnetization obtained on a super conducting quantum interference devise (SQUID). An observed correlation between the blocking temperature (T_B) and the average interparticle spacing suggests that our methodology could be used to tailor the magnetic profile of the nanoparticles.

INTRODUCTION

Many properties including collective magnetism, electronic interactions and optical transitions can be directly related to the volume of the nanoparticle. It is possible, however, to modulate these bulk properties by controlling interparticle interactions through the control of interparticle spacing. Martin et. al. have shown that one can effectively control interparticle spacing by varying the length of the monolayer protected clusters' (MPCs) monolayer [1]. While their method is provides reliable spatial control it is limited to practical chain lengths diminishing its effectiveness. Noncovalent spacing control was demonstrated in our lab using a random copolymer functionalized with a diaminotriazine and a thymine functinalized mixed monolayer protected clusters (MMPC) [2]. Specific noncovalent interactions between polymer and nanoparticle monolayer resulted in a singular interparticle increase from non-assembled to assembled. Dendrimers have many favorable properties for this type of assembly combining positive attributes of both assembly methods mentioned above [3]. By altering the generation of the dendrimer, in effect increasing total molecular weight, branching, and size, we can easily increase the space between the particles mirroring the method reported by Martin. Furthermore the dendrimers shape is malleable allowing it to effectively fill the space in between the particles similar to the linear polymeric mortar. We report here an investigation of the structural characteristics, interparticle spacing, of nanoparticle dendrimer composite materials as a function of dendrimer generation (figure 1).

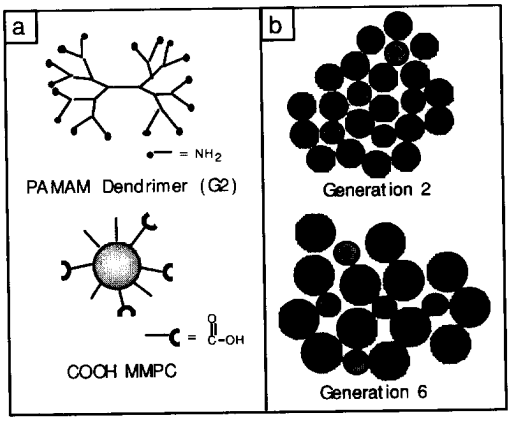

Figure 1. a) Each component of the assembly process possesses complimentary bonding units b) As the generation of dendrimer is increased the average interparticle spacing should increase accordingly.

EXPERIMENTAL DETAILS

MPCs were prepared in a toluene/water mixture using the Brust reduction of drogen tetrachloroaurate acid using sodium borohydride in the presence of octane thiol capping agent (Purchased from Aldrich). Preparation of MMPCs was carried out by passive place exchange with mercaptoundecanoic acid (Aldrich) resulting in an approximate surface coverage of ~30% carboxylic acid. PAMAM dendrimers were purchased from Aldrich and diluted to give solutions of 0.5 mg/ml. Films were prepared by mixing in 1:1 Tetrahydrofuran:Methanol MMPC/dendrimer in a ratio of 1:10 ensuring an excess of dendrimer in each sample. These films were allowed to precipitate onto Kapton and then analyzed using Small Angle X-ray Scattering (SAXS). A sealed tube source was used to produce the CuKα radiation (λ = 0.154 Å). The scattering intensity is presented as a function of the wave vector (1) where 2θ is the scattering angle and λ the CuKα radiation wavelength.

$$q = \left(\frac{4\pi}{\lambda}\right)\sin\left(\frac{2\theta}{2}\right) \qquad (1)$$

Immediately upon mixing the solution became turbid. This turbid solution was drop cast onto a copper coated Transmission Electron Microscopy (TEM) grid and analyzed on an JEOL 100-CX TEM operating at 100KeV. IR spectra were recorded as films drop cast from the turbid solutions on a CaF_2 window and recorded on a Midac M1200.

DISCUSSION

The assembly of amine capped PAMAM dendrimers and carboxylic acid functionalized MMPCs proceeds through the formation of a salt bridge as seen in figure 2. IR spectroscopy was used to clearly show that a salt bridge is indeed formed. The broad peak observed in the N-H region for hydrogen bound amine in the dendrimer becomes sharper and a new peak at 3069 cm^{-1} arising from the RNH_3^+ stretch appears.

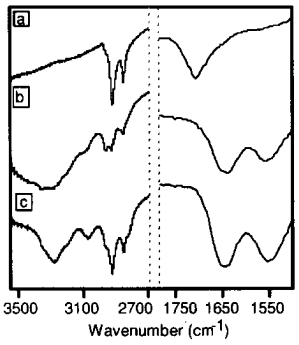

Figure 2. IR spectra (a) dendrimer (G4), (b) MMPC **1**, and (c) the precipitate resulting from a mixture of a 10-fold excess of dendrimer (G4) relative to MMPC **1**.

TEM was then used to investigate the morphology of the self-assembled structures. It was observed that the morphology depended on the ratio of nanoparticle to dendrimer. In cases where a low ratio of dendrimer to nanoparticle was investigated network like structures resulted from carboxylic acid dimerization. In contrast structures formed from high ratios of dendrimer to nanoparticle resulted in ~0.5-1.5 μm spheres as shown in figure 3.

PAMAM generations 0, 1, 2, 4, 6 were then used to assemble the carboxylic acid functionalized MMPCs and the spacing was analyzed using SAXS. Figure 4 shows the SAXS plots for each generation of dendrimer. The large maximum represents particle particle spacing caused by the dendritic mortar. The second smaller maximum is representative of medium range order, which can be modeled assuming a liquid like packing arrangement [5]. In classical liquid packing the first and second maximums have a ratio of two [6]. Comparing the data in Table I we see that for generations 2, 4, and 6 the ratio between Q_1 and Q_2 is very close to this value indicating a reasonable agreement with the classical liquid packing approximation.

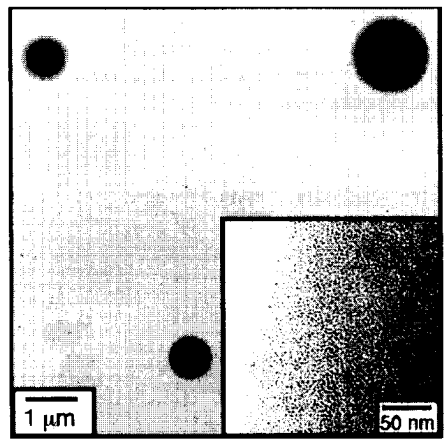

Figure 3. Spheres formed from high ratio of dendrimer to nanoparticle. Inset shows that each nanoparticle is well separated from its neighbor.

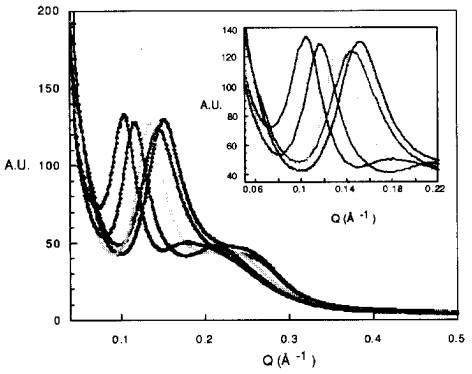

Figure 4. SAXS spectrum of PAMAM dendrimers generation 0, 1, 2, 4, 6 demonstrating increase in particle spacing as a function of dendrimer generation. Inset clearly shows Q_1 spacing.

We have applied our dendrimer mediated assembly method to magnetic nanoparticles to create a system from which to study the physics of individual domain interactions and possibly create functional materials. The basic premise of our research is that magnetostatic interactions between individual magnetic domains can be modulated by controlling the distance between the domains [7]. To this end we have synthesized 6.5 nm γ-Fe_2O_3 nanoparticles by the decomposition of iron cupferron at elevated temperatures in the presence of amine capping agents [3]. A diol ligand was synthesized and exchanged onto this monolayer placing a trimethyl ammonium salt moiety on the surface of the particle [4]. PAMAM dendrimers generation 2.5, 4.5, and 6.5 were then used to assemble the particles and the resulting precipitate was analyzed using SAXS, TEM, and SQUID. Figure 5 is a graph of the blocking temperature [8] versus the average interparticle spacing as a function of dendrimer generation.

Two trends are clearly observable from the data; as with the gold nanoparticles the average interparticle spacing increases with dendrimer generation, more interesting however is the resultant inverse relation between this increase in spacing and the blocking temperature. One explanation for this observed trend hinges on a decrease in the effective domain interaction particles are forced farther and farther apart [9]. Further magnetic characterization is needed before a more rigorous understanding of this spacing effect can be attempted.

Table I. Spacing and Q values for each dendrimer generation obtained using D (nm^{-1}) = $2\pi/Q$.

	G_0	G_1	G_2	G_4	G_6
Q_1[a]	0.152	0.145	0.133	0.116	0.103
Q_2[a]	0.257	0.261	0.241	0.220	0.200
D_1(nm)	4.1	4.3	4.7	5.4	6.1

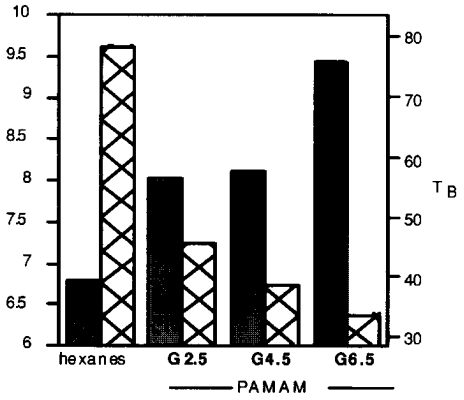

Figure 5. The blocking temperature (colored bars) shows a clear dependence on the interparticle spacing (hatch filled bars) indicating that our method might be an effective means to tailor bulk magnetic properties.

CONCLUSIONS

This study demonstrates that PAMAM dendrimers can be used to assemble and space properly functionalized MMPCs. It also shows that by altering the generation of the dendrimer mortar one can effectively control interparticle spacing ranging in this case from 4.1 to 6.1nm center to center.

ACKNOWLEDGMENTS

This research was supported by the National Science Foundation (CHE-9905492 (VR) DMI-0103024 (MT) and MRSEC instrumentation. We thank David Shultz for assistance with the SQUID magnetometry.

REFERENCES

1. J. E. Martin, J. P. Wilcoxon, J. Odinek, and P. Provencio, *J. Phys. Chem. B.* **104**, 9475 (2000).
2. A. K. Boal, F. Ilhan, J. E. DeRouchey, T. Thurn-Albrecht, T. P. Russell, and V. M. Rotello, *Nature* **404**, 746 (2000)
3. (a) L. Balogh, and D. A. Tomalia, *J. Am. Chem. Soc.* **120**, 7355 (1998). (b) G. Bar, S. Rubin, R. W. Cutts, T. N. Taylon, and T. A. Zawodzinski Jr, *Langmuir* **12**, 1172 (1996). (c) J. –A. He, R. Valluzzi, K. Yang, T. Dolukhanyan, C. Sung, J. Kumar, S. K. Tripthy, L. Samuelson, L. Balogh, and D. A. Tomalia, *Chem. Mater.* **11**, 3268 (1999). R. M. Crooks, and A. J. Ricco, *Acc. Chem. Res.* **31**, 219 (1998).
4. J. Rockenberger, E. Scher, and A. P. Alivisatos, *J. Am. Chem. Soc.* **121**, 11595 (1999).
5. A. K. Boal, K. Das, M. Gray, and V. M. Rotello, *Chem. Mater.* **14,** 2628 (2002).
6. D. Chandler, *Introduction to Statistical Mechanics*; OUP; New York, 1989.
7. (a) M. El-Hilo, K. O'Grady, and R. W. Chantrell, *J. Mag. Mag. Mater.* **114**, 295 (1992). (b) T. Jonsson, P. Nordblad, and P. Svedlindh, *Phys. Rev. B.* **57**, 497 (1998).
8. Blocking temperature is the transition between ferromagnetism and paramagnetism, it depends directly on the volume of the magnetic domain, in this case the nanoparticle, and weakly on the time scale of the magnetic measurement.
9. R. W. Chantrell, N. Walmsley, J. Gore, and M. Maylin, *Phys. Rev. B.* **63**, 1345 (2000).

Mat. Res. Soc. Symp. Proc. Vol. 739 © 2003 Materials Research Society

Synthesis by Self-Assembly of Iron-Cobalt Nanoalloys

Melissa A. Zubris and Rina Tannenbaum
School of Materials Science and Engineering, Georgia Institute of Technology
Atlanta, GA 30332-0245

ABSTRACT

In this paper we are proposing the synthesis of iron and cobalt nanoalloys via the co-decomposition of iron and cobalt carbonyl precursors in the presence of polystyrene as the surface stabilizing agent. In order to form iron-cobalt nanoalloys with no preferential aggregation of metal atoms resulting in phase segregation, the decomposition kinetics of the iron pentacarbonyl and dicobalt octacarbonyl precursors had to be firmly established. The kinetics of cobalt cluster formation has been thoroughly investigated, but data for iron pentacarbonyl decomposition is relatively scarce. To fully understand the formation of the iron nanoclusters, a kinetic study was performed by varying carbonyl concentrations and reaction media in order to establish reaction order and rate constants. Our results suggest this decomposition to be a higher order process (not first order as previously assumed), with a complicated intermediate mechanism, which has been postulated and experimentally verified. By using this kinetic data, we will be able to predict the necessary conditions for the creation of new in-situ iron-cobalt nanoalloys using carbonyl precursors.

INTRODUCTION

Nanoalloys are an exciting new class of materials in the growing field of nanotechnology. Nanoalloys consist of the nanoscale co-aggregation of two or more metals with a potential to form compositionally-ordered phases or superstructures that have properties unlike those of the individual types of clusters or of bulk alloys of the constituent metals.[1-4]

A convenient route to the formation of metal nanoalloy systems is the co-transformation and co-aggregation of their respective organometallic precursors.[5-8] If a stable nanoalloy is to be created, there must be no preferential aggregation of metal atoms into mono-metallic clusters in the system, i.e., there should be no kinetically-induced phase separation of the metal atoms within the nanoalloy cluster during its formation. This can be achieved by the concurrent transformation reactions of the organometallic precursors, and hence, these transformations should display similar kinetic features, i.e. similar reaction rates. The control of the individual reaction rates of each of the species in the system (by varying component concentrations, solvents or temperature) may be used to modulate the aggregation and initial phase separation of the different metallic atoms in the nanoalloy clusters.

A successful method for the preparation of zero-valent metal nanoclusters is the decomposition of metal carbonyls into metal clusters under an inert atmosphere to reduce the probability of oxidation. In addition, by decomposing these carbonyls in a polymer matrix, the size of the metal nanocluster may be controlled. The polymer adsorbs onto the surface of the cluster, restricting the extent of metal-metal interactions, thereby limiting cluster size.

The nanoalloy of interest in this work is Fe-Co, which was synthesized by the simultaneous co-decomposition of $Co_2(CO)_8$ and $Fe(CO)_5$ in the presence of polystyrene as a stabilizing agent. The decomposition of $Co_2(CO)_8$ in various media has been studied extensively,[5] but the decomposition mechanism and kinetics of $Fe(CO)_5$ under the same conditions has not been thoroughly established. Consequently, the kinetics and mechanism of this decomposition is the focus of this work. To achieve this goal, the order of the decomposition

reaction and its rate constants were studied by varying the initial $Fe(CO)_5$ concentrations, the type of the initial iron carbonyl complex and the solvents used. Once reaction order and rate constants are calculated for the iron system, the kinetics may be compared to those of the cobalt carbonyl decomposition and accurate reaction conditions may be determined.

EXPERIMENTAL PROCEDURE

$Fe(CO)_5$ (Alfa Aesar) was decomposed in a solution containing polystyrene (PS), $\overline{M}_w$ =100,000 g/mol (Avocado Chemicals). In a typical experiment, polystyrene was dissolved in 150 mL of solvent to obtain a solution with polymer concentration just below its critical coil overlap (1.86 wt % for this molecular weight and toluene solvent combination). Once the polystyrene was dissolved, the solution was heated in a jacketed three-neck flask to 90°C via an ethylene glycol bath, and flushed with dry nitrogen.

FT-IR analysis was performed using a Nexus 870 FT-IR spectrometer. Initial spectra of the PS solution and a $5 \cdot 10^{-3}$ M $Fe(CO)_5$ solution were measured prior to decomposition. Subsequently, the mixture was heated to 90°C and aliquots were removed every 15 minutes and their infrared spectra were recorded. Once the characteristic iron carbonyl bands of the spectrum had completely disappeared, the reaction was stopped and the solution was stored in vials under nitrogen.

This experiment was repeated under similar conditions using $Fe(CO)_5$ molar concentrations of $1.25 \cdot 10^{-3}$, $2.5 \cdot 10^{-3}$, and $7.5 \cdot 10^{-3}$ M. In addition, an experiment was performed in similar polystyrene solutions using $5 \cdot 10^{-3}$ M $Fe_2(CO)_9$ (Alfa Aesar) instead of $Fe(CO)_5$. This reaction vessel was covered with aluminum foil, since $Fe_2(CO)_9$ is light sensitive. Also, an experiment was performed using diethyl sulfide (Aldrich) solvent instead of toluene, under identical polymer concentration in the final solution and $5 \cdot 10^{-3}$ M $Fe(CO)_5$ concentration. Each of these reaction solutions was analyzed via FTIR as described.

Three different mixed-metal carbonyl decomposition experiments were performed. For the determination of the mutual presence of both precursors on decomposition kinetics, cobalt carbonyl was added with some delay into the iron pentacarbonyl solution. For the same rate experiments, an initial $5 \cdot 10^{-3}$ M concentration of $Co_2(CO)_8$ was chosen (as previously described), together with 0.7261 mL of $Fe(CO)_5$, corresponding to a concentration of 0.139 M. For the same concentration experiments, equal concentrations of $5 \cdot 10^{-3}$ M were introduced and co-decomposed simultaneously.

High resolution transmission electron microscopy (HRTEM) images were obtained using a Hitachi HF-2000 field emission gun (FEG) TEM (200 kV), equipped with a thin window EDS spectrometer. A Hitachi S800 FEG scanning electron microscope (SEM) was used for bulk EDS analysis.

RESULTS AND DISCUSSION

The kinetics of aggregation of the iron nanoclusters were based on the rate of decomposition of the iron carbonyl precursor, as indicated by the decrease of the intensity of the carbonyl absorption bands of $Fe(CO)_5$ monitored by infrared spectroscopy. The kinetic analysis of the decomposition process was based on the carbonyl absorption band of $Fe(CO)_5$ at the 1996 cm^{-1} band. The reaction order of the decomposition of $Fe(CO)_5$ to Fe clusters and CO was determined via plots of concentration (C) as a function of time. The statistical comparison of the plot of ln C vs. time with the plot of 1/C vs. time indicates the possibility of a second order decomposition reaction. The same phenomenon was also observed when similar decomposition reactions were carried out with different initial iron carbonyl concentrations. The second order

kinetics are further supported by the dependence of the initial decomposition rate, $(\Delta A_{1996}/\Delta t)_{init}$, on C_{init}, for each different initial iron pentacarbonyl concentration. These plots showed a parabolic dependence of the initial rate on concentration (Figure 1a), and a linear dependence of the initial rate on the square of the concentration (Figure 1b). Hence the initial decomposition rate may be approximated as $Rate_{init} = k_{eff} \cdot [Fe(CO)_5]^2_{init}$.

The possibility of a second order reaction presents a need to determine the decomposition mechanism. Instead of a direct decomposition from $Fe(CO)_5$ into CO and Fe metal clusters, there must be one or more intermediate reaction steps. A proposed mechanism is as follows:

$$2Fe(CO)_5 \longrightarrow Fe_2(CO)_9 + CO$$
$$nFe_2(CO)_9 \longrightarrow (Fe_2)_n + 9nCO$$

In order to support this mechanism, the decomposition of $Fe_2(CO)_9$ was analyzed under identical polymer and solvent conditions. According to this predicted mechanism, the decomposition into Fe clusters and CO should be first order. However, upon kinetic spectral analysis, no clear reaction order may be determined. The carbonyl concentration varies with no apparent order until approximately 165 minutes into the reaction, after which, a linear plot of lnC versus time may be constructed, as shown in Figure 2.

The difficulty in establishing order early in the decomposition may arise from an alternate reaction of the $Fe_2(CO)_9$ intermediate as follows:

$$3Fe_2(CO)_9 \longrightarrow Fe_3(CO)_{12} + 3Fe(CO)_5$$

where $Fe(CO)_5$ also reacts in the following manner:

$$Fe(CO)_5 \rightleftharpoons Fe(CO)_4 + CO$$
$$Fe(CO)_5 + Fe(CO)_4 \rightleftharpoons Fe_2(CO)_9$$

The presence of $Fe_3(CO)_{12}$ is indicated by a dark green color, whereas the $Fe(CO)_5$ and $Fe_2(CO)_9$ solutions are pale yellow or amber. Moreover, the infrared spectrum of $Fe_3(CO)_{12}$ has a distinctive carbonyl stretching band around 2056 cm^{-1}. The development of the characteristic green color during the decomposition of $Fe_2(CO)_9$, coupled with the transient appearance of a carbonyl band around 2048 cm^{-1}, indicates the formation and disappearance of $Fe_3(CO)_{12}$ during this experiment, as shown in Figure 3a.

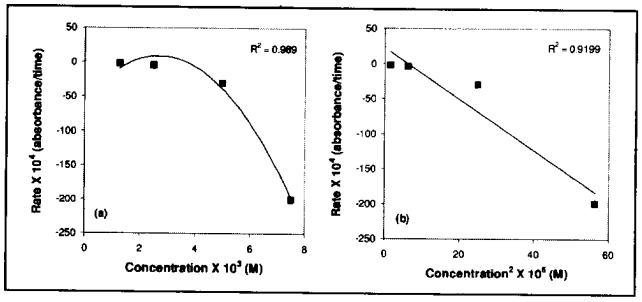

Figure 1: (a) Parabolic dependence of the initial rate on concentration; (b) Linear dependence of the initial rate on the square of the concentration.

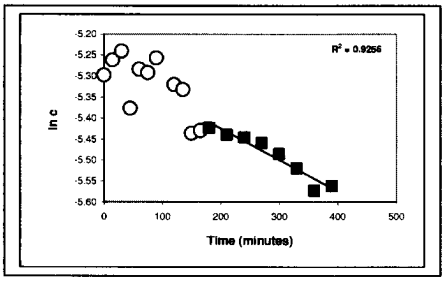

Figure 2: Decomposition kinetics of $Fe_2(CO)_9$

This absorption band is no longer detectable in the infrared spectra after 165 minutes. This supports the assumption that in the early stages of the decomposition of $Fe_2(CO)_9$, the $Fe_2(CO)_9 \rightarrow Fe_3(CO)_{12}$ transformation reaction is competitive with the main decomposition reaction of $Fe_2(CO)_9$, and as the various transformations occur, a pseudo-equilibrium is reached, upon which the decomposition proceeds to form iron nanoclusters. The original $Fe(CO)_5$ decomposes into $Fe_2(CO)_9$. The $Fe_2(CO)_9$ decomposes into either Fe and CO or $Fe_3(CO)_{12}$ and more $Fe(CO)_5$. This brings the reaction back to the decomposition of $Fe(CO)_5$ into $Fe_2(CO)_9$. This latter reaction involves the presence of the $Fe(CO)_4$ fragment. An additional experiment was needed in order to assess the role of the $Fe(CO)_4$ fragment in this complex reaction.

The decomposition of $Fe_2(CO)_9$ was conducted in diethyl sulfide, which was used both as a solvent and as a reactant in the presence of $Fe(CO)_4$. This sulfide ligand traps the $Fe(CO)_4$ fragments and prevents trimerization to $Fe_3(CO)_{12}$, according to the following mechanism:

$$H_3CH_2C\diagdown\ \diagup H_3CH_2C\!>\!S \;+\; Fe(CO)_4 \longrightarrow (CH_3CH_2)_2SFe(CO)_4$$

If the predicted mechanism shown above indeed takes place, the reaction will run out of $Fe(CO)_4$ and the overall decomposition will be then dominated by the reactions described earlier. This overall decomposition is shown in the following mechanism:

$$Fe_2(CO)_9 \xrightarrow{H_3CH_2C\diagdown\ \diagup H_3CH_2C\!>\!S} Fe(CO)_5 + (CH_3CH_2)_2S\text{-}Fe(CO)_4$$

$$2Fe(CO)_5 \longrightarrow Fe_2(CO)_9$$

$$Fe_2(CO)_9 \longrightarrow Fe_2$$

Hence, the decomposition of $Fe_2(CO)_9$ in diethyl sulfide will proceed via a first order reaction, as shown via spectra analysis. This supports the predicted decomposition mechanism of $Fe_2(CO)_9$. The toluene solvent experiments support the original assumptions made regarding the iron pentacarbonyl decomposition. The kinetic calculations for the diethyl sulfide solvent also reinforce the proposed second order decomposition mechanism for iron pentacarbonyl.

At this point, it was necessary to assess whether the decomposition kinetics of both $Fe(CO)_5$ and $Co_2(CO)_8$ were influenced by their simultaneous presence in the reaction solutions. Hence, the decomposition of $Fe(CO)_5$ was initiated alone followed by the addition of $Co_2(CO)_8$. The simultaneous decomposition of both species into metal clusters after the introduction of the cobalt carbonyl is clearly visible in the infrared spectral results shown in Figure 3b. The rate of

the decomposition of $Fe(CO)_5$ was calculated from the time of the introduction of $Co_2(CO)_8$. The decomposition rates of both carbonyl precursors are not influenced by their mutual presence in the reaction medium.

Two different approaches were used to explore the microstructure of the particles: (1) The co-decomposition of $Fe(CO)_5$ and $Co_2(CO)_8$ with similar initial concentrations; (2) The co-decomposition with concentrations that were calculated such that both decomposition rates will be equal, as shown below:

$$[Fe(CO)_5]^2_{init} = \frac{k_{Co}}{k_{Fe}} \cdot [Co_2(CO)_8]_{init}$$

Preliminary images were obtained via high resolution transmission electron microscopy (HRTEM) shown in Figure 4a-b. EDS analysis was performed on randomly selected particles in these images, and compared to EDS analysis done on the bulk samples with the polymer burned off. The normalized fractions of each metal in the individual clusters and in the bulk samples were calculated. The composition of the bulk samples for both decomposition approaches corresponds to the actual concentration of the precursors in the initial solution. On the other hand, the composition of the randomly chosen clusters is cluster-specific and depends on the initial reaction conditions. The composition for a random cluster produced by the same-rate method does not deviate considerably from the bulk composition, suggesting a mixed-metal characteristic. These samples were highly polycrystalline, and no electron diffraction pattern could be obtained. The composition for a random cluster produced by the same-concentration method, shows a different composition than the bulk composition, suggesting metallic domain segregation, as evidenced by the crystalline nature of the particles. The co-decomposition reaction conducted with similar initial rates produced particles (FeCo-a) with an average size of 21.6 nm, while the reaction with similar initial concentrations produced crystalline particles (FeCo-b) with an average size of 14.5 nm, as shown in Table I. The smaller average size of the crystalline clusters may be due to the higher packing order of the metallic domains in the cluster, and enhanced adsorption of the polystyrene chains on the surface, resulting in a more effective capping process.

CONCLUSIONS

FTIR and solvent effects were used to elucidate the kinetic and mechanism of the decomposition of $Fe(CO)_5$ in the presence of polystyrene as a stabilizing agent.

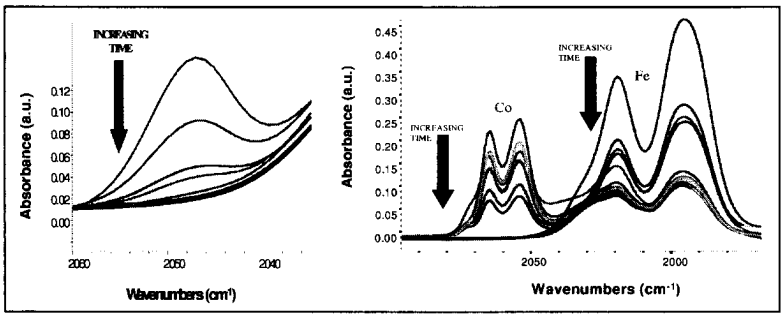

Figure 3: FTIR spectra of the 2046 cm-1 band of $Fe_3(CO)_{12}$ (left), and the co-decomposition of $Fe(CO)_5$ and $Co_2(CO)_8$ (right).

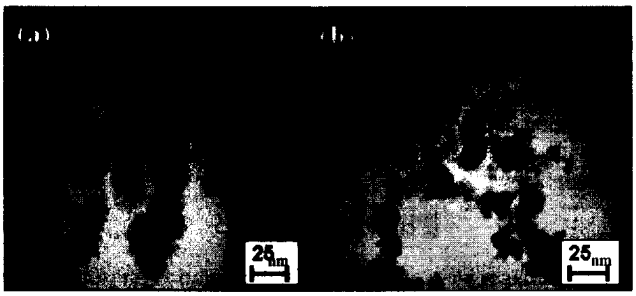

Figure 4: (a) Same rate co-decompositions; (b) Same initial concentrations co-decompositions.

Through the variation of initial iron carbonyl concentrations and solvents, the reaction order of the decomposition of $Fe(CO)_5$ was determined as second order, and the reaction rate coefficient was calculated. As a consequence, we were able to show that the conditions under which the co-decomposition reactions take place control the resulting microstructure of the Fe-Co binary nanoalloy formed. The study of the evolution and precise characterization of the Fe-Co nanoalloys microstructure as a function of initial co-decomposition conditions is currently underway in our laboratory.

ACKNOWLEDGEMENTS

This work was supported by the "Metamaterials" program funded by DARPA, by Georgia Tech Research Institute (GTRI), and by NSF-ERC.

REFERENCES

1. Sun, S.; Anders, S.; Hamann, H. F.; Thiele, J.-U.; Baglin, J. E. E..; Thomson, T.; Fullerton, E. E.; Murray, C. B.; Terris, B. D. *J. Am. Chem. Soc.* **2002**, *124(12)*, 2884.
2. Sun, S.; Murray, C. B.; Weller, D.; Folks, M.; Moser, A. *Science* **2000**, *287*, 1989.
3. Park, J., II; Cheon, J. *J. Am. Chem. Soc.* **2001**, *123(24)*, 5743.
4. Kiely, C. J.; Fink, J.; Zheng, J.G.; Brust, M.; Bethell, D.; Schiffrin, D. J. *Adv. Mater.* **2000**, *12*, 640-643.
5. Tannenbaum, R.; Flenniken, C. L.; Goldberg, E. P. *J. Polym. Sci. B* **1990**, *28*, 2421-2433.
6. Suslick, K. S.; Fang, M.; Hyeon, T. *J. Am. Chem. Soc.* **1996**, *118*, 11960.
7. Park, S.-J.; Kin, S. Lee, S.; Khim, Z. G.; Char, K.; Hueon, T. *J. Am. Chem. Soc.* **2000**, *122(35)*, 8581.
8. Choi, C. J.; Dong, X. L.; Kim, B. K. *Scrip. Mater.* **2001**, 44, 2225-2229.

Table I: Characteristics of Fe-Co alloys formed

Sample	Conditions	$Co_{(cluster)}$ (molar %)	$Fe_{(cluster)}$ (molar %)	$Co_{(bulk)}$ (molar %)	$Fe_{(bulk)}$ (molar %)	Average Size (nm)
FeCo-a	Same initial rates	8.13	91.87	20.03	79.98	21.6
FeCo-b	Same initial concentrations	88.94	11.06	52.19	47.81	14.5

Mat. Res. Soc. Symp. Proc. Vol. 739 © 2003 Materials Research Society

Dramatic Effect of Temperature on Metal-oxide Nanostructures: Oxidation of Cu Films by *In situ* UHV-TEM

Guangwen Zhou and Judith C. Yang
Materials Science and Engineering Dept, University of Pittsburgh, Pittsburgh, PA 15261

ABSTRACT

We investigated the temperature effect on the Cu_2O morphology by oxidizing Cu(100) thin films at the temperature ranging from 350°C to 1000°C. We demonstrated that dramatically different morphologies of oxide nanostructures can be achieved by modifying the oxidation temperature. Quasi-one-dimensional Cu_2O structures with aspect ratios as large as 40:1 were formed at the oxidation temperature of 600°C. The *in situ* observation data on the elongation of Cu_2O islands agree with the energetic calculations based on the balance between surface and interface energies and the elastic stress relaxation in the three dimensional islands.

INTRODUCTION

From the standpoint of thermodynamics all of the metals exhibit a tendency to oxidize. The oxidation driving force depends on the free-energy change for oxide formation. But the morphological changes of oxides during oxidation depend on kinetics, and microstructural considerations. Visualizing the oxidation process will provide essential insights into the complex kinetics and energetics of nano-oxide formation [1,2]. Furthermore, oxidation can be viewed as a processing tool for creating self-ordered nanostructures and the understanding of exact formation process of oxide would provide the guidance to control the oxide nanostructures [3]. *In situ* ultra high vacuum transmission electron microscope (UHV-TEM) allows us to study the nucleation and growth processes of oxide at nanometer scale, provides a unique view of dynamic reactions, and enables us to understand and therefore manipulate surface reactions. Since Cu has been chosen by many investigators as a model system to understand oxidation kinetics [4-7], we chose Cu films as a model system to study the formation of the oxide nanostructures by *in situ* UHV-TEM. We have examined the dependence of island density, size distribution, morphology on the oxidation parameters, such as substrate temperature, oxygen pressure, and orientation of the substrate. The focus of this paper is the dramatic effect of temperature on the oxide morphology formed on Cu(100) thin films. Copper forms two thermodynamically stable oxides, Cu_2O and CuO. Cu_2O is simple cubic lattice (space group pn-3m) with 4Cu and 2O atoms in its basis, and a lattice parameter of 4.22Å. The Cu atoms form a FCC lattice and the O atoms form a BCC lattice, where each O atom is surrounded by a tetrahedron of Cu atoms. CuO has a monoclinic structure. Cu is a FCC metal with a lattice parameter of 3.6Å. For the temperatures and very low oxygen partial pressures used in our experiments, only Cu_2O is expected to form [8].

EXPERIMENTAL

The microscope used in this work was a modified JEOL 200CX [9]. A UHV chamber was attached to the middle of the column, where the base pressure was less than 10^{-8} torr without the

use of the cryoshroud. The microscope was operated at 100 KeV to minimize irradiation effects. Single crystal 99.999% pure (by referring to the purity of the originally evaporated material) 700Å Cu films were grown on irradiated NaCl(100) substrates in an UHV e-beam evaporation system where the chamber pressure was at ~10^{-8} torr. The single crystal nature of the Cu films was determined by SAD in a TEM. The Cu films were removed from the substrate by dissolving the NaCl in de-ionized water. The native Cu oxide was removed inside the TEM by annealing the Cu films in methanol vapor at a pressure of 5×10^{-5} torr and 350°C, which reduces the copper oxides to copper [10]. Scientific grade oxygen gas of 99.999% purity can be admitted into the column of the microscope through a leak valve at a partial pressure between 5×10^{-5} torr and 760 torr. The specially designed sample holder allows for resistive heating at temperatures between room temperature and 1000°C.

RESULTS

We examined the Cu_2O island formation on Cu(001) as a function of oxidation temperature in the range of 350°C to 1000°C at constant oxygen pressure of $5x10^{-4}$ torr. The morphology of Cu_2O islands formed at different oxidation temperatures is shown in Figure 1 (bright field TEM images). At 350°C, only triangular geometry islands formed (Fig. 1a). The island size increased with continued oxidation, but the island shape did not change. At elevated temperatures, between 400°C and 550°C, the islands exhibited a shape change from triangular to square or round-based islands as they increase in size due to the continued exposure to oxygen (Figure 1b).

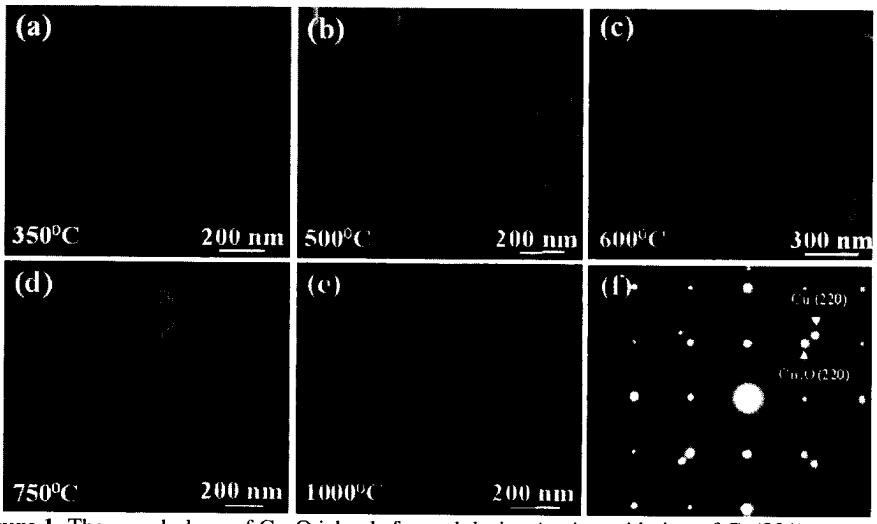

Figure 1. The morphology of Cu_2O islands formed during *in situ* oxidation of Cu(001) at a oxidation partial pressure of $5x10^{-4}$ torr and oxidation temperatures of (a) 350°C, (b) 500°C, (c) 600°C, (d) 700°C and (e) 1000°C.

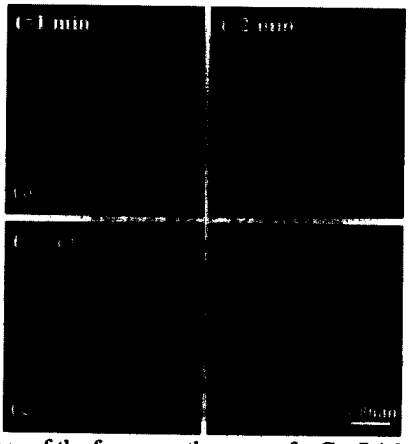

Figure 2. *In situ* TEM images of the four growth stages of a Cu_2O island as a function of oxidation time at constant oxygen partial pressure of 1×10^{-4} and temperature of 600°C.

In a narrow temperature regime near 600°C, elongated Cu_2O islands formed (Fig. 1c). These islands have varying lengths, but similar widths of ~110nm. The initial islands were square, and continued to grow uniformly, but showed a shape transition near 110nm to nanorods with continued oxidation. The elongation directions of the islands are along the two orientations, i.e., <001> and $<00\bar{1}>$ or <010> and $<0\bar{1}0>$, and roughly equally distributed. We have observed elongated islands with aspect ratios as large as *40:1*. In order to visualize the growth of one island for a long time without interference due to coalescence with neighboring islands, we oxidized the films at oxygen pressure of 1×10^{-4} torr. A sequence of images focusing on the growth of a single island is shown in Fig. 2. The initially formed island is square shaped (Fig. 2a), and continues to grow uniformly (Fig. 2b), when a critical size (~110nm) is reached, the island shows a shape transition to nanorod (Fig. 2c, d). The contrast around the island is related to the strain in the island and the film. This was confirmed by AFM which indicates no dip around the island for the initial growth stages (Fig. 2a-c), and a very small dip ~2nm for the larger island (Figure 2d).

Oxidation at temperatures between 650-800°C resulted in the formation of pyramid islands, which have a distinctive cross-hatched pattern as shown in Figure 1d. When the Cu film was oxidized at temperatures between 800-1000°C, pyramids with flat terraces formed (Figure 1e). The pyramid terraces have roughly equal width and length distribution.

For all the temperatures that we have examined, the Cu_2O islands are epitaxial with Cu substrate as shown in Fig. 1f, i.e. $(001)Cu_2O//(001)Cu$ and $[100]Cu_2O//[100]Cu$. The SAD only confirms the crystal structure is cubic form of copper oxide (as compared to the monoclinic CuO), there is the possibility of nonstoichiometry of the Cu oxide. EELS is the one method probe this issue, and one future work will focus on the oxidation states of the Cu across the interface.

The accurate estimates of the island thickness are beneficial for understanding of the formation of the nanostructured Cu_2O. Unfortunately the *in situ* UHV-TEM modifications included modifications of the sample holder such that no tilt was available. Currently, we used

AFM for height measurements. A detailed structural characterization of the oxide islands by ex situ methods is necessary in the future work.

DISCUSSION

Many parameters affecting the kinetics and thermodynamics of growth depend sensitively on temperature, different oxide morphologies would be expected to form at various temperatures. During oxidation at low temperatures (T < 400°C), the oxide islands adopt triangular shape, but at temperatures higher than 400°C, the islands have a more symmetrical geometry. Only a few investigators have examined the effect of the substrate temperature on the thin film growth and morphology such as Cr on Cu substrates [11], indium-doped tin oxide films [12] and plasma enhanced chemical vapor deposition (PECVD) polycrystalline Si films [13]. Yet, only Afify *et al.* [12] noted a distinct change in the island morphology due to the substrate temperature, where dendritic growth was noted at higher temperatures for indium-doped tin oxide films. A possible reason why this dramatic effect of temperature on the film morphology has not been widely observed in other systems could be that the temperature ranges previously investigated were considerably smaller (only ~200°C) than the temperature range we examined (350°C to 1000°C).

The oxide morphology is controlled by kinetic and thermodynamic factors during the oxidation. It is reasonable to expect that temperature would affect the kinetics and/or energetics of the oxide formation. The possible effects of temperature on the oxide morphology include (1) the enhanced diffusion of copper and oxygen atoms, (2) the decrease in interfacial strain due to the differences in thermal expansion coefficients, (3) the changes in mechanical properties.

Surface diffusion of oxygen plays an important role in the kinetics of the initial oxidation stage. [14] The rate of oxygen diffusion follows an Arhenius relationship with temperature. The diffusion path of oxygen is larger at higher temperature, and oxygen atoms can migrate longer distances on the surface and, hence, are more likely to be captured by the oxide islands. Therefore, the islands are more likely to form the energetically favorable configuration with increasing temperature. At higher temperatures, both oxygen and Cu can diffuse quickly to form more thermodynamically, equilibrium shaped oxides, such as the four-fold symmetric islands observed above 450°C. At lower temperatures, the oxide morphology is more likely to have low symmetry due to the slower kinetics, such as the triangular shaped islands formed below 400°C.

The formation of Cu_2O islands will induce tensile stress in the Cu film due to the large lattice mismatch. Therefore, a strain field exists around islands, and this strain field could inhibit the island growth by creating additional activation barriers for the incorporation of atoms at island edges [15]. Cu_2O has a thermal expansion coefficient of 1.9×10^{-6} °C^{-1}, and Cu has a thermal expansion coefficient of 17×10^{-6} °C^{-1}. With increasing temperature, the lattice mismatch becomes smaller, and this lattice mismatch induced strain becomes smaller too. This could explain the triangular shape at low temperatures, where the strain is high and so the interface area is minimized by the triangular shape. At higher temperatures, there is less lattice mismatch and therefore reducing interfacial strain with increasing temperatures. Hence, the chosen interfaces will be along the low energy interfaces (such as the low index planes). A third effect of temperature is on the mechanical properties of the oxide and substrate. At higher temperatures, the metal substrate and oxide become more ductile. The enhanced ductility provides a mechanical mechanism for strain relaxation affecting the oxide morphology development.

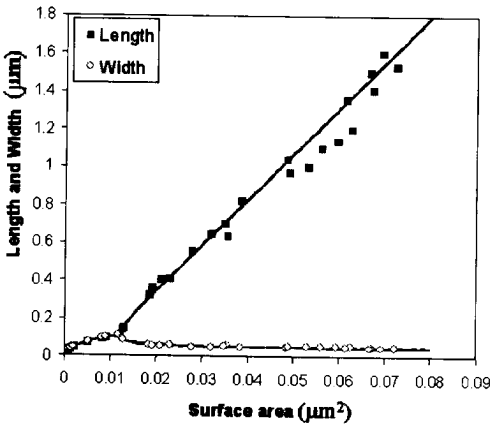

Figure 3. Dependence of both island length t(squares) and width s(circles) on the island surface area. The solid lines represent a theoretical fit based on Eq.(1). The initially square shaped island undergoes a shape transition at the critical size s=t=$e\alpha_0$=114nm. There is a reduction of the width to its optimal width, α_0. The data points are obtained from the experimental results.

Particularly intriguing was the observed shape transition from square to elongated nanorods at a very narrow temperature range of 600°C. Tersoff and Tromp have shown that strained epitaxial islands may undergo a shape transition as they grow in size [16]. Below a critical size, islands have a compact symmetric shape. However, at a larger size, they adopt a long thin shape, which has an energy minimum for the system because of the tradeoff between surface/interfacial energies and stress relaxation in the islands due to the lattice mismatch between the substrate and epitaxial film. We compared our results with this theoretical model by using the analytical expression for the energy per unit volume of a strained epitaxial island [16].

$$\frac{E}{V} = 2\Gamma\left(\frac{1}{s}+\frac{1}{t}\right)+\frac{1}{h}(r_i + r_t - r_s) - 2ch\left[\frac{1}{s}\ln\left(\frac{se^{3/2}}{h\cot\theta}\right)+\frac{1}{t}\ln\left(\frac{te^{3/2}}{h\cot\theta}\right)\right] \qquad (1)$$

where s, t, and h are the width, length, and height of the island, respectively; θ being the contact angle; Γ contains the surface and interface energies, $\Gamma = \gamma_e \csc\theta - (\gamma_i + \gamma_s - \gamma_i)\cot\theta$; γ_t, γ_s, and γ_e are the surface energies of the island's top, the substrate, and the island's edge facet, respectively; γ_i is the island-substrate interface energy. $c = \sigma_b^2(1-\nu)/2\pi\mu$, ν and μ are the Possion ratio and shear modulus of the substrate, σ_b is the island bulk stress. The optimal balance between surface energies and strain is obtained through the minimization of the total energy expression for an island of constant height h with respect to both s and t. This gives a square island with $s=t=\alpha_0$, where the optimal size α_0 is given by

$$\alpha_0 = e\phi h \exp(\Gamma / ch) \qquad (2)$$

where $\Phi = e^{-3/2}\cot\theta$. The island remains a square up to a critical size $s=t=e\alpha_0$. Due to continued oxidation, the island grows beyond this critical size, the square shape becomes unstable and a transition to rectangular shape takes place. As the island grows further, the aspect ratio increases.

To evaluate "c", we used standard values of μ_{Cu} (40GPa) and calculated σ_b for Cu_2O from the Young's modulus (30GN/m^2) and Poisson ration (0.455) of Cu_2O. The contact angle, θ = 30°,

and height, h=20nm, were measured by the AFM. By fitting with the critical size, $e\alpha_0$=114nm, we can estimate $\Gamma$from Eqn. (2). These values are substituted into Eqn. (1) to determine the energy per unit volume as a function of width s and length t. A comparison of Tersoff and Tromp's model with our data shows excellent agreement for the size evolution of the island as shown in Fig.3. Furthermore, we have developed a kinetic model of oxidation based on oxygen surface diffusion to the perimeter of the oxide island. We have noted an excellent agreement of volume evolution of the island with the kinetic model that validates the growth of the Cu_2O islands is initially dominated by the surface diffusion of oxygen [17].

CONCLUSION

We demonstrated that oxidation temperature has a dramatic effect on the kinetics/energetics of oxide formation, which results in different morphologies of oxide nanostructures. Our *in situ* observation data on the elongation of Cu_2O islands agree with the energetic model.

ACKNOWLEDGEMENTS

This research project is funded by NSF (# 9902863), DOE and NACE seed grant. The experiments were performed at the MRL, UIUC, which is supported by the U.S. DOE (#DEFG02-96-ER45439).

REFERENCES

1. N. Cabrera, N.F. Mott, *Rep. Prog. Phys.* **12**, 163 (1948)
2. J.C. Yang, B. Kolasa, J.M. Gibson, M. Yeadon, *Appl. Phys. Lett.* **73**, 2481 (1998)
3. S. Aggarwal, A.P. Monga, S.R. Perusse, R. Ramesh, V. Ballarotto, E.D. Williams, B.R.Chalamala, Y. Wei, R.H. Reuss, *Science* **287**, 2235 (2000)
4. F. Young, J. Cathcart, A. Gwathmey, *Acta Metall.* **4**, 145 (1956)
5. R.H. Milne, A. Howie, *Philos. Mag. A* **49**, 665 (1984)
6. A. Roennquist, H. Fischmeister, *J. Inst. Met.* **89**, 65 (1960-1961)
7. K. Heinemann, D.B. Rao, D.L Douglas, *Oxid. Met.* **9**, 379 (1975)
8. G. Honjo, *Phys. Soc. Of Japan Journal* **4**, 330 (1949)
9. M.L. McDonald, J.M. Gibson, F.C. Unterwald, *Rev. Sci. Instrum.* **60**, 700 (1989)
10. S.M. Francis, F.M. Leibsle, S. Haq, N, Xiang, M. Bowker, *Surf. Sci.* **315**, 284 (1994)
11. H. Lefakis. P.S. Ho, *Thin Solid Films*, **200(1)**, 67 (1991)
12. H.H. Afify, F.S. Terra, R.S. Momtaz, *J. of Mater. Sci.* **7(2)**, 149 (1996)
13. N.T. Tran. M.P. Keyes. *Physica Status Solidi A*, **126(2)**, 143 (1991)
14. J.C. Yang, M. Yeadon, B. Kolasa, J.M. Gibson, *Scripta Materialia*, **38**, 1237 (1998)
15. E. Penev, P. Kratzer, M. Scheffler, *Phys. Rev. B* **54**, 5401 (2001)
16. J. Tersoff, R.M. Tromp, *Phys. Rev. Lett.* **70**, 2782 (1993)
17. G.W. Zhou, J. C. Yang, *Phys. Rev. Lett.* **89**, 6101 (2002)

Mat. Res. Soc. Symp. Proc. Vol. 739 © 2003 Materials Research Society

Self-Organized ZnO Nanosize Islands with Low-Dimensional Characteristics on SiO_2/Si Substrates by Metalorganic Chemical Vapor Deposition

Sang-Woo Kim[1], Shizuo Fujita[2] and Shigeo Fujita[1]
[1]Department of Electronic Science and Engineering, Kyoto University,
Yoshida-honmachi, Sakyo, Kyoto 606-8501, Japan, swkim@fujita.kuee.kyoto-u.ac.jp
[2]International Innovation Center, Kyoto University
Yoshida-honmachi, Sakyo, Kyoto 606-8501, Japan

ABSTRACT

Self-organized ZnO nanosize islands on thermally grown SiO_2 layers on Si (111) with low-dimensional quantum characteristics were realized by metalorganic chemical vapor deposition. Investigation by atomic force microscopy showed that the density and size of the ZnO nanosize islands were changed by the growth conditions. In macroscopic photoluminescence measurements at 10 K using a 325 nm He-Cd laser, we observed the broad spectra with band tails, which were located at the higher energy with respect to band edge emission of ZnO thin films with the free exciton emission located at about 3.38 eV. These results indicate that these ZnO nanosize islands have low-dimensional quantum effect characteristics.

INTRODUCTION

ZnO is a semiconducting material with a wide band gap of 3.3 eV at room temperature. Due to its remarkable excitonic properties based on the large excitonic binding energy (60 meV) [1], significant exciton effects promising for achieving large oscillator strength, nonlinear optical properties, or multiexciton interaction may be expected in low-dimensional ZnO nanostructures. Therefore, the realization of ZnO nanostructure with low-dimensional quantum characteristics is strongly required. To date, ZnO nanostructures such as nanowires and nanoparticles have been reported [2,3]. However, there have been few reports to confirm quantum size effects in ZnO nanostructures grown by a conventional semiconductor growth method, such as molecular beam epitaxy or metalorganic chemical vapor deposition (MOCVD). In the present study, we report the successful growth of ZnO nanosize islands (nanoislands) with low-dimensional characteristics, which may lead to the enhancement of exciton confinement, on SiO_2/Si substrates by metalorganic chemical vapor deposition by introducing either nitrous oxide (N_2O) or nitrogen dioxide (NO_2) gas as an oxygen source and diethylzinc (DEZn) as a zinc source on thermally grown SiO_2 layers in Si (111) as a function of the growth condition.

EXPERIMENTAL DETAILS

The self-organized ZnO nanoislands in this study were prepared by MOCVD on thermally formed SiO_2 layers with a thickness of 25 nm on Si substrates, where DEZn as a zinc source and both N_2O and NO_2 gas as an oxygen source were utilized. The flow rate of DEZn was selected at 0.5-3 μmol/min when N_2O gas with the flow rates of 5000-10000 μmol/min was introduced in the MOCVD reactor maintained at 200 Torr as the total pressure. In other hands, the ZnO nanoislands grown by using NO_2 gas as an oxygen source were optimized under the typical flow rates of DEZn and NO_2 at 3 and 100 μmol/min, respectively. The total pressure was fixed at 10 Torr. The surface morphologies of the ZnO nanoislands were investigated by atomic force microscopy (AFM) in a contact mode. Photoluminescence (PL) was measured using 325 nm line of a He-Cd laser (10 mW) as an excitation source, which was dispersed with a 1 m double monochromator and processed utilizing time-correlated single-photon-counting electronics.

RESULTS AND DISCUSSION

Growth with N_2O as an oxygen source

In the first step, we grew ZnO nanoislands at 400°C using different growth times with intervals of 4 s, where the typical flow rates of DEZn and N_2O were fixed at 0.5 and 10000 μmol/min. For a growth time of less than 20 s, it was very difficult to confirm the formation of ZnO islands. However, at 20 s, the ZnO islands were steeply structured with a density of about 7×10^8 cm^{-2} as shown in figure 1. The density of the islands gradually increased with additional growth time, while their size rapidly increased. In addition, the size uniformity of the islands deteriorated with increasing growth time. In order to examine the effect of growth temperature on the formation of ZnO nanoislands, we grew the ZnO islands for the same growth time (28 s) at different growth temperatures with intervals of 50°C. As shown in figure 2, the island density increases and the island size decreases with the increase of growth temperature from 400 to 500°C. Uniform islands with a narrow size distribution and a high density of 5.7×10^9 cm^{-2} were achieved at the growth temperature of 500°C. The increase of growth temperature usually increases the adatom

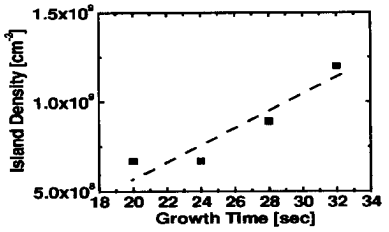

Figure 1. Density variation of ZnO islands grown at 400°C with different growth times.

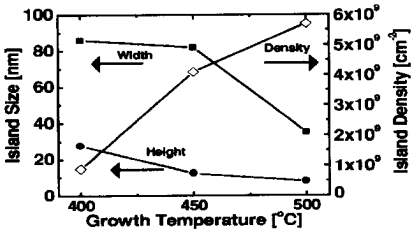

Figure 2. Variation of island sizes and density at different growth temperature for 28-s growth time.

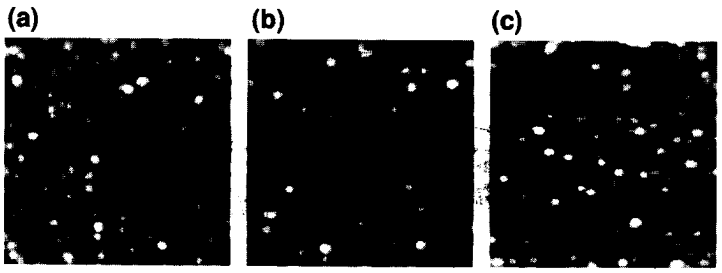

Figure 3. 600×600 nm^2 AFM images of the ZnO nanoislands on the SiO_2/Si substrates at 500°C for 30 s with the flow rate of DEZn as 3 μmol/min. (a) N_2O: 10000 μmol/min (island density: 5.8×10^{10} cm^{-2}), (b) N_2O: 7000 μmol/min (island density: 9.2×10^{10} cm^{-2}), and (c) N_2O: 5000 μmol/min (island density: 5.8×10^{10} cm^{-2}).

diffusion length, leading to the increase of the island size. However, the fragmentation due to elastic strain relaxation appears to compensate this effect at higher temperature. As a result, the island density increases and the average size decreases with increasing growth temperature, as shown in figure 2, in this oxygen abundant growth condition with the source ratio of N_2O/DEZn as 2×10^4. In PL spectra measured at 10 K, we could not observe any quantum size effects from the ZnO nanoislands grown by using N_2O under these conditions, which might be attributed to island size that is too big to cause quantum size effects.

There are reports on ZnO films with preferred *c*-axis orientation grown on amorphous SiO_2/Si by MOCVD [4]. The nucleation of ZnO crystallites is not efficient on SiO_2 substrates at the initial stage of growth due to the amorphous nature of SiO_2, which indicates that the nucleated ZnO crystallites have no specific epitaxial alignment with random distribution. This means that the adhesion probability of ZnO on SiO_2 is low. This fact suggested that optimized growth conditions to enhance stable nucleation in the initial stage of growth are strongly required.

In order to confirm low-dimensional quantum characteristics from ZnO nanoislands, we changed the growth condition. First of all, we varied the flow rate of N_2O gas from 10000 to 5000 μmol/min at the fixed DEZn flow rate as 3 μmol/min. Under these growth conditions, the density of ZnO nanoislands was steeply increased up to the order of 10^{11} cm^{-2} with decreasing the flow rate of N_2O as shown in figure 3. This result shows that the increment of DEZn/N_2O ratio can give a distinct enhancement of the island density by acceleration of the Volmer-Weber-type like three dimensional growth mode, which might be due to the increased sticking probability of Zn atoms on SiO_2/Si substrates by the suppressed pre-reaction between Zn and O atoms in the MOCVD reactor. To investigate optical properties of ZnO nanoislands presented in figure 3, we carried out PL measurements. In the PL spectra measured at 10 K from two ZnO nanoisland samples grown with the flow rate of N_2O gas as 10000 and 7000 μmol/min, the broad emission band with a tail up to about 3.65 eV over the ZnO band gap was observed in addition to a peak labeled "D^0X" which is attributed to the well-known neutral donor-bound exciton emission as shown in figure 4. This is an indication that the experimentally observed band-gap enhancement results from

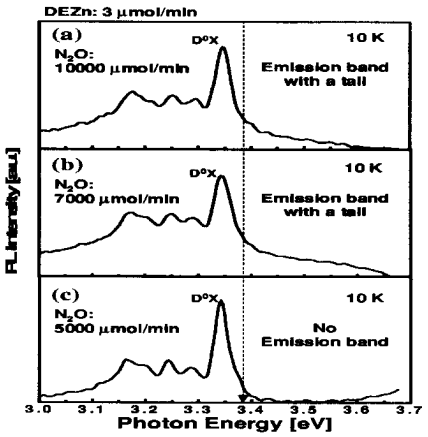

Figure 4. PL spectra, measured at 10 K, from the ZnO nanoisland samples grown on the SiO_2/Si substrates at 500°C for 30 s with the flow rate of DEZn as 3 μmol/min. (a) N_2O: 10000 μmol/min, (b) N_2O: 7000 μmol/min, and (c) N_2O: 5000 μmol/min.

low-dimensional quantum confinement characteristics. However, the D^0X emission from the ZnO nanoisland samples, which probably originates from large dots, is somewhat red-shifted which might be due to the insufficient crystal and optical properties of ZnO nanoislands. However, we could not observe the band tail emission over the ZnO band gap from the sample grown with the flow rate of N_2O as 5000 μmol/min, which might be attributed to the deteriorated stoichiometry of ZnO nanoislands due to the excessive supply of Zn atoms compared to that of the other two samples. With almost no expected diffusion of carriers from SiO_2 to the ZnO nanoislands, the luminescence from the islands is mainly attributed to carriers generated within the islands, leading to quantum size effects. Therefore, the structural and optical qualities of ZnO islands are very important to achieve efficient quantum size effects in our system, which indicates that ZnO nanoislands with the amorphous and/or poly-crystalline structure can act as nonradiative recombination centers and diminish the efficiency of the emissions with quantum size effects from ZnO nanoislands.

Growth with NO_2 as an oxygen source

For that reason, more reactive NO_2 gas for the oxygen source than N_2O was introduced in order to achieve effective quantum size effects from ZnO nanoislands by the enhancement of crystallinity. ZnO nanoislands were grown at 450 and 550°C for 90 s with the typical flow rates of DEZn and NO_2 being 3 and 100 μmol/min, respectively. In the sample grown at 550°C, the dot density is 1.8×10^{11} cm^{-2}, the average height is 6 nm, and the average width is 31 nm. However, island formation at relatively low growth temperature of 450°C is extremely dense and makes accurate measurements impossible. PL

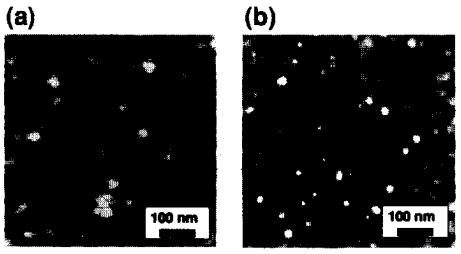

Figure 5. 600×600 nm^2 AFM images of nanoislands grown on the SiO_2/Si substrates by using NO_2 as the oxygen source. (a) ZnO nanoislands grown at 450°C for 90 s and (b) ZnO nanoislands grown at 550°C for 90 s.

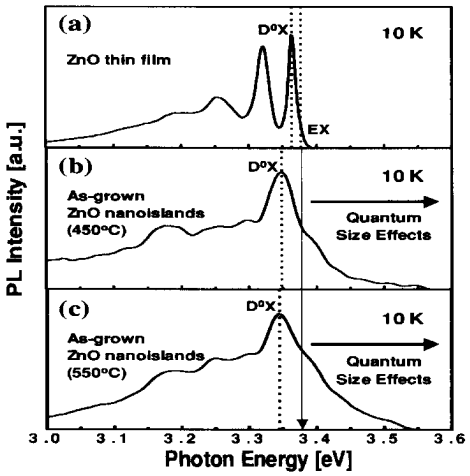

Figure 6. PL spectra, measured at 10 K, of the ZnO thin film and nanoislands grown on the SiO_2/Si substrates by using NO_2 as the oxygen source. (a) ZnO thin film grown at 550°C for 60 min, (b) ZnO nanoislands grown at 450°C for 90 s, and (c) ZnO nanoislands grown at 550°C for 90 s.

spectra measured at 10 K from the ZnO thin film (grown at 550°C for 60 min) and two ZnO nanoisland samples on the same SiO_2/Si substrates represented at figure 5, respectively, are presented in figure 6. In the PL spectrum from the ZnO thin film, a shoulder peak at 3.377 eV labeled "EX" and a sharp peak labeled "D^0X" are attributed to the free exciton emission and the neutral donor-bound exciton emission, respectively. For the ZnO nanoislands, we observed the broad emission band with a tail up to about 3.55 eV located at the higher energy with respect to band edge emission of ZnO thin films, where the free exciton emission is generally located at about 3.377 eV. This is an additional indication of the experimentally observed band-gap enhancement as mentioned before in the case of N_2O.

The band gap enhancement according to effective mass theory assuming infinite potential barriers to clarify quantum size effects was theoretically investigated. The energy E of the free exciton emission from low-dimensionally confined ZnO nanoislands is approximately given by [5]

$$E \approx E_{EX,ZnO} + \frac{\pi^2\hbar^2}{2}\left(\frac{1}{m^*_e} + \frac{1}{m^*_h}\right)\left(\frac{1}{l^2} + \frac{2}{w^2}\right)$$

neglecting the enhancement of exciton binding energy in nanoislands, where l and w is the dot height and width, respectively. The effective masses of electrons and holes are $m_e^* = 0.24m_0$ and $m_h^* = 0.45m_0$, respectively, for ZnO [6]. Here, $E_{EX,ZnO}$ is 3.377 eV as shown in figure 6, and l and w are expressed in nanometers. Substituting the average height of 6 nm and the average width of 31 nm, which were extracted from figure 5(b), the calculated emission energy is 3.45 eV, which fairly agrees with the experimental PL result shown in figure 6(c).

CONCLUSIONS

We have fabricated self-organized ZnO nanoislands with low-dimensional quantum characteristics on SiO_2/Si substrates by MOCVD, which has been confirmed by AFM and PL studies. In PL results measured at 10 K, we observed the broad spectra with band tails, which were located at the higher energy with respect to band edge emission of ZnO thin films. These results indicate that the ZnO nanosize islands grown on SiO_2/Si substrates have low-dimensional quantum effect characteristics.

ACKNOWLEDGEMENT

The authors wish to thank Dr. M. Funato for helpful discussions. This work was partly supported by the Kyoto University Venture Business Laboratory (KU-VBL) research program and also by a Grant-in-Aid for Scientific Research from the Ministry of Education, Culture, Sports, Science, and Technology of Japan.

REFERENCES

1. K. Hümmer, *Phys. Status Solidi B* **56**, 249 (1973).
2. Z. W. Pan, Z. R. Dai, and Z. L. Wang, *Science* **291**, 1947 (2001).
3. E. M. Wong and P. C. Searson, *Appl. Phys. Lett.* **74**, 2939 (1999).
4. S. Muthukumar, C. R. Gorla, N. W. Emanetoglu, S. Liang, and Y. Lu, *J. Cryst. Growth* **225**, 197 (2001).
5. S.-W. Kim, Sz. Fujita, and Sg. Fujita, *Appl. Phys. Lett.* **81**, 5036 (2002).
6. E. M. Wong and P. C. Searson, *Appl. Phys. Lett.* **74**, 2939 (1999).

Mat. Res. Soc. Symp. Proc. Vol. 739 © 2003 Materials Research Society

Morphology Evolution of Pyramid-like Nanostructures on Cobalt Thin Films during Deposition by Sputtering

Shih-Wei Chen[1], Jin-Ruey Wen[1], Chuan-Pu Liu[1] and Jiun-Nan Chen[2]
[1] Department of Materials Science and Engineering, National Cheng-Kung University, Tainan, Taiwan
[2] Department of Electrical Engineering, Fortune Institute of Technology, Kaohsiung, Taiwan

ABSTRACT

The cobalt thin films are grown by D.C. magnetron sputtering as a function of the target-to-substrate distance, bias and power on both Si (100) and (111) substrates. The crystal structure and morphology of the thin films are characterized by 4-point probe, x-ray diffraction, scanning electron microscopy, transmission electron microscopy and atomic force microscopy. It is found that the cobalt crystal structure can be varied from HCP to FCC by varying the target–to-substrate distance from 6 to 10 cm. The resistivity, roughness and the preferred orientation of the thin films are greatly affected by the substrate bias and power. The lowest resistivity of Co films is 9.8 $\mu\Omega$-cm when deposited at the target–to-substrate distance of 6cm, the applied power of 50W and the substrate bias of -75 volts. In addition, pyramid-like nanostructures with sharp tips are formed on the surface of the thin films when negative bias is applied. The faceted planes on the nanostructures depend on the resulting Co crystal structure while the size and density are determined by the growth parameters. The evolution of the surface nanostructures are systematically examined as a function of substrate bias and thin film thickness. The formation mechanism of the surface nanostructures is discussed in the paper.

INTRODUCTION

Cobalt possesses many superior properties including their electrical and magnetic properties and hence has attracted much attention [1,2]. For instance, cobalt has been successfully employ as catalyst for carbon nanotube (CNT) growth [3] and cobalt silicide has been investigated to replace titanium silicide in IC technology due to its thermal stability and lower resistivity [4]. Here we present the cobalt thin film growth by DC magnetron sputtering and show the microstructure evolution with various processing parameters. In addition, the pyramid-like nanostructures are found to form on cobalt thin film surface only under certain growth condition. The pyramid-like nanostructures has well defined shape and size with a sharp tip. The nanostructures might be applied in magnetic recording media or to grow CNT on its tip as the most active catalytic site. Therefore, we also investigate the nanostructure evolution with various processing parameters in great detail in this study.

EXPERIMENTAL DETAILS

A DC magnetron sputter is employed to deposit Co thin films on n-type Si(100) and (111) substrates. The substrates were chemically cleaned before loading into the chamber. The Co target (99.95% purity) is pre-sputtered for 10 minutes after base pressure of 3×10^{-6} torr is reached using argon (99.995% purity) as the sputtering gas. During deposition, the total gas flow and applied power are maintained at 40 sccm while other deposition parameters are varied to examine the microstructure evolution of the growing Co thin films. The experiment was performed at room temperature. On the characterization side, α-step and 4 point probe station are used to measure the film thickness and electrical resistivity; x-ray diffraction (XRD) is employed to determine the texture microstructures of thin-films; and scanning electron microscope (SEM) were employed to examine the surface morphology. TEM is employed to examine the phases of the evolving thin films.

RESULTS AND DISCUSSION

1. Co thin film evolution

Co has two stable phases, low temperature ε-Co (hcp structure) and high temperature α-Co (fcc structure) where the transformation temperature is about 400~420 °C. Through varying the target-to-substrate distance (d_{ts}) for the working pressure of 8m torr, we found

that the cobalt thin film can be varied efficiently from fcc (d_{ts} = 10cm) to hcp (d_{ts} = 6cm) for a thickness of about 1 μm as shown in Fig.1 from TEM images and diffraction patterns. Although the stable phase of cobalt at the deposition temperature is ε-Co, the activation energy is higher than α-Co, caused by the strain energy with Si (100). Hence, the formation of phases is certainly determined by the energy of arriving adatoms, while at short deposition distances, the adatoms with less scattering might have enough energy to undergo longer lateral diffusion and thus transform to stable ε-Co plase earlier.

The resistivity of the cobalt thin film is investigated with substrate bias for 6 and 10 cm deposition distance and is shown in Fig.2. The resisitvity decreases both with increasing positive or negative bias for both deposition distances, while the resistivity of α-Co is higher than that of ε-Co at zero bias, indicating different electrical properties of the two phases depending on the preferred orientation. The preferred orientation is rich in cobalt especially for the ε-Co phase as demonstrated in Fig.3, where the intensity ratio of each peak from XRD pattern is plotted with substrate bias. The thin film texture transforms from 10-10 to 0002 dominant as increasing negative bias. This illustrates the complex energy dependence of plane formation and should be examined further. Combining our preliminary study on the parameter space, the optimum electrical resistivity of 9.8 $\mu\,\Omega$-cm is deposited at the target–to-substrate distance of 6 cm, the applied power of 50W and the substrate bias of -75 volts.

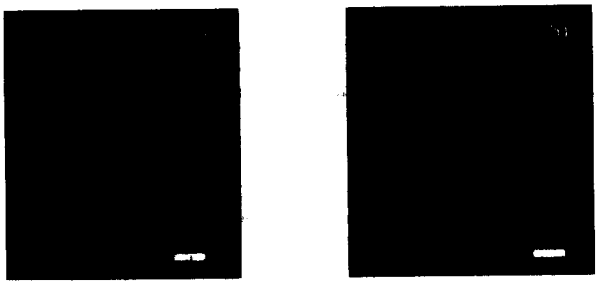

Fig.1 TEM bright field images and diffraction patterns of Co thin films deposited at (a) d_{ts} = 6cm, found ε-Co(HCP), (b)d_{ts} = 10cm, found α-Co(FCC).

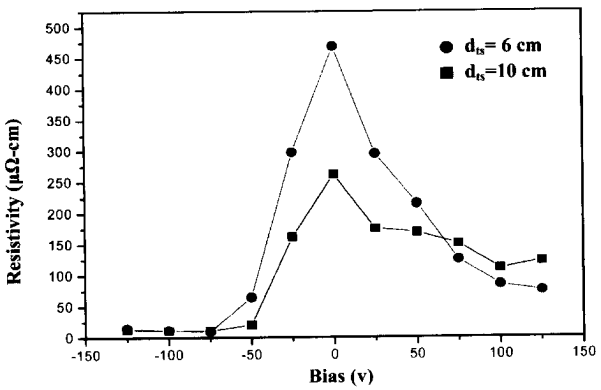

Fig.2 Electrical resistivity as a function of substrate bias for Co thin films deposited at 6 and 10 cm.

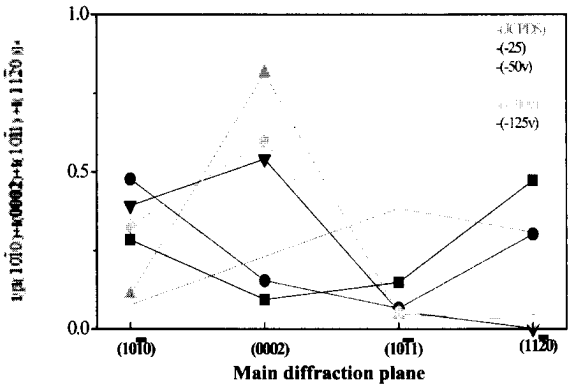

Fig.3 The preferred orientation is rich in cobalt especially for the ε-Co phase, where the intensity ratio of each peak from XRD pattern is plotted with substrate bias.

2. Pyramid-like nanostructure evolution

When studying the surface morphology evolution, the pyramid-like nanostrucutures are found to form on the growing surface as in Fig.4 where the SEM images are shown with substrate bias for the deposition distance of 6 cm and the applied power of 50W. It is worth noting that the nanostructures are only produced under negative bias. The nanostructures have well defined shapes with a sharp tip determined by its surface energy. The density increases with substrate bias while the size of the base width increases from about 100 nm at -30V to 250 nm at -50V followed by a decrease to 100 nm at -60V. This certainly states that the formation of nanostructures is related to the energy of the deposited adatoms which is varied by the negative bias. However, the ion bombardment effect prevents the nanostructure from further growth at higher negative bias.

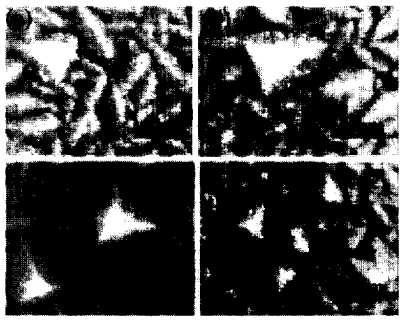

Fig.4 SEM plan view images of Co thin films, as a function of substrate bias (a)-30V (b)-40V (c)-50V (d)-60V.

Since the nanostructure formation is related to the energy, we examine the morphology evolution with applied power from 40 to 70 W as shown in Fig.6 for plan view images and Fig.7 cross sectional images. The pyramid-like nanostructure has the biggest size of about 250 nm at the power of 50 W, while the size distribution changes from 60-220nm for 40 W to 20-150nm for 70 W. With increasing applied power, the average size decrease and density increases, indicating that the ion bombardment effect is more pronounced than the energetic

ions. Fig.8 demonstrates the film thickness effect on the nanostructures morphology evolution from 720 to 1260 nm. It can be seen that the density of smaller sized nanostructures decreases and that of larger sized nanostructures increases with thickness. It reflects that film thickness also affect the nanostructure array, which suggests the volume related strain is involved in the mechanism. The formation mechanism is thus strain-driven surface diffusion process, since cobalt has a high diffusion coefficient than other elements, in combination with surface modification by ion bombardment. The above results are obtained from hcp phase under the deposition distance of 6 cm, and thus the faceted planes on nanostructures must be related to the low index planes in hcp according to the γ plot, which awaits more studies by cross section TEM. We found two types of faceted planes of the pyramid structures on Co thin films, where type I is composed of 01-10 and 11-20, type II is composed of only 01-10 plane, and base plane is 10-10.(Fig.5)[5]

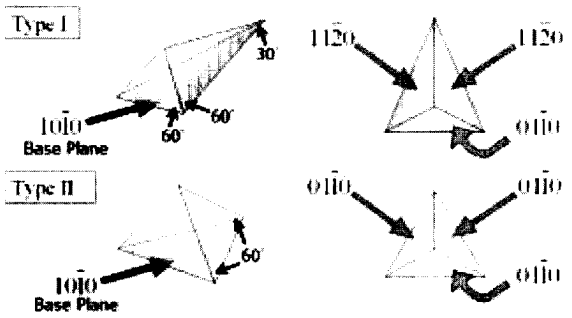

Fig.5 Sketch of the faceted planes of the pyramid structures on Co thin films, where Type I is composed of 01-10 and 11-20, Type II is composed of only 01-10 plane, and the base plane is 10-10.

We then also study the surface morphology on fcc cobalt films deposited using 10 cm deposition distance with various power from 60 to 90 W as shown in Fig.9. Surprisingly, no nanostructures are formed on the surface for all conditions and the surface becomes smooth with increasing applied power. The reason is not clear now but could be related to the surface diffusion coefficient difference between hcp and fcc crystals.

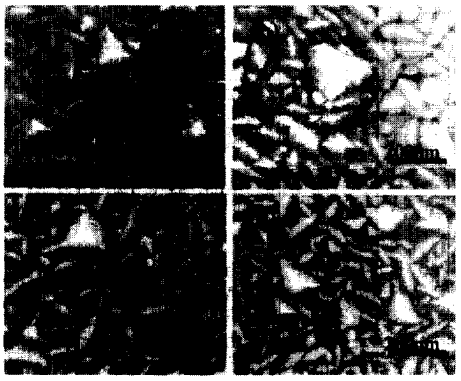

Fig.6 SEM plan view images of Co thin films, as a function of applied power (a) 40W (b)50W (c)60W (d)70W.

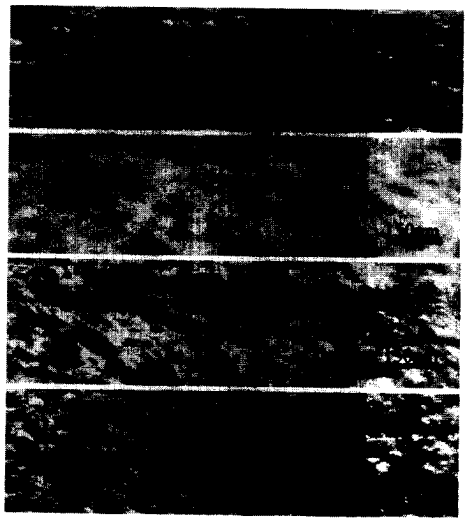

Fig.7 SEM cross sectional images of Co thin films, as a function of applied power (a) 40W (b)50W (c)60W (d)70W.

In order to visualize the substrate effect, cobalt is also deposited on Si(111) substrate using applied power of 75 and 125 W as shown in Fig.10. The shape becomes more complicated, where pyramid-like nanostructures with pentagon or various polygon bases are observed. Nanostructures disappears when the ion bombardment become more serious at higher applied power analogous to the case in Si(100) substrate.

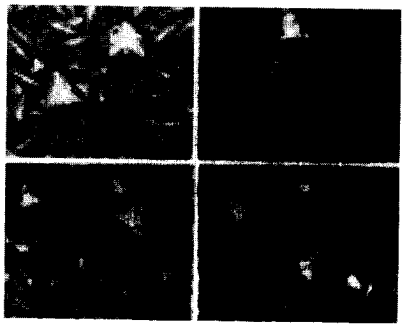

Fig.8 SEM plan view images of Co thin films, as a function of thickness (a)1260nm (b)1080nm (c)900nm (d)720nm.

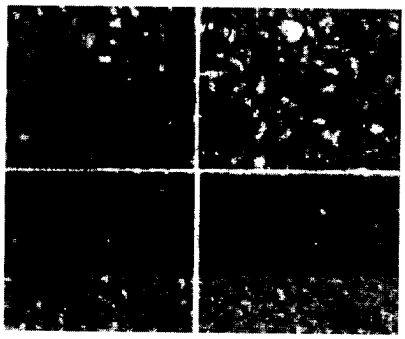

Fig.9 SEM plan view images of Co thin films deposited at the deposition distance of 10cm, as a function of applied power (a)60W (b)70W (c)80W (d)90W.

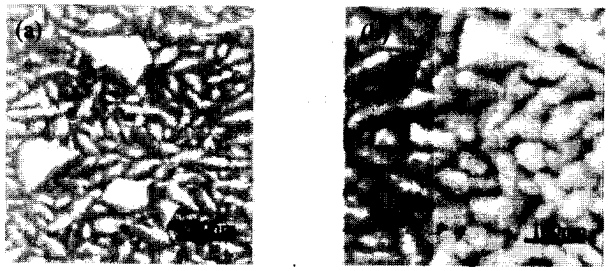

Fig.10 SEM plan view images of Co thin films deposited at Si(111) substrate, as a function of applied power (a)75W (b)125W

CONCLUSIONS

Cobalt thin film can evolve into stable ε-Co(hcp) or α-Co(fcc) phases by DC magnetron sputtering using deposition distance of 6 and 10 cm, respectively. The preferred orientation evolution of cobalt thin film with substrate bias is complex, while the resistivity as low as 9.8 $\mu\,\Omega$-cm can be achieved under the target-to-substrate distance of 6cm, the applied power of 50W and the substrate bias of -75 volts. Pyramid-like nanostructures are formed on Co thin films only under negative bias and size, density and shape are modified by bias, applied power, microstructure and substrate type. This suggests the strain driven surface diffusion and ion bombardment are the two dominant mechanisms responsible for the nanostructure formation. There are two types of faceted planes of the pyramid structures on Co thin films, where type I is composed of 01-10 and 11-20, type II is composed of only 01-10 plane, and base plane is 10-10.

ACKNOWLEDGEMENTS

The work is supported by NSC, Taiwan under the project number of NSC90-2218-E-006-053. We are also grateful for the use of the sputter equipment in the Semiconductor Lab, which is supported and maintained by the Department of Materials Science and Engineering at National Cheng-Kung University, Taiwan.

REFERENCES

1. G. J. van Grup, W. F. van der Weg, and D. Sigurd, "interaction in the Co/Si Thin Film System. ¢". Diffusion Maker Experimenrts", J. Appl.Phys. 49 (1978) 4011-4020.
2. K. N. Tu and J. M. Mayer, "Silicide Formation ", in Thin Films-Interdifusion and Reactions, edited by J. M. Poate, K. N. Tu and J. W. Mayer (Wiley, New York, 1978) p.359
3. Peter J.F.Harris, Cambridge(1999) "Carbon Nanotubes and Related Structures"
4. K. Maex, "Silicides for Integrated Circuits ¡ ĞTiSi2 and C0Si2",Materials Science and Engineering R11,p.53-p.153(1993)
5. Taylor, A., and Leber S., Trans., AIME, 200, 190 (1954)

Mat. Res. Soc. Symp. Proc. Vol. 739 © 2003 Materials Research Society H7.37

Wet-Process Molecular Planting in A Specific Site on Silicon with Si-C Covalent Bonds

Hirokazu Tada[1,2], Masato Ara[2] and Shoji Tanaka[1,2]
[1]Institute for Molecular Science, Okazaki National Research Institutes
Myodaiji, Oakzaki 444-8585, Japan
[2]Department of Structural Molecular Science, The Graduate University for Advanced Studies
Myodaiji, Okazaki 444-8585, Japan

ABSTRACT

Alkyl monolayers anchored covalently on silicon were prepared through the reaction between 1-alkenes and hydrogen-terminated silicon (111) surfaces. The 2D-patterning of the surface was done by local oxidation with an atomic force microscope (AFM) and 3D-molecular assemblies were fabricated by immobilization of molecules in a specific site of the patterned surface. The surfaces were anodized with a contact-mode AFM by applying a positive bias voltage to the surface with respect to the platinum-coated cantilever under ambient conditions, which resulted in nanometer-scale oxidation of surfaces. The anodized areas were etched and terminated with hydrogen atoms by NH_4F solution, in which we could immobilize various molecules having C=C bonds. We put arylamine molecules to which organic dyes such as fluoroscein were anchored. The intensity of luminescence varied depending on dopant concentration of substrates. Luminescence was very weak on highly-doped silicon possibly due to effective energy transfer from dyes to substrates. The method demonstrated is one of the promising ways to fabricate 3D-assemblies of molecular-scale electronic devices with a stable interface on silicon.

INTRODUCTION

Much attention has recently been paid to preparation and characterization of molecular-scale electronic devices [1]. Molecular assemblies based on thiolate / gold systems have been intensively studied as one of the most promising ways to fabricate nanometer scale devices. But the interface between Au and S atoms has not yet been well characterized. In addition, the method to put the molecule in the specific sites of metal electrodes has not been established.

One promising way to overcome these difficulties is to assemble organic molecules on inorganic semiconductors including silicon through covalent bonds such as Si-C. A number of dry [2-5] and wet [2, 6-11] processes have been examined to provide organic/inorganic systems based on Si-C covalent bonds. The advantage of Si-C systems comparing to Au-S systems is as follows: (a) the interface is thermally and chemically stable, (b) the substrates with various dopant levels are available, and (c) micro- and nano-fabrication techniques established in the field of semiconductor devices are applicable. In the previous papers, we demonstrated the preparation of highly ordered organic monolayers anchored covalently to Si(111) and 2-dimensional nano-patterning using an atomic force microscope (AFM) [12, 13].

Figure 1 shows nano-patterning and chemical modification of a silicon surface which is covered with alkyl monolayers. Nanometer-scale anodization of the surface was done using contact-mode AFM (Jeol, JSPM-1300) with platinum-coated cantilevers (NT-MDT, spring constant 0.6 N/m) under ambient conditions (a). Typical bias voltage applied to the surface was

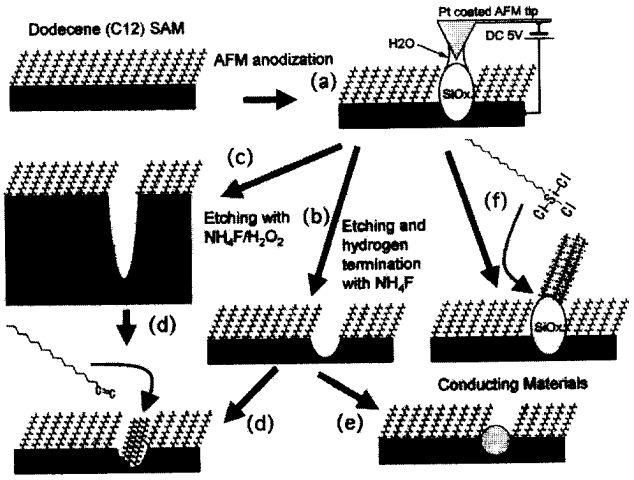

Figure 1. Schematic view of nano-patterning and chemical modification of the silicon surface covered with alkyl monolayers.

+5 V with respect to the cantilever. The scan speed was set to 200 nm/s. Anodized areas were etched by 8% NH_4F for 5 min at room temperature, and were rinsed with ultrapure water (b). When we used H_2O_2/NH_4F solution, the deep grooves were formed (c). The etched surface was terminated with hydrogen atoms, on which various molecules having a C=C bond were immobilized (d). The etched area could be plated with metals and conducting polymers (e). In addition, the oxidized areas were covered selectively with silane-coupling agents such as octadecyltrichrolosilane (OTS; $CH_3(CH_2)_{17}SiCl_3$) (f).

A next step of this work is to immobilize functional molecules such as dyes. In the present work, we have prepared arylamine monolayers anchored covalently to silicon, on which we planted fluorescein dyes. It was found that the luminescence from dyes varied depending upon dopant levels of silicon substrates.

EXPERIMENTAL

Hydrogen termination of Si(111) surfaces was carried out according to the method of Wade and Chidsey [14]. Organic monolayers were prepared through the reaction between molecules having C=C bonds and hydrogen terminated silicon (H-Si). We used arylamine (CH_2=CH-CH_2NH_2) in the present study. Figure 2 shows a schematic of the process. The direct reaction of arylamine with H-Si resulted in disorderd layers possibly due to the reaction of amino group instead of the C=C bond. In order to avoid undesirable reactions, we synthesize the molecule 1 by the coupling of 3-amino-propene with 1,2-bis (chlorodimethylsilyl) ethane. The molecule 1, called protected-amine, was identified with NMR.The H-Si(111) substrates were transferred into a 4:6 mixture (v/v) of protected-amine and mesitylene, which was deoxygenated

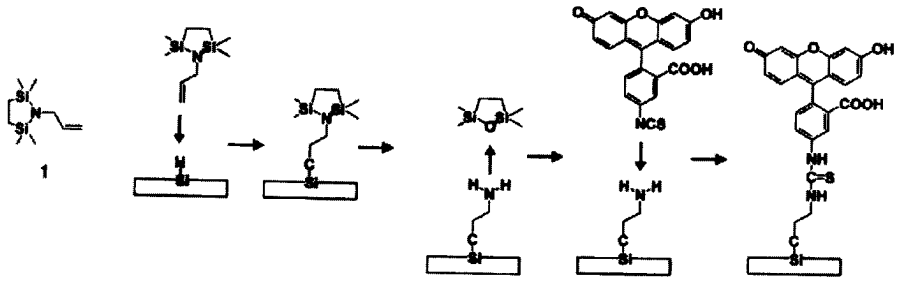

Figure 2. Immobilization of fluorescein dye molecules on silicon via arylamine molecules. The NH_2-group of arylamine was terminated with 1,2-bis (chlorodimethylsilyl) ethane to avoid the reaction of NH_2-group with H-Si(111). The protecting group was removed in acid and fluorescein dye with NCS-terminal was immobilized.

by argon bubbling for at least 1 h prior to the reaction. Then the solution was heated at 433K for 24 h under continuous argon bubbling and cooled to room temperature. The sample was taken out of the solution and rinsed with petroleum ether, ethanol and dichloromethane.

It is possible to remove the protecting group under acidic conditions. After immersing the films in acid solution, they were rinsed in triethylamine to neutralize the surface. Fluorescein isothiocyanate (FITC) was purchased from Dojindo Chemical and used without further purification. The reaction of FITC with arylamine monolayer surface was performed by immersing the substrate in 0.1mg/ml aqueous solution of FITC for 1h at room temperature. Subsequently, the specimen was sonicated thoroughly in acetone to remove physical adsorbates.

The surface structure was characterized with contact-mode AFM, force curve measurements, and water contact angle measurements. Luminescence spectra of FITC-arylamine monolayers on Si were measured using a fluorometer (SPEX, Fluorolog-2) at an excitation wavelength of 450 nm. The measurement was performed at room temperature in ambient air. Arylamine monolayers on Si were used as references.

RESULTS AND DISCUSSION

Figure 3(a) and 3(b) show contact-mode AFM images (1 μm x 1μm) of a protected-amine monolayer and FITC layers immobilized, respectively. Terraces with monoatomic height steps can be seen, although some corrugations especially in Fig. 3(b) exist possibly due to steric hindrance between molecules. When arylamine molecules without protection reacted on the surface, the terraces could not be observed. The protection of amino groups was effective to prepare ordered arylamine monolayers.

Figure 4 shows luminescence spectra of FITC-arylamine monolayers anchored covalently to various silicon substrates. The curves (a), (b) and (c) are the spectra of a monolayer on n-type (1300 Ωcm), p-type (8.4-8.9 Ωcm) and n-type (1-10 Ωcm) silicon substrates, respectively. Luminescence of the dyes immobilized on high conductive substrates was weaker than that on low conductive ones. This is possibly due to energy transfer from excited dyes to substrates.

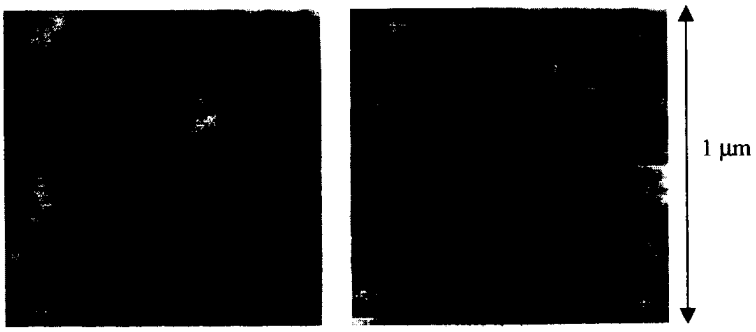

Figure 3. AFM images (1 μm x 1μm) of (a) protected-amine monolayers and (b) FITC layers on Si(111).

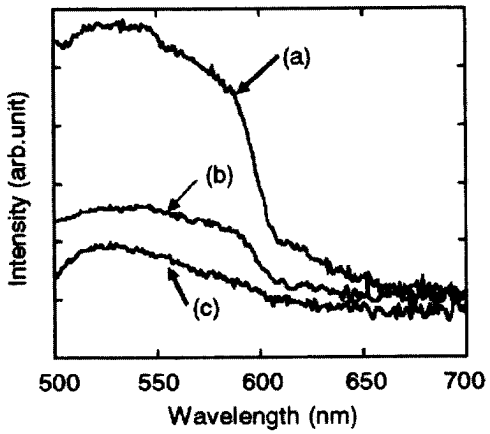

Figure 4. Luminescence spectra of FITC-arylamine monolayers immobilized on various Si substrates; (a) 1300 Ω cm (n-type), (b) 8.4-8.9 Ω cm (p-type), and (c) 1-10 Ω cm (n-type).

Although it is well known that the luminescence of dyes is effectively quenched on metal surfaces, there are few reports about luminescence of organic molecules on semiconductor surfaces. Suto et al. have reported that the luminescence of porphyrin films on SnO_2 was quenched effectively [15].

It was found that carriers in semiconductors play an important role for luminescence quenching. It is interesting to study the mechanism of electron and/or energy transfer between neighboring molecules, and molecules and substrates by controlling the distance between molecules and length of anchor molecules. The method demonstrated here can provide such systems.

CONCLUSION

Organic monolayers anchored covalently to silicon surfaces via silicon-carbon covalent bonds were prepared by wet process. The nanometer-scale patterning of the surface was done with AFM. The patterned areas could be terminated with various molecules such as fluoroscein dyes. The method demonstrated is one of the promising ways to fabricate 3D-assemblies of molecular scale electronic devices on silicon with a stable intarface.

ACKNOWLEDGEMENTS

This work was partly supported by Grant-in-Aid for Exploratory Research (No. 13874094) from the Japan Society for the Promotion of Science. H. T. and M. A. are grateful for funding from the Toray Science Foundation and the Sasagawa Science Foundation, respectively.

REFERENCES

1. C. Joachim, J. K. Gimzewski, and A. Aviram, *Nature* **408**, 541 (2000).
2. R. A. Wolkow, *Ann. Rev. Phys. Chem.* **50**, 413 (1999).
3. J. Yoshinobu, H. Tsuda, M. Onchi, and M. Nishijima, *J. Chem. Phys.* **87**, 7332 (1987).
4. J. S. Hovis and R. J. Hamers, *J. Phys. Chem.* **B102**, 687 (1998).
5. G. P. Lopinski, D. D. M. Wayner, and R. A. Wolkow, *Nature* **406**, 48 (2000).
6. M. R. Linford and C. E. D. Chidsey, *J. Am. Chem. Soc.* **115**, 1231 (1993).
7. M. R. Linford, P. Fenter, P. M. Eisenberger, and C. E. D. Chidsey, *J. Am. Chem. Soc.* **117**, 3145 (1995).
8. A. Bansal, X. Li, I. Lauermann, N. S. Lewis, S. I. Yi, and W. H. Weinberg, *J. Am. Chem. Soc.* **118**, 7225 (1996).
9. A. B. Sieval, V. Vleeming, H. Zuilhof, and E. J. R. Sudhölter, *Langmuir* **15**, 8288 (1999).
10. T. Yamada, N. Takano, K. Yamada, S. Yoshitomi, T. Inoue, and T. Osaka, *Jpn. J. Appl. Phys.* **40**, 4845 (2001).
11. L. H. Lie, S. N. Patole, E. R. Hart, A. Houlton, and B. R. Horrocks, *J. Phys. Chem.* **B106**, 113 (2002).
12. M. Ara, H. Graaf and H. Tada, *Appl. Phys. Lett.* **80**, 2565 (2002).
13. M. Ara, H. Graaf and H. Tada, *Jpn. J. Appl. Phys.* **41**, 4894 (2002).
14. C. P. Wade and C. E. D. Chidsey, *Appl. Phys. Lett.* **71**, 1679 (1997).
15. S. Suto, W. Uchida, M. Yashima and T. Goto, *Phys. Rev.* **B35**, 4393 (1987).

Physics, Chemistry and Modeling of Nanostructures

Mat. Res. Soc. Symp. Proc. Vol. 739 © 2003 Materials Research Society H7.40

Synthesis, Self-assembly and Magnetic Properties of FePtCu Nanoparticle Arrays

Xiangcheng Sun, S. S. Kang, J. W. Harrell and David E. Nikles

Center for Materials for Information Technology, The University of Alabama, Tuscaloosa, Alabama, 35487-0209
Z. R. Dai, J. Li and Z. L. Wang
School of Materials Science and Engineering, Georgia Institute of Technology, Atlanta, Georgia 30332-0245

ABSTRACT

FePtCu nanoparticles with varying composition were synthesized by chemical solution-phase reduction of platinum and copper reagents and thermal decomposition of iron pentacarbonyl in the presence of oleic acid and oleyl amine stabilizers. As prepared the particles had fcc structure with an average diameter of 3.5 nm and were superparamagnetic. The particles were well dispersed in hydrocarbon solvents and could be self-assembled into two or three dimensions particles arrays with a variety of close-packing arrangements. Heat-treatment of the self-assembled films at temperatures above 550°C transformed the particles from the fcc to the $L1_0$ phase, giving in-plane coercivities as high as 9000 Oe. X-ray diffraction revealed that the Cu remained in the annealed FePtCu films and the presence of an extra peak, indicated a second phase was present. Consistent with one or more phases, the magnetic hysteresis curves could be decomposed into a hard component (H_c > 5,000 Oe) and a soft component (H_c < 2,000 Oe). Unlike our earlier results for Ag in FePt, adding Cu to FePt did not lower the temperature required for phase transformation from the fcc to the fct $L1_0$ phase.

INTRODUCTION

The important report by S. Sun et al [1] on the synthesis, self-assembly and magnetic properties of nanometer-sized FePt particles caused an explosion of interest in the use of these particles in granular magnetic recording media. The FePt nanoparticles were prepared by the polyol reduction of platinum acetylacetonate and thermal decomposition of iron pentacarbonyl in dioctyl ether in the presence of oleyl amine and oleic acid. As made the FePt particles with particle size from 3 to 5 nm showed fcc structure and were superparamagnetic. The particles could be dispersed in hydrocarbon solvents using oleic acid and oleyl amine as surfactants. When the dispersions were cast onto solid substrates and the solvent evaporated, the particles self-assembled into close-packed arrays. After heat treatment at temperatures above 550°C the particles transformed to the $L1_0$ phase, having high magnetocrystalline anisotropy [2], giving films with high coercivity. However, there was considerable particle coalescence and loss of particle positional order when the films were heated to temperatures above 550°C [3]. Particle coalescence leads to increased switching volumes and increases the distribution of particle volumes, which defeats the

objective of making small monodisperse nanoparticles. It would be highly desirable if the temperature required for the fcc to fct (tetragonal phase) transformation were lower, at least below temperatures where the particles coalesce, preferably below the temperature where the organic surfactants decompose.

Maeda et al [4] observed that adding copper into FePt sputtered films greatly reduced the ordering temperature. For films containing $[FePt]_{85}Cu_{15}$ the coercivity was 5,000 Oe after just annealing at 300°C, while H_c for films containing FePt particles was only a few hundred Oe after annealing at 300°C. Takahashi and coworkers [5] found that adding 4 atomic percent Cu into FePt sputtered films decreased the temperature required for fcc to $L1_0$ ordering from 500 to 400°C. They suggested that the addition of Cu lowered the melting point for the alloy, increasing the atomic diffusivity, thereby enhancing the kinetics of ordering. These reports suggest the possibility of lowering the temperature needed to bring about the fcc to $L1_0$ phase transformation for FePt nanoparticles by adding copper. Accordingly we set about the task of preparing FePt nanoparticles containing Cu. Unlike sputtered thin films using a Cu target, a suitable chemical procedure had to be found for introducing Cu into FePt. The synthesis of FePtCu nanoparticles and the effect of the added copper on the phase transformation temperature are presented.

EXPERIMENTAL

All chemicals were purchased from Aldrich Chemical Company and used as received. The particle composition was determined by energy dispersive x-ray analysis on a Philips model XL 30 scanning electron microscope. X-ray diffraction data were obtained on a Rigaku D/MAX-2BX Horizontal XRD Thin Film Diffractometer using Cu K_α radiation. Transmission electron microscopy (TEM and HRTEM) images and smaller angle and selected area electron diffraction patterns (ED) were obtained on Hitachi HF-2000 FE field emission at 200 keV and JEOL-4000 EX at 400 keV transmission electron microscopes. Magnetic hysteresis loops were measured with a Princeton Measurements Model 2900 alternating gradient magnetometer (AGM) with a maximum field of 20 kOe.

The synthesis of typical $Fe_{45}Pt_{44}Cu_{11}$ nanoparticles is described as follows. A 50 mL three-necked round bottom flask was equipped with magnetic stirring, a reflux condenser, a thermometer, a rubber septum, and an argon atmosphere. Teflon sleeves were used for all ground glass joints. To the flask was added 0.25 mmol platinum acetylacetonate, 0.08 mmol copper bis(2,2,6,6-tetramethyl-3,5-heptanedionate) and 10 mL phenyl ether. The mixture was heated to 80°C, whereupon it turned brown. Then 0.50 mmol oleic acid, 0.50 mmol oleyl amine and 0.1 mL (0.08 mmol) iron pentacarbonyl were added by syringe. The septum was replaced with a glass stopper and the reaction mixture heated to the reflux temperature of phenyl ether (~260°C). After refluxing for 30 minutes, the reaction mixture was allowed to cool to room temperature, giving a dark dispersion. Ethanol (25 mL) was added to precipitate the particles and the particles were isolated by centrifuging. The particles were re-dispersed in hexane, precipitated with ethanol and isolated by centrifuging. The particles were dispersed in a 50/50 mixture of hexane and octane, the dispersion cast onto either a silicon wafer or a carbon-coated TEM grid, and the solvent was allowed to evaporate at room temperature. The films were heat-treated in a Lindberg tube furnace for 30 minutes in flowing 5% hydrogen in argon atmosphere.

RESULTS and DISCUSSION

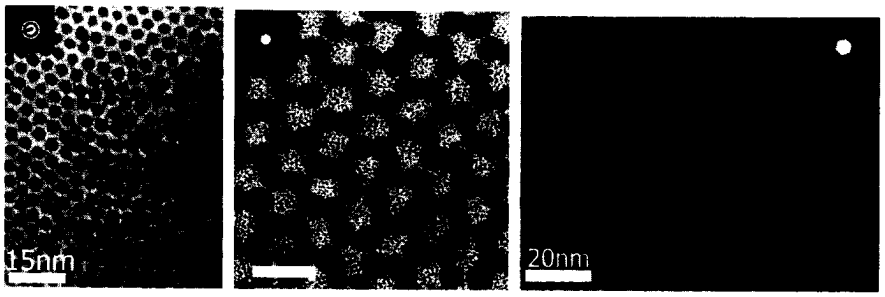

Figure 1. TEM images and the corresponding ED patterns for self-assembled FePtCu particles.

Fig. 1 is a series of TEM overview images and ED patterns of the self-assembled FePtCu particles, showing an average particle size of about 3.5nm in diameter. The inset selected area electron diffraction pattern in Fig. 1 and the following x-ray diffraction in Fig. 2 revealed the particles had fcc structure. Spontaneous self-assembled superstructures were observed when colloidal solutions of FePtCu particles were spread onto a substrate (e.g. TEM grids) with subsequent slow evaporation of the carrier solvent. The particles were well dispersed in hydrocarbon solvents and self-assembled into two or three dimensions particles arrays with a variety of close-packing arrangements. Domain of monolayer, bilayer and multilayer arrays were frequently detected in TEM specimens.

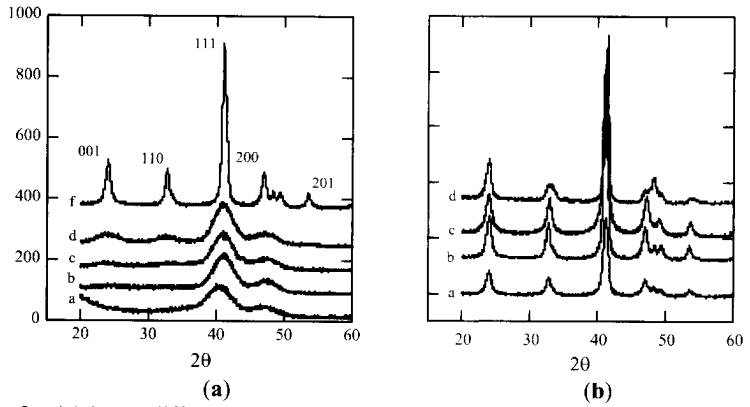

Figure 2. (**a**) X-ray diffraction curves for $Fe_{45}Pt_{44}Cu_{11}$ films anealed at different temperatures. As prepared curve a; 500°C, curve b; 550°C, curve c; 600°C, curve d; and 700°C, curve e. (**b**) Comparison of the x-ray diffraction curves or the different FePtCu films after annealing at 700°C, $Fe_{35}Pt_{50}Cu_{15}$, curve a; $Fe_{45}Pt_{44}Cu_{11}$, curve b; $Fe_{48}Pt_{40}Cu_{12}$, curve c; and $Fe_{55}Pt_{35}Cu_{10}$, curve d.

The FePtCu particles films were heat-treated in a tube furnace under flowing 5% hydrogen in argon for 30 minutes. The purpose of the hydrogen was to avoid oxidation. Unlike the case with films containing $[Fe_{49}Pt_{51}]_{88}Ag_{12}$ nanoparticles or with FePt sputtered films containing Cu, there was no decrease in the temperature required to transform the FePtCu nanoparticles from the fcc phase to the $L1_0$ phase. In Fig. 2a are a series of x-ray diffraction curves for films containing $Fe_{45}Pt_{44}Cu_{11}$ nanoparticles heat-treated at different temperatures. The evolution of the x-ray diffraction curves for films containing $Fe_{55}Pt_{35}Cu_{10}$, $Fe_{48}Pt_{40}Cu_{12}$ or $Fe_{35}Pt_{50}Cu_{15}$ nanoparticles was very much the same as Fig. 2a. In contrast to the case for the with films containing $[Fe_{49}Pt_{51}]_{88}Ag_{12}$ nanoparticles where the Ag <111> peak appeared as the Ag phase separated for the FePt, there was no new peak at $2\theta = 43.3°$ that could be attributed to the Cu <111> diffraction. Cu remains in the particles after heat treatment. However, when heated to high enough temperatures, the films did transform to an $L1_0$ phase as indicated by the appearance of the superlattice peaks <001> and <110>. For all compositions heat-treated at 500°C, there were no superlattice diffraction peaks, indicating the particles remained in the fcc phase. For three of the compositions, $Fe_{55}Pt_{35}Cu_{10}$, $Fe_{48}Pt_{40}Cu_{12}$, and $Fe_{35}Pt_{50}Cu_{15}$, the superlattice peaks appeared after heating at 550°C, while the film having $Fe_{45}Pt_{44}Cu_{11}$ nanoparticles the superlattice peaks appeared after heating at 600°C.

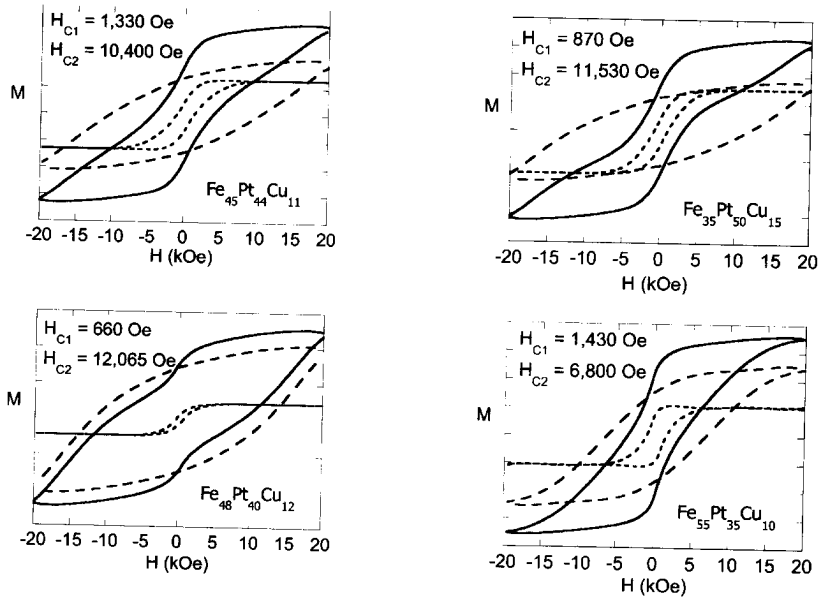

Figure 3. Magnetic hysteresis curves for the film containing $Fe_{45}Pt_{44}Cu_{11}$, $Fe_{48}Pt_{40}Cu_{12}$, $Fe_{35}Pt_{50}Cu_{15}$, and $Fe_{55}Pt_{35}Cu_{10}$ (solid line), and the corresponding decomposed curves for the hard component (dashed line) and the soft component (dotted line).

Tulameenite ($FeCuPt_2$) is an iron-platinum-copper mineral from the Tulameen river area of British Columbia [6]. Tulameenite has a $L1_0$ phase with a = 389.1 pm, c = 357.7 pm and c/a = 0.923. The ternary Fe-Pt-Cu phase diagram shows a one-phase region for FePtCu and other regions where the $L1_0$ phase and the fcc phase coexist [7]. Careful examination of the x-ray diffraction curves for the films heat-treated at 700°C, Fig. 2b, revealed an extra peak near $2\theta = 48.5°$, between the <200> and the <002> peaks. This peak may be due to the presence of a small amount of the fcc phase ($L1_0$ $CuFePt_2$ or cubic $FePt_3$). The extra peak was not seen for $Fe_{48}Pt_{40}Cu_{12}$.

Fig.3 shows the magnetic hysteresis loops measured for the $Fe_{45}Pt_{44}Cu_{11}$, $Fe_{48}Pt_{40}Cu_{12}$, $Fe_{35}Pt_{50}Cu_{15}$, and $Fe_{55}Pt_{35}Cu_{10}$ particles films annealed at 700°C. All the shapes of the loops suggested a mixture of magnetically hard and soft phases. All FePtCu compositions annealed at 700°C had this characteristic shape, and all could be decomposed into hard and soft loops. The coercivities of the hard and soft components are indicated in Fig.3, along with the coercivities of the full loops. The hard component coercivities of $Fe_{45}Pt_{44}Cu_{11}$, $Fe_{48}Pt_{40}Cu_{12}$, and $Fe_{35}Pt_{50}Cu_{15}$ are all comparable to that of $Fe_{48}Pt_{52}$ annealed at 700°C [1]. In all cases, the shape of the loops suggested that the maximum field of the AGM was not sufficient to saturate the loops and that the actual coercivities were higher. These results are consistent with the XRD spectra that suggest phase segregation of the FePtCu particles into $L1_0$ and disordered fcc phases. The hysteresis loop for the $Fe_{48}Pt_{40}Cu_{12}$ particles has the weakest soft magnetic fraction (<20%), which is consistent with the fact that the XRD shows no evidence of a cubic phase. The soft magnetic phases may also consist of iron oxides, which if disordered, would not exhibit well-defined XRD peaks. In addition, the temperature required for significant coercivity enhancement is higher for the particles with copper. This is in sharp contrast to sputtered FePtCu films, in which the coercivity enhancement occurs at much lower temperatures relative to sputtered FePt films [4,5].

For the case of FePt nanoparticles containing Ag, the Ag phase separated from the particles, leaving behind lattice vacancies that allowed the Fe and Pt atoms to move to their $L1_0$ lattice positions at lower temperatures [8]. Here the Cu remains in the FePt lattice to make a FeCuPt alloy, which transformed at higher temperatures to the $L1_0$ phase. Our results are quite different from the results for sputtered FePt films containing Cu, even though we prepared particles with compositions (11 to 15% Cu) that gave a strong reduction in the ordering temperature for the sputtered films [4,5]. Furthermore, two of the compositions had a nearly 1:1 ratio of Fe to Pt. It is not clear why the results for chemically synthesis FePtCu differ from those for sputtered films. One of factors may be grain growth, which is quite large in the sputtered films but is more limited in the chemically synthesized particles.

CONCLUSIONS

New FePtCu nanoparticles with varying composition have successfully been synthesized by a high temperature chemical solution approach. As prepared FePtCu particles spontaneously self-assembled into particles arrays with two- or three-dimensional close-packing when particles were spread onto solid substrates (such as, carbon-coated Cu TEM grids). However, Cu is not effective in reducing the ordering temperature in these chemically synthesized FePtCu nanoparticles, which is quite different with sputtered FePtCu films. Magnetic hysteresis loops can be decomposed into hard and soft component

for annealed FePtCu granular film after 700°C. XRD patterns showed extra crystalline phases after annealing at high temperatures, besides the $L1_0$ phases, which were related to soft magnetic components. Further work to identify the extra phases (e.g., $L1_0$ $CuFePt_2$ or cubic $FePt_3$) is underway.

ACKNOWLEDGEMENTS

This work has been supported by the NSF Materials Research Science and Engineering Center award number DMR-9809423.

REFERENCES

1. S. Sun, C. B. Murray, D. Weller, L. Folks and A. Moser, *Science* **287**, 1989 (2000).
2. D. Weller, A. Moser, L. Folks, M. E. Best, W. Le, M. F. Toney, M. Schweickert, J. L.Thiele and M. F. Doerner, *IEEE Trans. Magnetics* **36(1)**, 10 (2000).
3. Z. R. Dai, S. Sun and Z. L.Wang, *Nano Letters* **1(8)**, 443 (2001).
4. T. Maeda, T. Kai, A. Kikitsu, T, Nagase and J. Akiyama, *Appl. Phys. Lett.* **80(12)**, 2147 (2002).
5. Y. K. Takahashi, M. Ohnuma and K. Hono, *J. Magn. Magn. Mater.* **246**, 259 (2002).
6. L. J. Cabri, D. R. Owens and J. H. G. LaFlamme, *Canadian Mineralogist* **12**, 21 (1973).
7. M. Shahmiri, S. Murphy and D. J.Vaughan, *Mineralogical Mag.* **49**, 547 (1985).
8. S. Kang, J. W. Harrell and D. E. Nikles, *Nano Letters*, **2**, 1033 (2002).

Mat. Res. Soc. Symp. Proc. Vol. 739 © 2003 Materials Research Society

Phase Transitions in Octanethiol-Capped Ag, Au and CdS Nanocluster Assemblies

A.V. Ellis[§], K. Vijayamohanan[§†], C. Ryu[‡], and G. Ramanath[§*]
[§]Materials Science and Engineering Department, and [‡]Chemistry Department, Rensselaer Polytechnic Institute, Troy, NY 12180, USA. [†]National Chemical Laboratories, Pune, India

ABSTRACT

We describe phase transitions in assemblies of octanethiol (OT)-capped nanoclusters of Ag and Au and CdS of sizes ranging from 2 to 5 nm, created by a new variant of the Brust synthesis method, without the use of phase transfer agents. We probed the stability of these assemblies by a combination of UV-Visible spectrometry, differential scanning calorimetry (DSC), thermogravimetric analysis (TGA) and *in situ* polarized microscopy (PLM). Our results show that Ag nanoclusters form a crystalline assembly at ambient temperatures. Upon heating, these assemblies undergo two reversible phase transitions corresponding to melting of (i) a phase comprised of excess thiols that are not linked to the nanoclusters, and (ii) the nanocluster assembly, at ~60 and 124 °C, respectively. In contrast, Au nanocluster assemblies are softer, waxy solids, and show sub-zero melting transitions. Both these assemblies show no observable mass loss up to ~180 °C. CdS nanocluster assemblies are also waxy solids, but show a non-reversible melting transition at 137 °C, with simultaneous mass loss due to OT desorption. From our results the thermal stability of the nanoclusters was OT-Ag > OT-Au > OT-CdS.

INTRODUCTION

Creating ordered assemblies of protected organic-inorganic hybrid assemblies, with selective sizes, is of great technological interest, and is critical in reaping the benefits of these properties in potential applications such as microelectronics, sensors, catalysis, nonlinear optics and single electron devices [1-3]. For example, assembly of superstructures of semiconductor nanoclusters (quantum dots) comprising of arrays of alternating small and large sized clusters adjacent to each other could give rise to resonant tunneling effects that could be harnessed to make nanodevices for optical applications [4]. From a fundamental viewpoint, it is of interest to understand the thermal and chemical stability of different nanocluster assemblies.

Nanoclusters that are isolated from each other, e.g., by capping agents, tend to coalesce slower than their uncapped counterparts, and are hence more stable. Typically these types of "protected" nanoclusters can be prepared by different methods, including hydrolysis and reduction of precursors, thermal decomposition, photolysis and nanosphere lithography [5, 6]. Commonly studied monolayer-protected nanoclusters involve the attachment of a thiol to the nanocluster surface, be it single metals [7], alloys [8] or semiconductors [1]. Of particular importance is maximizing the self-assembly of the thiol protecting layer to produce strong binding asymmetry and a high degree of conformal packing. This effectively exploits chain-length dependent lateral van der Waals forces, thus preventing many of the oxidative processes that can occur at the metal/semiconductor core surface [9,10]. In addition, this minimizes nanocluster coalescence.

In this work we use a modified Brust method to maximize thiolate bond formation and minimize nanocluster size, by using a high capping agent to metal ion ratio to produce octanethiol (OT)-capped Ag, Au and CdS nanoclusters assemblies. Our annealing experiments

show that the phase transitions in the nanocluster assemblies are closely related to the strength of the bond between the thiols and the nanocluster surface. In particular, melting-type reversible transitions are observed in Ag and Au nanocluster assemblies due to the increased mobility of the capping molecules during heating. This behavior is not observed in CdS nanocluster assemblies due to rapid desorption of thiols from the CdS nanocluster.

EXPERIMENTAL DETAILS

We used an adaptation of the Brust method [11] to prepare Au, Ag, and CdS nanoclusters capped with octanethiol (OT), by reducing metal salts from a two-phase liquid mixture. In order to produce smaller particle sizes and maximize thiolate bond formation we use high thiol to metal ion ratios and obviate the use of a phase transfer agent.

We prepared Au and Ag nanoclusters from a biphasic mixture of 1 mM aqueous solutions of $AuCl_3$ or $AgNO_3$ and an equal volume of 46 mM OT in toluene. The mixture was stirred vigorously at 600 rpm, for 30 minutes and the metal ions were reduced by slow addition of 7.4 mM aqueous $NaBH_4$ to form OT-capped nanoclusters, which then migrate to the toluene layer. CdS quantum dots where prepared in a similar manner by the reduction of 1 mM $CdCl_2$ using 7.4 mM aqueous Na_2S. The toluene layer, containing the newly formed OT-capped nanoclusters, was separated from the bottom aqueous layer using a separating funnel, washed 5 times with deionized water, and dried in flowing N_2. This is unlike the typical method used to separate nanoclusters from toluene by methanol addition-induced precipitation. Assemblies of the capped Ag nanoclusters were solids at room temperature, while those of CdS and Au were waxy solids.

A Varian Cary 500 Scan UV-VIS-NIR spectrophotometer was used to obtain UV-Visible absorption spectra from diluted suspensions of the nanoclusters in toluene placed in a quartz cell with a path length 1 cm. The nanocluster size was calculated from the spectral characteristics and verified using transmission electron microcopy (TEM).

Differential scanning calorimetry (DSC) measurements were carried out in an indium-calibrated Mettler Toledo DSC822® instrument to investigate phase changes in the OT-capped nanoclusters. Thermograms were collected from 3-7 mg samples of Ag, Au and CdS nanocluster assemblies, sealed in aluminum pans under a 40 mL/min N_2 flow. Each sample was repeatedly heated from 0 °C to 150 °C at 10 °C/min, and cooled to -30 °C at different rates between 5 and 30 °C/min. We also carried out thermogravimetric analyses (TGA) in a Mettler Toledo TGA/SDTA851® instrument on 5-10 mg samples of the Ag, Au and CdS nanocluster assemblies to track decomposition and desorption processes. Each sample was heated under a 20 mL/min N_2 atmosphere from 25-800 °C at 10 °C/min.

In situ polarized light microscopy (PLM) was used to visually capture phase changes and correlate them with DSC peaks measured from Ag nanocluster assemblies. The PLM measurements were carried out in a Linkam TMS (93) heating stage interfaced with a Nikon Eclipse E600 Microscope. The samples were heated at 1 °C/min to 150 °C, and cooled to room temperature at the same rate.

RESULTS AND DISCUSSION

Figure 1a shows representative UV-Vis spectra obtained from OT-capped Ag, Au and CdS nanocluster assemblies, respectively. Ag nanoclusters have a unimodal size distribution, with an average cluster size of 2-4 nm. In contrast, Au nanoclusters show a bimodal distribution

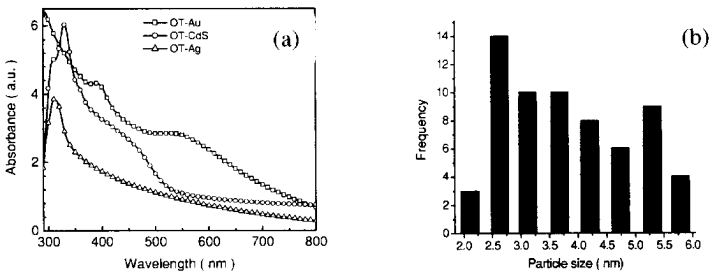

Figure 1. (a) UV-Visible spectra from OT-capped nanocluster assemblies of —Δ— Ag; —□— Au; and —o— CdS. (b) Particle size distribution obtained from transmission electron microscopy (TEM) measurements.

indicated by two surface plasmon peaks at 390 and 523 nm, associated with cluster sizes < 5 nm [12] and > 5 nm [13], respectively. This is confirmed by particle size distributions (see Figure 1b) obtained from analysis of TEM images. CdS cluster assemblies show a broad bandgap between 400-500 nm, characteristic of ~4 nm nanoparticles [14]. Ag and CdS particle size distributions were confirmed by TEM images, not shown here [15,16].

Silver

Figure 2a shows the DSC thermograms for the Ag nanocluster assemblies. Two reversible peaks are seen at ~60 °C (see inset) and ~124 °C. The enthalpy changes for the phase transitions, extracted from the endothermic peak areas at the two temperatures are ~19 J/g, and 102 J/g, respectively. Enthalpy values obtained from exothermic peaks yield similar values, indicating the negligible effect of impurities and defects.

TGA measurements (Figure 2b) showed no observable mass-loss in the temperature range where the phase transitions are observed. However, heating above 200 °C resulted in rapid mass loss from the assemblies due to desorption of thiols from the nanocluster assembly. No phase transitions were observed during subsequent cooling/reheating of assemblies heated above 200 °C, indicating that the observed phase transitions are related to the presence of OT molecules.

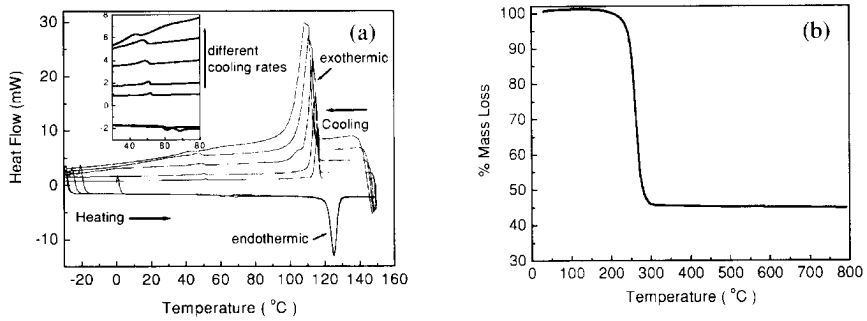

Figure 2. (a) DSC thermograms corresponding to different cooling rates between 5 and 30 °C/min and (b) TGA mass-loss profile of Ag nanocluster assemblies.

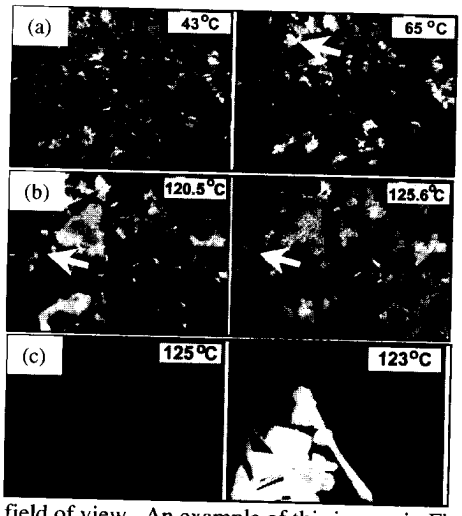

Figure 3. Optical polarized light micrographs obtained from silver capped nanoclusters during heating from (a) 43-65 °C and (b) 120-126 °C; and (c) cooling from 125-123 °C.

The phase transition temperatures indicated by DSC are consistent with major changes in visual contrast observed during *in situ* PLM measurements. In this technique, changes in the contrast features reveal crystalline-amorphous transitions. Representative PLM micrographs captured from Ag nanocluster assemblies during heating and cooling are shown in Figures 3a-c. Upon heating to ~60-65 °C regions of white contrast (e.g., see arrow in Figure 3b) appear at isolated locations. At ~120 °C, the crystalline contrast arising from the nanocluster assembly begins to unravel at a larger scale throughout the field of view. An example of this is seen in Figure 3b (see right micrograph), where regions of orange contrast take on a white hue (see arrows), similar to that observed at 60 °C. Upon further heating, or holding at ~125 °C, the entire assembly becomes devoid of contrast similar to the left micrograph in Figure 3c. Cooling results in the emergence of faceted crystalline regions (see right micrograph in Figure 3c) from the melt. Based on the DSC, TGA and PLM measurements, we propose that the second phase transition at ~120 °C corresponds to the melting/recrystallization of the nanocluster assembly due to the changes in the mobility of the OT molecules capping the nanoclusters. Initially, the assembly is held together by interdigitating OT molecules attached to the nanoclusters. Heating increases the flexibility of the molecules, resulting in the melting of the nanocluster assembly. Upon subsequent cooling, the OT molecules capping the nanoclusters become rigid, and rebind the adjacent nanoclusters into a solid phase. We attribute the first transition at ~60 °C to melting of assemblies of excess OT molecules—i.e., those not bound to the nanocluster surfaces, as reported previously [7]. This view is supported by the fact it takes a lower temperature and enthalpy to flex the excess OT-molecules that are not bound to the nanocluster surfaces, but are entrapped between OT-capped nanoclusters.

Gold

Unlike Ag nanocluster assemblies, Au nanocluster assemblies show two reversible peaks at much lower temperatures, namely at ~-8 °C and ~-4 °C (see Figure 4a). Both peaks, however, correspond to the same transition, and arise due to bimodal cluster size distribution, as described earlier. Upon thermal cycling the enthalpy of assembly melting for the ~-8 °C peak decreases from 32.05 to 12.85 J/g, and that of the higher temperature peak, ~-4 °C, increases from 55.73 to 76.37 J/g. This result suggests that upon repeated annealing smaller clusters coalesce into larger ones. Larger clusters have a smaller surface/volume ratio, and allow for a greater degree of packing of the alkyl chains, and result in a higher melting temperature [17], as seen here.

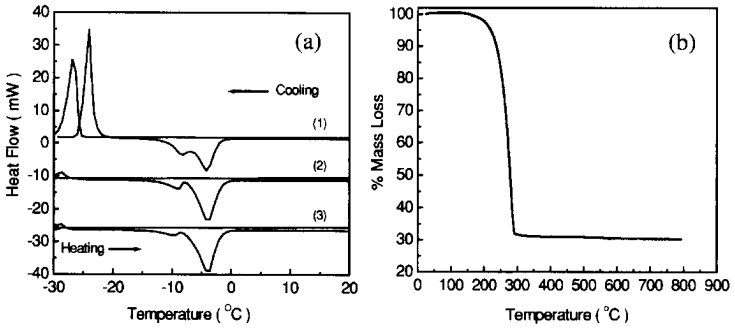

Figure 4. (a) DSC thermograms of OT-Au nanoclusters; 10 °C/min heating and three different cooling rates between 5 and 30 °C/min. (b) TGA mass-loss profile of from OT-Au nanocluster assemblies.

We note that OT molecules desorb from Au nanocluster assemblies at 180 °C (see Figure 4b), a slightly lower temperature than OT-capped Ag nanoclusters, indicating that the Au-OT interactions are weaker than that between Ag-OT.

Cadmium sulfide

CdS nanocluster assemblies show lower thermal stability than that of Au or Ag nanoclusters, and exhibit an irreversible endothermic transition at ~137 °C after the first cycle (see Figure 5a main curve). As in the case of Ag and Au nanoclusters, this endotherm is due to the melting of the CdS nanocluster assembly. However, unlike the Ag and Au assemblies, subsequent heating and cooling do not show this endotherm (see inset). We attribute this to facile OT-desorption at from CdS nanocluster surfaces which results in nanocluster coalescence and destruction of the CdS-OT assembly. This is consistent with TGA profiles showing the commencement of mass loss ~ 140 °C (see Figure 5b), which is ~ 40-60 °C lower than the OT desorption temperatures in Ag and Au nanocluster assemblies, respectively.

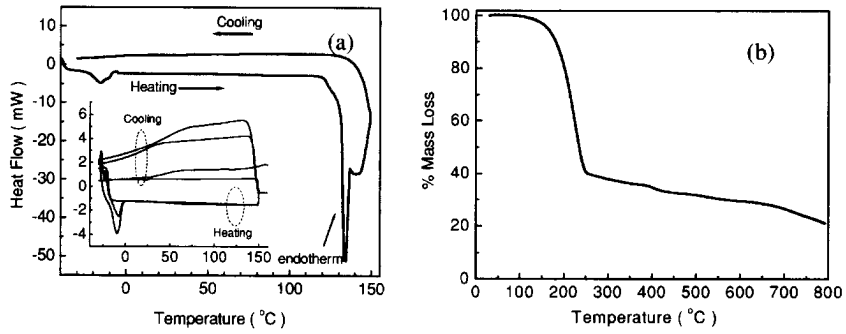

Figure 5. (a) DSC thermograms of OT-CdS nanoclusters. Inset shows thermograms obtained during subsequent runs. (b) TGA profile showing mass loss in OT-CdS nanocluster assemblies.

CONCLUSIONS

OT-capped Ag nanocluster assemblies prepared from solutions with high OT/Ag^+-ion ratios reveal two melting-type reversible transitions at ~60 and 125 °C. The first corresponds to melting of excess OT molecules unattached to nanoclusters. The second transition corresponds to the melting of the nanocluster assembly, caused by increased chain flexibility and resultant decrease in attractive interactions between OT molecules capping the nanoclusters. Au nanocluster assemblies also show a reversible melting transition similar to the latter, but at much lower temperatures. In contrast, CdS nanocluster assemblies show no reversible transitions. The primary reason for this is that the thiolate bonds on Au and CdS surfaces are weaker than that on Ag. Neither Au nor CdS nanocluster assemblies show transitions corresponding to melting of excess thiol, because they are not entrapped by the nanoclusters in the assembly. The thermal stability order is OT-Ag > OT-Au > OT-CdS.

ACKNOWLEDGEMENTS

This work was supported by Philip Morris USA, seed-funding at NSF- Nanoscale Science and Engineering Center at RPI, and NSF CAREER Award supplement DMR 994478.

REFERENCES

1. J. Aldana, A. Wang and X. Peng, *J. Am. Chem. Soc.* **123**, 8844 (2001).
2. S. –H. Kim, G. Medeiros-Ribeiro, D. A. A. Ohlberg, R. Stanley Williams and J. R. Heath, *J. Phys. Chem. B.* **103**, 10341, (1999).
3. D. J. Schriffrin, *MRS Bulletin*, Dec, 1015, (2001).
4. O. Kulakovich, N. Strekal, A. Yaroshevich, S. Maskevich, S. Gaponenko, I. Nabiev, U. Woggon and M. Artemyev, *Nano Lett.* **2**, 1449 (2002).
5. T. Lee, J. Liu, N-P. Chen, R. P. Andres, D. B. Janes and R, Reifenberger, *J. Nanoparticle Res.* **2**, 345, (2000).
6. T. R. Jensen, G. C. Schatz and R. P. van Duyne, *J. Phys. Chem B.* **103**, 2394, (1999).
7. N. Sandhyarani, M. P. Antony, G. P. Selvam and T. Pradeep, *J. Chem. Phys.* 113, **9794** (2000).
8. N. Sandhyarani and T. Pradeep, *Chem. Mater.* **12**, 1755 (2000).
9. P. E. Laininis and G. M. Whitesides, *J. Am. Chem. Soc.* **114**, 9022 (1992).
10. Z. Mekhalif, J. Riga, J. –J. Pireaux and J. Delhalle, *Langmuir* **13**, 2285 (1997).
11. M. Brust, M. Walker, D. Bethell, D. J. Schriffrin and R. Whyman, *J. Chem. Soc., Chem. Commun.* **801** (1994).
12. J. Strähle in *Homonuclear and Heteronuclear Cluster Compounds of Gold in: Metal Clusters in Chemistry*, edited by Herausgeber: P. Braunstein, L. A. Oro and P. R. Raithby, (Wiley-VCH, Germany, 1999) pp. 535-560.
13. A. C. Templeton, W. P. Wuelfing and R. W. Murray, *Acc. Chem. Res.* **33**, 27 (2000).
14. A. P. Alivisatos, *Science* **271**, 933 (1996).
15. X. Wang, *Synthesis and Characterization of Cadmium Sulfide Nanoclusters*, (Master's Thesis, Rensselaer Polytechnic Institute, Troy, NY, USA 2002).
16. A.V. Ellis, K. Vijayamohanan, C. Ryu, R. Goswami and G. Ramanath (2002) (Unpublished).
17. R. W. Meulenberg and G. F. Strouse, *J. Phys. Chem. B* **105**, 7438 (2001).

Mat. Res. Soc. Symp. Proc. Vol. 739 © 2003 Materials Research Society

Finite Element Analysis of Nanoscale Thermal Measurements of Superlattices

Jason R. Foley and C. Thomas Avedisian
Thermal Sciences Laboratory
Sibley School of Mechanical and Aerospace Engineering
Cornell University
Ithaca, New York, 14853

ABSTRACT

A finite element analysis applicable to two- and three-dimensional heat flow in samples of arbitrary geometry and composition is presented for use in a thermal wave experiment. The finite element formulation is summarized, including the use of symmetry to simplify the problem, and the governing differential equations for the heat transport are found to be in the form of the Helmholtz equation for the specific case of a modulated heat source. Simulated data for a Nb/Si superlattice is calculated using the finite element code and is shown to agree with predictions from an analytical model, validating the approach taken.

INTRODUCTION

Finite element analysis (FEA) is a powerful tool for approximating solutions to problems for which an analytic solution is either intractable or nonexistent. These problems can include calculating fields from non-uniform sources, fluid flow over an irregularly shaped surface, or the propagation of waves in an inhomogeneous medium. One such field equation is the Helmholtz equation, which has the general form

$$\frac{\partial}{\partial x}\left(k_x \frac{\partial \phi}{\partial x}\right)+\frac{\partial}{\partial y}\left(k_y \frac{\partial \phi}{\partial y}\right)+\frac{\partial}{\partial z}\left(k_z \frac{\partial \phi}{\partial z}\right)+\lambda\phi+f(x,y,z)=0\,, \tag{1}$$

where λ is a constant, ϕ is the field that is to be calculated and f represents a source (or body force) term. The Helmholtz equation describes many physical systems, including waves in shallow water, electromagnetic waves in a waveguide, or acoustic vibrations [1].

One specific application where the Helmholtz equation arises naturally is in thermal diffusion wave thermometry [2], for which the theoretical basis can be traced to the pioneering work of Anders J. Ångström [3]. Thermal diffusion waves, which are generated through harmonic heating, have several interesting characteristics (e.g., an infinite propagation speed). However, the most useful property is the characteristic thermal penetration depth l_T [4], which defines the physical distance over which the thermal oscillations are significant:

$$l_T=\sqrt{\frac{2k}{\omega C}}\,, \tag{2}$$

where k is the thermal conductivity, C is the volumetric heat capacity, and ω is the angular frequency of the modulated heat source. This feature allows the thermal field to be "tuned" to a desired size simply by changing the modulation frequency of the heat source and experimentally

results in a variable probe that is sensitive to spatial variations in the material properties (which must be determined through inverse techniques).

Implementing FEA allows much greater freedom in selection of test geometry, etc., and represents an enabling tool that allows non-standard geometries to be thermally characterized. For example, specific properties (e.g., components of anisotropic thermal conductivity) can be measured by nanofabricating structures so that the heat flow has the desired characteristics, such as lower dimensionality.

In this paper, we briefly outline the theoretical basis for the finite element method with the long-term goal of implementing FEA for nanoscale thermal experiments. The concept for the experimental thermometry technique is briefly reviewed and simulations of experimental data are shown for a Nb/Si superlattice on a glass substrate. The simulated results are then compared with analytic expressions for the same system.

THEORY

Thermal Wave Thermometry

All modulated thermal wave techniques share some characteristic features, including the generation of heat from a modulated source (typically optical or electrical) and measuring the resulting change in a physical parameter due to the temperature fluctuations. One such technique is photothermal deflection spectroscopy (PDS) [5, 6], which is schematically illustrated in Fig. 1. Photothermal deflection spectroscopy, also called the "mirage technique", uses a modulated "pump" laser beam to generate thermal waves in a sample via optical absorption. This creates a thermal field in the sample itself, which creates a thermal field in the adjacent gas (air) layer by conduction. The thermal fluctuations in the air lead to small but measurable changes in the index of refraction. Any light passing through the region is bent by the so-called "mirage effect." Another laser beam, the "probe" beam, is passed through the heated region and the subsequent deflections are measured by a quadrant photodetector. The deflection signal is analyzed to reconstruct the thermal field and, using inverse techniques, the material properties can be estimated. A detailed description and theoretical treatment of the technique can be found in Ref. 7.

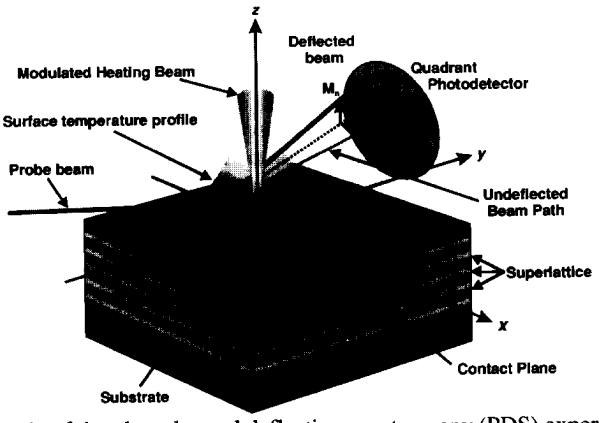

Figure 1. Schematic of the photothermal deflection spectroscopy (PDS) experimental concept.

The heat conduction equation is used to model the temperature distribution in the system:

$$\nabla \cdot (k \nabla \theta) + q'''(x, y, z, t) = C \frac{\partial \theta}{\partial t}, \tag{3}$$

where $\theta \equiv T - T_\infty$ represents the temperature fluctuations above the steady state temperature. Since the heat source in Eq. 3 is harmonic in time, it can be recast in the form of a Helmholtz equation (see Eq. 1) by using the complex combination technique [8] with $\phi = \theta$, $\lambda = -i\omega C$ and $f = -q'''$.

Finite Element Model

With the governing differential equation in the form of a Helmholtz equation, a variational statement can be immediately written, which is, in two dimensions:

$$I(\theta) = \frac{1}{2} \int_\Omega \left[k_{xx} \left(\frac{\partial \theta}{\partial x} \right)^2 + k_{yy} \left(\frac{\partial \theta}{\partial y} \right)^2 - \lambda \theta^2 - 2 q''' \theta \right] d\Omega + \int_\Gamma W \, d\Gamma \tag{4}$$

where Ω represents the domain of the problem, Γ is the boundary of the domain, and W is the boundary work term (found from applying boundary conditions). The domain is meshed using T3 elements—triangular elements with linear interpolation of the functional values between nodes (locations where the function is evaluated). The solution (all nodal values) is then calculated from the matrices found by discretizing and minimizing Eq. 4 for each element. For a detailed review of the finite element technique, refer to any introductory text on the finite element method (for example, Ref. 1).

Setting appropriate boundary conditions is key to accurately modeling the thermal field, especially if the sample is thermally thin (dimensions smaller than the penetration depth) or is thermally isolated from the environment. Additionally, other interfacial effects can be of interest. One such case is the presence of a thermal boundary resistance at the interface between different media. Defined in terms of the local temperature difference ΔT across the interface and the incident heat flux q'', the thermal boundary resistance R_{bdy} is

$$R_{bdy} = \frac{\Delta T}{q''}. \tag{5}$$

This boundary condition effectively couples the two domains, leading to a larger global problem. Additionally, the boundary resistance can play a significant—or even dominant—role in the overall heat transport in systems with many interfaces, e.g., superlattices. While the theoretical treatment necessary to demonstrate the resulting domain coupling in the global model is beyond the scope of this review, it is nonetheless an important feature of modeling nanoscale structures.

Symmetry can be used to greatly simplify problems solved by FEA. Using PDS, there is cylindrical (radial) symmetry due to the Gaussian laser heat source. The symmetry allows the size of the problem to be reduced, as shown in Fig. 2, by introduction of an "insulated" boundary; this is done due to the symmetry, since the gradient across the boundary is zero (identical to that of an insulated boundary).

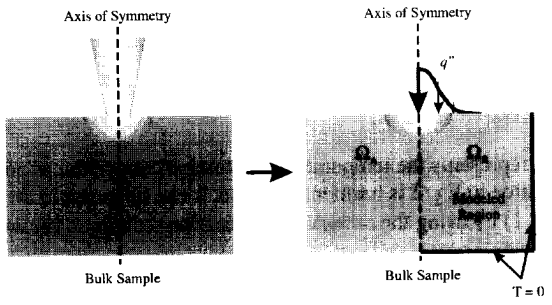

Figure 2. Boundary conditions of the solution domains Ω_i.

RESULTS AND DISCUSSION

The temperature fields were calculated using linearly interpolated triangular (T3) elements. The solution domains were meshed using the CASCA program (a preprocessor for the FRANC2D fracture mechanics code [9]) that output the mesh to a file; approximately 2500 nodes and 6000 elements were used in the calculation. All simulations were run using Matlab code written by the first author and run on Windows-based workstations (with Athlon processors and 512 MB of memory).

The heat source was modeled as an incident flux distribution equivalent to that of laser focused to a 10 μm beam waist with 10 mW of absorbed power. The modulation frequency was set at 20 kHz, a value typical for PDS experiments. The material properties and geometry were chosen to simulate a 500 nm Si/Nb superlattice on a bulk SiO_2 substrate. The heat capacity and density of the superlattice was modeled using the average values of bulk Si and Nb, while the effective thermal conductivity was taken to be 10 W/m·K to account for the reduction of thermal conductivity due to microscale effects.

Qualitatively, the FEA simulations exhibited all of the expected characteristics of thermal waves. For example, the change in the thermal penetration depth is evident in the cross-section temperature distributions shown in Fig. 3(a.) and (b.). The FEA simulations also agreed very well with analytic results (obtained using the model in Ref. 7). Figure 4 shows the surface temperature distribution agrees within 7% while the tangential probe beam deflections calculated in Fig. 5 show similar agreement. Improved accuracy in the FEA can be obtained by several means, including modeling the system with more elements, a process called *h*-convergence (refining the mesh), or using higher-order interpolation (such as quadratic elements in *p*-convergence).

The preliminary results obtained here are encouraging. However, much work remains to make FEA a useful tool for measuring the thermal properties of nanoscale systems with irregular geometries. In order to estimate the material properties, the FEA results must be integrated with an inverse problem algorithm, e.g., a least squares estimator, in order to match the experimental data to the model output. Once accomplished, however, the completed finite element analysis technique will provide greater flexibility in experimental configurations and in the systems investigated.

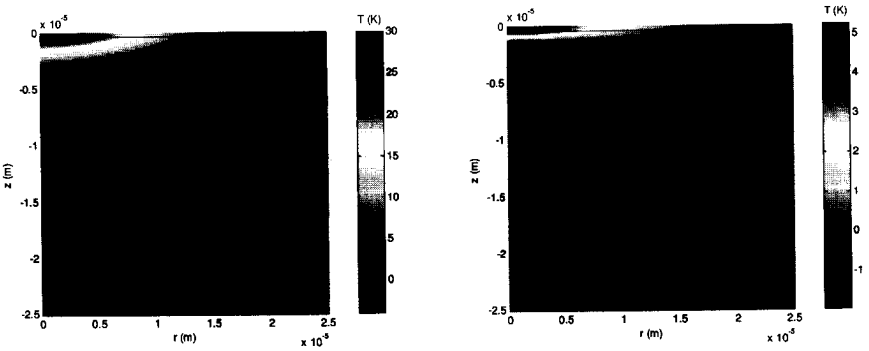

Figure 3. FEA prediction for the cross-section temperature at $t = 0$ in a 500 nm Nb/Si superlattice (a.) $f = 20$ kHz and (b.) $f = 200$ kHz. Both cases were heated with a 10 μm laser; the reduced magnitude of the temperature oscillations and smaller thermal penetration depth in the z direction is evident at the higher f.

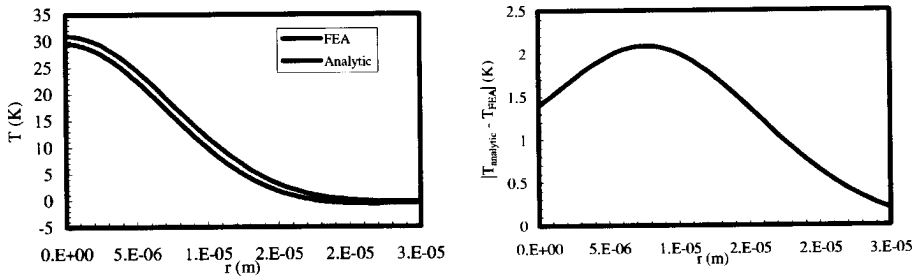

Figure 4. Surface temperature distribution and error for the Nb/Si system heated at $f = 20$ kHz. The peak error is ~7% of the maximum temperature.

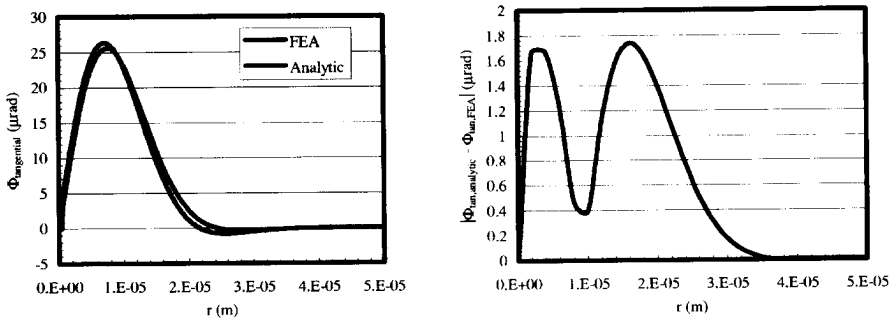

Figure 5. Simulated tangential beam deflection data and error between the FEA and analytical models.

CONCLUSIONS

This exploratory research focused on developing a finite element analysis applicable to two- and three-dimensional heat flow in thermal wave experiments on samples of arbitrary geometry and composition. Simulated data for a Nb/Si superlattice system was obtained both from an analytic model and the finite element analysis described. The results showed good agreement, with a maximum error of ~7% for the mesh size used. This promising result indicates that a fully-integrated FEA analysis scheme will enable thermal characterization of nanoscale systems with geometries that are difficult to model.

ACKNOWLEDGMENT

This work made use of the Cornell Center for Materials Research (CCMR), supported by the NSF under Award No. DMR-0079992, and the Cornell node of the National Nanofabrication Users Network (NNUN). The authors would like to thank Prof. Subrata Mukherjee of Theoretical and Applied Mechanics, Prof. Tony Ingraffea of Civil and Environmental Engineering, and Prof. Nicholas Zabaras of Mechanical and Aerospace Engineering for helpful advice on the finite element method, and Dr. William Schaff of the Cornell's Department of Electrical and Computer Engineering (ECE) for useful discussions on superlattices.

REFERENCES

1. K. H. Huebner, D. L. Dewhirst, D. E. Smith, and T. G. Byrom, *The Finite Element Method for Engineers*, 4th ed., Wiley, New York, pp. 40-56, 288-303, 654-655 (2001).
2. A. Mandelis, *Phys. Today* **20**, 29-34 (2000).
3. A. J. Ångström, *Annln. Phys. Lpz.* **114**, 513-520 (1861).
4. D. G. Cahill, *Rev. Sci. Instrum.* **61**, 802-808 (1990).
5. W. Jackson, N. M. Amer, A. C. Boccara, and D. Fournier, *Appl. Opt.* **20**, 1333-1344 (1981).
6. J. C. Murphy and L. C. Aamodt, *J. Appl. Phys.* **51**, 4580-4588 (1980).
7. J. R. Foley and C. T. Avedisian, *Proc. of the 2002 IMECE*, ASME, IMECE2002-32443 1-9 (2002).
8. V. S. Arpaci, *Conduction Heat Transfer*, Addison-Wesley, Reading, 167-178 (1966).
9. CASCA and FRANC2D are available from the Cornell Fracture Group (downloadable from www.cfg.cornell.edu), courtesy of Prof. Tony Ingraffea.

Mat. Res. Soc. Symp. Proc. Vol. 739 © 2003 Materials Research Society

Evolution of Carbon Self-Assembly in Colloidal Phase Diagram

V. Bouda
Department of Mechanics and Materials, Faculty of Electrical Engineering, Czech Technical University in Prague,
Technická 2, 166 27 Praha 6, Czech Republic

ABSTRACT

The growth of the self-assembled structure of carbon colloidal particles has been studied [1]. The system of carbon particles was processed in electrical field in polymer melt with controlled ionic concentration. The interpretation of the complex evolution of the self-assembled structure of carbon particles was given in terms of phase transitions of colloidal systems of carbon particles.

Interactions between doublets of carbon black (CB) particles are interpreted in terms of DLVO approximation of interaction energy as multiples of average thermal fluctuation kT. Plots of the sum of energy of electrostatic repulsion and energy of van der Waals attraction versus separation between the doublets show the energy barriers to coagulation of high B and the energy wells with the secondary minima of depth W. The colloidal phase transitions appear at critical conjuncture of the concentration of ions in the medium and surface potential on the colloids. Six transition lines determine five phases of the assembly of carbon colloids in the proposed colloidal phase diagram: lateral vapor + axial vapor (vapor), lateral liquid + axial vapor (columnar liquid crystal), lateral liquid + axial liquid (smectic LC), lateral liquid + axial solid (nematic LC), and lateral solid + axial solid (solid).

The diagram provides a tool to control the evolution of carbon self-assembly. The eventual morphology depends on the route of the steps of the processing. During the time elapsed in the LC state, the structure can reorganize and the eventual coagulation produces various crystals. On the contrary, the route outside the LC state can produce glass.

INTRODUCTION

In a stable, dilute, dispersed system, all particles are in permanent Brownian motion and randomly distributed due to thermal energy. At moment the particles interact, the randomness is disturbed, and structures are built in the dispersion. The onset of structure formation manifests itself often by optical, electrical, or mechanical phenomena as turbidity, change in conductivity or viscosity, etc. Especially the electrical conductivity of structured carbon colloidal dispersion is of great practical relevance. Carbon and carbon-based composite materials may create their own revolution in the development of entirely new applications in electronics and micro- or nano-electromechanical systems. Carbon can form various agglomerates with a fine, solid or reversible structure using colloidal carbon-black (CB) particles, specific processing routes and control systems. The mechanics of such structures growth and metamorphosis is not well understood. The growth and metamorphosis of the self-assembled structure of CB colloidal aggregates in polymer melt has been studied recently both by theoretical modeling and experiments [1, 2].

The two main types of energy between particles in dispersion are the attractive and the repulsive ones (sometimes it is better to use the term force as the first derivative of the energy to the distance $F = dE/dd$). They determine which type of structure is possible. The energies of interest are van der Waals-Hamaker (dispersion) energy (attraction), electrostatic energy (repulsion), steric interaction, dipol-dipol interaction, H-bridging energy, and hydrophobic interaction [3]. The aggregation is usually supposed to be determined by the height of the energy barrier between the particles. Usher [4] was probably the first to mention the formation of linear aggregates, favored at defined electrolyte concentration. Thomas [5] modeled the particle chain in aqueous thoria sols by a cylinder and showed that the height of the barrier at the head was only 50-60% of that at the sides. Sonntag et al [6] studied theoretically the process of multiparticle aggregation. He found that the chains, which were built by head-to head coagulation, became longer during the coagulation process.

The presence of particle chains decreases the critical volume fraction for percolation of electrical conductivity. E.g., Schueler et al showed that CB-filled resins conduct with as little as 0.06 vol% [7]. Schueler and Bouda [8, 9, 10] published independently that by applying the theory of colloids, the electrical behavior of CB-filled polymers could be explained.

In this study, we demonstrate in details, that by applying the Derjaguin-Landau-Verwey-Overbeek (DLVO) theory of colloids, a useful colloidal equilibrium phase diagram can be constructed.

INTERACTION ENERGY AND COLLOIDAL PHASE DIAGRAM

When two particles approach each other, the attraction occurs and a doublet of the particles is created. The same procedure may occur between singlets and doublets, doublets and doublets, and so on. Three possible first steps are shown in Fig. 1. The next steps are more complex. However, the primary tendency of the particles to form wires or compact aggregates may be estimated with help of interactions between the doublets in the case C. The formation of the structure C1 (axial arrangement of doublets) means the preferential 1D arrangement of the particles (wires). The formation of the structure C3 (lateral arrangement of doublets) means the preferential 3D arrangement of the particles.

The second simplification is neglect of steric interactions, dipol-dipol interactions, H-bridging energy, and hydrophobic interactions. The interaction energy is a sum of energy of electrostatic repulsion and energy of van der Waals attraction in this approximation.

Rectangular blocks in Fig. 2 substitute the doublets of particles in our approximation. Their length L is a double of the diameter of the spherical particles and their side s equals the diameter of the particles. Complex interactions between doublets of carbon-black colloidal particles are interpreted in terms of DLVO approximation of interaction energy for planar surfaces of the blocks as multiples of average thermal fluctuation kT [1, 3a]. The interaction energy is a sum of energy of electrostatic repulsion and energy of van der Waals attraction in this approximation. The axial and lateral interaction energies are (limited in applicability if the distance $d >>$ thickness of *"double layer"* of screening ions κ^{-1}):

$$E_{AXI}/kT = s^2 64 n \kappa^{-1} \gamma_0^2 \exp(-d/\kappa^{-1}) - s^2 A/(12\pi kT)\,[(d^{-2} + (d+2L)^{-2} - 2(d+L)^{-2}] \qquad (1)$$

$$E_{LAT}/kT = sL64n\kappa^{-1}\gamma_0^2\exp(-d/\kappa^{-1}) - sLA/(12\pi kT)\,[(d^{-2} + (d+2s)^{-2} - 2(d+s)^{-2}] \qquad (2)$$

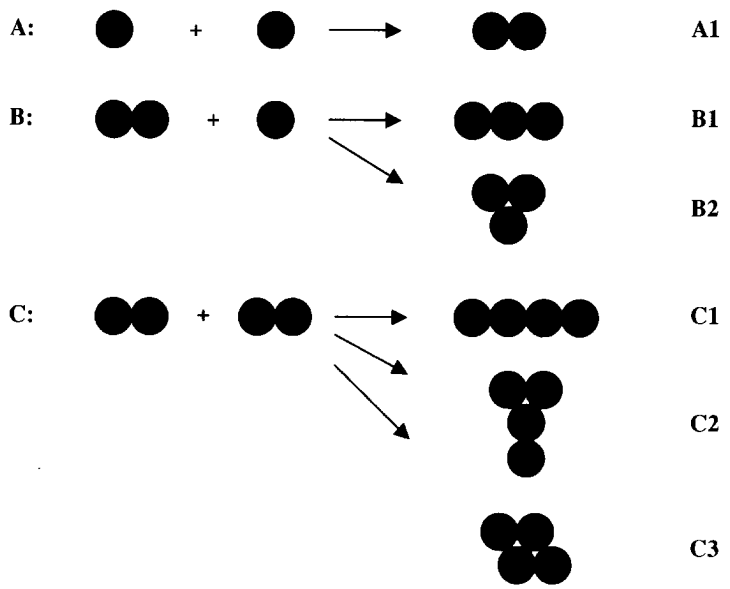

Figure 1. Model for the first steps of coagulation. The procedure leading to axial arrangement of doublets C;C1 represents the general tendency of 1D structure of particles formation. The procedure leading to lateral arrangement of doublets C;C3 represents the general tendency of 3D structure of particles formation.

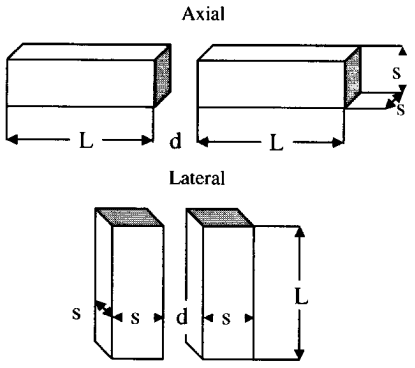

Figure 2. Interaction of two plain blocks

n ... bulk concentration of ions, m^{-3}
κ^{-1} ... "thickness" of the double layer, m,
γ_0 ... parameter of surface potential, (0 ... 1). For surface potential $\Psi_0 > 100$ mV, parameter $\gamma_0 \rightarrow$ [3b].

A...effective Hamaker constant of CB in polyethylene melt was computed 2.86 x 10^{-19} J [1].

The "thickness" of the double layer

$$\kappa^{-1} = (\varepsilon_0 \varepsilon_R kTe^{-2}z^{-2}n^{-1})^{1/2} \qquad (3)$$

ε_0 ... permittivity of vacuum, 8.854 x 10^{-12} Fm^{-1}
ε_R ... relative permittivity of polymer
e ... elementary charge, 1.602 x 10^{-19} C
z ... valence of the ions in polymer

Exemplary plot of E_{AXI}/kT from Equation (1) versus d in Fig.3 (solid line) shows the energy barrier to coagulation of high B and the energy well with the secondary minimum of depth W. The states (Vapour V, Liquid L, Solid S) and the transitions of the assembly are determined by this way:

V:	B > 1, W < 1	V – L transition:	B > 1, W = 1
L:	B > 1, W > 1	V – S transition:	B = 1, W < 1
S:	B < 1, W < 1	L – S transition:	B = 1, W > 1
		Triple point:	W = B = 1

For given colloids (Hamaker constant, the size) and medium (Hamaker constant and temperature), the state depends only on ionic concentration in medium n and parameter of surface potential on colloids γ_0. Relevant equilibrium phase diagram is shown in Fig..4.

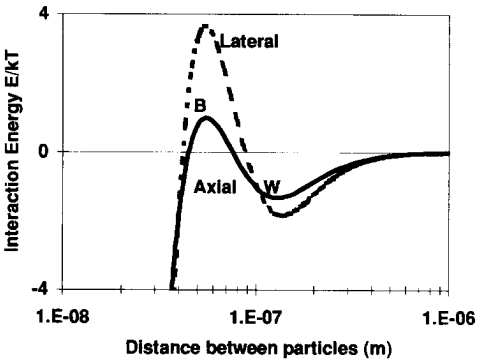

Figure 3. Graphs E_{AXI}/kT (solid line) and E_{LAT}/kT (dashed line) vs. distance between carbon plain blocks 200x200x400 nm in polyethylene at 190°C, n =1.5E21 m^{-3}, z =4, γ_o=1

Because the critical conjuncture of n and γ_0 of transitions in axial interactions differs from the critical conjuncture of n and γ_0 of transitions in lateral interactions (dashed line in Fig. 3), the liquid crystal domain is subdivided in columnar, smectic, and nematic liquid colloidal crystal domains, respectively.

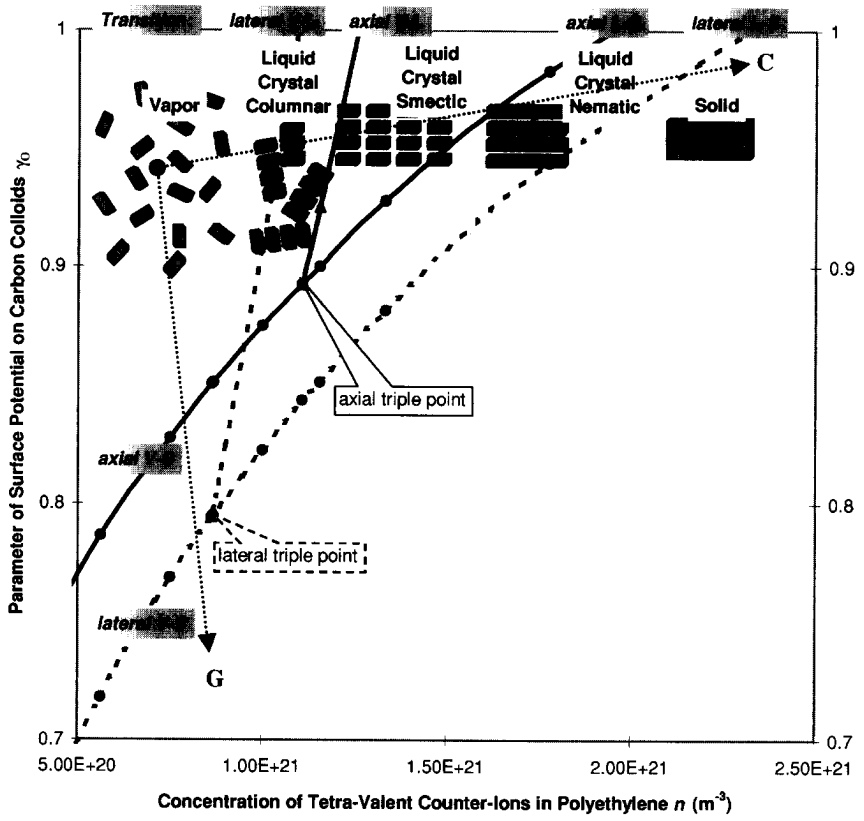

Figure 4. Equilibrium phase diagram of assembly of carbon colloids 200x200x400 nm in polyethylene at 190 °C determines domains of
vapour (both axial and lateral interactions induce dispersion),
columnar LC (axial interaction induces dispersion, lateral interaction induces liquid),
smectic LC (both axial and lateral interactions induce liquid),
nematic LC (axial interaction induces solid, lateral interaction induces liquid), and
solid (both axial and lateral interactions induces coagulation).
Dotted lines represent examples of processing routes to colloidal crystals (C) or glass (G).

CONCLUSIONS

The equilibrium phase diagram presented above, illustrates schematically the conditions for the states of dispersion, coagulation, and liquid carbon black colloids. Of course, the real states can differ from the equilibrium ones substantially. The diagram provides an effective tool to control the evolution of morphology of carbon self-assembly. The eventual morphology depends on the route of the steps of the processing. The exemplary route (C) in Figure 4 crosses the domain of LC state. Colloids are kept apart each other in a certain distance in LC state and are separated by melted polyethylene. During the time elapsed in the LC state, the structure can reorganize and the eventual coagulation produces various crystals. On the contrary, the route G may produce glass. The equilibrium distance between conducting carbon particles or aggregates is determined by two parameters: ionic concentration and electrical potential on the surface of colloids. It ranges from hundreds of nanometers (dispersion, liquid crystal) to zero at contact after coagulation. The relaxation time of the change of structure, which follows the change of one or both the parameters, ranges from fraction of second to many years. A micro- or nano-electromechanical system is one possible application. Another one is the evolution and function of sarcomere in a live muscle cell, which has been interpreted as a phase transition of the lattice of myosin heads [11].

ACKNOWLEDGEMENT

The Research Programme of Czech Technical University in Prague "Diagnostics of Materials" supported this work.

REFERENCES

1. V. Bouda and J. Chladek in *Filled and Nanocomposite Polymer Materials*, edited by A.I. Nakatani, R.P. Hjelm, M. Gerspacher, and R. Krishnamoorti, (Mat. Res. Soc. Symp. (*Mater. Res. Soc. Proc.* **661**, Warrendale, PA, 2001) pp. KK5.17.1 – KK5.17.6
2. V. Bouda, J. Chladek and J. Mikesova, *Proceedings of 6th European Conference on Rheology*, ed. by H. Muenstedt et al, p.97-98, LSP, University Erlangen, 97 (2002)
3. R. Rajagopalan and P. C. Hiemenz, *Principles of Colloid and Surface Chemistry*, 3rd ed., Marcel Dekker, Inc., New York (1997) a) ibid. p. 585, b) ibid. p. 518
4. F. L. Usher, *Proc. Roy. Soc.* (London) **A 125**, 143 (1924)
5. J. L. Thomas and H. H. McCorcle, *J. Colloid Interf. Sci.* **36**, 110 (1971)
6. H. Sonntag, Th. Florek, and V. Silov, *Adv. Colloid Interf. Sci.* **16**, 337 (1982)
7. R. Schueler, J. Petermann, K. Schulte, H. Wentzel, J. Appl. Polym. Sci., **63**, 1741 (1997)
8. V. Bouda, *Manual of Process Engineering and Technology Series* 10/1996, Czech Society of Chemical Engineering, Prague 1-68 (1996)
9. V. Bouda, J. Rajman, *Journal of Electrical Engineering* **48** 51 (1997)
10. V. Bouda, *ASME Int. Mechanical Engineering Congress 1997 Dallas*, TX, Proceedings: CAE and Intelligent Processing of Polymeric Materials, ASME, 281-298 (1997)
11. V. Bouda, L. Boudova, D. Haluzikova, *1st Meeting of Czech and Slovak Structural Biologists*, South Czech University Nove Hrady (2002).

Mat. Res. Soc. Symp. Proc. Vol. 739 © 2003 Materials Research Society H7.41

Molecular-Dynamics Study of the Mechanical Properties of Metallic Nanowires

T. Nakajima and K. Shintani
Dept of ME & Intelligent Sys, Univ of Electro-Comm,
1-5-1 Chofugaoka, Chofu, Tokyo 182-8585, Japan
E-mail: shintani@mce.uec.ac.jp, URL: http://www.shintani.mce.uec.ac.jp/

ABSTRACT

The method of molecular-dynamics is employed to simulate and investigate the deformation of metallic nanowires under tensile strain. The interactions between metallic atoms are calculated by using the embedded-atom method potential. A model nanowire is preliminarily equilibrated at a specified temperature. Then, the uniform uniaxial extension of the nanowire is performed. The thinning process of a metallic nanowire is observed in the sequential snapshots of its morphological change.

INTRODUCTION

In recently years, nanoscale materials such as fullerenes, carbon nanotubes, and metallic and semiconductor nanowires have attracted much attetion of the researchers in nanotechnology. Nanoscale materials are expected to be applied to not only opto-electronic devices but also MEMS/NEMS (micro/nano-electromechanical systems) and nanomanipulators.

Observations of single arrays of metallic atoms in scanning tunneling microscopy studies have provoked prosperity of investigations of nanowires. Nanowires have some unique properties at their nanoscale such as quantized conductance and long bond-length which are not observed for materials at the larger dimensions [1-4]. It can also be guessed that the mechanical behaviors of nanowires under external forces, e.g. their stress-strain relationship and plasticity, are different from the ones of the macroscopic materials.

In this simulation study, the deformation characteristics of gold nanowires under uniaxial tension are investigated by the molecular-dynamics (MD) simulation, paying attention to the effects of the elongation conditions such as defomation speed and temperature on the defomation behaviors of nanowires.

METHOD OF SIMULATION

The simualtion cell is shown in figure 1. Its x,y, and z axes are along the $[1\bar{1}0]$, $[11\bar{2}]$, and $[111]$ directions in the fcc crystal structure. The model nanowire at its initial state is constructed by stacking 24 layers of seven gold atoms in the $[111]$ direction. The length of the initial simulation cell is L_z = 56.53 Å.

The embedded atom method (EAM) potential [5-7] is adopted to calculate the interactions between gold atoms. The 6-value Gear algorithm is empolyed to integrate the equations of motion. The MD time step is 1.28fs. The simulation procedure is as follows. The periodic boundary condition is imposed in the z direction. Firstly, the temperature of the nanowire is controlled by the velocity-scaling method to attain the specified temperature. This equilibration phase needs 20000 MD steps. After equilibration, the MD calculation in the microcanonical

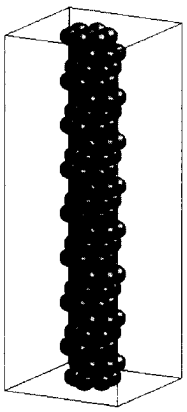

Figure 1. Initial configuration of the simulation cell. The nanowire consists of 168 atoms.

ensemble is carried out. Next, the simulation proceeds to elongation phase. The model nanowire is elonagated in the *z* direction by a unit displacement at each 4000 MD steps. The unit displacements and specified temperatures are shown in table I. Elongation phase is continued untill the nanowire breaks.

RESULTS AND DISCUSSION

The maximum lengths of the simulation cells and the maximum potential energies of the nanowires at the final stages of elogation phase when nanowires break are shown in table II. The transitions of the potential energies of the nanowires are shown figure 2. The potential energies increase during nanowires are being elongated, and steeply descend when they break. The nanowire that is elongated at the speed 0.391m/s and at 500K breaks at the much smaller length than the other nanowires do. Except this model, nanowires break when the heights of the simulation cells are in the range of from 140Å to 150Å, and the maximum of the potential energies is -3.14 eV. The larger the elongation speed is and the lower the temperature is, the longer the nanowires can elongate without breaking. The effect of the former is smaller than that of the latter.

Table I. Parameters for the elongation of nanowires.

Unit displacement (Å)	Elongation speed (m/s)	Temperature(K)
0.10	1.95	4
0.10	1.95	300
0.10	1.95	500
0.02	0.391	4
0.02	0.391	300
0.02	0.391	500

Table II. The maximum lengths of the simulation cells and maximum potential energies of the wires at ther final stages of elongation.

Elongation speed (m/s)	Temperature (K)	Maximum length of the simulation cell (Å)	Maximum potential energy (eV)
1.95	4	149.63	-3.134
1.95	300	146.03	-3.139
1.95	500	139.43	-3.135
0.391	4	150.65	-3.143
0.391	300	148.53	-3.139
0.391	500	93.35	-3.298

Snapshots of the morphlogies of nanowires just before they break are shown in figure 3. Formation of single arrays of gold atoms can be observed. In figure 3(a)-(c), the critical distance at the breaking point becomes longer as the temperature is higher. However, this tendency cannot be observed at the lower elongation speed (in figure 3(d)-(f)). In figure 3(f), constriction at the narrow portion of the nanowire can be observed. This point contact is constructed by the two pyramidal-shaped ends facing each other. Such strcutures were also observed in the results obtained by the tight-binding calculation [8].

Sequential snapshots of the morphologies of the nanowire elongated at the speed 1.95m/s and at 4K are shown figure 4. In the early phase of elongation (figure 4(b)), the nanowire attains a helical hexagonal lattice structure. Such a structure was characteristically observed by ultra high vacuum transmission electron microscopy (UHV-TEM) [9]. As elongation progresses, the threads of gold atoms are spun out to the upper and lower directions from the middle part of the nanowire. This thinning process was not observed in the tight-binding calculation with annealing process[8]; there is no annealing process in our simulation, and the velocity-scaling takes the place of it. This difference of the morphological change of the elongated nanowires suggests that the deformation behaviors of nanowires depend sensitively on the temperature and elongation process.

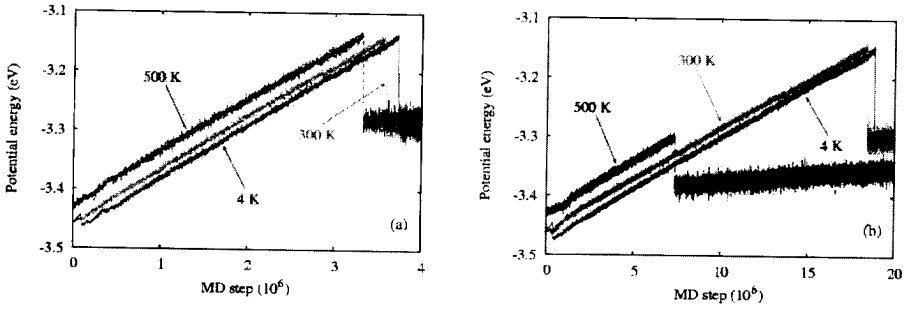

Figure 2. The transitions of the potential energies of the nanowires. The elongation speed is (a) 1.95 m/s, and (b) 0.391 m/s.

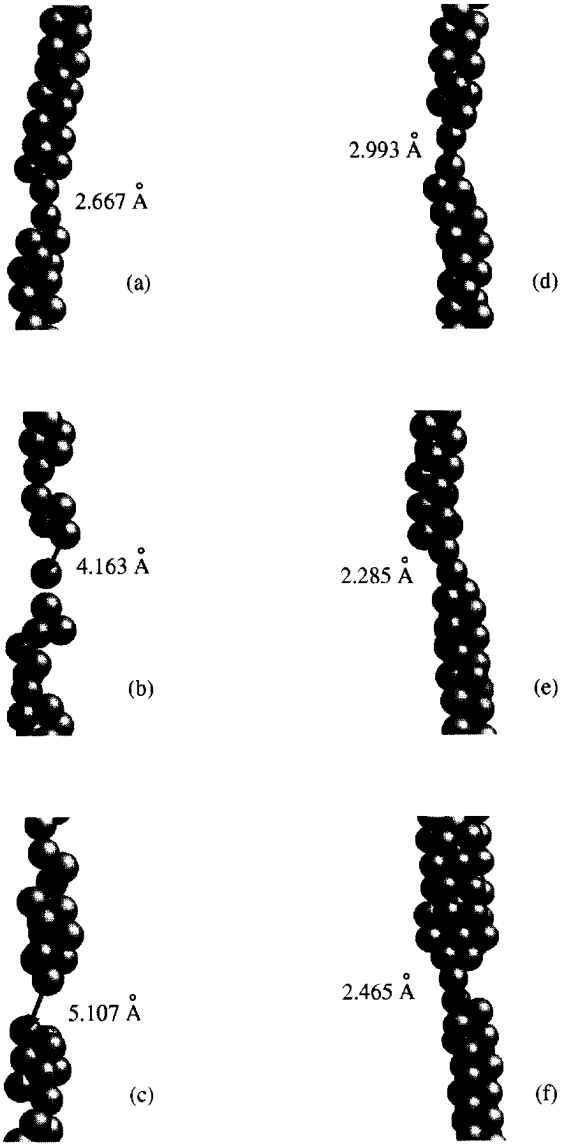

Figure 3. Snapshots of the morphologies of nanowires at the moments they break. The elongation speeds and temperatures are (a)1.95m/s and 4K, (b)1.95m/s and 300K, (c)1.95m/s and 500K, (c)1.95m/s and 500K, (d)0.391m/s and 4K, (e)0.391m/s and 300K, and (f)0.391m/s and 500K, respectively. The distances of the atoms at the points where breakings occur are indicated.

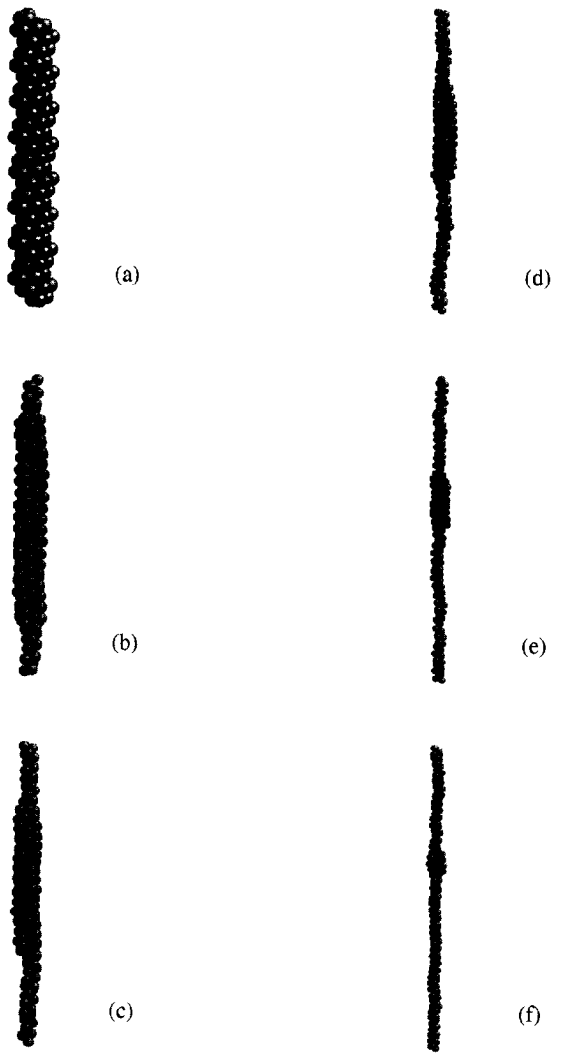

Figure 4. Sequential snapshots of the morphologies of nanowires in their elongation process. The elongation speed and temperature are 1.95 m/s and 4K, respectively. The MD steps counted from the start of elongation and the simulation cell lengths are (a)0MD steps and 56.53 Å, (b)0.6million MD steps (0.768 ns) and 71.53 Å, (c)1.2 million MD steps (1.536 ns)and 86.53 Å, (d)1.8 million MD steps (2.304 ns) and 101.53 Å, (e)2.4 million MD steps (3.072 ns) and 116.53 Å, and (f)3 million MD steps (3.84 ns) and 131.53 Å, respectively.

CONCLUSIONS

The elongation process of gold nanowires was investigated by the molecular-dynamics simulation. At 4K, the maximum length and the maximum potential energy of elongated nanowires just before breaking do not depend on the elongation speed. The helical structure observed in the experiments appears in the early phase of elongation.

REFERENCES

1. A. I. Yanson, G. Rubio, H. E. Brom, N. Agraït, and J. M. Ruitenbeek, Nature **395**, 783 (1998).
2. H. Ohnishi, Y. Kondo, and K, Takayanagi, Nature **395**, 780 (1998).
3. G. Rubio, S. R. Bahn, N. Agraït, K. W. Jacobsen, and S. Vieira, Phys. Rev. Lett. **87**, 26101 (2001).
4. V. Rodrigues, T. Fuhrer, D. Ugarte, Phy. Rev. Lett. **85**, 4124 (2000).
5. M. S. Daw and M. I. Baskes, Phys. Rev. Lett. **50**, 1285 (1983).
6. M. S. Daw and M. I. Baskes, Phys. Rev. B **29**, 6443 (1984).
7. R. A. Johnson, Phys. Rev. B **37**, 3924 (1988).
8. E. Z. Silva, A. J. R. Silva, and A. Fazzio, Phys. Rev. Lett. **87**, 256102 (2001).
9. Y. Kondo and K. Takayanagi, Phys. Rev. Lett **79**, 3455 (1997).

Mat. Res. Soc. Symp. Proc. Vol. 739 © 2003 Materials Research Society

Effective Medium Calculations of the Electromagnetic Behavior of Single Walled Carbon Nanotube Composites

John W. Schultz, Rick L. Moore
Georgia Tech Research Institute
Atlanta, GA 30332-0824, U.S.A.

ABSTRACT

Dielectric properties of single walled carbon nanotube assemblies were calculated with an effective medium approximation at frequencies from 200 MHz to 200 GHz. The model treats the carbon nanotubes as layered cylinders, each with a core, a graphene layer and an outer layer, to investigate the dielectric properties of coated and filled nanotubes. The graphene and metal layer properties were modeled with a Drude approximation based on literature data. A generalized Bruggeman model was then used to determine the macroscopic behavior of the modified carbon nanotubes in a composite structure as a function of volume fraction, frequency, and aspect ratio. The depolarization factors in this model were scaled by the normalized effective permittivity to better account for percolation behavior. The model showed a wide variety of frequency dependent dielectric properties. Uncoated tubes were calculated to form highly conductive materials at volume fractions of just a few percent and metal-coated tubes enhanced the conductivity by an order of magnitude. Calculations of nanotubes with insulating coatings showed that high dielectric constants with moderate to low dielectric loss were possible.

INTRODUCTION

With their unique electrical and mechanical properties, single wall carbon nanotubes (SWNT) are under intense study for a wide variety of potential applications. The high aspect ratio and unique conductive behavior of carbon nanotubes provide opportunities for new composite materials with useful RF and microwave properties. Coating or filling carbon nanotubes with insulating or metallic materials can provide further enhancements to their electromagnetic properties. Some applications in EMI and telecommunications require lightweight conductive materials while other applications call for low loss substrate materials with high dielectric constants. By dictating the appropriate SWNT nano-structure, the materials designer can choose a conducting or semiconducting phase while using the same lightweight, strong, thermally stable chemistry. Thus, SWNT composites may be used to achieve controlled electromagnetic permittivity and conductivity in composite materials. However, there is limited understanding of how SWNTs can be effectively and practically manipulated to obtain the enhanced composite properties. Towards this end, an electromagnetic dispersion model was developed that predicts macroscopic permittivity for carbon nanotubes in a dielectric matrix. This SWNT model includes the capability to model 'decorated nanotubes', which include dielectric and metallic substances coating the exterior and/or filling the interior of the SWNT.

NANOTUBE MODEL DESCRIPTION

The composite SWNT model for frequency dispersive permittivity consists of four physical scales, and thus represents a 'multi-scale effective medium' model. At each physical scale electrical conductivity/permittivity of the SWNT component is calculated with the appropriate physics. "Pure" material properties are predicted from Drude models of the materials. When two

or more materials make up a surface, interior region, or the composite, conduction originates in percolation (i.e. long range DC conductivity occurring at a critical volume fraction of conducting material).

Scale 1:

The smallest SWNT scales are the layer thickness, tube diameter, and the <10 nm scale of coatings and/or filler particulates. The exact size and shape of these particulates along with the type of SWNT impact macroscopic properties and scale dependent conductivity of the particulates is important.

The theoretical model for the permittivity of the carbon nanotube requires an estimate of the permittivity of the graphene layer. The theoretical model for calculating the permittivity of the carbon nanotube requires an estimate of the permittivity of the graphene layer. This is complicated by the anisotropy of the graphene layer, with in-plane permittivity being substantially different than out-of-plane permittivity. A modified Drude model that includes a conductivity offset, σ_0, was used for the graphene layer,

$$\varepsilon(\omega) = \varepsilon_{\inf} - \varepsilon_0 \frac{\omega_p^2}{\omega^2 - i\omega\gamma} - i\frac{\sigma_0}{\varepsilon_0 \omega}, \tag{1}$$

where ω is frequency (in rad/s), ε_0 is the permittivity of free space, ω_p is the plasma frequency, γ is the damping frequency, and ε_{inf} is the permittivity at $\omega \to \infty$. The conductivity offset accounts for the proportion of semiconductive nanotubes that may exist in the mixture. The out-of-plane conductivity of the graphene layer was assumed to be a factor of 500 smaller than in-plane, in accordance with known behavior in graphite.

Scale 2:

The second size scale addresses granule agglomerates that may or may not form a percolating system on the surface, or form a percolating system of "wires" within the nanotube. The possibility of metallic coatings was demonstrated by Y. Zhang et al. [1]. Granules on the surface may form a two-dimensional conducting surface. The nanotube interior particulate distribution will be one-dimensional and thus might be represented as isolated particulates or short connected wires, which are surrounded by the semiconducting or conducting SWNT surface.

In the model considered here, metal coatings are treated as an assembly of spherical granules covering the surface of the nanotube. A symmetric Bruggeman approximation is used to calculate the effective permittivity of the metal shell, ε_1,

$$0 = v\frac{\varepsilon_1 - \varepsilon_{metal}}{p_c\varepsilon_{metal} + (1-p_c)\varepsilon_1} + (1-v)\frac{\varepsilon_1 - \varepsilon_d}{p_c\varepsilon_d + (1-p_c)\varepsilon_1}, \tag{2}$$

where ε_{metal} is the bulk permittivity of the metal used in the coating, ε_d is the matrix permittivity of the composite, and p_c is the percolation threshold. Since the metal granules are assumed to form a two-dimensional surface over the outside of the nanotube, the percolation threshold for a two dimensional system of spheres, $p_c \sim 0.59$, was used [2]. The metal permittivities as a function of frequency are calculated using the Drude model similar to Equation (1). The finite size of the metal granules restricts electron mobility and the modified damping frequency that results is [3],

$$\gamma = \gamma_b + \frac{v_f}{\pi x}, \tag{3}$$

where γ_b is the bulk damping frequency in rad/s, v_f, is the Fermi velocity, and x is the grain size of the metallic particulate. Approximate plasma and damping frequencies used for Drude model estimates of metal permittivies were taken from [4].

Scale 3:

The third scale accounts for the combined assembly of surface-SWNT and interior modifications. The overall structure remains small compared to RF wavelengths. The complete assembly can be modeled as a short but high aspect ratio multi-layer cylinder with end-caps as shown in Figure 1. Parallel to the tube axis, the nanotube permittivity is approximated as an infinite cylinder in series with the tube end-cap layers,

$$\varepsilon_{\|}^{tube} = \frac{L_0}{\left(\frac{L_0}{\tilde{\varepsilon}_{\|}} + \frac{L_1}{\varepsilon_{1\perp}} + \frac{L_2}{\varepsilon_{2\perp}}\right)}, \tag{4}$$

$$\text{where } \tilde{\varepsilon}_{\|} = v_1\varepsilon_{1\|} + v_2\varepsilon_{2\|} + v_3\varepsilon_{3\|}, \tag{5}$$

and $v_i = \frac{R_i^2 - R_{i+1}^2}{R_1^2}$ is the area fraction, R_i is the radius, and $\varepsilon_{i\|}$ is the permittivity of the i-th layer parallel to the tube axis. L_0 is the half-length of the tube (equal to the aspect ratio of the nanotube, Γ, multiplied by R_2). L_i and $\varepsilon_{i\perp}$ are the thickness and radial permittivity of the i-th layer.

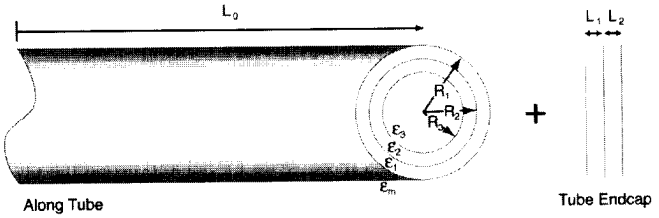

Figure 1 Nanotube geometry for hybrid parallel and series models

The perpendicular component of the permittivity of a nanotube can be calculated by solving the electrostatic problem of a layered cylinder for an electric field directed perpendicular to the tube axis. This assumes that the diameter of the nanotube is much smaller than the wavelength of the external radiation. The calculated polarizability of the layered cylinder is then compared to the polarizability of a simple homogeneous cylinder to obtain an effective permittivity,

$$\varepsilon_{\perp}^{tube} = \varepsilon_{eff} = \varepsilon_1 \frac{u+v}{u-v}, \tag{6}$$

where,

$$u = R_1^2\left[R_2^2(\varepsilon_3+\varepsilon_2)(\varepsilon_2+\varepsilon_1) + R_3^2(\varepsilon_3-\varepsilon_2)(\varepsilon_2-\varepsilon_1)\right]$$
$$v = R_2^2\left[R_2^2(\varepsilon_3+\varepsilon_2)(\varepsilon_2-\varepsilon_1) + R_3^2(\varepsilon_3-\varepsilon_2)(\varepsilon_2+\varepsilon_1)\right] \tag{7}$$

Scale 4:

The final mesoscale composite permittivity is modeled using a generalized Bruggeman effective medium equation [1] to calculate the effective permittivity of the ensemble of nanotubes in their

dielectric matrix. The composition includes nanotubes in a dielectric matrix. Therefore, a two-component effective medium model is used,

$$0 = v\left[\alpha\frac{\varepsilon_{i\|}-\varepsilon_e}{\varepsilon_e+g_{\|}(\varepsilon_{i\|}-\varepsilon_e)}+(1-\alpha)\frac{\varepsilon_{i\perp}-\varepsilon_e}{\varepsilon_e+g_{\perp}(\varepsilon_{i\perp}-\varepsilon_e)}\right]+(1-v)\frac{3(\varepsilon_d-\varepsilon_e)}{2\varepsilon_e+\varepsilon_d}, \quad (8)$$

where α= 1/3 for randomly aligned nanotubes, ε is the complex permittivity, v is the volume fraction of nanotubes, and the subscripts i, d, e represent the nanotube inclusions, dielectric matrix, and effective composite properties respectively. The subscripts $\|$ and $\perp$ represent the components parallel and perpendicular to the nanotube axis. Because the nanotubes are anisotropic they are described with two terms corresponding to the perpendicular and parallel properties of each tube. The depolarization factors, $g_{\|}$ and $g_{\perp}$, are given by,

$$g_{\|}=\frac{1}{\Gamma^2}\frac{\varepsilon_e}{\varepsilon_d}\ln\left(1+\Gamma\frac{\varepsilon_d}{\varepsilon_e}\right) \text{ and } g_{\perp}=\frac{1}{2}(1-g_{\|}), \quad (9)$$

where Γ is the average nanotube aspect ratio.

Note the effective medium theory of Equations (8) and (9) do not fully account for microstructure effects (e.g. agglomeration or other network topologies) in the dispersion of nanotubes within the composite. Thus they may be considered as a qualitative model, especially with respect to the percolation threshold. The quantitative volume fraction of the percolation threshold will depend on the specific microstructure of the actual composite, which depends on the processing conditions

NANOTUBE MODEL CALCULATIONS

To estimate typical nanotube conductivity properties, the effective medium model derived here was iteratively applied to measured permittivity data of carbon nanotube mats from Hilt and coworkers [5,6]. Because the mats were made up of fibers randomly oriented within a plane, Equation (8) was used with α = 0.5. The fit between model and measured data are shown in Figure 2. The measured data from 75 to 400 GHz were from a focused beam apparatus while the data at 10 and 15 GHz were from waveguide measurements, which may have errors associated with air gaps (i.e. incomplete sample – waveguide contact). Since the measured samples in [5,6] were obtained from Rice, the SWNT outer diameters were assumed the same as those published by Smalley et al. in [8], 1.7 nm. The thickness of the graphene layer was assumed to be 3.45 angstroms, similar to the layer-to-layer spacing in bulk graphite. Based on information in [5,6], the average tube aspect ratio was taken to be 1000, the volume fraction of tubes was 32.5%, and the tubes were randomly oriented within the plane of the sample. The data fit of Figure 2 uses graphene layer parameters of ω_p = 1.3e14 rad/s, γ= 4e11 rad/s, ε_{inf} = 1, and σ_0 = 3000 S/cm. These three parameters were obtained by iteratively fitting the model to the measured data. The fitted graphene layer's plasma frequency is an order of magnitude lower and the damping frequency is two orders lower than bulk graphite.

The multiscale model derived here was applied to evaluate the range of frequency dependent dielectric properties available in SWNT composites. In all modeled cases, the nanotubes were in a dielectric matrix with permittivity, ε = 3 - 0.001i, which is representative of many polymers at microwave frequencies. Nanotubes were assumed to have an average outer diameter of 1.7 nm and electrical parameters as fitted to the measured data of Hilt and coworkers [5,6].

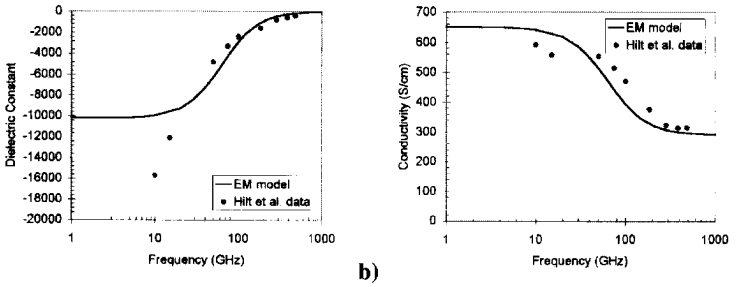

Figure 2 Model fit of a) Dielectric permittivity and b) conductivity measured to data measured by Hilt et al. [5,6] of a mat of single-walled carbon nanotubes

Uncoated tubes were predicted to form highly conductive composite materials at nanotube volume fractions as low as 0.45 percent. Metal-coated tube composite simulations showed enhanced conductivity, an order of magnitude above uncoated tubes for volume concentrations above the percolation threshold. Composites with nanotubes below the percolation threshold, either with or without metal coatings, were predicted to have high dielectric constants with moderate to low dielectric loss tangents.

When insulating coatings were placed on the nanotubes, high dielectric constants were predicted; however, a dielectric Debye-like relaxation was predicted in the microwave frequency range. An example calculation, which compares composites with uncoated tubes (0.1 vol% SWNTs) to dielectrically coated tubes with the same graphene volume fraction is shown in **Figure 3**. The dielectric coating imposes a more dispersed microsctructure in the composite (i.e. the tubes are separated by insulating layers), resulting in modified electromagnetic properties. Variation of the coating thickness manipulates the amplitude and frequency of the dielectric relaxation, thereby providing a possible route for controlling electromagnetic dispersion. Metal filled SWNT composites had only minor differences with unfilled SWNT composites. However, this model does not account for quantum effects that can modify the electronic transport in the nanotubes, particularly when metals are in contact with the graphene layer.

CONCLUSIONS

A classical model was developed to predict the effective frequency dispersive permittivity of single walled carbon nanotubes (SWNTs) and distributions of these nanotubes in a dielectric matrix. The model combines the electrostatic polarizability of a layered cylinder with the Drude model of conductive materials and scaled effective medium theories to calculate dielectric permittivity of the nanotubes and composites. The model is constructed to predict properties of "decorated nanotubes" and their composites. The tubes are modeled as layered cylinders, each with a core, a graphene layer and an outer layer. Graphene and metal properties were modeled with a Drude approximation based on plasma and collision frequency estimates, which were derived from measured data in the literature. A Bruggeman model was used to determine the macroscopic behavior of the modified carbon nanotubes in a composite structure as a function of volume fraction, frequency, alignment, and aspect ratio. The depolarization constants in this effective medium model were scaled by the normalized effective permittivity to better account for percolation behavior. Note that the results presented here are not yet validated. While the

conductivity parameters of the graphene layer used here were inferred from measured free-space data of a highly filled composite, additional measurements are needed to confirm the model's accuracy for other volume fractions.

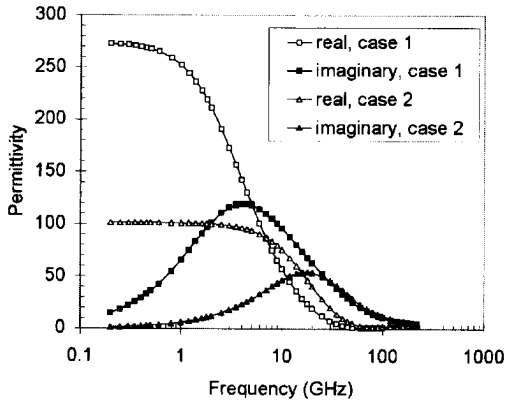

Figure 3 Comparison of dielectric properties between uncoated (case 1) and dielectric coated (case 2) nanotube mixtures with the same volume fraction of nanotube (excluding the coating)

ACKNOWLEGEMENTS

This research was supported by NASA, Langley under contract no. NAS1-99073-1011.

REFERENCES

1. Y. Zhang, N.W. Franklin, R.J. Chen, H. Dai, *Chem. Phys. Lett*, **331**, 35-41, (2000)
2. J.P. Clerc, G. Giraud, J.M. Laugier, J.M. Luck, *Advances in Phys.*, **39**(3), 191-309, (1990)
3. J. Perrin, B. Despax, E. Kay, Phys. Rev. B, **32**(2), 719-725, (1985)
4. I. El-Kady, M.M. Sigalas, R. Biswas, K.M. Ho, C.M. Soukoulis, *Phys. Rev. B*, **62**(23), 15299-15302, (2000)
5. O. Hilt, H.B. Brom, M. Ahlskog, *Phys. Rev. B*, **61**(8), 5129-5132, (2000)
6. H.C.F. Martens, J.A. Reedijk, H.B. Brom, D.M. de Leeuw, R. Menon, *Phys. Rev. B*, **63**, 073203, 1-4, (2001)
7. A.N. Lagarkov, A.K. Sarychev, *Phys Rev B*, **53**(10), 6318-6336, (1996)
8. A. Thess, R. Lee, P. Nikolaev, H. Dai, P. Petit, J. Robert, C. Xu, Y.H. Lee, S.G. Kim, A. G. Rinzler, D.T. Colbert, G.E. Scuseria, D. Tomanek, J.E. Fischer, R.E. Smalley, *Science*, **273**, 483-487, (1996)

Mat. Res. Soc. Symp. Proc. Vol. 739 © 2003 Materials Research Society

Formation of 3-Dimensionally Orientated Nano-sized Crystals in an Amorphous Alloy under Ion Beam Irradiation

Takuya Kamikawa, Ryuichi Tarumi, Kazuki Takashima and Yakichi Higo
Precision and Intelligence Laboratory, Tokyo Institute of Technology,
4259 Nagatsuta-cho, Midori-ku, Yokohama 226-8503, Japan

ABSTRACT

We have succeeded to form three-dimensionally orientated nano-sized crystals in a Ni-P amorphous alloy under focused ion beam (FIB) irradiation. The FIB micro-fabrication was performed on an electroless deposited Ni-P amorphous alloy and thin films with a thickness of 100 nm were prepared. Transmission electron microscopy (TEM) observation for irradiated areas revealed the formation of crystallographically orientated nano-sized crystals (NCs) in the irradiated region. The grain size of NCs was less than 10 nm in diameter. Electron diffraction analysis showed that the formed NCs have a face-centered-cubic (f.c.c.) structure and the following orientation relationships among the specimen, the NCs and the FIB direction: irradiated plane // $\{111\}_{f.c.c.}$ and ion beam direction // $<110>_{f.c.c.}$.

INTRODUCTION

Nano-sized crystals (NCs) have been expected to be more widely applied to many industrial fields. Over the past decade, many studies have been achieved to form NCs, since NCs have a potential to improve mechanical or magnetic properties of materials [1, 2]. To date, several methods, deposition on substrates, recrystallization following severe plastic deformation, precipitation of a secondary phase, and crystallization from a amorphous state, have been proposed to form NCs. It is, however, difficult to obtain crystallographically orientated NCs while controlling their size less than 10 nm diameter.

Ion beam irradiation is one of the attractive methods to control the structure of materials in the order of nanometers. Several kinds of structural changes, precipitation of implanted ions [3], formation of dislocation loops [4], phase transformation from crystalline to amorphous structure [5], and *vice versa* [6], have been reported under ion beam irradiation. Amorphous alloys are in a nonequilibrium thermal state so that a phase transformation from amorphous into crystalline structure can be expected under ion beam irradiation, but the details have not been identified.

In this study, we have investigated the structural changes of a Ni-P amorphous alloy

under focused ion beam (FIB) irradiation by using transmission electron microscopy (TEM).

EXPERIMENTAL DETAILS

In this investigation, a Ni-11.5 wt% P amorphous alloy prepared by electroless deposition on an Al-Mg alloy substrate was employed (Fig. 1 (a)). The thickness of the amorphous alloy layer was 12 μm. The amorphous layer was separated from the Al-Mg alloy substrate using a NaOH aqueous solution (Fig. 1 (b)). Specimens were then heat treated at 473 K for 30 minutes. The amorphous layer was mechanically cut into a circular disk with a diameter of 3 mm (Fig. 1 (c)). Electrical polishing was performed in a HCl_4-CH_3COOH (9:1) mixed solution at 273 K to reduce the thickness of the amorphous film (Fig. 1 (d)). The disk was mechanically cut into a semicircular disk (Fig. 1 (e)). FIB micro-fabrication was then carried out. Figure 2 (a) shows schematic drawings of FIB micro-fabrication procedure. As shown in the figure, micro-fabrications were performed on both sides (top and bottom sides) of the specimen. The hatched area in Fig. 2 (b) corresponds to the irradiation damage area of the FIB micro-fabrication. Structural changes of the irradiated area were investigated using TEM (Fig. 2 (b)). To track the position of the ion beam a Cartesian coordinate system was referred to the specimen as shown in Fig. 2. In this coordinate system, the z-axis was parallel to the surface normal of specimens and the y-axis was set parallel to the FIB direction. The FIB apparatus used was a HITACHI FB2000-A operated at 30 keV with a liquid metal ion source of

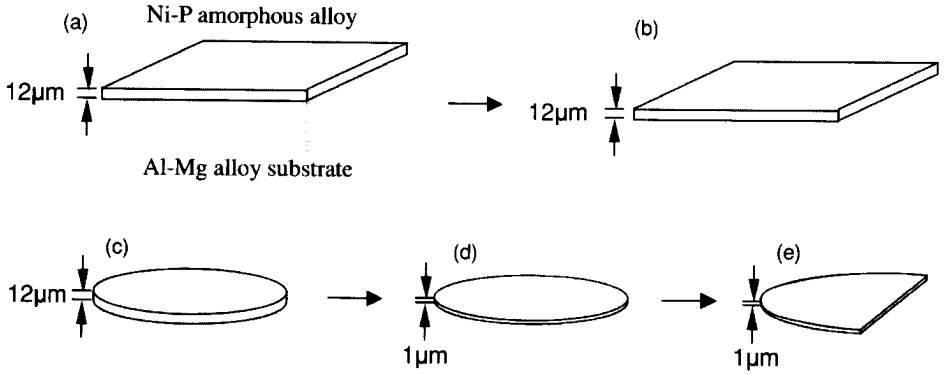

Figure 1. Schematic drawings of the experimental procedure. (a) As electroless deposited state on a Al-Mg substrate. (b) Dissolving the substrate by NaOH aqueous solution. (c) Mechanically cut into circular disk with a diameter of 3 mm. (d) Electrical polishing to be a thickness of approximately 1 μm. (e) Mechanically cut into semicircular disk.

Ga. The beam current was decreased from 3.53 to 0.08 nA by decreasing the thickness of the specimens. Transmission electron microscopy observation was carried out using a Philips CM200 operated at 200 keV.

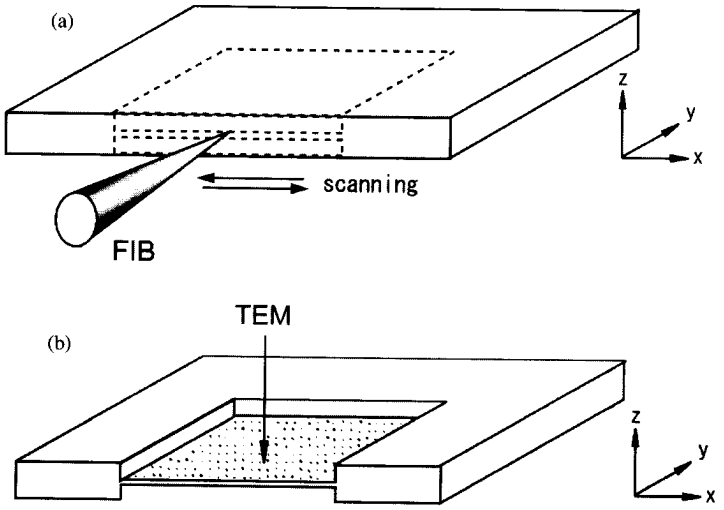

Figure 2. Schematic drawings for (a) the FIB micro-fabrication procedure and for (b) TEM observation of the irradiated area. As shown in the figures, the y and z axes of the Cartesian coordinate were set parallel to the FIB and irradiated plane normal, respectively.

RESULTS AND DISCUSSION

Figure 3 (a) shows a selected area electron diffraction (SAED) pattern obtained from an area irradiated by the FIB (Fig. 2 (b)) where, the incident electron beam direction was set parallel to the z-axis. In the SAED pattern, six clear reflections were observed in addition to halo rings from the amorphous matrix. These reflections indicate the existence of crystallographically orientated crystals in the amorphous matrix. Figure 3 (b) shows a schematic drawing of the electron diffraction pattern. As shown in the figure, the observed SAED pattern corresponded to that of [111] incident diffraction pattern of $Ni_{f.c.c.}$. The FIB direction (y-axis) corresponded to that of [110] incident diffraction pattern of $Ni_{f.c.c.}$. As a result of reference to the Cartesian, the orientation of the formed NCs can be expressed as follows:

z-axis // <111>, y-axis // <110>.

Figure 3 (c) shows a low magnification dark field micrograph taken using a reflection in the SAED pattern (Fig. 3 (a)). In the micrograph, a large amount of NCs was uniformly distributed throughout the irradiated plane. Figure 3 (d) shows a high magnification dark field micrograph. As shown in the figure, the size of the formed NCs was less than 10 nm in diameter.

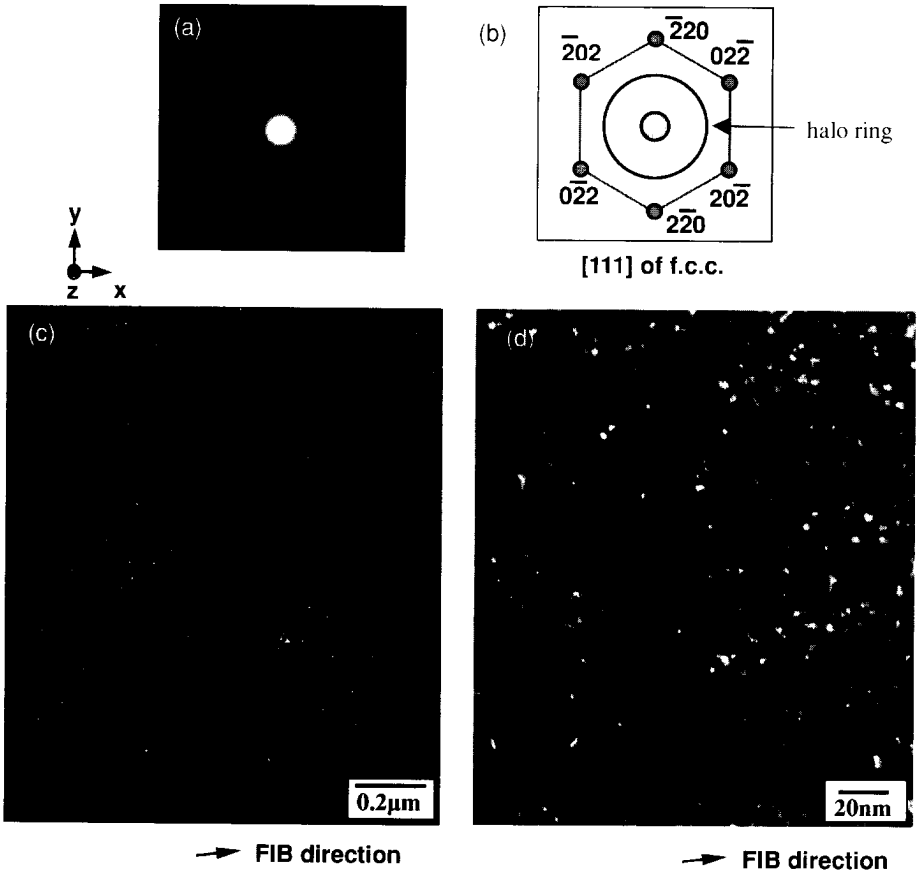

Figure 3. (a) A SAED pattern taken from the irradiated area. Reflections in the SAED pattern represent orientated crystalline phase. (b) A schematic drawing of the SAED pattern. (c) A low magnification and (d) dark field micrograph of the irradiated plane. Size of the formed NCs was less than 10 nm in diameter.

To identify the orientation of the formed NCs, it is essential to determine their crystalline structure. The formed NCs have a f.c.c. structure with the orientation described above. A series of electron diffraction analyses revealed that irradiated plane // (111) and ion beam direction // <110>.

Here is an explanation for the oriented formation of NCs under ion beam irradiation. During the FIB irradiation, increase in temperature is considered to occur in local area of the amorphous alloy. Generally, amorphous alloys transform into crystalline structure due to thermal diffusion. Crystals induced by thermal diffusion in amorphous alloys, however, do not have correlated orientation. Furthermore, phases in thermal equilibrium of the Ni-P amorphous alloy are Ni (f.c.c.) and Ni_3P (bct) [7]. Thus, crystallographic features of the NCs induced by the FIB irradiation are completely different from those of thermal diffusion. It is, therefore, considered that the formation of orientated NCs can not be explained only by an increase in temperature during the irradiation. Under ion beam irradiation, atoms in the amorphous matrix are considered to be displaced preferentially in the direction of the incident ion beam due to the knock-on effect. Furthermore, a free surface of the specimen may affect the orientation of NCs because of image force. Thus, orientation of the formed NCs is considered to be related to the preferential displacements of atoms by the FIB under the constraint of the free surface. To clarify the mechanism of the oriented formation of the NCs further investigations are required.

CONCLUSIONS

In the present study, we have investigated the structural changes of amorphous Ni-P alloy under FIB irradiation using TEM. In the irradiated areas, uniformly distributed NCs, with an average grain size of less than 10 nm, were found in the amorphous matrix. A series of electron diffraction analyses revealed that the precipitated NCs in the irradiated plane were Ni with a f.c.c. structure, while the specimen, the formed NCs and FIB direction had following orientation relationships: irradiated plane // $\{111\}_{f.c.c.}$ and projected ion beam direction // $<110>_{f.c.c.}$.

REFERENCES

1. A. Inoue, Y. Yokohama, and T. Masumoto, *Mater. Sci. Eng., A* **181**, 2 (1994).
2. A. M. Tonejc, N. Ramsak, A. Prodan, A. Tonejc, A. Khalladi, S. Surinach, and M. D. Baro, *Nanostruct. Mater.* **12**, 677 (1999).
3. C. W. Allen, R. C. Birtcher, S. E. Donnelly, K. Furuya, N. Ishikawa, and M. Song, *Appl. Phys. Lett.* **74**, 2611 (1999).
4. E. Oliviero, M. F. Beaufort, and J. F. Barbot, *J. Appl. Phys.* **89**, 5332 (2001).
5. S. Takeda and J. Yamasaki, *Phys. Rev. Lett.* **83**. 320 (1999).
6. T. Nagase, Y. Umakoshi, and N. Sumida, *Mater. Sci. Eng., A* **323**, 218 (2002).
7. M. L. Sui, K. Lu, and Y. Z. He, *Philos. Mag. B* **63**, 993 (1991).

Fabrication and Properties of 1D Nanostructures

Mat. Res. Soc. Symp. Proc. Vol. 739 © 2003 Materials Research Society H5.2

The Effects of Crystallinity and Catalyst Dynamics on Boron Carbide Nanospring Formation

D. N. McIlroy, D. Zhang, Y. Kranov, H. Han, A. Alkhateeb, and M. Grant Norton[1]
Department of Physics, Engineering and Physics Bldg., University of Idaho, Moscow, ID, 83844-0903, U.S.A.
[1]School of Mechanical and Materials Engineering, Washington State University, Pullman, WA 99164-2920, U.S.A.

ABSTRACT

The formation of helical nanowires—nanosprings—of boron carbide have been observed and a growth mechanism, based on the work of adhesion of the metal catalyst and the tip of the nanowire, developed. The model demonstrates that the asymmetry necessary for helical growth is introduced when the following conditions are met:

(1) The radius of the droplet is larger than the radius of the nanowire, and
(2) The center of mass of the metal droplet is displaced laterally from the central axis of the nanowire.

Furthermore, this model indicates that only amorphous nanowires will exhibit this unique form of growth and that in monocrystalline nanowires it is the crystal structure that inhibits helical growth. High-resolution transmission electron microscopy and electron diffraction has been used to compare the structure of both amorphous and crystalline nanowires.

INTRODUCTION

A revolution is on the horizon for optics and electronic devices as we currently know them. It is being spurred on by breakthroughs in the development of nanoscaled materials. Over the past decade it has been demonstrated that nanoscale materials exhibit novel optical [1-4] and electronic [5-7] properties attributable to quantum confinement. This, in turn, has accelerated efforts to develop new nanoscale materials, as well as new techniques for their synthesis. A major area of research on nanoscale materials has focused on the development of solid nanowires because of their potential use in nanoelectronics, nanomechanics, and flat panel displays [8-11]. Critical to the implementation of nanotubes and nanowires into high tech commercial applications will be the ability to develop techniques for their self-assembly. The ability to control the self-assembly of nanotubes and nanowires, however, may be on the horizon.

The synthesis of nanotubes [7,12,13] and nanowires [14-17] on surfaces can be promoted through the introduction of a metallic catalyst. This growth mechanism is known as the vapor-liquid-solid (VLS) growth mode, first described by Wagner and Ellis [18]. Briefly, in VLS growth a liquid droplet of a metal or a eutectic alloy resides on a substrate. The droplet absorbs the necessary components for nanowire growth from the surrounding vapor. Once the concentration of the element, or elements, in the droplet reaches a level of supersaturation, the excess material is secreted at the liquid/solid interface. As more material is secreted to this interface the droplet is lifted off the surface concomitantly with wire formation beneath the droplet. Wire growth is sustained by

maintaining a steady rate of delivery of source material to the droplet. It is clear from this description of the VLS growth mode that self-assembly of nanotubes and nanowires will depend on the ability to control the nature of the catalyst, i.e., the metal droplet.

In addition to promoting nanowire growth, the catalyst can also introduce fluctuations in the growth that results in the formation of novel nanostructures. For example, nanocrystals spanned by nanowires have been observed for Si [19, 20] and B_4C [14], which we refer to as nanonecklaces. In the case of single crystal B_4C nanowires, the nanocrystals exhibit the rhombohedral symmetry of the B_4C unit cell, with no observable discontinuity in the crystal orientation at the nanowire/nanocrystal interface. The formation of nanonecklaces has been attributed to instabilities arising from fluctuations in the growth conditions [14,19]. Far more startling has been the discovery of helical growth of large whiskers of Si_3N_4 [21] and C [22], and more recently boron carbide nanosprings [23], as well as helical nanotubes [24, 25] and nanowires [19,26]. The formation of helical nanotubes and nanowires is a keen example of the unique types of nanowire structures that can be achieved through VLS growth. In order to explain the mechanism driving the growth of nanosprings, a dynamic model of the liquid metal catalyst must be developed. In this report we present recent observations of helical growth of boron carbide nanowires, as well as a model to explain the mechanism driving nanospring formation.

EXPERIMENTAL DETAILS

The nanowires were grown on (100)-oriented silicon substrates. Prior to insertion into the chamber the Si substrates were cleaned for five minutes in a 5% HF/ deionized water solution followed by a rinse in deionized water. The boron carbide nanowires were grown in a custom parallel plate 13.56 MHz PECVD chamber, which has been described in more detail elsewhere [22]. The substrates were located on the grounded electrode during deposition. The deposition temperature was 1050 °C and the plasma power 50 W. The source compound was *closo*-1,2-dicarbadodecaborane—orthocarborane. Argon was the carrier gas and was allowed to flow through the source bottle that was held at 60 °C during deposition. The gas mixture consisted of 65 mTorr of Ar (10 sccm) and 25 mTorr of orthocarborane/Ar (3.5 sccm). Using these deposition conditions a low density layer of nanowires/nanosprings was obtained after 20 minutes.

The structural properties of the boron carbide nanowires were examined using an Amray 1830 scanning electron microscope (SEM) operated at 10 kV and a Philips CM200-FEG analytical transmission electron microscope (TEM) operated at 200 kV.

DISCUSSION

Shown in Fig.1 is a SEM image of boron carbide nanowires lying across a silicon substrate. Figure 2 is a TEM image showing a single nanowire from the same sample.

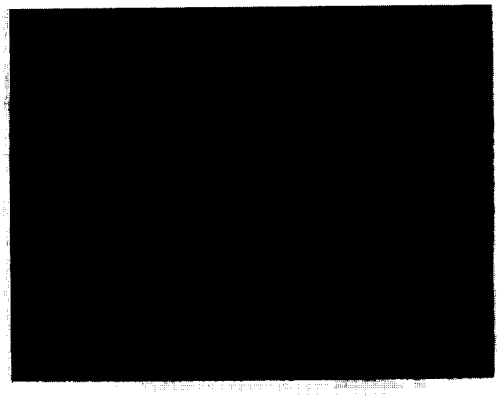

Figure 1. SEM image of boron carbide nanowires on silicon.

The nanowire consists of a linear segment that transforms to helical growth, i.e., a nanospring. The dark region at the transition point is iron boride, the catalyst material used in this study. The nanospring in Fig.2 is 32 nm in diameter and approximately 1 μm in length, with a pitch of 32 nm. The diameter of the wire proper is 22 nm.

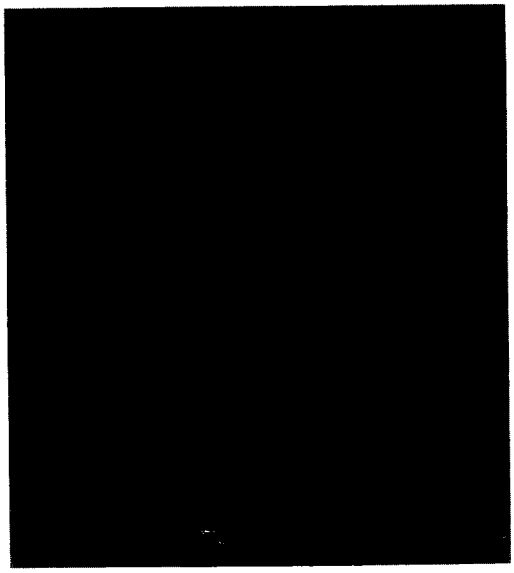

Figure 2. TEM image of an amorphous boron carbide nanowire at the transition from a linear to helical growth.

The diameters of the boron carbide nanosprings in this sample ranged from 20 to 60 nm, with pitches from 20 to 30 nm and nanowire diameters from 20 to 30 nm. The typical time required to grow a 10 μm long single crystal nanowire is two hours [14,15], yet the nanowire in Fig. 2 grew an equivalent length in approximately 30 minutes. The significance of this accelerated growth rate is addressed later. Only about 20% of the nanowires in this sample were in the form of nanosprings, the remaining 80% grew linearly. To the best of our knowledge, the only other observations of helical growth in the size regime reported here are for helical Si nanowires by Tang *et al.* [19] and helical SiC nanowires by Zhang *et al.* [26]. However, the helical Si nanowires were irregular and not as well formed as the boron carbide nanospring produced in our laboratory. In the case of the helical SiC nanowires the observed pitches were on the order of 80 to 100nm, a factor of three larger than the nanospring in Fig.2. Again, to the best of our knowledge, helical growth of the quality (uniform diameter and pitch) exhibited in Fig. 2 has only been reported by Motojima *et al.* for micron sized helixes of Si_3N_4 [21] and C [22].

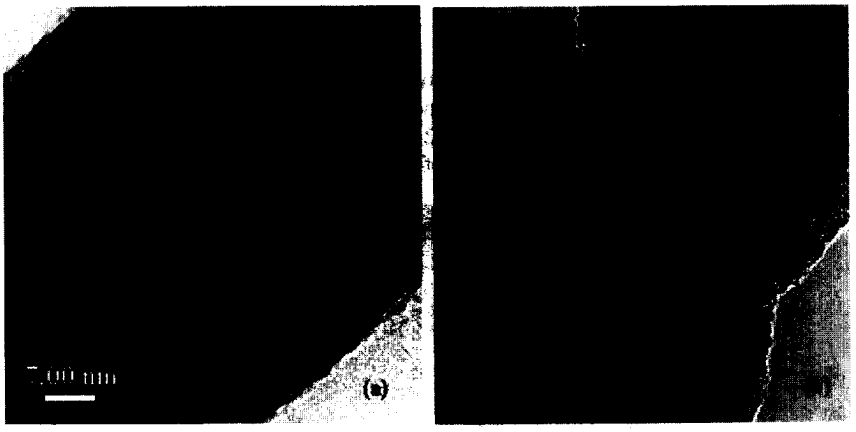

Figure 3. High resolution TEM images of (a) crystalline boron carbide nanowire(see scale bar in (b)) and (b) amorphous boron carbide nanospring.

The structure of the nanowires can be viewed as a constraint that will dictate the type of allowable growth, i.e., straight or helical. Therefore, it is important to identify potential differences between the structures of the straight and helical forms. Displayed in Fig. 3(a) is a high-resolution transmission electron microscopy (HRTEM) image of a single crystal boron carbide nanowire in which the well defined lattice planes are clearly visible. Using electron diffraction the structure was determined to be B_4C [14]. In contrast, the signature of an ordered lattice is absent in the HRTEM image of the boron carbide nanospring in Fig. 3(b), which indicates that the structure is amorphous. The composition of the nanospring was determined to be close to the B_4C stoichiometry.

In the majority of the cited cases of helical growth [21-23] the structure was found to be amorphous. The only exceptions were for helical Si [19] and SiC nanowires [26]. For the Si nanowires the structure of the helixes is less clear due to the coexistence of single crystal Si and amorphous SiO_2 within a single nanowire. In the case of the helical

SiC nanowires the structure is crystalline, the helical trajectory of the nanowire has been attributed to screw dislocation induced growth. We believe that the large pitches (≥80 nm) of the helical SiC nanowires are a consequence of their crystalline structure.

For single crystal nanowires the preferential direction of growth will be driven by the need to minimize the surface free energy of the nanowire. The growth of rhombohedral nanocrystals of boron carbide spanned by single crystal nanowires [14], i.e. nanonecklaces, illustrates this point nicely. The interface between the rhombohedral nanocrystals and the nanowires was probed by HRTEM in an effort to identify the presence of dislocations between the two phases of growth. No dislocations were observed, which indicated that the transition from nanocrystal growth to nanowire growth was continuous. The direction of nanowire growth, relative to the orientation of the rhombohedral nanocrystal, indicated that the preferential direction of growth of single crystal boron carbide nanowires is along the c-axis of the rhombohedral cell. In addition, this result indicates that for single crystal nanowire growth the dynamics of the metal droplet (catalyst) has little effect on determining the preferential direction of growth, and therefore can be ignored.

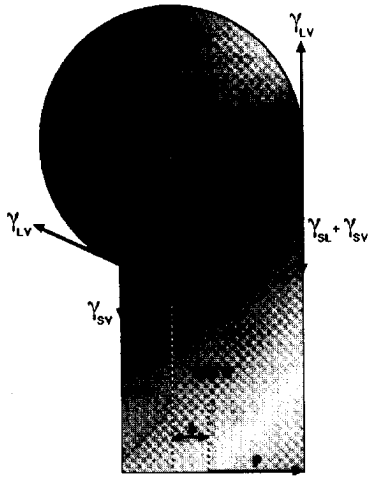

Figure 4. Schematic representation of the nucleation of helical growth at the catalyst-nanowire interface.

In contrast, we suggest that the constraint against helical growth that is imposed by crystallinity be lifted if the nanowires are amorphous. Furthermore, we suggest that it is the dynamics of the metal droplet (catalyst) that is driving helical growth. The dynamics of the droplet can be quantified by examining the work needed to shear the droplet from the tip of the nanowire, which is related to the surface tensions (γ) between the liquid-vapor (γ_{LV}), solid-vapor (γ_{SV}), and solid-liquid (γ_{SL}) interfaces. Figure 4 illustrates a cross-sectional view of the catalyst atop a nanowire, where R is the radius of the droplet, ρ is the radius of the nanowire and Δ is the displacement of the center of mass of the droplet from the central axis of the nanowire. The droplet has been offset from the central axis of the nanowire in order to accentuate the fact that the surface

tension along the droplet-wire interface varies as a function of the contact angle between the droplet and the nanowire. At interface A in Fig.4 the interfacial surface tensions associated with the liquid-vapor interface (γ_{LV}) and the solid-liquid interface (γ_{SL}) are antiparallel, while the interfacial surface tension associated with the solid-vapor interface (γ_{SV}) is rotated by an angle θ out of the plane containing γ_{LV} and γ_{SL}. However, at interface B the interfacial surface tensions associated with the three phases lie within the same plane, where γ_{SV} is parallel to γ_{SL}. Consequently, there is a non-zero torque on the droplet, which will cause the droplet to shear from the nanowire.

The work required to shear the droplet from the nanowire can be quantified in terms of the interfacial surface tensions [27]. At the interface, the work per unit area required to shear the droplet from the nanowire, the work of adhesion (W_A), is given by:

$$\begin{aligned} W_A &= \gamma_{SV} + \gamma_{SL} - \gamma_{LV} \\ &= \gamma_{SV} + \gamma_{SL} - (\gamma_{SL} + \gamma_{SV}\cos\theta) \\ &= \gamma_{SV}(1-\cos\theta). \end{aligned}$$

This equation demonstrates that the work of adhesion will depend on the angle between the surface tensions γ_{SV} and γ_{SL}. At interface A in Fig. 4 the interaction between the droplet and the nanowire is a nonwetting interaction. While at interface B in Fig. 4 the droplet is in a condition of spontaneous wetting. Spontaneous wetting can only occur under the conditions depicted in Fig. 4. The work of adhesion at the perimeter of the droplet-wire interface has been calculated for the droplet symmetrically over the central axis of the nanowire (Fig. 5(a)) and for the geometry in Fig. 4 (Fig. 5(b)). From examination of Fig. 5 we see that the work of adhesion is symmetric when the droplet is symmetrically located over the nanowire and is asymmetric for the geometry in Fig. 4. In addition to the asymmetry in Fig. 5(b), a well defined cusp in the work of adhesion occurs at the interface corresponding to point B in Fig. 4. The cusp corresponds to a point of minimum work of adhesion. If this offset is maintained, but the radius of the droplet is

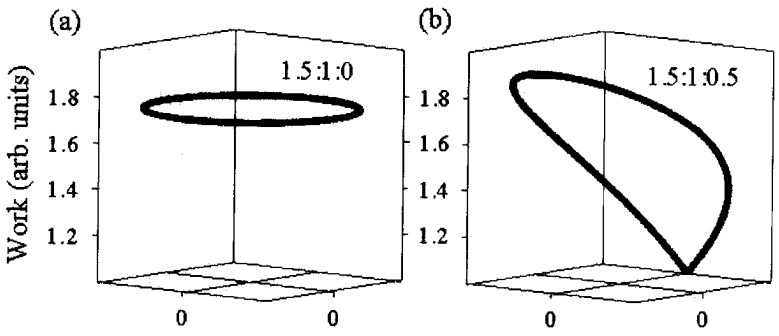

Figure 5. Work of adhesion ($W_A(R:\rho:\Delta)$) of a metal droplet to a nanowire as a function of droplet radius (R), nanowire radius (ρ), and the offset of the center of mass of the droplet from the axis of the nanowire (Δ). The work of adhesion has been calculated for (a) (1.5:1.0:0.0), (b) (1.5:1.0:5), where all of the variables ($R:\rho:\Delta$) have been normalized to the radius of the nanowire.

increased, for example, to five times the radius of the nanowire, the asymmetry and the cusp in Fig. 5(b) is eliminated and the value of the work of adhesion is symmetric (Fig. 5(a)), i.e., a geometry that promotes linear growth.

The significance of this asymmetry in the work of adhesion is as follows. The probability of a boron or carbon atom diffusing through the droplet and attaching itself to a point at the droplet-nanowire interface will be a function of the energy needed to break a droplet-nanowire bond, less the energy gained by making a new B or C bond to the nanowire. The amount of energy needed to accomplish this will depend macroscopically on the work of adhesion, where the probability of attachment of a B or C atom at the droplet-nanowire interface is higher at the points of lower work of adhesion. Therefore, the nanowire will grow asymmetrically, which will cause the trajectory of the center of mass of the droplet to curl back upon the nanowire. The asymmetry, however, does not produce the pitch necessary to form nanosprings. However, the cusp is a point of instability. Consequently, a small lateral perturbation will produce the necessary pitch to drive the droplet into a helical trajectory. It has been demonstrated that the trajectory of the catalyst can be altered by small temperature fluctuations during nanowire formation [27]. Consequently, we believe that a small temperature fluctuation, in conjunction with the geometry in Fig. 4 led to transition in the nanowire shown in Fig. 2.

Based on the analysis of the work of adhesion of the metal droplet to the nanowire, we have concluded that the optimal geometry for promoting helical growth is achieved when the radius (R) of the droplet is larger than the radius (ρ) of the nanowire and the extreme edge of the droplet coincides with the edge of the nanowire, as depicted in Fig. 4. In support of our model for helical growth is the image of the linear-helical interface shown in Fig. 2. The spherical particle at the point of transition from straight to helical growth is a remnant of the catalyst that promoted the growth of the straight portion of the nanowire. While the cause is yet unclear, the droplet became pinned and the nanowire began to grow around the droplet. The smaller diameter of the droplet relative to the diameter of the nanowire indicates that prior to becoming pinned its diameter was larger than its present size. We hypothesize that as the wire began to encase the droplet a fraction of the droplet was ejected. The point of ejection appears to have occurred at the lower left side of the droplet in Fig. 2, where a small section of the encased droplet is exposed. Note, that this corresponds to the beginning of helical growth. If the diameter of the droplet was originally equal to the diameter of the linear nanowire (38 nm), then the diameter of the ejected droplet would be 35 nm. The diameter of the nanowire forming the nanospring in Fig. 2 is 22 nm, which gives a ratio of the droplet radius to the radius of the nanowire forming the nanosping of 1.6, which is very close to the ratio used to calculate the work of adhesion in Fig. 5(b). In addition, the point of ejection of the droplet could easily produce the droplet-nanowire geometry depicted in Fig. 4. The TEM image in Fig. 2 clearly supports the proposed model of nanospring growth.

CONCLUSION

The observed growth of helical amorphous boron carbide nanowires, in conjunction with the development of a model for this type of growth based on the dynamics of the metal catalyst, illustrates the importance of controlling the catalyst in the

quest to develop well defined processes for growing unique nanowire structures. While many questions remain to be answered, such as the non-circular cross sections observed for nanosprings and helical, the most important issue is whether it is possible to drive wires into helical growth. The possibility of controlling the diameter of the nanowire, the diameter of the helix and the pitch of a nanospring opens up exciting applications in nanoelectronics and nanomechanics.

ACKNOWLEDGEMENTS

D.N.M. would like to acknowledge the support by the NSF (EPS-0132626). The high-resolution TEM work was performed at Oak Ridge National Laboratory through the SHaRE Program and was sponsored by the Division of Materials Sciences and Engineering, U.S. Department of Energy, under contract DE-AC05-00OR22725 with UT-Battelle, LLC.

REFERENCES

1. A. P. Alivisatos, *Science* **271**, 933 (1996).
2. J. Hasen, L. N. Pfeiffer, A. Pinczuk, Song He, K. W. West, B. S. Dennis, *Nature* **390**, 54 (1997).
3. X. Duan, Y. Huang, Y. Cui, J. Wang, and C. M. Lieber, Nature 409, **66** (2001).
4. J.-M. Bonard, T. Stöckli, F. Maier, W. A. de Heer, A. Châtelain, J.-P. Salvetat, and L. Forró, *Phys. Rev. Lett.* **81**, 1441 (1998).
5. D. L. Klein, R. Roth, A. K. L. Lim, A. P. Alivisatos, P. L. McEuen, *Nature* **389**, 699 (1997).
6. P. G. Collins, A. Zettl, H. Bando, A. Thess, and R. E. Smalley, *Science* **278**, 100 (1997).
7. J. Hu, M. Ouyang, P. Yang, and C. M. Lieber, *Nature* **399**, 48 (1999).
8. J.-M. Bonard, J. P. Salvetat, T. Stöckli, W. A. de Heer, L. Forró, and A. Châtelain, *Appl. Phys. Lett.* **73**, 918 (1998).
9. Q. H. Wang, T. D. Corrigan, J. Y. Dai, R. P. H. Chang and A. R. Krauss, *Appl. Phys. Lett.* **70**, 3308 (1997).
10. F. C. K. Au, K. W. Wong, Y. H. Tang, Y. F. Zhang, I. Bello, and S. T. Lee, *Appl. Phys. Lett.* **75**, 1700 (1999).
11. K. W. Wong, X. T. Zhou, F. C. K. Au, H. L. Lai, C. S. Lee, and S. T. Lee, *Appl. Phys. Lett.* **75**, 2918 (1999).
12. J. M. Mao, L. F. Sun, L. X. Qian, Z. W. Pan, B. H. Chang, W. Y. Zhou, G. Wang, and S. S. Xie, *Appl. Phys. Lett.* **72**, 3297 (1998).
13. Z. P. Huang, J. W. Xu, Z. F. Ren, J. H. Wang, M. P. Siegal, and P. N. Provencio, *Appl. Phys. Lett.* **73**, 3845 (1998).
14. D. Zhang, D. N. McIlroy, Y. Geng, and M. G. Norton, *J. Material Sci. Lett.* **18**, 349 (1999).
15. D. N. McIlroy, D. Zhang, R. M. Cohen, J. Wharton, Y. Geng, M. Grant Norton, G. De Stasió, B. Gilbert, L. Perfetti, J. H. Streiff, B. Broocks, and J. L. McHale, *Phys. Rev. B* **60**, 4874 (1999).
16. D. Zhou and S. Seraphin, *Chem. Phys. Lett.* **222**, 232 (1994).

17. A. M. Morales and C. M. Lieber, *Science* **279**, 208 (1998).
18. R.S. Wagner and W.C. Ellis, *Appl. Phys. Lett.* **4**, 89 (1964).
19. Y. H. Tang, Y. F. Zhang, N. Wang, C. S. Lee, X. D. Han, I. Bello, and S. T. Lee, *J. Appl. Phys.* 85,7981 (1999).
20. H. Y. Peng, N. Wang, W. S. Shi, Y. F. Zhang, C. S. Lee, and S. T. Lee, *J. Appl. Phys.* **89**, 727 (2001).
21 S Motojima, S. Ueno, T. Hattori, and K. Goto, *Appl. Phys. Lett.* **54**, 1001 (1989).
22. S. Motojima, Y. Itoh, S. Asakura and H. Iwanaga, *J. Mater. Sci.* **30**, 5049 (1995).
23. D. N. McIlroy, D. Zhang, Y. Kranov, and M. Grant Norton, *Appl. Phys. Lett.* **79**, 1540 (2001).
24. S. Amelinckx, X. B. Zhang, D. Bernaerts, X. F. Zhang, V. Ivanov, and J. B. Nagy, *Science* **265**, 635 (1994).
25. S. H. Irons, N. I. Nemchuk, H. W. Rohrs, T. Kowalewski, B. O. Faircloth, R. R. Krchnavek, and R. S. Ruoff, *Electrochem. Soc. Proc.* **Vol. 97-14**, 875 (1997).
26. H.-F. Zhang, C-M. Wang, and L.S. Wang, *Nano Lett.* **2**, 941 (2002).
27. R. S. Wagner, *Whisker Technology* (Wiley Interscience, New York, 1970), p. 257; p.109.

Mat. Res. Soc. Symp. Proc. Vol. 739 © 2003 Materials Research Society

Graphyne nanotubes: New Families of Carbon Nanotubes

Vitor R. Coluci[1,2], Scheila F. Braga[1], Sergio B. Legoas[1], Douglas S. Galvão[1] and Ray H. Baughman[2]
[1]Instituto de Física, Universidade Estadual de Campinas, 13083-970,Campinas, SP,Brazil
[2]NanoTech Institute and Department of Chemistry, University of Texas at Dallas, 830688, Richardson, Texas

ABSTRACT

Fundamentally new families of carbon single walled nanotubes are proposed. These nanotubes, called graphynes, result from the elongation of covalent interconnections of graphite-based nanotubes by the introduction of *yne* groups. Similarly to ordinary nanotubes, armchair, zig-zag, and chiral graphyne nanotubes are possible. We present here results for the electronic properties of graphyne based tubes obtained from tight-binding and *ab initio* density functional methods.

INTRODUCTION

The early report of carbon nanotubes (CNTs) by Iijima [1] generated an enormous amount of research activity. New and exciting phenomena have been observed [2], from field emission to thermal conductivity higher than diamond [3-6]. Depending upon structure, the nanotubes are either metallic or insulating, which is a feature intensively investigated and exploited in prototype devices [2].

Alternative nanotube structures containing heteroatoms (N, B, etc.), as well as various carbon free nanofibers, have been recently synthesized [2]. While previous works have focused on graphitic nanotubes, we believe that other types of pure carbon nanotubes are feasible using different accessible hybridization states of carbon. One possibility that has been overlooked in the literature is to use graphyne sheets as structural motif for carbon nanotubes. The γ-graphyne [Fig. 1(c)] is the lowest energy member of a family of carbon phases consisting of planar molecular sheets containing only *sp* and sp^2 carbon atoms. It is an allotropic form of carbon proposed by Baughman, Eckhardt, and Kertesz [7] in 1987, and has recently become the focus of new investigations [8, 9]. The presence of acetylene groups in these structures introduces a rich variety of optical and electronic properties quite different that from ordinary carbon nanotubes [10].

CNTs can be considered as formed by rolling up graphite sheets [2,11]. In the same way we can imagine graphyne nanotubes (GNTs) as formed by rolling up graphyne sheets to form seamless cylinders (Figs. 1 and 2). Preserving the *(n,m)* nomenclature, we defined the chiral vector $\mathbf{C_h}$ as $\mathbf{C_h} = n\mathbf{a_1} + m\mathbf{a_2} = (n,m)$. Zig-zag and armchair tubes were then generated from the vectors $(n,0)$ and (n,m), respectively.

As there are many members in the graphyne family [7] new families of pure carbon nanotubes can be generated with diverse electronic and structural characteristics. Because of space constraints, we describe here in details only the results for two families of graphynes nanotubes, the α-graphynes (α-GNTs) and γ-graphynes (γ-GNTs) [Fig. 1 and Fig.2]. This choice was based on the fact that α-graphyne is the graphyne most analogous to graphene and the one with the

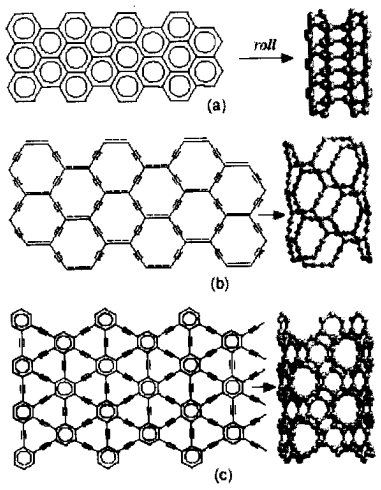

Figure 1 – The structural relationships between carbon sheets and single wall carbon nanotubes for sheets of (a) graphene (a graphite sheet), (b) α-graphyne, and (c) γ-graphyne. Depending upon the axis used for rolling the carbon sheet, the nanotube is armchair (a and b, right), zig-zag (c, right), or chiral. See text for discussions.

smallest number of carbon atoms in the unit cell (eight). γ-graphyne is the lowest energy member of the graphyne family being an important target for synthesis.

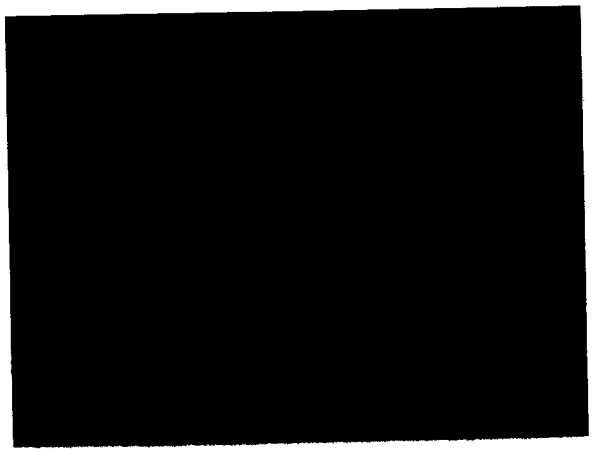

Figure 2 – Three dimensional view of (a) conventional carbon nanotube (CNT); (b) α-GNT; and; (c) γ-GNT (Fig. 1). The increment in nanotube sidewall porosity goes from CNT to γ-GNT and α-GNT. The same van der Waals radius values were used for all structures.

METHODOLOGY AND DISCUSSION

The graphynes structures investigated in this paper present a hexagonal unit cell (Fig. 3) and the same space group of graphene (*p6m*), which facilitates the comparison between GNTs and CNTs. The α- and γ-graphyne sheet structures were initially geometric optimized in the framework of *ab initio* density functional theory (DFT) using the SIESTA code [12]. DFT calculations were carried out in the generalized gradient approximation (GGA) with Perdew-Burke-Ernzerhof exchange-correlation functional [13]. The core electrons were described by norm-conserving pseudopotentials in its fully nonlocal (Kleinman-Bylander) form and a basis set of a linear combination of numeric atomic orbitals was used. Double zeta basis with polarization orbitals was used with core radii r_c of 2.2 and 2.6 Å for 2s and 2p basis orbitals, respectively. The Siesta optimizations were carried out on IBM Power3 375 machines, demanding dozens of hours of CPU time computing. Alternatively to DFT-Siesta, we have also used other DFT package like as DMol3 [14], in order to compare the geometric optimized structures. The results are quite similar.

The obtained DFT optimized geometry to α-graphyne sheet showed a perfect hexagon (similar to graphene) following the bonds length distribution on each side: 1.400, 1.244, 1.400 Å, with the corresponding lattice parameter being $a=4.04\sqrt{3}$.

Considering these optimized data, two approaches were chosen to determine the band structure of the sheets: tight-binding (TB) and DFT calculations.

Figure 4 shows the band structure for graphene and α-graphyne from DFT calculations. The structures present some common electronic features as zero gap values and same k-band crossing points. We can then predict that α-GNTs (generated from α-graphynes) and CNTs (generated from graphenes) will exhibit similar electronic behaviors.

In order to investigate the α-GNTs properties, we considered the band structure to α-graphyne sheets determined by the TB calculations. These calculations followed the Saito et al. [15] and Wallace [16] methodology, where each carbon atom is described by one $2p_z$ orbital with first-neighbors interactions. The molecular orbital energy and hopping integral values were calculated

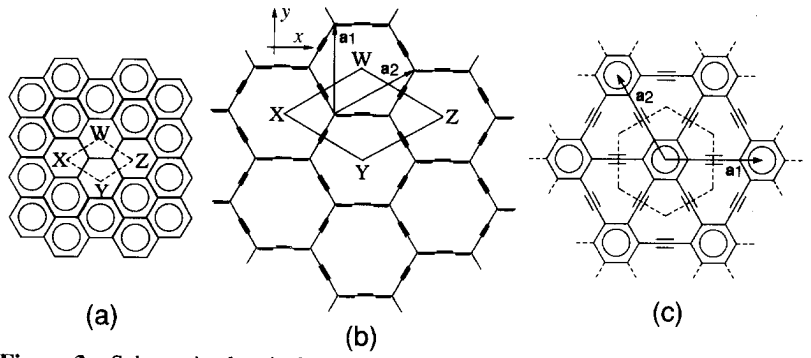

Figure 3 – Schematic chemical structure and unit cell representation for:
(a) Graphene
(b) α-graphyne (lattice vectors given by $\mathbf{a_1} = a\mathbf{y}$ and $\mathbf{a_2} = 0.5\ a\ (\sqrt{3}\mathbf{x} + \mathbf{y})$)
(c) γ-graphynes sheets (lattice vectors given by $\mathbf{a_1} = a\mathbf{x}$ and $\mathbf{a_2} = 0.5\ a\ (-\mathbf{x} + \sqrt{3}\mathbf{y})$)

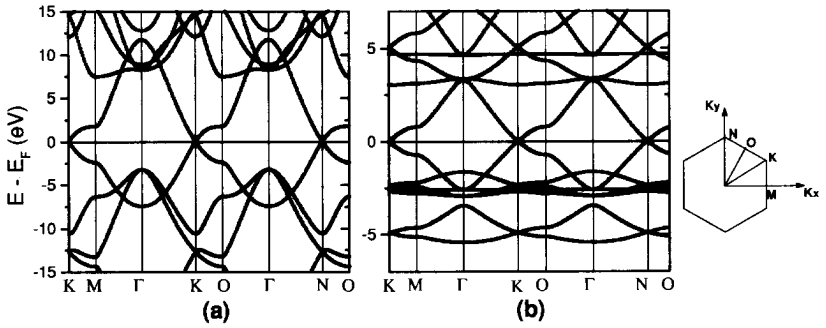

Figure 4 – Band structure of (a) graphene and (b) α-graphyne sheet obtained from DFT calculations. The Brillouin zone is also shown. E_F refers to the Fermi energy.

in the Extended Hückel framework [17], using the parameterization proposed by Clementi and Raimondi [18]. Although the TB approach is quite simple, it has reliably predicted the main electronic features for graphyne sheets when compared to DFT-SIESTA calculations and has the great advantage that the geometrical transformation of flat sheets into cylinders (tubes) can be easily simulated using the 'slicing' process [2]. It consists in obtaining the tubes band structure considering constraints applied to that predicted for their planar sheets. This approach is not feasible using DFT methods.

Similarly to CNTs, all armchair α-GNTs present metallic behavior and zig-zag ones are metallic when *n* is multiple of three, otherwise they are semiconductors.

This behavior can be seen in Fig. 5 where the expected gaps, from TB calculations using DFT optimized geometries, decrease as a function of α-GNT diameter. A bandgap oscillatory behavior with increasing values of n is also clear.

In order to fully investigate the rich diversity of these new proposed nanotubes new studies are being carried out for other members of the graphyne family and to charged graphynes. Preliminary calculations indicate that to some graphyne sheets a shift in the crossing band point could occur, introducing a behavior to the corresponding GNTs completely new, with fractional rules defining the zig-zag electronic properties.

Following the same procedure applied to α-graphyne, the γ-graphyne sheet was structurally optimized and its band structure was obtained from DFT and TB calculations.

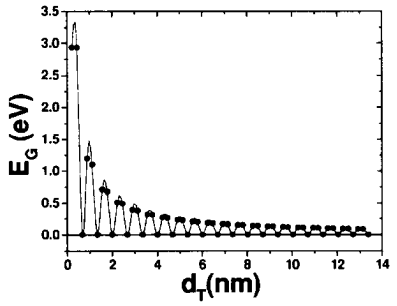

Figure 5 – Dependence of gap energy (E_G) for zig-zag α-GNT as a function of the tube diameter (d_T).

Following the same procedure applied to α-graphyne, the γ-graphyne sheet was structurally optimized and its band structure was obtained from DFT and TB calculations.

In Fig. 6 we show that the γ-graphyne DFT band structure presents a semiconductor gap of 0.42 (eV) occurring at the M point in the first Brillouin zone. The γ-GNTs, obtained by the 'slice' technique, will consequently exhibit semiconductor features for all tube diameters, a quite differentbehavior of the metal/semiconductor aspects observed in CNTs and α-GNTs.

The high porosity of all the graphyne-based nanotubes is also an interesting aspect, since this porosity would enable unprecedented shell doping, as well as rapid materials transport through the nanotube sidewalls, which could be important for materials storage and electrochemical charging process.

The stability of forms of graphyne and methods of synthesis are key remaining issues. The heat of formation of α-graphyne is so high (about 1 eV / carbon above graphyne) that it would be extremely difficult to synthesize. In fact, it might even decompose explosively to a lower energy form of carbon. Graphynes and related GNTs are more attractive synthetic targets since they have both lower energy and much higher expected stability than does α-graphyne. γ-graphyne is predicted to be about 0.5 eV / C lower in energy than α-graphyne.

Pioneering synthetic efforts in different laboratories have already produced large fragments of graphyne sheets [19-21]. Hence there are reasons to believe that the synthesis of large sheets of graphyne may be soon achieved.

CONCLUSION

In summary, we are proposing new families of single walled carbon nanotubes based on graphyne motifs. These structures show a rich variation in electronic properties. As for usual carbon nanotubes, these new tubes can be armchair, zig-zag or chiral. Besides new electronic and mechanical properties, due to the presence of C-C triple bonds, graphynes could be also promising materials for third-order nonlinear optical applications with high hyperpolarizability and good transparency [22], similarly to the recently observed for structurally related dendrimeric supermolecules [23]. Reflecting interest in these unusual properties, we are now trying to make GNTs, so that the fascinating predicted properties can be experimentally investigated.

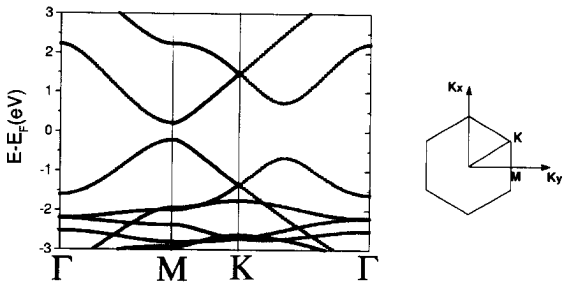

Figure 6 – Band structure predicted for a sheet of γ-graphyne using *ab initio* density functional calculations.

ACKNOWLEDGEMENTS

The authors wish to thank the Brazilian agencies (CNPq, FINEP, FAPESP, and CAPES) and the Robert. A. Welch Foundation for financial support and CENAPAD-SP for computational assistance.

REFERENCES

1. S. Iijima, *Nature* (London) **354**, 56 (1991).
2. S. B. Sinnott and R. Andrews, *Crit. Rev. Sol. St. Mat. Sci.* **26**,145 (2001), and references therein.
3. A. G. Rinzler *et al.*, *Science* **269**, 1550 (1995).
4. S. J. Tans *et al.*, *Nature* **386**, 474 (1997).
5. M. Kociak *et al.*, *Phys. Rev. Lett.* **86**, 2416 (2001).
6. P. Kim, L. Shi, A. Majumdar, and P. L. McEuen, *Phys. Rev. Lett.* **87**, 215502 (2001).
7. R. H. Baughman, H. Eckhardt, and M. Kertesz, *J. Chem. Phys.* **87**, 6687 (1987).
8. N. Narita, S. Nagai, S. Suzuki, and K. Nakao, *Phys. Rev. B* **58**, 11009 (1998).
9. N. Narita, S. Nagai, S. Suzuki, and K. Nakao, *Phys. Rev. B* **62**, 11146 (2000).
10. H. W. Kroto and D. R. M. Walton, in "The Fullerenes, New Horizons for the Chemistry, Physics and Astrophysics of Carbon", ed. H. W. Kroto and D. R. M. Walton (Cambridge University Press, 1993), pp. 103-112.
11. N. Hamada, S.-I. Sawada and A. Oshiyama, *Phys. Rev. Lett.* **68**, 1579 (1992).
12. P. Ordejón, E. Artacho, and J. M. Soler, *Phys. Rev. B* **53**, R10441 (1996). For more information about the Siesta package, access the Web page: http://www.uam.es/siesta.
13. J. P. Perdew, K. Burke, and M. Ernzerhof, *Phys. Rev. Lett.***77**, 3865 (1996).
14. B. Delley, J. Chem. Phys. **92**, 508 (1990); **113**, 7756 (2000). DMol3 is available from Accelrys, Inc. as part of the Cerius2 program suite. http://www.accelrys.com.
15. R. Saito, M. Fujita, G. Dresselhaus, and M. S. Dresselhaus, *Phys. Rev. B* **46**, 1804 (1992).
16. P. R. Wallace, *Phys. Rev.* **71**, 622 (1947).
17. R. Hoffman, *J. Chem. Phys.* **39**, 1397 (1963).
18. E. Clementi and D. L. Raimondi, *J. Chem. Phys.* **38**, 2686 (1963).
19. M. Sonoda et. al., *Org. Lett.* **3**, 2419 (2001).
20. M. Srinivasan et. al., *Org. Lett.* **2**, 3849 (2000).
21. W. Brad. Wan and M. M. Haley, *J. Org. Chem.* **66**, 3893 (2001)
22. Y. Zhou and S. Feng , *Sol. St. Commun.* **122**, 307 (2002).
23. D. Rana and G. Gangopadhyay, *Chem. Phy. Lett.* **334**, 314 (2001).

Mat. Res. Soc. Symp. Proc. Vol. 739 © 2003 Materials Research Society H5.7

Field Emission Properties of BN/C and BN@C Hybrid Nanotubes

Vincent Meunier[1,2], Marco Buongiorno Nardelli[1,2], William Shelton[1], Christopher Roland[2], Jerry Bernholc[1,2], and Thomas Zacharia[3].

[1] Center for Computational Sciences and Computer Science and Mathematics Division, Oak Ridge National Laboratory, Oak Ridge, TN
[2] Department of Physics, North Carolina State University, Raleigh, NC
[3] Computing and Computational Sciences Directorate, Oak Ridge National Laboratory, Oak Ridge, TN

ABSTRACT

Our simulations predict that boron-nitride (BN) doping in carbon nanotubes can greatly improve the field emission properties of these systems. The intrinsic electric field associated with the polarity of the B-N bond enhances the emitted current density through a reduction of the work function at the tip. Using a combination of real-space and plane-wave *ab initio* methods, we show that this effect is present in both coaxial (BN@C) and linear (BN/C) nanotubular assemblies. While in the coaxial geometry the improvement amounts to a factor of five, the current density is predicted to increase by up to two orders of magnitude in BN/C superlattices.

INTRODUCTION

One decade after their discovery [1], it has been shown that carbon nanotubes possess outstanding potential for their mechanical and electrical properties [2]. The advent of carbon nanotubes, together with recent progress in nanomaterials design and processing, has led to a quest for other novel graphene-based materials with technologically desirable properties. The closely-related boron nitride (BN) nanotubes and mixed BN-C systems [3, 4, 5, 6, 7, 8], which are now produced in macroscopic quantities, have electronic properties that are complementary to pure carbon nanotubes and could therefore be useful in a variety of novel electronic devices. For instance, an early theoretical study predicted that BN/C junctions may well be a practical way to realize stable, nanoscale heterojunctions [9].

In this paper, we investigate BN/C heterojunctions and BN@C coaxial systems using large-scale *ab initio* simulations [10]. Our calculations show that the polarity of the B-N bond in BN/C heterostructures and related coaxial BN@C systems do dramatically enhance field emission properties, and lead to attractive electronic devices. Although carbon nanotubes are already considered to be good emitters, these desirable properties may be further enhanced by making use of the electronic properties of BN-doped carbon systems. The idea here is to make use of the dipole field as means to *reduce* the work function at the tips, thereby enhancing the extraction of electrons from the system.

The orderly introduction of BN in pure carbon nanotubes may be obtained with two different techniques: either by substituting one CC pair by one BN pair in the hexagonal lattice and therefore mixing the C and BN phases (Fig. 1a), or by creating a system that presents two coaxial homogeneous phases of C and BN (Fig. 1b).

The synthesis of pure BN nanotubes through a substitution reaction from a pure C nanotube offers a potentially new route for the design of BN/C heterostructures [11]. The method

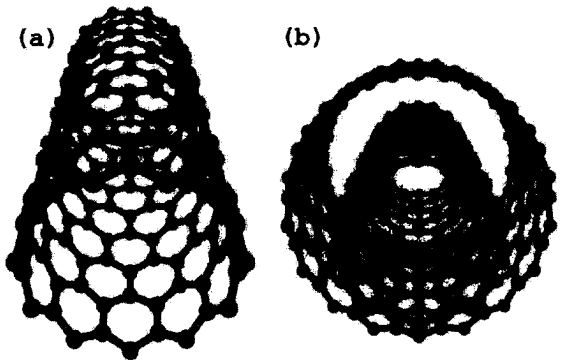

Figure 1: Prototypes of BN-C hybrids: (a) a BN/C heterojunction based on the (11,0) nanotube and (b) a $C_{(9,0)}@BN_{(17,0)}$ biwalled system.

involves three basic steps: (1) the coverage of portions of a carbon nanotube by a chemical mask (2) the $C_2 \rightarrow$B-C substitution reaction of the unmasked system and, (3) the removal of the chemical mask, leaving the untouched carbon chemically bounded to BN. This idealized scheme may be subject to practical difficulties. The most significant is undoubtedly the diffusion of the reactants inside, or through the mask. It is worth noting that a similar idea has already been successfully applied to the design of p-n junctions in the K-doping of a carbon nanotube partially masked by PMMA [12]. We also note that earlier attempts at synthesizing BN-C tubular systems from a B-C-N powder have not led to the formation of heterostructures as depicted in Fig. 1a, but rather to biwalled systems in which the BN and C materials are segregated into individual, nested shells, as shown in Fig. 1b [5]. Nevertheless, all of these systems represent potentially interesting structures for materials investigations.

$(BN/C)_n$ SUPERLATTICES and HETEROJUNCTIONS

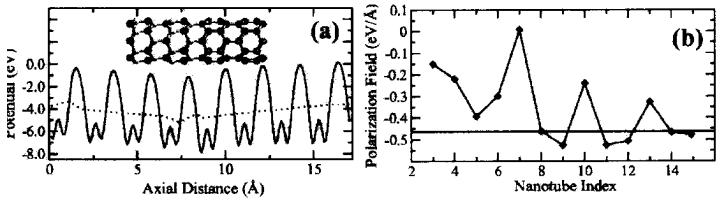

Figure 2: (a) Average electrostatic potential (full line) and macroscopic average (dotted line) along a BN/C (6, 0) superlattice (insert) and (b) macroscopic dipole field for zigzag $(l, 0)$ tubes as a function of the helicity index. The asymptotic value for planar BN/C in the zigzag direction is represented by the horizontal line.

The majority of BN/C nanotube superlattices are characterized by an axial dipolar electric field, which is a direct consequence of the polar nature of the B-N bond. In a periodic

superlattice of polar and non-polar materials (such as BN and C) any polarization field will manifest itself in the behavior of the total electrostatic potential of the system. In fact, the latter displays a typical sawtooth behavior that is the signature of the presence of the field superimposed onto the periodic crystalline potential [14]. For convenience, we have computed the planar average of the electrostatic potential along the nanotube axis, as shown in Fig. 2a. This average, which is over the directions perpendicular to the tube axis, displays strong oscillations due to the varying strength of the ionic potentials. To subtract out this effect, we have implemented the averaging procedure of Ref. [13], and thereby calculated the one-dimensional *macroscopic* average of the electrostatic potential of the system. The value of the dipole field is then obtained from the slope of the macroscopic average potential [14] and is shown in Fig. 2b.

From simple geometric considerations, it is clear the strongest effects will be observed in the $(l,0)$ zigzag nanotubes, since this geometry maximizes the dipole moment of the B-N bond. Hence, we have primarily concentrated on zigzag nanotubes, and the flat sheet as the limit for large diameter tubes. The corresponding electric fields are summarized in Fig. 2b. In contrast, the (l,l) armchair nanotubes are not expected to display any dipole field. This is because any individual nanotube ring must be charge neutral, so that no field is possible. Chiral nanotubes will have fields that are between the zigzag and armchair values and will depend on the individual terminations.

From Fig. 2b, it is clear that the magnitude of the macroscopic electric field for the various

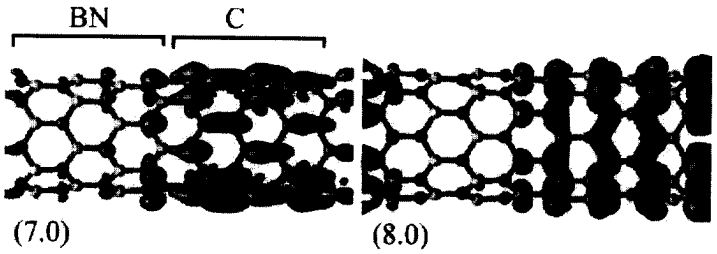

Figure 3: 3D plots of the valence state for (7,0) and (8,0) BN/C superlattices.

superlattices has strong oscillatory character. Nanotubes with helicity indices 7, 10,... $3n+1$ are characterized by a substantially smaller field. This effect originates from the fact that the carbon sections effectively screen the macroscopic dipole field with an efficiency that depends on the nanotube helicity. BN/C band offset calculations have shown that the valence state of the BN/C superlattices is always spatially localized in the carbon region [15]. This state plays an important role in determining the response to the macroscopic electric field induced by the BN section. For small diameter nanotubes the valence state displays either a longitudinal or a transverse symmetry as exemplified by the (7,0) and (8,0) tubes on Fig. 3 [16]. Specifically, for $(l = 3n+1, 0)$ nanotubes, such as the (7,0) tube, the valence state always assumes longitudinal character. The axial distribution of valence electrons therefore induces a *depolarization* field that is *opposite* to the one induced by the BN section. This field is very effective in small diameter nanotubes, so that for the (7,0) nanotube the screening is almost total and the observed macroscopic field is close to zero. For larger diameter nanotubes, the symmetry of the valence state gradually loses its peculiar axial or longitudinal character and

the macroscopic field asymptotically approaches the value found for a flat BN/C sheet in the "zigzag" direction.

Despite the screening by the valence electrons which are distributed over the carbon portion of the BN/C superlattices, a net electric field is built up along any zigzag structure. The existence of such a macroscopic field clearly influences the extraction of electrons from BN/C systems. Qualitatively, a good electron emitter is characterized by a large geometrical field enhancement factor β and a small work function ϕ. the latter is of course an intrinsic property of the emitter material. Quantitatively, the current at the emitter tip is calculated from the well-known Fowler-Nordheim relationship [17].

To assess the efficacy of BN/C systems as emitters, we have computed the field enhancement factor for tubes of length 15.62 Å in an applied field of 0.11 $V/$Å. As expected, the applied field is very well screened inside the system and a local field enhancement factor of ~ 2.1 is obtained for the different BN/C systems. Since the field enhancement factor increases *linearly* with the size of the nanotubes, large enhancement factors are clearly possible for long nanotubes [18].

To examine this effect quantitatively, we have built up a set of finite sized (6,0) zigzag structures using B, N, and C in various combinations. The work functions were then computed as the difference between the vacuum level and the Fermi energy of the system. The former was obtained by the previously discussed potential average procedure, while the latter was simply given by the highest occupied eigenstate of the system. In order to avoid any spurious effects arising from the periodic calculation, we have used the so-called *dipole correction* in a unit cell surrounded by a vacuum of at least 15 Å [19].

Turning to the heterostructures, we consider a finite NB/C (6,0) system consisting of four alternating N and B layers followed by 8 C layers, giving a total of 96 atoms. Due to the intrinsic electric field experienced by the electron, the work function is reduced to 5.04 eV at the C tip and increased to 7.52 eV at the N tip. The same trend is observed for the BN/C system, where the work function at the B tip is equal to 5.00 eV while at the C tip it equals 6.45 eV. The work function is reduced by 1.40 eV, a significant decrease as compared to the pure carbon system. This large difference leads to significant macroscopic effects. According to the Fowler-Nordheim relationship, the logarithm of the current density (J) depends upon the work function ϕ as $\ln J \sim -\phi^{3/2}$. It follows that the insertion of BN segments in C nanotubes will increase the current density by up *to two orders in magnitude* as compared to pure carbon nanotube systems.

BN@C BIWALLED HYBRIDS

It is clear from the previous discussion that the presence of BN atoms induces a remarkable improvement of the field emission properties at the carbon tip in a NB/C heterojunction. However, the use of such devices as *performant* field emitters is limited by the issues surrounding their synthesis. From a practical point of view, the related nested BN@C or C@BN systems offer a more direct way to take advantage of the polarity associated with the BN phase.

To assess the field emission properties of BN@C devices, we have performed calculations of the field enhancement factor and of the work function. In particular, we investigated the effect of the presence of a finite BN nanotube shell surrounding a C nanotube–the C(5, 5)@BN(18, 0), as shown on Fig. 4. As expected from classical electrostatics. the field enhancement factor is not modified by the presence of the BN shell, since the insulating BN layer does not disturb the screening properties of the underlying C tube. On the contrary, the dipole field induced

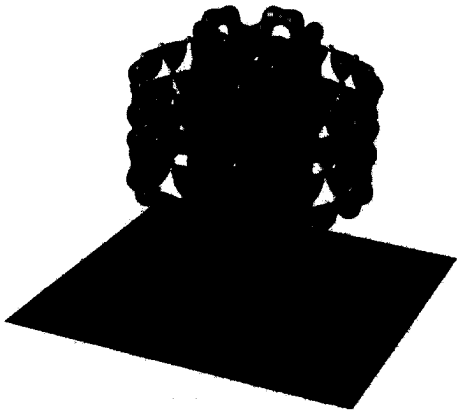

Figure 4: Electron density 5 Å from the tip of a C(5, 5)@BN(18, 0) biwalled system.

by the BN shell produces a net decrease of the work function ($\sim$ 0.5 eV) and a subsequent increase of the emitted current (up to a factor of 5), as compared to the current emitted by a bare (5,5) carbon nanotube.

SUMMARY

Our simulations predict that ordered BN-C systems are characterized by the presence of a dipolar electric field, whose value is highly sensitive to the helicity of the underlying nanotubes. This macroscopic field can reduce the work function of the C nanotube tips, thereby increasing the field emitting properties of carbon nanotube tips by up to two orders of magnitude for the linear BN/C nanotube and a factor of five for BN@C biwalled systems.

ACKNOWLEDGEMENTS

This research is sponsored in part by the Mathematical, Information and Computational Sciences Division, Office of Advanced Scientific Computing Reasearch of the U.S. D.O.E. under Contract No. DE-AC05-00OR22725 with UT-Battelle, LLC. J.B. was supported in part by DOE Grant No. DE-FG02-98ER45685. This work was supported in part by NASA, and ONR. We also thank the CCS, DOD and NC Supercomputing Centers for extensive computer support.

REFERENCES

1. S. Iijima, *Nature* (London) **354**, 56 (1991).

2. For a recent review of the electronic and structural properties of carbon nanotubes, see for example: J. Bernholc, D. Brenner, M. Buongiorno Nardelli, V. Meunier, and C. Roland, *Annu. Rev. Mater. Res.* (2002).

3. A. Rubio, J. L. Corkill, and M. L. Cohen, *Phys. Rev. B* **49**, 5081 (1994).

4. N. G. Chopra, R. J. Luyken, K. Cherrey, V. H. Crespi, M. L. Cohen, S. G. Louie, and A. Zettl, *Science* **269**, 966 (1995).

5. O. Stephan, P. M. Ajayan, C. Colliex, P. Redlich, J. M. Lambert, P. Bernier, and P. Lefin, *Science* **266**, 1683 (1994).

6. A. Loiseau, F. Willaime, N. Demoncy, G. Hug, and H. Pascard, *Phys. Rev. Lett.* **76**, 4737 (1996).

7. J. Cumings and A. Zettl, *Chem. Phys. Lett.* **316**, 211 (2000).

8. R. S. Lee, J. Gavillet, M. L. de la Chapelle, A. Loiseau, J.-L. Cochon, D. Pigache, and J. T. F. Willaime, *Phys. Rev. B* **64**, 121405 (2001).

9. See for example: X. Blase, J. C. Charlier, A. DeVita, and R. Car, *Appl. Phys. Lett.* **70**, 197 (1997).

10. The *ab initio* calculations were carried out via a combination of standard multigrid-based real-space [E.L. Briggs *et al*, *Phys. Rev. B* **52**, RC5471 (1995); *ibid* **54**, 14362 (1996)] and plane-wave methods [S. Baroni *et al*, http://www.pwscf.org]. We have employed the Perdew-Zunger parameterization [J. P. Perdew and A. Zunger, *Phys. Rev. B* **23**, 5048 (1981)] of the Ceperley-Alder [D. M. Ceperley and B. J. Alder, *Phys. Rev. Lett.* **45**, 566 (1980)] exchange-correlation energy and non-local norm-conserving pseudopotentials [N. Troullier and J. L. Martins, *Phys. Rev. B* **43**, 1993 (1991)]. An equivalent (real-space) or effective (plane-wave) energy cut-off of 60 Rydberg was chosen to ensure convergence. All calculations were carried on a massively parallel IBM POWER3 system at the North Carolina Supercomputing Center and a massively parallel IBM pseries POWER4 at the Center for Computional Sciences located at Oak Ridge National Laboratory. After a careful minimization of the atomic coordinates, the structural parameters and electronic band structures obtained were in perfect agreement with those of previous calculations [9].

11. W. Q. Han and Y. Bando and K. Kurashima and T. Sato, *Appl. Phys. Lett.* **73**, 3085 (1998).

12. V. Derycke, R. Martel, J. Appenzeller, Ph. Avouris, *Nano Lett.* **1**, 453 (2001).

13. A. Baldereschi, S. Baroni, and R. Resta, *Phys. Rev. Lett.* **61**, 734 (1988).

14. M. Posternak, A. Baldereschi, A. Catellani, and R. Resta, *Phys. Rev. Lett.* **64**, 1777 (1990).

15. V. Meunier, C. Roland, J. Bernholc, and M. Buongiono Nardelli, *Appl. Phys. Lett.* **81**, 47 (2002).

16. C. L. Kane and E. J. Mele, *Phys. Rev. B* **59**, R12759 (1999).

17. R. H. Fowler and L. W. Nordheim, *Proc. Roy. Soc. Lond.* **A119**, 173 (1928).

18. S. Han and J. Ihm, *Phys. Rev. B* **61**, 9986 (2000).

19. L. Bengtsson, *Phys. Rev. B* **59**, 12301 (1999).

Mat. Res. Soc. Symp. Proc. Vol. 739 © 2003 Materials Research Society

Simple Use of SiO_2 Film Thickness for the Control of Carbon Nano-Tube Diameter During Ferrocene Catalyzed CVD Growth

N. Chopra, P.D Kichambare, R. Andrews, B.J. Hinds

Dept. of Chemical and Materials Engineering, University of Kentucky
Center for Applied Energy Research, University of Kentucky
Lexington, KY 40506-0046 USA

ABSTRACT

Selective growth of carbon nano-tubes (CNT) on micron scale patterned substrates has been accomplished by taking advantage of the non-reactivity of ferrocene catalyst on H-terminated Si surfaces in a CVD process. Demonstrated here is that this phenomenon can be used to control the diameter of CNTs when sufficiently narrow lines of SiO_2 surrounded by H-terminated Si are used. Narrow lines of SiO_2 (12-60nm) are formed at the etched face of a $Si/SiO_2/Si$ multilayer structure. This allows the precisely controllable thickness of an SiO_2 film to determine an exposed SiO_2 line width. There is no need for e-beam lithography since film thickness determines nm-scale line dimensions. CNTs are then formed by CVD with a ferrocene/H_2/Ar mixture at 700°C. CNTs are observed to grow only on the exposed SiO_2 surface at the edge of the 'mesa' structure. CNT diameters of 13.2, 20.5, 34.2, 64.3nm are observed for SiO_2 film thickness of 12, 19, 35, and 65 nm. The larger distribution of CNT diameter with increased line width is consistent with wider SiO_2 linewidths not being able to affect smaller nucleation centers. These results are consistent with the use of self-assembly chemistry of iron catalyst onto nano-particles of catalyst support.

INTRODUCTION

Carbon nanotubes (CNT) have many potential applications in electronics [1], sensors[2], and nano electromechanical systems (NEMS).[3] Particularly interesting is that due to the long length of tubes, it is possible to use commercially prevalent micron scale lithography to result in nm-scale line features if one can selectively incorporate CNTs. Thus the development of a method to control CNT diameter and its placement becomes critical for applications. A particularly promising study has shown that it is possible to bridge the tops of photolithographically defined 'posts' with CNTs grown from nano-scale catalyst support particles.[4,5] Further refinements of the concept of growing CNTs between photolithographically defined pillars could become the basis of nm-scale wide wiring. There are a variety of growth techniques for CNT synthesis, but the CVD method offers the most commercially viable technique due to a large uniform reaction area and high mass flux flows.[6] CNT diameter is determined largely by the size of nm-scale catalyst particle.[7] These catalyst can be metal particles[8] or a coating of transition metal on catalyst support particles.[9,10] Catalytic nano-particles can be supplied during growth in a xylene and ferrocene based CVD process. This process has been used to grow CNTs at high densities with noteworthy vertical alignment.[7] The diameter of resultant CNTs is a complex system that involves the surface free energy of catalyst and substrate, surface migration, diffusion/silicide formation and ferrocene

decomposition rates. Under certain temperature, xylene and ferrocene feed rate it is possible to determine CNT diameter in the range of 30-100nm with a dispersion approximately 30%.[14] Importantly CNT growth with ferrocene catalyzed CVD process can be selective to substrate composition.[11,12,13,14] A hydrogen-terminated Si surface will not grow CNTs while a SiO_2 surface will in this xylene/ferrocene CVD process.[12] Because of the limitation of conventional lithography in the near-micron regime, it is not known if resultant CNT diameter could actually be determined by line width of an SiO_2 surface acting as a catalytic support.

EXPERIMENTAL DETAILS

The experimental procedure for controlled CNT growth from the exposed edge of a $Si/SiO_2/Si$ multilayer is outlined in Scheme 1. An important experimental subtlety is that the bottom a-Si layer is required, since the 'liftoff' process does not result in a perfect break at the substrate. A relatively large and uncontrolled area of SiO_2 would be exposed if only a Si/SiO_2 bilayer was used. Immediately prior to CNT growth, HF etching of the "post" structure on patterned substrate is required so as to remove any native oxide from Si exposed to atmosphere. HF etch time was approximately 5 seconds longer than necessary for the substrate to become hydrophobic. The time duration of HF etch is minimized to reduce undercutting of middle SiO_2 layer. Finally the CNTs were grown on samples by pyrolysis of xylene and ferrocene mixture under Ar/H_2 atmosphere in tubular furnace as described by Andrews *et al.*[7] Approximately 6.5 mol % of ferrocene (Aldrich) was dissolved in xylene (Fisher Scientific) and continuously fed into the reactor. The liquid feeding mixture was passed through a capillary tube and preheated to 175°C prior to its entry into the furnace. At this temperature, the liquid exiting the capillary tube was immediately volatilized and swept into the reaction zone of the furnace at 700°C by the flow of argon with 10 % hydrogen. Growth times were 30 minutes. After the reaction, the furnace was allowed to cool to room temperature in flowing argon. The microstructure of resultant CNT growth was characterized by SEM (Hitachi S900 field emission electron source with sub-nm resolution). A sub-nm thin film of Pd/Au was sputtered over the sample to reduce charging for SEM analysis. TEM analysis was performed with a JEOL JEM-2000FX. TEM sample was prepared from the ultrasonic removal of CNTs from the substrate and 'floated' onto an a-C coated TEM grid.

RESULTS AND DISCUSSION

Figure 1 shows resulting CNT growth from the edges of a $Si/SiO_2/Si$ multilayer pattern. As expected, there is growth from pattern edges where there is exposed SiO_2 and no growth on surface hydrogen terminated Si (Si-H). Although, in a few samples small amounts of CNTs are seen to grow on Si-H surface, that is likely a result of slight HF underetch and native oxide formation during sample transfer. TEM images (not shown) of dispersed CNTs taken from the same sample shown in Figure 1A, show multiwalled CNTs with diameter of 12nm, consistent with SEM observation. The catalyst particle is of the same diameter as the CNT, as had been observed with previous TEM studies of this CVD growth process.[11,14] The catalyst particle appears to be at the tip of the CNT, as there is an encapsulating layer of a-C. Table I shows the resultant CNT diameter as a function of SiO_2 layer thickness from SEM observations.

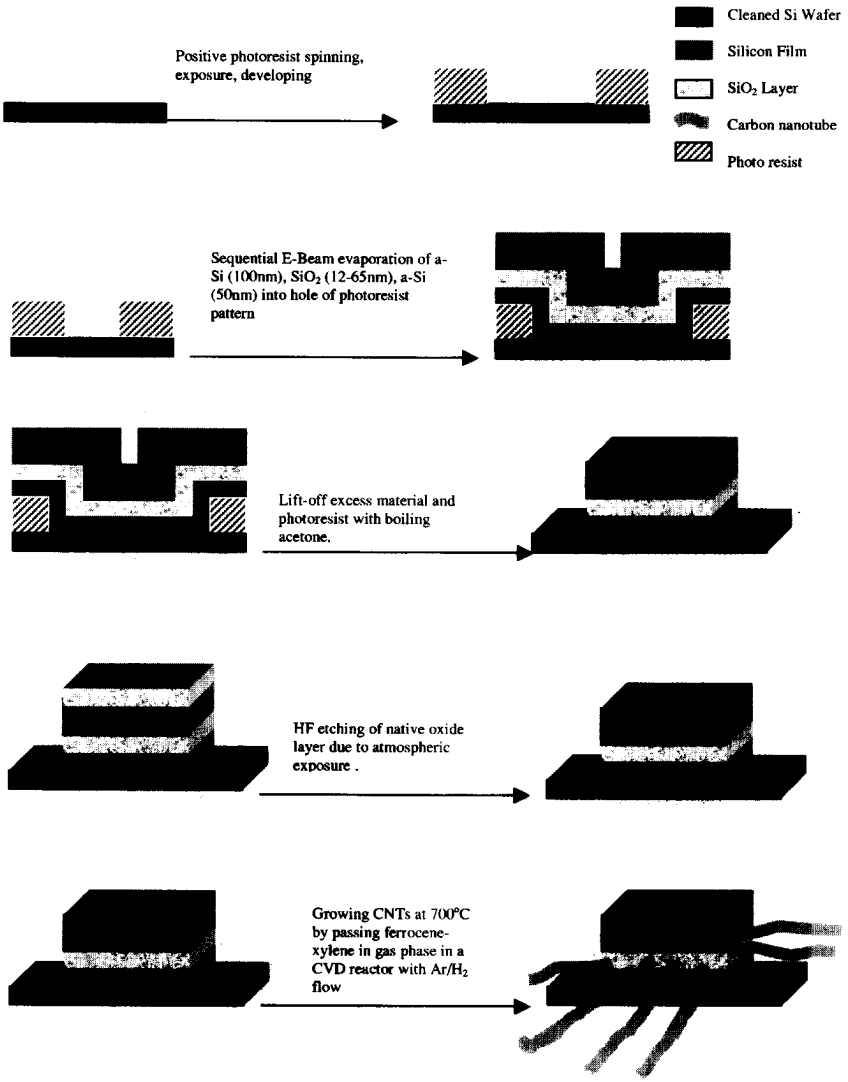

Schematic 1. Experimental procedure for controlled CNT growth from the exposed edge of a $Si/SiO_2/Si$ multilayer structure

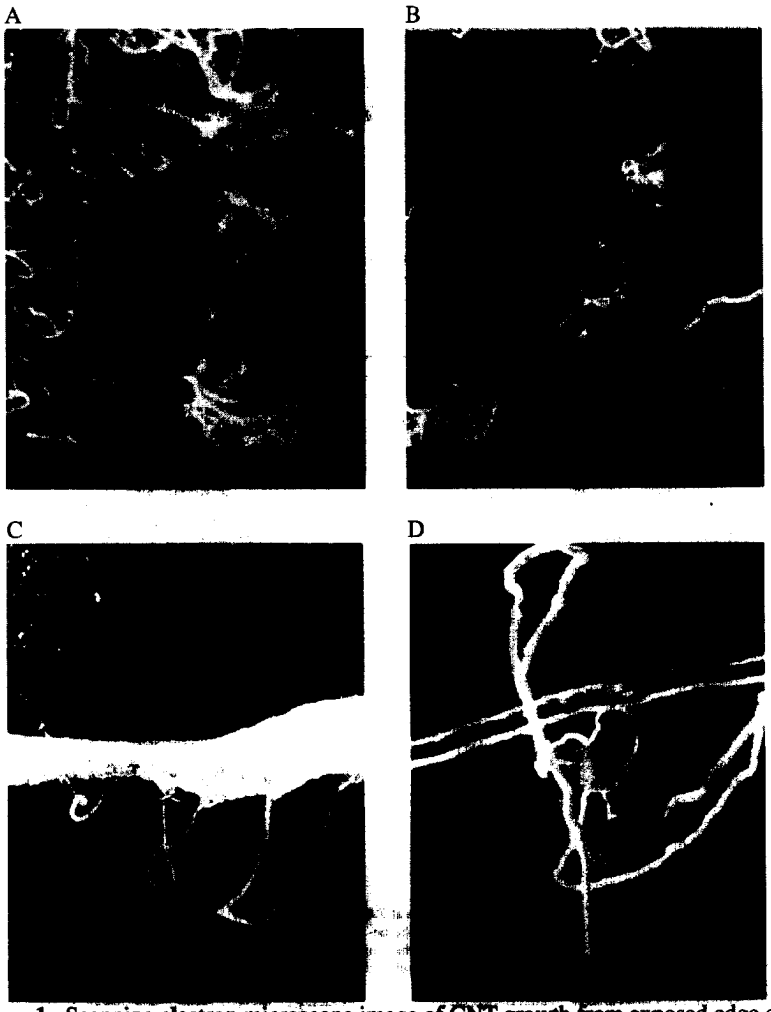

Figure 1. Scanning electron microscope image of CNT growth from exposed edge of a $Si/SiO_2/Si$ multilayer structure. SiO_2 interlayer film thickness A) 12nm, B) 17 nm, C) 19nm, D) 65nm. In A-B, tilt angle is 40°. For statistical analysis, the arrow in 1A shows the step edge (top to bottom of image) from which every visible CNTs diameter are measure directly at their root. Crossed mark (X) shows artifacts that are eliminated from statistical analysis due to SEM charging, defects, or intertwined CNTs.

Remarkable control of CNT diameter is achieved by conventional film growth techniques with a strong correlation of observed diameter to SiO_2 film thickness. This is presumably a result of the selective chemical decomposition of ferrocene only on the oxide surface. There is variability in

SiO_2 thickness from the e-beam evaporation process, that can be responsible for the observed diameter variation of near ±3nm. Si thermal oxidation would result in better thickness control, but high temperatures are not compatible with current liftoff process. Other factors may include surface migration and nucleation of Fe particles only on the oxide, however the exact mechanism is not known. Table II shows observed CNT diameter grown from nanoparticles of SiO_2 that are coated with a monolayer of Aminopropyltriethoxysilane functionalization (APTES). These particles readily coordinate $FeCl_3$ from solution and act as a catalyst support during CVD growth of CNTs without ferrocene present. The correlation of observed diameters suggests that size of catalyst support determines CNT diameter. Thus the decomposition/migration of Fe from H-Si regions is not the dominant mechanism in the CNT growth from the $Si/SiO_2/Si$ multilayer structure.

The use of an exposed edge of a multilayer structure is a highly scalable process that works well with the stable Si/SiO_2 system. Future work is to find lower limits of CNT diameter using thermal oxides for finer control by SiO_2 layer thickness. Finer control of multilayer edges would be expected by ion milling. In principle, the diameter of CNTs can be reduced to the 1-2 nm thickness of oxide film, however the minimum Fe nanoparticle size from ferrocene decomposition conditions needs to be investigated.

Table I. Observed CNT diameter as measured by SEM on the edge of multilayer post structure as a function of SiO_2 layer thickness.

SiO_2 layer thickness (nm)	Average CNT diameter (nm)	Std. Deviation of CNT diameter (nm)
12	**13.4**	**3.7**
17	**19.0**	**3.0**
19	**20.5**	**1.4**
35	**34.2**	**3.9**
65	**64.3**	**6.3**

Table II. Comparison of CNT diameter to nano-particles of SiO_2 with SAM of APTES (3-Aminopropyltriethoxysilane) coordinated with $FeCl_3$. No ferrocene is supplied during CNT growth.

Sample	Average diameter (nm)	Mean median Diameter (nm)	Average Standard Deviation (nm)
Nanoparticles on wafer attached With SiO_2, APTES*, and Iron	49.16	40.00	23.78
Carbon nanotubes Grown on wafer attached with SiO_2, APTES*, and Iron.	43.41	43.64	5.86

CONCLUSIONS

By using the exposed edges of a thin film multilayer structure with 10-60 nm thick SiO_2 layer, we demonstrate that CNT diameter can be controlled in a CVD growth process. Importantly this CNT diameter is determined by thin film thickness of SiO_2 that is easily controlled by conventional semiconductor processing. These CNTs can be used directly in wiring between 'post' structures or 'harvested' into solution for later self-assembly processes. This technique can be readily applied to other selective growth systems or self-assembly chemistry as a general tool in nano-fabrication. The authors thank the NSF-MERSEC Advanced Carbon Materials Center (DMR-9809686) as well as sponsorship by the Air Force Research Laboratory (DEPSCoR program) under agreement number F49620-02-1-0225.

REFERENCES

1. A. Bachtold, P. Hadley T. Nakanishi, and C. Dekker, *Science*, **294**, 1317 (2001)
2. H. Chang,; J. D. Lee, S. M. Lee, and Y. H. Lee, *Appl. Phys. Lett.*, **79**, 3863 (2001)
3. P. A. Williams, S. J. Papadakis, M. R. Falvo, A. M. Patel, M. Sinclair, A. Seeger, A. Helser, R. M. Taylor, S. Washburn, and R. Superfine, *Appl. Phys. Lett.*, **80**, 2574 (2002)
4. A. M. Cassell, N. R. Franklin, T. W. Tombler, E. M. Chan, J. Han, and H. J. Dai, *J. Am. Chem. Soc.* **121,** 7975-7976 (1999).
5. N. R. Franklin and H. J. Dai, *Adv. Mater.* **12,** 890-894 (2000).
6. R. Andrews, D. Jacques, A. M. Rao, F. Derbyshire, D. Qian, X. Fan, E. C. Dickey, and J. Chen, *Chem. Phys. Lett.* **303,** 467-474 (1999).
7. S. B. Sinnott, R. Andrews, D. Qian, A. M. Rao, Z. Mao, E. C. Dickey, and F. Derbyshire, *Chem. Phys. Lett.* **315,** 25-30 (1999).
8. G. W. Ho, A. T. S. Wee, J. Lin, and W. C. Tjiu, *Thin Solid Films* **388,** 73-77 (2001).
9. K. Hernadi, A. Fonseca, J. B. Nagy, D. Bernaerts, A. Fudala, and A. A. Lucas, *Zeolites* **17,** 416-423 (1996).
10. K. Hernadi, A. Fonseca, P. Piedigrosso, M. Delvaux, J. B. Nagy, D. Bernaerts, and J. Riga, *Catal. Lett.* **48,** 229-238 (1997).
11. B. Q. Wei, Z. J. Zhang, P. M. Ajayan, and G. Ramanath, *Carbon* **40,** 47-51 (2002).
12. B. Q. Wei, R. Vajtai, Y. Jung, J. Ward, R. Zhang, G. Ramanath, and P. M. Ajayan, *Nature* **416,** 495-496 (2002).
13. D. Qian Ph.D. Dissertation, University of Kentucky (2001)
14. A. M. Rao, D. Jacques, R. C. Haddon, W. Zhu, C. Bower, and S. Jin, *Appl. Phys. Lett.*, **76**, 3813 (2000).

Mat. Res. Soc. Symp. Proc. Vol. 739 © 2003 Materials Research Society

FIB-assisted Pt Deposition for Carbon Nanotube Integration and 3-D Nanoengineering

K. Dovidenko, J. Rullan, R. Moore, K.A. Dunn, R.E. Geer, F. Heuchling
School of NanoSciences and NanoEngineering, UAlbany Institute for Materials, The University at Albany-SUNY
251 Fuller Rd., Albany, New York 12203

ABSTRACT

In this study, the Focused Ion Beam (FIB) instrument has been used for carbon nanotubes integration and nanoegineering studies. Results of thorough investigation (electrical, structural and chemical) of ultra-thin Pt contact lines and pads fabricated by the FIB, along with evaluation of nanomodification of the carbon nanotubes under the Ga^+ ion beam and during Pt deposition are presented. The initial stages of FIB-assisted Pt deposition on multi-wall nanotubes are studied by transmission electron microscopy (TEM). The FIB parameters are optimized to provide non-destructive imaging and controllable Pt deposition with minimal damage on the nanotubes. We have demonstrated effective use of FIB-fabricated Pt pads as means of attaching the nanotubes to the substrate for atomic force and ultrasonic force microscopy studies.

INTRODUCTION

Carbon nanotubes (CNTs) [1] are potential candidates for a variety of new types of nanoscale devices and some interconnect applications. High mechanical strength combined with good heat conductance and a range of attractive electrical properties make CNTs particularly interesting 'building blocks' for rapidly emerging nanoelectronics and nanoengineering. Successful integration of the nanotubes with metal aiming for CNT application as an active part of a device or as a nano-wire requires understanding of the effects of the metal fabrication process on the structure and chemistry of the nanotube, and on the stability of the CNT-metal interfaces. A Focused Ion Beam (FIB) microscope can be used to fabricate ultra-thin metal lines on carbon nanotubes to measure electrical properties or for integration and nanoegineering purposes. The structural modification produced by FIB is also often called FIB micromachining due to the microscopic scale of alterations. FIB-assisted metal deposition is an approach alternative to the e-beam lithographic contact fabrication, and has certain advantages and disadvantages. The main advantage is the ease of locating and contacting the desired nanotube at the desired locations. The main disadvantage is the difficulty to control the surface modification typically produced by 30 keV Ga^+ ion beam of FIB microscope. The quality of the interface between the CNT and the metal contact line is of high interest, as the 30 kV focused Ga ion beam of the FIB can produce sufficient surface modification to affect the future device performance. To date, no studies on effects of FIB Ga^+ ion beam on carbon nanotubes have been carried out.

The width of FIB-produced metal lines can be as small as 10-15 nm, while the length can reach tens of microns. The FIB employs highly-focused (down to 10 nm spot) 30keV Ga^+ ion beam scanned over the desired areas of the sample surface. The FIB microscope used in this study is equipped with gas-injection systems allowing introduction of Pt metalorganic precursor (methylcyclopentadienyl trimethyl platinum) during the ion beam scanning thus providing the well-controlled local ion-assisted deposition of the metal. Therefore, the Pt lines can be fabricated directly over the desired area of a CNT with the ~30 nm precision which is the

apparent advantage of the method. Estimation of the dose of Ga^+ ion exposure on the CNT is not quite straightforward during the Pt deposition. As the Pt layer grows, it makes a barrier for Ga^+ ions. The projected length of 30keV Ga^+ ions in carbon (graphite density was used in our calculations by TRIM [2]) is about 35 nm, and is much lower in FIB-fabricated contact line. Depending upon the density of the material deposited, the projected length of Ga^+ ions will be different too. So, it is important to evaluate the precise composition of the FIB-deposited metal lines and also estimate the Pt growth rate for the CNT implantation dose calculation. Another factor to consider is the possibility of sputtering of the material instead of depositing during the Pt line fabrication. It is well understood that the FIB-assisted deposition is a balance between the two competing processes: sputtering of the material under the scanning Ga^+ beam and material deposition from the decomposing metalorganic. Generally, when the ion beam current is below 350 pA, the deposition prevails over sputtering, while at higher currents the sputtering rate is higher than that of the deposition. However, no detailed study of the composition or the structure of the Pt lines deposited by FIB has been done so far.

In this study, we have carried out optimization of Pt deposition parameters to provide the non-destructive FIB imaging and controllable Pt deposition with minimal damage on a nanotube and also evaluated the effects of FIB-assisted Pt deposition on the multi-wall carbon nanotubes (MWNTs). Using these optimized parameters, we have fabricated the Pt contacts on multi-wall carbon nanotubes for transport measurements and to make Pt pads attaching MWNTs to the substrate for Atomic Force Microscopy (AFM) and Ultrasonic Force Microscopy (UFM) study.

EXPERIMENTAL

We have used the FEI FIB 200 microscope to fabricate the Pt contacts (down to 100 nm size) on multi-wall carbon nanotubes. Auger Electron Spectroscopy (PHI 600 spectrometer) was used to characterize the composition of the FIB-fabricated Pt lines. Resistance of the Pt lines deposited under different FIB conditions was measured via two-point-probe and four-point-probe methods. We have studied the effects of FIB-assisted Pt deposition on multi-wall nanotube structure by transmission electron microscopy (TEM). The study was carried out in Jeol 2010F field emission transmission electron microscope operated at 200kV, equipped with EDAX Energy Dispersive X-Ray spectrometer (EDX) and Gatan Image Filter. Successful electrical tests (four-point-probe method) and AFM/UFM studies using a Jeol Atomic Force Microscope have been carried out on these Pt/MWNT structures. For the TEM study, the multi-wall carbon nanotubes were dispersed from solution over the thin carbon film supported by a Cu grid (standard TEM holey carbon supporting grids). For Pt lines structural, chemical and electrical characterization, the patterned SiO_2/Si substrate with pre-fabricated Al pads (40x40 μm or 100x100 μm) were used. This setup is typically used for CNT transport measurements with the FIB-fabricated Pt contacts connecting a CNT and Al pads (MWNTs dispersed over the SiO_2 surface). The illustration of this setup is presented in Fig. 1, which demonstrates top-down view of a CNT connected with the Al pads via thin FIB-fabricated Pt lines. We typically employ a three-stage deposition of contacts: starting with thin and narrow Pt lines (down to 100 nm) contacting the CNT itself,

Fig. 1 A top-down view (from FIB) of a CNT connected with the Al pads via thin FIB-fabricated Pt

and continuing contacts as thicker and wider lines (500-5000 nm) in areas remote from the CNT. Small size of the contacts over the CNT is required to (1) be able to contact the smallest possible features, (2) minimize formation of the 'halo' region, a region around Pt line which experienced some Pt deposition as well, as described below.

RESULTS AND DISCUSSION

Fig. 2 demonstrates image of a MWNT contacted by two 100 nm-wide Pt lines fabricated in FIB. Wider (~5 μm) Pt lines have been fabricated to contact the 100 nm-wide lines to Al pads (the latter is not shown in the image in Fig. 2). Strong bright contrast is visible around the Pt lines, revealing the area on the surface where secondary deposition of Pt has occurred, the so-called 'halo' area. It is clear that if special care is not taken, the halo area can cover the total surface of a nanotube and thus alter the electrical properties of the nanostructure. Possible adverse effects can also include the structural and chemical changes on the nanotube surface and Ga implantation into the nanotube body. Carrying out a number of experiments, we established that longer deposition times and higher ion beam currents produce larger 'halo' area. The Auger Electron Spectroscopy (AES) has been carried out on Pt lines fabricated using beam currents of 70 and 150 pA as those currents provide the smaller probe size and thus the smaller Pt line dimensions. The following line geometry was used: 15μm x 1μm x 1μm. The typical AES spectrum taken from the Pt line fabricated using 150 pA FIB ion beam current is shown in Fig. 3. Typical composition of the FIB-fabricated Pt lines is found to be as follows: ~ 30-32% of Pt, ~62-64% of C, ~ 4% Ga, and ~2% of O (standardless analysis, error ±50%, relative). Incorporation of carbon from the Pt precursor occurs due to the nature of the deposition process employed: room temperature deposition assisted by the ion beam. Lines fabricated using 70 pA beam current had higher carbon content as compared to the lines prepared at 150 pA current. Auger spectra and depth profiles taken within the 'halo' area showed presence of Pt. No Ga incorporation into the 'halo' area was detected by AES (detection limit ≅ 0.5 atom %). To study the structure of the Pt lines deposited using different ion beam currents the cross-sectional transmission electron microscopy has been employed. Two Pt lines have been deposited on SiO_2/Si substrate, one line on top of the other, using 11 pA and 350 pA FIB ion beam currents.

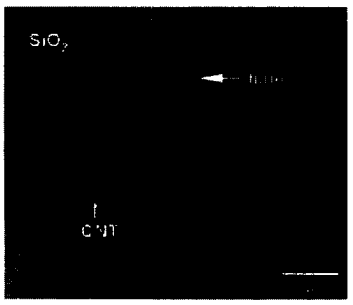

Fig. 2 A top-down view of a CNT on SiO_2/Si contacted by two Pt lines. Image from FIB.

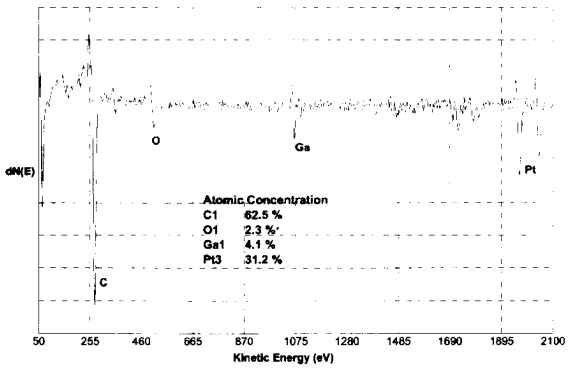

Fig. 3 AES Survey of the FIB-fabricated (150 pA) platinum line after sputtering of topmost 2 nm.

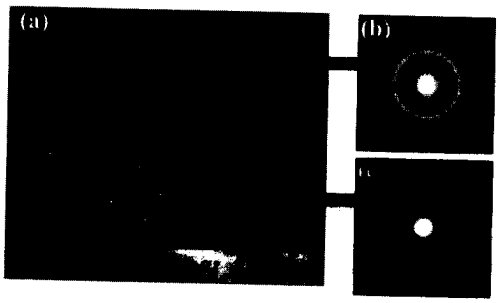

Fig. 4
Dark Field cross-sectional TEM image (a) of two Pt lines grown by FIB-assisted deposition on SiO_2/Si substrate using different Ga^+ ion beam currents: 11 pA and 350 pA. Selected area diffraction patterns (b) and (c) have been taken from the top and the bottom Pt layers,

Lateral dimensions of the lines were 10 μm x 1 μm, while thickness was set to be 0.2 and 0.4 nm, respectively. A cross-sectional TEM sample has been prepared using the FIB-based 'lift-out' site-specific cross-sectioning technique [3]. A dark field cross-sectional TEM image in Fig. 4(a) shows difference in the microstructure of the layers: top layer (deposited using 350 pA beam current) is amorphous, whereas the bright spot contrast visible in the image of the bottom layer (deposited using 11 pA) is associated with polycrystalline structure. Selected area diffraction pattern from the top Pt layer showing its amorphous nature and the diffraction pattern taken from the bottom Pt layer showing the layer is polycrystalline are presented in Fig. 4(b) and Fig. 4(c), respectively. The three diffraction rings (Fig. 4c) correspond to {111}, {200} and {220} planes of the Pt cubic structure with a=0.392 nm (Fm3m symmetry group). High-resolution TEM study of the line deposited at the 11 pA beam current showed Pt nanocrystals (5 nm size on average) imbedded into the carbon matrix. We have also observed about twice higher Pt growth rate when using 11 pA as compared to 350 pA. Resistance of the Pt lines has been measured using the two-point probe technique on lines deposited using the 70 and 150 pA ion beam currents (dimensions: 20μm x 1μm x 1μm). Substrate similar to the one imaged in Fig. 1 has been used. Resultant line resistivity was in the range 1-5 mΩ-cm (higher resistivity associated with lines deposited using lower ion beam current). This is in agreement with the AES compositional data which showed higher carbon content for lines grown at lower beam currents, other conditions being identical.

The final part of this study is on evaluation of the effects of Pt deposition on carbon nanotubes. Several MWNTs dispersed over carbon holey film were exposed to FIB imaging and Pt deposition under various conditions. We have observed amorphization of the nanotube material under ~10^{18} ions/cm^2 exposure dose. No amorphization or significant changes of the nanotube structure were observed at Ga^+ doses 10^{16} ions/cm^2. The dose of exposure of MWNTs to Ga^+ ions during Pt growth has been estimated based on knowledge of Pt growth rates and Pt line composition (discussed above), and kept below 10^{16} ions/cm^2. Transmission Electron Microscopy image in Fig. 5(a) is taken from a MWNT and the Pt contact fabricated on the nanotube in FIB using 11 pA ion beam current. Approximate dose on the MWNT was 10^{16} ions/cm^2. Magnified region of the MWNT-Pt contact is shown in Fig. 5(b). The selected area diffraction pattern (Fig. 5c) from the area denoted by a circle in Fig. 5b shows both the diffused ring pattern corresponding to amorphous Pt and the arc pattern corresponding to 0.34 nm inter-wall distance of MWNT confirming that the multi-wall structure under the Pt is preserved. High resolution TEM (Fig. 6 a) carried out at the Pt/MWNT interface in the area corresponding to 'halo' region shows Pt nanocrystals forming on the nanotube outmost wall and the surrounding material. Inner wall structure of the MWNT appears to be preserved as evident by the lattice-resolution image in Fig.6 (b).

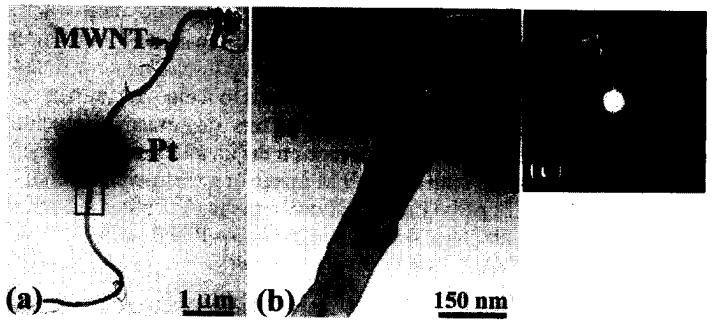

Fig. 5
(a) TEM image of the MWNT and the Pt contact fabricated in FIB.
(b) Magnified Pt-MWNT region boxed in the image (a).
(c) Selected area diffraction pattern of area circled in (b).

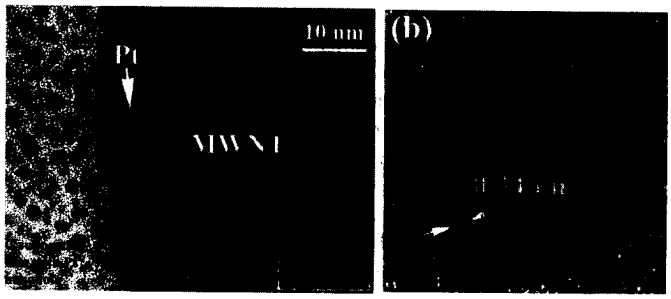

Fig. 6
TEM images of the initial stages of Pt growth on a MWNT surface. Pt is visible as darker contrast on the side of the tube (a). The region boxed in image (a) is magnified in image (b).

Using the knowledge of the details of FIB-assisted Pt deposition and its effects on MWNT structure developed in this study, we have fabricated the contacts to MWNTs and carried out transport measurements [4]. Another application of localized Pt deposition, which we have suggested and successfully implemented, is attachment of MWNTs to the substrate for Atomic Force and Ultrasonic Force Microscopy study. The known problem of AFM/UFM observations of nanotubes is that they are being easily dragged away with an AFM tip during scanning. Attaching the tubes to the substrate surface effectively overcomes this problem. An AFM image in Fig. 7(a) shows a MWNT attached to the Si substrate with two FIB-fabricated Pt pads. The simultaneously obtained UFM image of this nanotube is presented in Fig. 7(b). In UFM mode, an

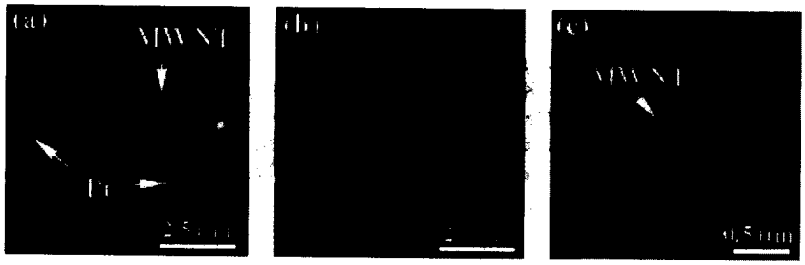

Fig. 7 The AFM (a) and UFM (b, c) images of MWNT attached to the Si substrate using the FIB-fabricated Pt lines.

AFM tip is dragged across a sample which is vibrated at ultrasonic frequencies, where the amplitude of the oscillation is varied systematically [5]. At or above some critical value of the amplitude dependent on the elastic compliance of the material, the tip loses contact with the surface of the sample. Dark contrast in the UFM image corresponds to a more compliant material, while bright contrast corresponds to a stiffer material. Thus, important information on the elastic properties of carbon nanotubes and its dependence on the nanotube structural defects can be obtained. High-magnification (small scan area) UFM image of a multi-wall carbon nanotube attached to the substrate with Pt pads (Fig. 7 c) shows a range of contrast variations related to the tube elasticity changes at structural defects and, partially, to the surface topography. A thorough UFM study of MWNTs is currently underway.

CONCLUSIONS

In conclusion, we have studied chemical, structural and electrical properties of Pt lines deposited in FIB using different ion beam currents for possible application in nanoengeneering and nanoelectronics. Growth of polycrystalline Pt is established for lower (11 pA) beam current, as opposed to amorphous Pt grown using higher (150-350 pA) currents. Composition of FIB-fabricated Pt lines studied by AES showed high concentration of carbon in the lines (62-64% carbon). Resistivity of the Pt lines was found to be in the range of 1-5 mΩ-cm. The smallest width/height of Pt line fabricated in FIB is 0.1x0.1μm. Transmission electron microscopy study of the Pt/MWNT structures shows that the multi-wall structure under the Pt layer is preserved in case of the Pt deposited at low (11 pA) FIB ion beam current while keeping dose of Ga^+ exposure below 10^{16} ions/cm^2. The Pt lines and pads fabricated in FIB using the optimized conditions have been used for transport measurements on MWNTs as well as for AFM/UFM observations.

ACKNOWLEDGMENT

This work has been supported by NSF Grant NER 0210249 and IBM Faculty Award 2002. Authors would like to thank Dr. E. Sun (Nanocs International, Inc.) and Prof. P. Ajayan (Rensselaer Polytechnic Institute) who provided multi-wall nanotubes for this study.

REFERENCES

1. S. Ijima, *Nature*, **354**, 56 (1991)
2. J.P. Biersack, *Nucl. Instr. and Meth.* **B 27**, 21 (1987).
3. L.A. Giannuzzi, J.L. Drown, S.R. Brown, R.B. Irwin, F.A. Stevie, *Specimen Preparation for Transmission Electron Microscopy of Materials IV*, Symposium, 19-27 (1997).
4. J. Ziroff, J. Rullan, G. Agnello, K. Dovidenko, *Proceedings of MRS Spring 2003 meeting, Symposium: Nanotube-Based Devices,* submitted.
5. G.S. Shekhawat, O.V. Kolosov, G.A.D. Briggs. E.O. Shaffer, S. Martin, R.E. Geer, *Proceedings of the IEEE 2002 International Interconnect Technology Conference*, 96 (2000).

Mat. Res. Soc. Symp. Proc. Vol. 739 © 2003 Materials Research Society H7.10

Vertical Alignment of Single-Walled Carbon Nanotubes on Chemically Functionalized Silicon Substrates

Ha-Jin Lee, Hyeyoung Park, Sunyoung Koo, and Haiwon Lee*
Department of Chemistry, Hanyang University,
Seoul, 133-791, Korea

ABSTRACT

Carbon nanotubes have been widely investigated as an essential component for fabricating nanoelectronic devices and for their numerous applications. We investigated the vertical alignment of single-walled carbon nanotubes (SWNTs) on chemically functionalized Si surfaces using chemical reactions between chemical groups in SWNTs and surfaces. For controlling the high selectivity of a specific chemical reaction, a pre-patterned 3-D nanostructure was used by using AFM anodization lithography for achieving the vertical alignment of SWNTs. To consider the subsequent chemical reaction with chemically modified Si surface, the carboxylic acid groups were converted into acid chloride groups followed by the reaction with chemically functionalized surfaces. The protruded structures on pre-patterned areas strongly suggest the vertically oriented SWNTs, and the distribution of the vertically aligned SWNTs becomes denser and their heights are longer with prolonged reaction time. The aspect ratio of SWNTs aligned on -OH functionalized surface is independent from the reaction time (H/W = 0.2). After random alignment of relatively shorter nanotubes on the substrate, their bundle size increases with increasing the reaction time due to strong van der Waals interaction between the lateral sides of nanotubes described as 'nucleation growth'. Longer tubes get also adsorbed on the surface by increase in the bundle size and nanotube length, simultaneously. Based on the chemical reactions of the modified SWNTs with functionalized surfaces, selective attachments of SWNTs were carried out onto pre-patterned surfaces. Detailed characterization of aligned SWNTs will be discussed.

INTRODUCTION

Carbon nanotubes have been widely investigated as an essential component for fabricating nanoelectronic devices and for their numerous applications [1,2]. Especially, well-arrayed carbon nanotubes are highly desirable to prepare chemical sensors [3], nanoprobes for scanning probe microscopy [4], field emitter devices [5,6]. Besides their capabilities as functional components, carbon nanotubes are good building blocks for organizing 3-D nanostructures which are another

important factor in molecular electronics [7]. In this study, we investigate the vertical alignment of single-walled carbon nanotubes (SWNTs) on chemically functionalized surfaces using chemical reactions between chemical groups in SWNTs and surfaces. If we can control the selectivity of a specific chemical reaction, we can design an effective 3-D nanostructure for nano-sized devices using SWNTs as a main frame of the structure. In order to achieve this goal, we have aligned SWNTs vertically on the surface patterned by AFM anodization lithography.

EXPERIMENTAL DETAILS

The purified single-walled carbon nanotubes were purchased from Carbon Nanotechnologies Inc. USA (HiPCO SWNTs), and used without further purification. The carboxylic acid groups-terminated SWNTs (SWNT-COOH) were prepared by shortening and etching processes using ultrasonication in mixed acids according to a procedure reported elsewhere [8]. To consider subsequent chemical reaction with chemically modified surface, the carboxylic acid groups were converted into acid chloride groups by treatment with thionylchloride [8]. The acid chloride-functionalized SWNTs (SWNT-COCl) were dispersed in pyridine by ultrasonication and immediately reacted with chemically functionalized surfaces [9]. The formation of the functional groups attached to SWNT was confirmed by FT-IR. We prepared two kinds of Si surfaces: (i) a surface covered with hydroxyl groups (-OH), simply prepared by piranha treatment [10] and (ii) an amine groups ($-NH_2$) functionalized surface by a self-assembly method using 3-(aminopropyl)triethoxylmethylsilane [11]. The modified SWNTs were reacted with the two different surfaces in pyridine suspension of SWNT-COCl for a given time in order to accomplish their vertical alignment. (Scheme 1)

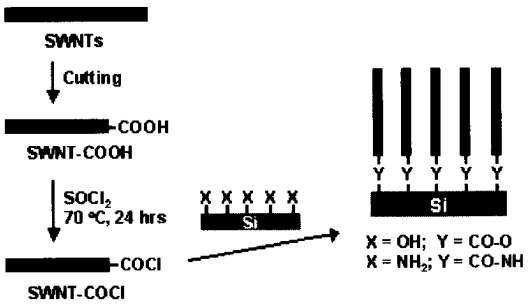

Scheme 1. Steps for the vertical alignment of single-walled carbon nanotubes on the chemically functionalized substrates.

After completing the attachment, the reacted substrates were rinsed with deionized water under sonication and dried under a stream of nitrogen. Tapping mode atomic force microscopy (AFM, Nanoscope IIIa, Digital Instruments, USA) was exploited to characterize the surface morphologies modified by the SWNT on functionalized surfaces.

DISCUSSION

As illustrated in Figure 1, needlelike protrusions were formed on both of the surfaces functionalized with $-NH_2$ and -OH groups after reaction with SWNT-COCl. This protruded structure suggests the vertically oriented SWNTs that are formed by a reaction between terminal groups in SWNTs and functionalized groups on substrates as previously reported [9]. Since they were still observed after ultrasonic treatment, the nature of the bond between the SWNTs and the modified substrate is believed to be chemisorption. The length and the density of the protrusions on the $-NH_2$ functionalized surface are higher than those on the -OH functionalized one due to the rather rapid reaction of acid chlorides with amines to give amides than reaction with hydroxyls to produce esters. The length and the width of the protrusions obtained after a 24 hr-reaction are in the 7 - 25 nm range and 25 - 75 nm range for $-NH_2$ surfaces, respectively, while in the 6 - 22 nm range and 40 - 80 nm range for -OH surfaces, respectively. Generally, the distribution of the vertically aligned SWNTs becomes denser and their heights are longer on both surfaces as the reaction time increases [12-14].

In order to figure out the correlation between sizes of the attached SWNTs and chemical reactivity, we analyzed their aspect ratio, namely the height (H) to the width (W) of the protrusion produced on the specific functionalized surface. Figure 2 represents the aspect ratios of the attached nanotubes. The aspect ratio of SWNTs aligned on -OH functionalized surface is independent of reaction time (H/W = 0.2). This feature can be explained as follows:

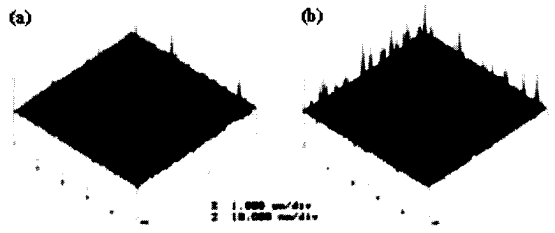

Figure 1. Tapping mode AFM images of the vertically aligned SWNTs on (a) -OH and (b) $-NH_2$ functionalized silicon substrates.

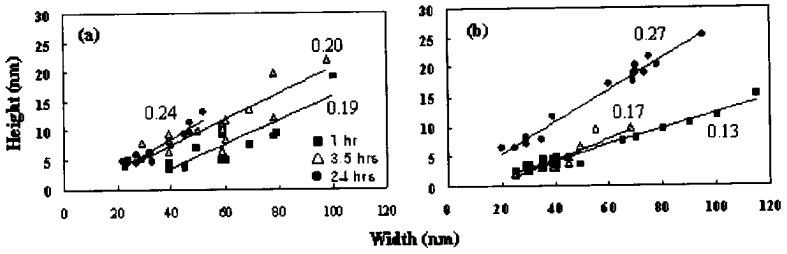

Figure 2. Aspect ratio of the attached nanotubes on (a) -OH and (b) -NH_2 functionalized surfaces.

after random alignment of relatively shorter nanotubes on the substrate, their bundle size increases with increasing reaction time due to strong van der Waals interaction between the lateral sides of nanotubes described as 'nucleation growth' [12,13]. Longer tubes get also adsorbed on the surface by increase in the bundle size and nanotube length, simultaneously. Hence, only SWNTs with a specific aspect ratio were vertically aligned on the -OH functionalized surface regardless of reaction time. On the contrary, the reactivity of SWNT-COCl on -NH_2 surface is dependent on reaction time. As the reaction time increases, the aspect ratio increases from 0.13 to 0.27. In other words, small bundle size-long length carbon nanotubes can be attached on surfaces when the reaction time of SWNT with -NH_2 surface is long enough to complete the reaction. This time-dependent feature of SWNT-COCl on the -NH_2 surface implies that there exists different mechanisms besides 'nucleation growth' observed in a reaction of SWNT-COCl on -OH surface. Evidently, reactivity of SWNT-COCl on -NH_2 functional group is more effective than that on -OH functional groups in aligning vertically longer SWNT on a substrate. Since each chemical reaction is governed by a different mechanism, further attempts to develop other reactions will play an important role in fabricating 3-D nanostructures.

Based on the chemical reactions of the modified SWNTs with functionalized surfaces, selective attachments of SWNTs were carried out on nanolithographic-patterned surfaces as shown in Figure 3. A self-assembled monolayer of hexamethyldisilazane (HMDS) was covered by methyl groups (-CH_3). Since there is no reaction between chemically modified SWNTs and -CH_3 groups [15], SWNTs were used as resists whose surface COCl will react with only the patterned area covered with -OH groups. In AFM anodization lithography, patterning was achieved by the growth of silicon oxide terminated with -OH groups [16]. As a result, the patterned area is covered by -OH groups while unpatterned area is by -CH_3 group. Figure 3 shows selectively attached SWNTs on the protruded SiO_2 region. The height of the attached SWNTs on patterned surfaces ranges from 6 nm to 18 nm, as in the case of -OH functionalized silicon substrates.

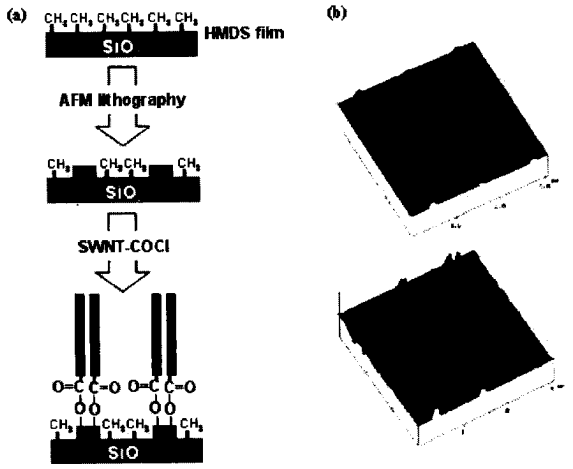

Figure 3. (a) Scheme for selective alignment of SWNTs on pre-patterned surfaces. (b) Tapping mode AFM images of pre-patterned HAMD SAM before (top), and after reaction with SWNTs (down).

CONCLUSIONS

In conclusion, we have demonstrated selective vertical alignment of SWNTs on chemically functionalized silicon substrates by controlling chemical reactivity. This work will contribute to develop the fabrication of 3-D nanostructures on various substrates. Furthermore, it enables us to develop nanotube-based electronic devices.

ACKNOWLEDGMENTS

The authors would like to acknowledge financial support by the National Program for Tera-level Nanodevices of the Ministry of Science and Technology as one of the 21st Century Frontier Program.

REFERENCES

1. T.W. Ebbesen, *Carbon Nanotubes: Preparation and Properties*, (CRC Press, Boca Raton, FL, 1997).
2. P.G. Collins, A. Zettl, H. Bando, A. Thess, and R.E. Smalley, *Science*, **278**, 100 (1997); S. Saito, *ibid.*, **278**, 77 (1997); S. Frank, P. Poncharal, Z. Wang and W.A. De Heer, *ibid.*, **280**, 1744 (1998).
3. J. Kong, N.R. Franklin, C.W. Zhou, M.G. Chapline, S. Peng, K. Cho, and H. Dai, *Science* **287**, 622, (2000); P.G. Collins, K. Bradley, M. Ishigami, and A. Zettl, *ibid.*, **287**, 1801 (2000).
4. S.S. Wong, E. Joselevich, A.T. Woolley, C.L. Cheung, and C.M. Lieber, *Nature* **304**, 52 (1998).
5. W. B. Choi, Y.W. Jin, H.Y. Kim, S.J. Lee, M.J. Yun, J.H. Kang, Y.S. Choi, N.S. Park, N.S. Lee, and J.M. Kim, *Appl. Phys. Lett.* **78**, 1547 (2001).
6. W A. De Heer, A. Chatelain, D. Ugarte, *Science* **270**, 1179 (1995); A.G. Rinzler, J.H. Hafner, P. Nikolaev, L. Lou, S.G. Kim, D. Tománek, P. Nordlander, D.T. Colbert, R.E. Smalley, *ibid.*, **269**, 1550 (1995); S. Fan, M.G. Chapline, N.R. Franklin, T.W. Tombler, A.M. Cassell, H. Dai, *ibid.*, **283**, 512 (1999).
7. C.N.R. Rao, *Chemistry of Advanced Materials*, (Blackwell Science, Cambridge, MA, 1993).
8. J. Liu, A.G. Rinzler, H. Dai, J.H. Hafner, R.K. Bradley, P.J. Boul, A. Lu, T. Iverson, K. Shelimov, C.B. Huffman, F. Rodriguez-Macias, Y.-S. Shon, T.R. Lee, D.T. Colbert, and R.E. Smalley, *Science* **280**, 1253 (1998); J. Chen, M.A. Hamon, H. Hu, Y. Chen, A.M. Rao, P.C. Eklund, and R.C. Haddon, *ibid.*, **282**, 95 (1998).
9. P.A. Heiney, K. Bruneberg, and J. Fang, C. Dulcey, and R. Shashidhar, *Langmuir* **16**, 2651 (2000).
10. A. Ulman, *An Introduction to Ultrathin Organic Films from Langmuir-Blodgett to Self-Assembly*, (Academic Press, New York, 1991).
11. J.H. Moon, J.W. Shin, S.Y. Kim, and J.W. Park, *Langmuir* **12**, 4621 (1996).
12. Z. Liu, Z. Shen, T. Zhu, S. Hou, and L. Ying, *Langmuir* **14**, 3569 (2000).
13. B. Wu, J. Zhang, Z. Wei, S. Cai, and Z. Liu, *J. Phys. Chem. B.* **105**, 5075 (2001).
14. D. Chattopadhyay, I. Galeska, and F. Papadimitrakopoulos, *J. Am. Chem. Soc.* **123**, 9451 (2001).
15. J. Liu, M.J. Casavant, M. Cox, D.A. Walters, P. Boul, W. Lu, A. J. Rimberg, K.A. Smith, D.T. Colbert, and R.E. Smalley, *Chem. Phys. Lett.* **303**, 125 (1999).
16. S.J. Ahn, Y.K. Jang, H.S. Lee, and H. Lee, *Appl. Phys. Lett.* **80**, 2592 (2002); H. Lee, S.A. Kim, S.J. Ahn, and H. Lee, *ibid.*, **81**,138 (2002).

Mat. Res. Soc. Symp. Proc. Vol. 739 © 2003 Materials Research Society

Controlled Deposition and Applied Field Alignment of Single Walled Carbon Nanotubes for CNT Device Fabrication.

Jan Smits, Buzz Wincheski[†], JoAnne Ingram[††], Neal Watkins[†], Jeff Jordan[†]
Lockheed Martin Space Operations
[†]NASA Langley Research Center
[††]Swales Aerospace
Hampton VA, 23681

ABSTRACT

Carbon nanotubes (CNTs) offer great potential for advanced sensing devices due to their unique electronic transport properties. However, a significant obstacle to the realization of practical CNT devices is the formation of controlled, reliable and reproducible CNT to metallic contacts. In this work, a procedure for the deposition and alignment of CNTs onto metallic electrodes using chemically functionalized lithographic patterns is reported. This method uses photo and electron beam lithography to pattern simple Cr/Au thin film circuits on oxidized Si substrates. The circuits are then re-patterned with a self-assembled monolayer (SAM) of 3-aminopropyltriethoxysilane (APTES) to specify desired CNT locations between electrodes. The application of an electric field to the metallic contacts during the deposition of solution suspended single walled CNTs causes alignment of the CNTs in the field direction. This method consistently produces aligned CNTs in the defined locations.

INTRODUCTION

Over the past several years, carbon nanotubes have been in the spotlight of materials research due to their remarkable strength and conductive properties [1]. The single walled carbon nanotube (SWNT) is the strongest known material with a Young's modulus of approximately 1TPa making it an excellent candidate to be the mainstay of next generation structural materials. Also, the SWNT can be either a semiconductor or a metal based on the chirality of the tube while ballistically transporting electrons and maintaining their spin state down the length of the tube [1]. By exploiting these unique electronic transport properties, CNTs offer great potential for use in advanced sensing devices. However, a significant obstacle to the realization of practical CNT devices is reproducible, controlled formation of reliable CNT-to-metallic contacts.

CNTs can be immobilized on a surface via electrostatic interactions between the nanotubes and surface-bound moieties. The strength of this interaction greatly depends on the nature of the terminal groups on the substrate. CNTs have previously been shown to adhere strongly to amino-terminated surfaces and weakly to methyl-terminated surfaces [2, 3, 4].

In this work, we report a procedure for the deposition and alignment of CNTs onto metallic electrodes using standard lithographic techniques and chemical surface functionalization as depicted in Figure 1. Photo and electron beam lithography first are used to pattern simple Cr/Au thin film circuits on oxidized Si substrates. The samples are then re-patterned with a self-assembled monolayer (SAM) of 3-aminopropyltriethoxysilane (APTES) to delineate the desired

CNT locations between electrodes. During the deposition of solution-suspended single walled CNTs, the application of an electric field to the metallic contacts causes alignment of the CNTs along the field direction. This method consistently produces aligned CNTs in the defined locations.

EXPERIMENTAL

The substrates used in all experiments were silicon wafers upon which a 500 nm SiO_2 layer had been thermally grown. Prior to modification, the wafers were cleaned in "piranha" solution (70:30 H_2SO_4:H_2O_2) for 30 minutes at 100 °C to remove any organic contaminants present. After cleaning, the wafers were rinsed with de-ionized water four times, ethanol four times, and finally dried with a nitrogen stream.

Depositing gold electrodes on the surface was accomplished by conventional photo and electron beam lithographic techniques. First, a layer of photoresist [5] was deposited on the surface by spin coating at 3000 rpm for 30 sec. Square windows were defined on the photoresist layer by UV exposure of the resist through a 100-mesh TEM grid. Following development of the photoresist, an adhesion layer of Cr (10nm) and a thin layer of Au (20 nm) were evaporated onto the surface, resulting in an array 205 μm^2 contact pads separated by 50 μm. To create the thin parallel electrodes, a layer of PMMA was deposited onto the array by spin-coating at 3500 rpm for 30 sec [6]. An electron beam was then used to define pairs of electrodes connected to neighboring pads. The electrodes were designed so that they were 300 nm wide and had a spacing of 1 μm. Following development, the sample was cleaned with an oxygen plasma to remove any residual PMMA in the defined locations. Cr (10 nm) and Au (20 nm) were then evaporated onto the surface, followed by lift-off of the remaining photoresist.

To define the areas for CNT deposition, another thin layer of photoresist, was deposited onto the electrode surface by spin-coating. Using the previously deposited electrodes for alignment, an electron beam was used to expose small areas of the photoresist such that portions of each electrode were exposed. After development, the sample was again cleaned with an oxygen plasma, and then immersed in an aqueous 1 mM APTES solution for 20 minutes to deposit a self-assembled monolayer of amine-terminated moieties. After immersion, the sample was rinsed four times with water and then dried in a nitrogen stream, followed by lifting-off of the undeveloped photoresist. A diagram of the resulting device is shown in Figure 2.

Purified SWCNTs synthesized by the HiPCO process were purchased from Carbon Nanotechnologies, Inc., and used as received [7]. A small amount of the CNTs were dispersed in toluene by ultrasonication for 24 hours. Because the concentration of CNTs in the toluene was very small, only a slight discoloration of the solution could be observed.

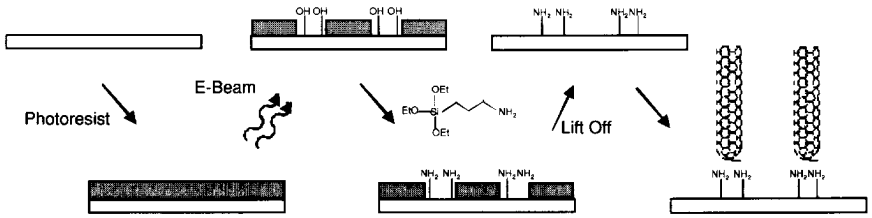

Figure 1. Lithographic patterns are created in e-beam photoresist. Amino terminated groups are then deposited into nanotube attracting patterns. The remaining photoresist is removed, nanotubes are deposited with the applied field present and the excess nanotubes are lifted off.

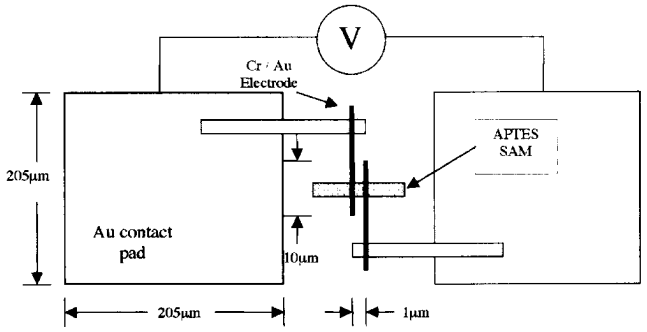

Figure 2. Diagram of simple CNT circuit with Cr / Au contact pads and electrodes fabricated by basic photo and e-beam lithography methods.

Deposition and alignment of the CNTs on the APTES-modified areas was performed using a procedure similar to that described by Chen et al [8]. Several drops of the nanotube dispersion were placed on the sample, covering the surface. Two spring-loaded pins were then used to make contact with the pads and a $10V_{pp}$ sine-wave at 5 MHz was applied to the pads for 6 minutes to generate an electric field. After applying the electric field, the sample was immersed in N-methylpyrrolidone, sonicated for 10 seconds, and blown dry with a nitrogen stream [9]. Immersion in N-methylpyrrolidone was found to remove CNTs from all parts of the silicon surface that had not been modified with APTES. The dispersion and alignment of the SWCNTs was verified by imaging with an atomic force microscope [10].

RESULTS AND DISCUSSION

To verify the effectiveness of this deposition method, various lithographic patterns have been designed, fabricated, and tested. Two different patterns are displayed below in Figures 3 and 4. Figure 3 shows an AFM image of a 4 x 13mm rectangular section of APTES positioned over the Au / Cr electrodes illustrated in Figure 2, after depositing the CNTs and lifting off the excess. Here we can see how the application of the electric field has aligned the CNT bundles to the field lines and how the CNTs are localized to the APTES modified surface. AFM topography measurements of the aligned nanotubes indicate relatively large bundles of SWCNTs, with bundle diameters measuring 10-30nm.

Resistively measurements performed on various aligned and unaligned samples show a large drop in the contact resistance in the aligned junctions. Generally, resistance values in the tens of kΩ's are measured in the aligned junctions while similarly processed unaligned junctions show resistances in excess of 10MΩ. In a similar attempt to align Au nanowires, Smith et al [11] noticed that when a nanowire bridges adjacent electrodes, the electric field between them is eliminated since the nanowire shorts out the electrodes. This then greatly impedes further alignment of additional nanowires. With CNTs, the large contact resistance of the nanotubes prevents the shorting out of the electrodes and a large potential difference is still seen instead of being eliminated while the field is applied.

The electric field alignment not only aligns the CNTs but also concentrates them between the electrodes. This effect can be observed in both Figures 3 and 4 where large populations of CNTs are located between the electrodes. Similar results have been reported by X.Q. Chen et al [8] in their CNT alignment work. Away from the electrodes, there is less alignment and more even dispersion due to a weaker field in those locations.

The circuit used in Figure 4 is identical to Figure 3 but the pattern used for the electron beam lithography is different. In this case, we produced aligned CNTs in three locations between the electrodes by patterning the APTES in three parallel lines, which intersect the electrodes.

This process could be used to consistently deposit single SWCNTs or small bundles of SWCNTs between electrodes. One method for realizing this is to achieve better dispersion of the CNTs in solution. Here we report bundles approximately 10-30nm in diameter between the electrodes, for many applications single tubes are most desirable [12]. Our testing has also shown the quantity of CNTs found in the CNT - electrode junctions can be controlled by adjusting the density of CNT suspended in solution. Diluting the solution results in fewer CNTs found between the conductive traces.

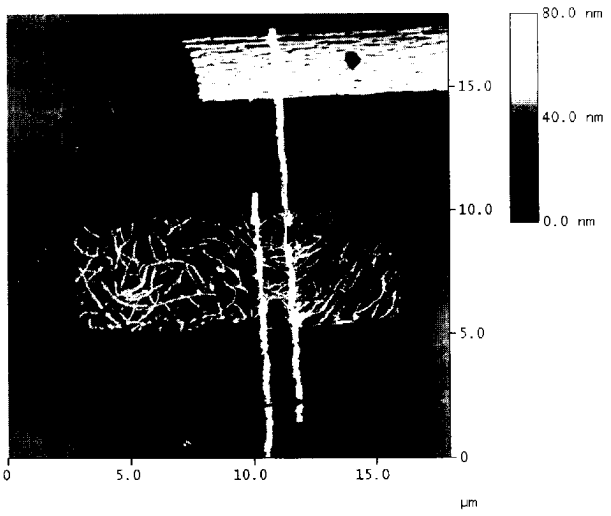

Figure 3. Applied field alignment of SWCNTs on a patterned APTES monolayer, 4x13 mm.

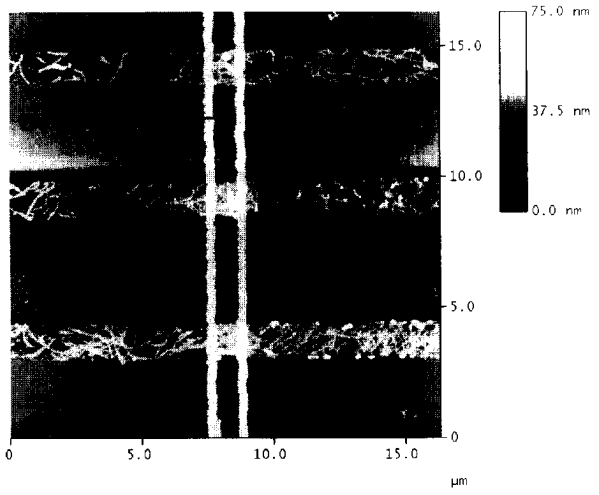

Figure 4. Applied field alignment of SWCNTs between electrodes and located only with in the patterned locations.

CONCLUSION

A method of controlled CNT deposition and electric field alignment has been presented which enables reproducible, controlled, formation of CNT-to-metallic contacts. The ability to deposit nanotubes in precise locations while controlling their orientation using e-beam lithographic patterning, self-assembled surface functionalization, and applied field alignment techniques has been demonstrated. Further refinement of the technique is currently underway to extend this process to the deposition of single SWCNTs between electrodes. The application of this process, which has been shown to consistently produce aligned CNTs in the defined locations, should help to overcome some of the obstacles in the path towards practical CNT device development.

REFERENCES

1. *Carbon Nanotubes: Synthesis, Structure, Properties and Applications*; edited by M. Dresselhaus, G. Dresselhaus, P. Avouris, Springer-Verlag: Berlin, (2001).
2. J. Liu et al, *Chem. Phys Letters* **303** 125-129 (1999).
3. B. Wincheski, J. Smits, M. Namkung, J. Ingram, N Watkins, J. Jordan, R Louie, SEM Conference Proceedings, Spring (2002).
4. J.C. Lewenstein, T. P. Burgin, A. Ribayrol, L.A. Nagahara, and R.K. Tsui, *Nano Letters*, 2(5), 442-446 (2002).
5. Shipley 1805 Photoresist
6. Nano 950 PMMA A2 Positive Radiation Sensitive Resist, MicroChem Corp, Newton, Ma.
7. A.G. Rinzler, et al, *Appl. Phys. A*, **67**, 29-37 (1998).
8. X.Q. Chen, T. Saito, H. Yamada and K. Matsushige. *Appl. Phys. Lett.* **78**, No. 23, 4 June (2001).
9. Nano Remover PG, MicroChem Corp, Newton, MA.
10. Digital Instruments Nanoscope IIIa
11. P.A. Smith et al *Appl. Phys. Lett.* **77**, No 9, 28 August (2000).
12. P. McEuen, *Physics World*, **13**, 31-36, June (2000).

Mat. Res. Soc. Symp. Proc. Vol. 739 © 2003 Materials Research Society H5.3

The Effect of Nanotube Loading and Dispersion on the Three-Dimensional Nanostructure of Carbon Nanotube-Conducting Polymer Composite Films

Mark Hughes,* George Z. Chen, Milo S. P. Shaffer, Derek J. Fray and Alan H. Windle
Department of Materials Science and Metallurgy, University of Cambridge, Pembroke Street, Cambridge CB2 3QZ, UK.

ABSTRACT

Nanoporous composite films of multi-walled carbon nanotubes (MWNTs) and either polypyrrole (PPy) or poly(3-methylthiophene) (P3MeT) were grown using an electrochemical polymerization technique in which the nanotubes and conducting polymer were deposited simultaneously. The concentration and dispersion of MWNTs in the polymerization electrolyte was found to have a significant effect on the thickness of polymer coated on each MWNT and hence the loading of MWNTs in the films produced. It has been shown that for an increasing concentration of MWNTs in the polymerization electrolyte, the thickness of polymer coated on each MWNT decreases. This relationship made it possible to minimize ionic diffusion distances within the nanoporous MWNT-PPy films produced, reducing their electrical and ionic resistance and increasing their capacitance relative to similarly prepared pure PPy films.

INTRODUCTION

The electrochemical growth of carbon nanotube-conducting polymer composites offers the ability to produce three-dimensional nanostructured films that combine the redox charge storage mechanism of conducting polymers with the high surface area and conductivity of carbon nanotubes [1-3]. This desirable merging of properties presents new opportunities to produce superior materials for applications such as supercapacitors, sensors and actuators. Given the bearing that the nanostructure of these composite films has on their electrochemical properties, it is important to develop an understanding of how the film structure can be controlled via manipulation of the growth conditions. In this way, it becomes possible to take full advantage of the remarkable properties of these composite films by tailoring their nanostructure as required. The work described here relates to electrochemically grown composite films of multi-walled carbon nanotubes and conducting polymers (PPy and P3MeT) and the influence of carbon nanotube loading and dispersion on their structure and electrochemical behavior.

EXPERIMENTAL DETAILS

Carbon nanotube-conducting polymer composite films were grown using an electrochemical method in which MWNTs and either PPy or P3MeT were simultaneously deposited on a graphite disk working electrode (0.33 cm^2) in a single compartment cell. A graphite rod (0.65 cm diameter) counter electrode was used in combination with either a saturated calomel reference electrode (SCE) or a silver wire pseudo-reference electrode with the choice of reference electrode depending on the polymerization electrolyte used. Electrochemical synthesis was performed using a Model 273A EG&G Princeton Applied Research Potentiostat-Galvanostat.

When growing composite films of MWNTs and PPy, an aqueous polymerization electrolyte was used which generally consisted of 0.5 M pyrrole monomer (supplied by Aldrich) and

0.025 wt% to 0.4 wt% of suspended oxidized MWNTs. The suspended catalytically-grown nanotubes (supplied by Hyperion Catalysis International) were oxidized using a 3:1 ratio of sulfuric acid and nitric acid refluxed at 130 °C for 1 hour. After deaerating the electrolyte using argon, anodic polymerization of the pyrrole monomer was achieved at the working electrode via the application of a constant potential of 0.7 V (versus SCE). The polymerization reaction is accompanied by the deposition of MWNTs, resulting in the formation of an integrated composite structure. The net negative charge of the nanotubes, arising from the functional groups attached to the oxidized tube surface (predominately hydroxyl, carbonyl and carboxylic groups), enables them to act as both a supporting electrolyte during polymerization (contributing to conduction in the electrolyte), and provide some doping for the deposited PPy [3,4].

When growing composite films of MWNTs and P3MeT, a slight variation on the polymerization conditions described above was used since the growth of P3MeT generally requires the use of an organic electrolyte. Therefore an acetonitrile polymerization electrolyte was used, necessitating a solvent exchange for acid treated catalytically-grown MWNTs (from water to acetonitrile). Since the concentration of MWNTs remaining in suspension after the solvent exchange was comparatively low (0.003 wt%), suspension of untreated MWNTs using an ultrasonic bath was also explored. In this case, both untreated catalytically-grown MWNTs (supplied by Hyperion Catalysis International) and untreated arc-grown MWNTs (supplied by the Sussex Fullerene Research Centre) were investigated. The untreated MWNTs were suspended in the polymerization electrolyte via ultrasonication in an Ultraware U100 30 kHz ultrasonic bath for 30 minutes prior to polymerization. Again, MWNT suspension concentrations were relatively low at about 0.013 wt% for both types of MWNT. As a result, the concentration of MWNTs in the polymerization electrolyte was significantly lower for MWNT-P3MeT composites than that used for MWNT-PPy composites (0.025 – 0.4 wt%). In addition to MWNTs, the polymerization electrolyte used to grow the MWNT-P3MeT films contained 0.1 M of 3-methylthiophene monomer (supplied by Aldrich) and 0.5 M of $LiClO_4$. The low concentration of suspended MWNTs in the polymerization electrolyte (for both acid treated and untreated MWNTs) meant that effective polymerization could not proceed without the $LiClO_4$ supporting electrolyte. To avoid contaminating the acetonitrile polymerization electrolyte with water from the SCE reference electrode, a pseudo-reference electrode (a 1.5 mm diameter silver wire) was used when growing MWNT-P3MeT films. MWNT-P3MeT deposition was initiated via the application of a constant current of 5 mA cm^{-2}.

Once formed, composite films of various film-formation charges (a measure of the amount of film grown) were compared to similarly prepared pure PPy (Cl^- doped) and pure P3MeT (ClO_4^- doped) films using scanning electron microscopy (SEM) and electrochemical impedance spectroscopy (EIS). SEM was performed on a JEOL JSM6340F field emission gun scanning electron microscope. EIS was carried out using a Solartron 1260 impedance/gain-phase analyzer coupled with a Solartron 1287 electrochemical interface employing a sine-wave amplitude of 10 mV and a frequency range of 5×10^5 Hz to 1×10^{-2} Hz. EIS was conducted using a 0.5 M KCl aqueous electrolyte and SCE reference (for films containing PPy) or a 0.5 M $LiClO_4$ acetonitrile electrolyte and silver wire pseudo-reference electrode (for films containing P3MeT). In each case, the electrolyte was deaerated using bubbled argon prior to testing. MWNT-PPy films were tested at EIS bias potentials between -0.4 V and 0.4 V (vs. SCE), whereas MWNT-P3MeT films were generally tested at EIS bias potentials between -2.8 V and 1.0 V (vs. silver wire pseudo-reference).

RESULTS AND DISCUSSION

Figure 1 compares the nanoporous MWNT-PPy composite structure to that of a similarly prepared pure PPy film. It was observed for a film-formation charge of approximately 0.2 C cm^{-2}, that as the concentration of MWNTs suspended in the polymerization electrolyte was increased, the thickness of PPy coated on each MWNT decreased (Table 1). The MWNT loadings in the composite films determined from these PPy coating thickness values (assuming a PPy and MWNT density of 1.5 g cm^{-3} and 1.75 g cm^{-3}, respectively) [5,6] are relatively similar to the relevant concentrations of MWNTs suspended in the polymerization electrolyte. This relationship between the concentration of MWNTs in the thin composite films and that in the polymerization electrolyte indicates that the nanotube loading in the MWNT-PPy films is dictated largely by nanotube availability in the proximity of the growing film.

Theoretical calculation of the maximum thickness of PPy that could be doped by the negatively charged surface groups along the nanotube backbone (2.4 meg g^{-1}) [7] yields a PPy coating thickness of approximately 8 nm (assuming there are four pyrrole units per negative surface charge) [8]. This estimation implies that only a fraction of the deposited PPy is actually in the oxidized state since the acid treated MWNTs were the only source of dopant anions added to the polymerization electrolyte. Therefore, the MWNTs allow the continuous electrochemical growth of PPy, which would otherwise cease due to the insulating nature of unoxidised PPy. However, the mechanism by which this occurs seems to be the formation of a conductive network comprising the MWNTs and adjacent layer of doped PPy, rather than the incorporation of sufficient anionic dopant to ensure comprehensive oxidation of the PPy.

Table 1. The change in average PPy coating thickness and MWNT loading (calculated from the PPy coating thickness) in the composite films for various MWNT concentrations in the polymerization electrolyte (film-formation charge ~ 0.2 C cm^{-2}).

MWNT conc. in electrolyte (wt%)	Coated tube diameter (nm)	PPy coating thickness (nm)	MWNT loading in film (wt%)
0.4	100	45	1.2
0.3	130	60	0.7
0.025	350	170	0.1

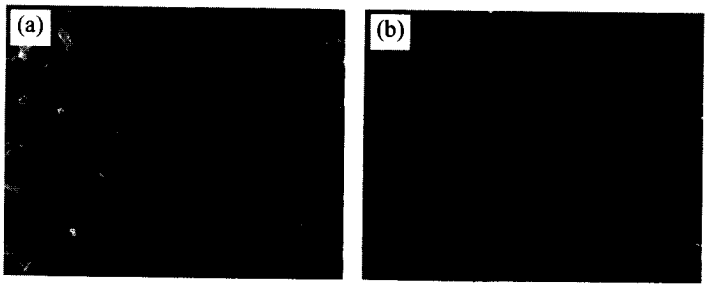

Figure 1. SEM images of the film surface of: (a) a nanoporous MWNT-PPy film (grown using an aqueous polymerization electrolyte containing 0.3 wt% of suspended catalytically-grown MWNTs, film-formation charge ~ 1.8 C cm^{-2}) and (b) a pure PPy film (grown using an aqueous polymerization electrolyte containing 0.5 M KCl, film-formation charge ~ 1.0 C cm^{-2}).

The difference in uncompensated electrical resistance of MWNT-PPy films grown using various MWNT concentrations was estimated from the real impedance (Z') axis intercepts of their complex plane impedance plots (assuming the electrical resistance of the electrolyte and electrical leads were the same for each sample) [9]. For a film-formation charge of approximately 1.8 C cm^{-2} and bias potential of 0.4 V versus SCE, the intercepts were observed to decrease with increasing MWNT concentration from 14.1 Ω for pure PPy to 12.4 Ω, 11.4 Ω and 9.64 Ω for 0.025 wt%, 0.3 wt% and 0.4 wt% MWNTs, respectively (Figure 2a). The improvement in electrical conductivity with increasing nanotube concentration is indicative of a conductive contribution from the MWNTs in the composite films. The increase in film surface area with MWNT concentration may have also contributed to the observed decrease in electrical resistance. While the real impedance (Z') axis intercepts reported are for a bias potential of 0.4 V versus SCE, these values remained approximately constant for bias potentials as low as -0.2 V versus SCE.

The ionic resistance values determined from the projected length of the high frequency component of the complex plane impedance plots on the real axis (Z') indicate that the ionic resistance of pure PPy increased from about 50 Ω to 160 Ω as the bias potential was decreased from 0.4 V to -0.2 V (Figure 2a) [9]. For the same range of bias potentials, the ionic resistance of the MWNT-PPy films remained at 5.0 Ω, 1.7 Ω and 1.0 Ω for MWNT concentrations of 0.025 wt%, 0.3 wt% and 0.4 wt%, respectively (1.8 C cm^{-2} film-formation charge). These results indicate that the nanoporous network structure created by the MWNTs enables superior ionic transport in the solution pores of the composite films over the entire redox cycle. The slight improvement in porosity resulting from the reduction in PPy coating thickness on each nanotube with increasing MWNT concentration is reflected in the decreasing ionic resistance between 0.025 wt% and 0.4 wt% MWNTs.

The low frequency capacitance (C_{lf}) of the films produced was determined from the slope of a plot of the imaginary component of impedance (Z'') at low frequency versus the inverse of frequency (f), using Equation 1 (Figure 2b).

$$C_{lf} = (2\pi f Z'')^{-1} \qquad (1)$$

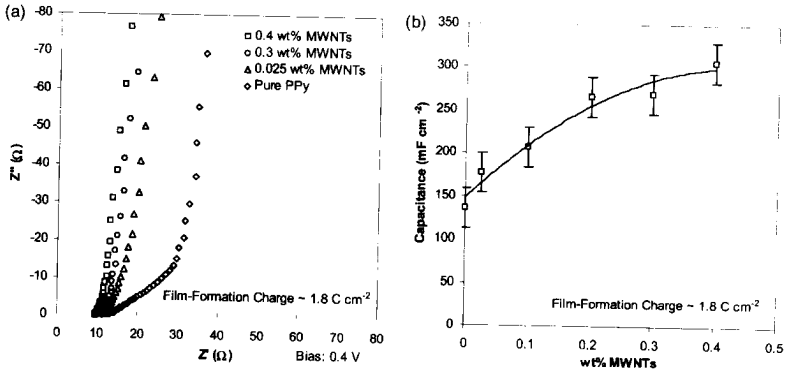

Figure 2. EIS data for films made using different MWNT concentrations in the polymerization electrolyte: (a) complex plane impedance plots and (b) low frequency capacitance (EIS electrolyte: aqueous 0.5 M KCl).

It can be seen that as the MWNT concentration was increased, so too did the specific capacitance for a given film-formation charge (Figure 2b). This improvement reflects the closer interaction between the dopant MWNTs, PPy coating and ions from solution that is facilitated by a greater degree of MWNT doping and reduced ionic diffusion distances. The increase in capacitance with MWNT concentration was non-linear, indicating that only limited improvements would be available for MWNT concentrations in the polymerization electrolyte beyond 0.4 wt%. For film-formation charges as large as ~ 12 C cm^{-2} the capacitance per geometric area of the MWNT-PPy films reached about 2.0 F cm^{-2} when using a MWNT concentration of 0.4 wt% in the polymerization electrolyte. For this concentration of MWNTs, the capacitance per mass of deposited film was as high as approximately 190 F g^{-1}. These values of capacitance are greater than double that of similarly prepared pure PPy films (90 F g^{-1} and 0.8 F cm^{-2}) [10] or the catalytically-grown MWNTs used (49 F g^{-1} and 0.07 F cm^{-2}) [11].

The SEM images of the MWNT-P3MeT composite films grown using untreated MWNTs (Figure 3) give a clear indication of the nanoporosity that can also be achieved for MWNT-P3MeT films grown using an organic polymerization electrolyte. However, the porous structures shown in Figure 3 did not extend over the entire surface of the MWNT-P3MeT films. Rather, there were large regions of the composite film that exhibited a similar structure to that of the pure P3MeT films examined (Figure 4). This observation is indicative of the low loading and uneven distribution of MWNTs through the composite structure arising from the low concentration and poor dispersion of ultrasonically suspended MWNTs in the acetonitrile electrolyte. The use of longer sonication times or acid treated catalytically-grown MWNTs offered little improvement in the concentration and dispersion of suspended MWNTs in acetonitrile. Therefore, it was not possible to test higher MWNT concentrations for MWNT-P3MeT films. In future work it may be possible to improve the loading and distribution of MWNTs in MWNT-P3MeT films via the use of a different solvent or a more robust surface functionalization technique.

Not surprisingly, the low loading and limited distribution of MWNTs in the MWNT-P3MeT films tested gave rise to EIS results that were essentially the same as those of pure P3MeT films, within experimental error. As a result, these MWNT-P3MeT films did not offer a significant improvement in capacitance over the pure P3MeT case.

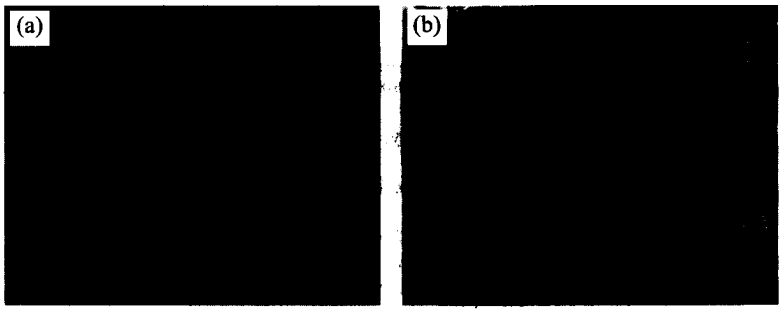

Figure 3. SEM images of the MWNT-P3MeT structures produced when using untreated: (a) catalytically-grown MWNTs (film-formation charge: 5.0 C cm^{-2}) and (b) arc-grown MWNTs (film-formation charge: 2.5 C cm^{-2}).

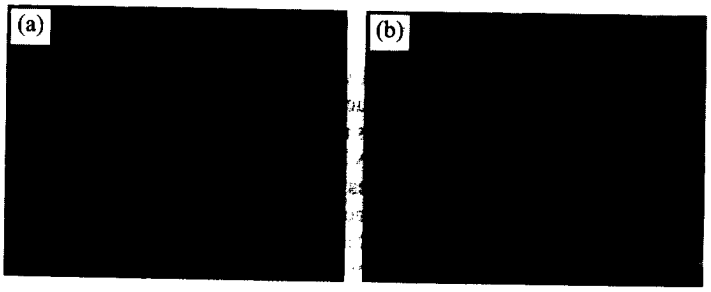

Figure 4. SEM image of the surface of (a) a catalytically-grown MWNT-P3MeT film (film-formation charge: 5.0 C cm^{-2}) and (b) a similarly prepared pure P3MeT film (film-formation charge: 2.5 C cm^{-2}).

CONCLUSIONS

Nanoporous composite films of MWNTs and either PPy or P3MeT were grown using an electrochemical polymerization technique in which the nanotubes and conducting polymer were simultaneously deposited. The concentration and dispersion of MWNTs in the polymerization electrolyte was found to have a significant effect on the thickness of polymer coated on each MWNT and hence the loading of MWNTs in the films produced. The poor dispersion of MWNTs in the acetonitrile electrolyte used to grow MWNT-P3MeT films gave rise to composite films with low loadings of largely agglomerated MWNTs. The larger concentration of well dispersed MWNTs in the aqueous electrolyte used to grow MWNT-PPy films made it possible to produce composite films with larger loadings of well dispersed MWNTs. In this way, it was possible to minimize ionic diffusion distances within the nanoporous MWNT-PPy films produced, in addition to reducing their electrical and ionic resistance. Consequently, electrochemical capacitances per mass and geometric area in excess of 190 F g^{-1} and 2.0 F cm^{-2} were obtained for MWNT-PPy films (more than double that of either component material) when using 0.4 wt% of suspended acid treated MWNTs in the aqueous polymerization electrolyte.

REFERENCES

1. M. Hughes, G. Z. Chen, M. S. P. Shaffer, D. J. Fray, A. H. Windle, *Chem. Mat.* **14**, 1610, (2002).
2. M. Hughes, M. S. P. Shaffer, A. C. Renouf, C. Singh, G. Z. Chen, J. Fray, A. H. Windle, *Adv. Mater.* **14**, 382, (2002).
3. G. Z. Chen, M. S. P. Shaffer, D. Coleby, G. Dixon, W. Z. Zhou, D. J. Fray, A. H. Windle, *Adv. Mater.* **12**, 522, (2000).
4. K. Yoshino, H. Kajii, H. Araki, T. Sonoda, H. Take, S. Lee, *Fullerene Sci. Technol.* **7**, 695, (1999).
5. J. S. Jang, B. Lim, J. Lee, T. Hyeon, *Chem. Commun.* 83, (2001).
6. M. S. P. Shaffer and A. H. Windle, *Adv. Mater.* **11**, 937, (1999).
7. M. S. P. Shaffer, *Carbon Nanotubes: Dispersions, Assemblies, and Composites*, (University of Cambridge, Cambridge, UK, 1999).
8. Q. B. Pei and O. Inganas, *J. Phys. Chem.* **97**, 6034, (1993).
9. W. J. Albery, Z. Chen, B. R. Horrocks, A. R. Mount, P. J. Wilson, D. Bloor, A. T. Monkman, C. M. Elliott, *Faraday Discuss.* **88**, 247, (1989).
10. E. Frackowiak, K. Jurewicz, S. Delpeux, F. Beguin, *J. Power Sources* **97-8**, 822, (2001).
11. C. M. Niu, E. K. Sichel, R. Hoch, D. Moy, H. Tennent, *Appl. Phys. Lett.* **70**, 1480, (1997).

Mat. Res. Soc. Symp. Proc. Vol. 739 © 2003 Materials Research Society

Nanowire and Nanotube Materials Prepared from Polymer Fiber Templates

By Hong Dong, Verrad Nyame, Wayne E. Jones, Jr.*
Department of Chemistry
State University of New York at Binghamton
Binghamton, NY 13902

ABSTRACT

The preparation of well-defined nanomaterials using template methods is well established in the materials literature including porous ceramics, open-framework layered structures and porous membranes. In an effort to prepare thermally and electrically conductive nanowire and nanotube materials, we have recently prepared carbon tubes using polymer fibers produced from an electrostatic, non-mechanical "electrospinning" process as templates. Poly(methyl methacrylate) (PMMA) fibers with average diameter of 150-200 nm were initially fabricated as core materials. The fibers were subsequently coated with a thin layer (20~50 nm) of conductive polypyrrole (PPy) by in-situ polymerization. Upon high temperature (1000 °C) treatment under inert atmosphere, the PMMA core fibers decomposed completely, followed by carbonization of the PPy wall. The structure of the carbon tubes subsequently produced was demonstrated by SEM and TEM. The carbon tubes were analyzed by infrared, elemental analysis and electron diffraction. The results show that the tubes are largely carbon with a small amount of nitrogen and a relatively low crystallinity.

INTRODUCTION

Nanowire and nanotube materials are predicted to possess unique physical, chemical and electronic properties, which have made them attractive for a variety of applications. For example, nanometer-sized probes [1], electron field emitters [2] and battery applications have been proposed. Various methods for the preparation of nanowires and nanotubes have been reported, including self-assembly and template techniques. Among the template approaches, nanoporous membranes have been frequently used for the synthesis of fibrils and tubules composed of metals [3], conducting polymers [4], semiconductors [5], carbon and graphite [6,7], and composite materials [8].

Recently, we have been exploring a new approach using polymer fibers as templates to synthesize nanowire and nanotube materials. This method entails the fabrication of polymer fibers using a simple, electrostatic method known as "electrospinning" [9-11]. The long fibers produced have diameters ranging from several microns down to tens of nanometers [9], and the diameter is controllable by adjusting the physicochemical parameters of the initial polymer solution [12]. The deposition of different wall materials on the surface of the ultrafine fibers can be achieved by various techniques including chemical vapor deposition [13], sol-gel [14], in-situ polymerization and electroless plating. Using electrospun polymer fibers as templates, tubules of poly(p-xylylene)[13] and titanium dioxide [14] have been prepared by Greiner et al. In our group, we have successfully synthesized fibers and tubes of conductive polyaniline and metal (e.g. Au, Ni).

Here we report a study of conductive nanowires and carbon tubes prepared using electrospun polymer fibers as templates. Thermally degradable polymer, poly(methyl methacrylate) (PMMA), was selected as the core fiber material. A coating of conducting polymer polypyrrole (PPy) on the surface of the PMMA fibers was achieved by in-situ polymerization. The PPy/PMMA composite fibers were then subjected to heat treatment. Carbon tubes were subsequently formed by completely removed the PMMA core and carbonized the PPy wall.

EXPERIMENTAL

Materials

Pyrrole (Aldrich) was distilled prior to use and stored at low temperature. PMMA (M.W. 350,000) (Aldrich), ammonium persulfate (Aldrich), p-toluene sulfonic acid (Aldrich), tetrabutyl ammonium chloride (Fluka) and N,N-dimethyl formamide (DMF) (Fisher) were used as received.

Fabrication of polymer fiber template

The PMMA fiber template was produced by the electrospinning process using a variable high voltage power supply as described elsewhere [9-11]. The PMMA solution was prepared by dissolving 6% PMMA in DMF, followed by addition of 5% (relative to PMMA) tetrabutyl ammonium chloride. The PMMA solution was placed in a glass pipette, at a distance of 25cm from a metal cathode such as aluminum foil acting as a collection screen. The pipette was tilted at approximately 5~10° from horizontal so that a small viscous drop was maintained at the capillary tip. The anode of the power supply was attached to a copper wire inserted into the polymer solution in the glass pipette. The potential difference applied between the polymer solution and the collection screen was 12.5 kV (0.5 kV/cm). In the electric field, a polymer jet formed, stretched to the opposite elctrode, and long, dry fibers accumulated on the collection screen.

Preparation of PPy/PMMA composite nanowire fibers

The coating of conductive PPy on the surface of the electrospun PMMA fibers was achieved by in-situ polymerization. The PMMA fiber mat was peeled from the aluminum foil and immersed in a 0.008 M aqueous solution of pyrrole (10 ml), followed by addition of a 0.008 M aqueous solution (10 ml) of ammonium persulfate containing 2 equivalent amount of p-toluene sulfonic acid. The mixture was stirred gently for 8 min. The surface of the PMMA fibers changed from white to dark gradually with a homogenous black coating of polypyrrole. These coated fibers were rinsed with distilled water to remove some loosely bonded polypyrrole particles and then dried prior to thermal treatment.

Formation of carbon tubes

The dried PPY/PMMA composite fiber mat was put in a quartz tube furnace, and purged with N_2 for 15 min at room temperature. Under a N_2 atmosphere, the furnace

temperature was raised up to 1000 °C at a constant rate of 10 °C /min. The furnace temperature was held at 1000 °C for 3 hours before cooling down to room temperature.

Characterization

Scanning electron microscopic (SEM) images were obtained using a Hitachi ETEC Autoscan. The samples were sputtered with Pt/Pd prior to SEM observation. Transmission electron microscopic (TEM) images were obtained using a Hitachi H-7000. The TEM specimens were prepared by ultrasonic dispersion of the carbon tubes in anhydrous ethanol and then transferred a drop onto a copper grid covered with lacy carbon film. An electron diffraction pattern was obtained using the same instrument. The accelerating voltage of the electron beam was 100 KV.

Thermogravimetric analysis (TGA) was performed by TA-2000 at a heating rate of 10 °C /min in N_2 atmosphere. Infrared spectra (IR) were recorded on Bruker Equinox 55 in the range 4000-400 cm^{-1}, using the KBr pellet technique to prepare samples of the fiber and tubular materials.

RESULTS AND DISCUSSION

Morphologies of PMMA fibers and PPy/PMMA fibers

PMMA was selected as the polymer fiber core, as it can be easily fabricated into ultrafine fiber mat. More importantly, the hydrophilic surface property of the electrospun PMMA fiber due to the carbonyl groups makes the deposition of PPy in aqueous solution more homogenous and uniform. The addition of organic ammonium salt (5% relative to PMMA) reduced the fiber diameter by increasing the solution conductivity. Thin fibers with diameter 150~200 nm were produced from 6% PMMA in DMF solution containing ammonium salt.

The morphology and fiber diameter of the PMMA electrospun fibers was examined using SEM. The SEM image, shown in Figure 1a, revealed that the average diameter of the PMMA fiber was ~ 190 nm. The long electrospun PMMA fibers appear to be randomly distributed in a fiberous mat with uniform thickness.

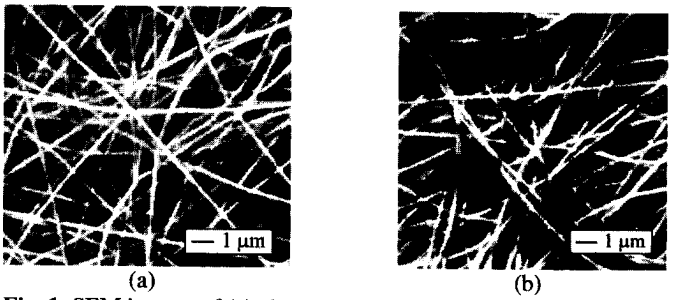

(a) (b)

Fig. 1. SEM images of (a) electrospun PMMA fibers (b) PPy/PMMA composite fibers

The PPy coating on the surface of the PMMA fibers was applied by in-situ deposition. To get homogenous layers of conductive PPy, a variety of concentrations and deposition times were tested. It was found that higher concentration of the reaction solution and longer deposition time resulted in PPy particles on the surface of the PMMA fibers. The optimized conditions used in our experiment included very dilute solution (0.008M) and coating time of 8 min for the deposition. The SEM image of PPy/PMMA composite nanowire fibers, shown in Figure 1b, indicates a smooth coating of PPy. The average diameter of PPy/PMMA fibers was 230 nm with PPy wall ~ 20 nm.

The thickness of electrospun polymer fiber core can be varied by simply changing the parameters of the polymer solution, including concentration, molecular weight and solvent. Thicker walls can be obtained by multiple coating cycles. Thus, it is possible to control the wall thickness of PPy layer and the size of the tubes.

Formation of carbon tubes

The carbon tubes were obtained by annealing the PPy/PMMA fibers at 1000 °C for 3 hours. Figure 2 shows the SEM and TEM images of the resulting carbon tubes. From the SEM image, the outer surface of the tubes appears relatively smooth, though small particles can be seen on the fiber structure. The TEM image confirms that the shape of the carbon sample is tubular.

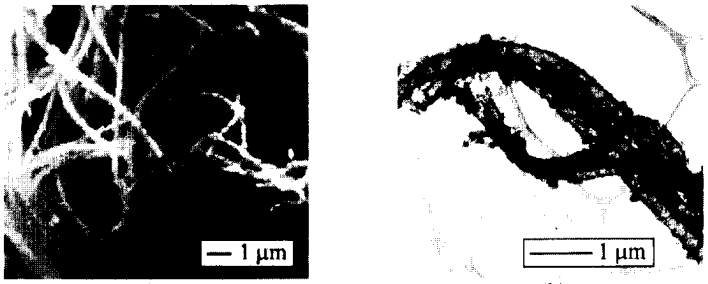

(a) (b)

Fig. 2. SEM (a) and TEM (b) images of carbon tubes resulted from heat treatment of PPy/PMMA composite fibers.

The thermal properties of PMMA fibers (containing 5% ammonium salt), polypyrrole (doped) and PPy/PMMA composite fibers were studied by TGA. The TGA data in Figure 3 indicates that the decomposition of the core PMMA fibers starts at 320 °C. Most of the PMMA core had decomposed and disappeared at temperature 410 °C, leaving behind hollow tubes. The mechanism of pyrolysis of PPy up to 1000 °C has been studied in detail in the literature [16]. The weight loss at low temperature results mainly from the evolution of SO_2 associated with decomposition of the dopant. It has been shown that the weight loss between 500 °C and 1000 °C is mainly caused by the decomposition of the PPy layer to form various N-containing byproducts such as HCN and N_2, thus leading to the reduction of N/C atomic ratio in the resultant pyrolyzed tubes [15,16].

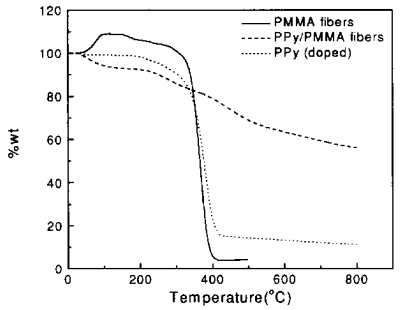

Fig. 3. TGA thermograms of PMMA fibers, PPy/PMMA fibers and PPy (doped).

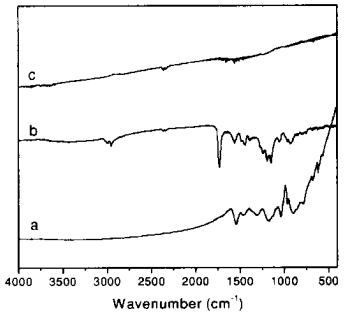

Fig. 4. IR spectra of (a) PPy (doped) (b) PPy/PMMA fibers (c) carbon tubes. The spectra are offset for clarity.

Characterization of Carbon Tubes

The carbon tubes, PPy/PMMA nanowire fibers and PPy (doped) particles were analyzed by infrared spectroscopy, shown in Figure 4. IR spectra of PPy and PPy/PMMA fibers all show a vibration peak at ~1550 cm^{-1} due to the C=N stretch of pyrrole (Figure. 5ab). Besides the characteristic peaks of PPy, the spectrum of PPy/PMMA fibers clearly shows absorption of the carbonyl groups of PMMA at 1730 cm^{-1}. All the peaks in IR spectra of PPy/PMMA fibers were removed completely after thermal treatment. A featureless IR spectrum resulted as expected for the carbon tubes. This suggests that all the functional groups in PPy and PMMA have been eliminated, leaving behind symmetric carbon that shows no IR absorption in this region.
Carbon tubes produced by thermal treatment at 1000 °C were found to be mostly carbon. Elemental analysis showed that the N content was around 4%, and H was < 1%.
The electron diffraction pattern exhibits a pair of fuzzy rings, which indicate the carbon produced from pyrolyzing PPy at 1000 °C is a low crystallinity. Optimization of the thermal process is currently under way.

CONCLUSION

We have developed a new approach for preparing bulk carbon nanotubes. This approach involves using electrospun polymer fibers as templates, and pyrolyzing the wall material, polypyrrole, at high temperature. Since the uniform polymer fibers can be fabricated from tens of nanometers to several microns in diameter, it is possible to control the diameter of the carbon tubes. By changing the number of cycles in the coating process, the wall thickness of carbon tubes can be varied. Further, the electrospun fibers have been reported to be aligned using an electrostatic field-assisted assembly technique [17]. This new approach provides a convenient, flexible and feasible method for the preparation of large amounts of carbon and graphite tubes required for electrically and thermally conducting applications.

ACKNOWLEDGEMENT

We thank Henry Eichelberger in Department of Biological Science of Binghamton University for SEM and TEM images collection. This work is financially supported by Semiconductor Research Corporation (SRC) and the Integrated Electronics and Engineering Center (IEEC). The IEEC receives funding from the New York State Science and Technology Foundation, the National Science Foundation and a consortium of industrial members.

REFERENCE

1. S. S. Wong, E. Joselevich, A. T. Woolley, C. L. Cheung, C. M. Lieber, *Nature* **1998,** 394,52.
2. W. A. d. Heer, A. Chatelain, D. Ugarte, *Science* **1995,** 270, 1179.
3. G. L. Hornyak, J. A. Stockert, C. R. Martin, *J. Phys. Chem.* **1994**, 98, 2963.
4. R. V. Parthasarathy, C. R. Martin, *Chem. Mater.* **1994**, 6, 1627.
5. J. D. Klein, R. D. I. Herrick, D. Palmer, M. J. Sailor, C. J. Brumlik, C. R. Martin, *Chem. Mater.* **1993**, 5, 902.
6. R. V. Parthasarathy, K. L. N. Phani, C. R. Martin, *Adv. Mater.* **1995**, 7, 896.
7. G. Che, B. B. Lakshmi, C. R. Martin, E. R. Fisher, *Chem. Mater.* **1998**, 10, 260.
8. V. M. Cepark, J. C. Hulteen, G. Che, K. B. Jirage, B. B. Lakshmi, E. R. Fisher, C. R. Martin, *Chem. Mater.* **1997**, 9, 1065.
9. D. H. Reneker, I. Chun, *Nanotechnology* **1996**, 7, 216.
10. A. G. MacDiarmid, W. E. Jones, Jr., I. D. Norris, J. Gao, A. T. Johnson, Jr., N. J. Pinto, J. Hone, B. Han, F. K. Ko, H. Okuzaki, M. Llaguno, *Synth. Met.* **2001**, 119, 27.
11. D. H. Reneker, A. L. Yarin, H. Fong, S. Koombhongse, *J. Appl. Phys.* **2000**, 87, 4531.
12. H. Fong, I. Chun, D. H. Reneker, *Polymer* **1999**, 40, 4585.
13. H. Hou, Z. Jun, A. Reuning, A. Schaper, J. H. Wendorff, A. Greiner, *Macromolecules* **2002**, 35, 2429-2431.
14. R. A. Caruso, J. H. Schattka, A. Greiner, *Adv. Mater.* **2001**, 13, 1577.
15. C. Han, J. Lee, R. Yang, H. Chang and C. Han, *Chem. Mater.* **1999**, 11, 1806.
16. C. Han, J. Lee, R. Yang, and C. Han, *Chem. Mater.* **2001**, 13, 2656.
17. A. Theron, E. Zussman, A. L. Yarin, *Nanotechnology* **2001**, 12, 384.

Mat. Res. Soc. Symp. Proc. Vol. 739 © 2003 Materials Research Society H7.24

Thermoelectric Nanowires By Template Synthesis: Fabrication, Contacts and Properties

Oded Rabin [a], Yu-Ming Lin [b], Stephen B. Cronin [c], Gang Chen [d], Mildred S. Dresselhaus [b,c]
Massachusetts Institute of Technology, Cambridge, MA 02139, U.S.A.
[a] Dept. of Chemistry.
[b] Dept. of Electrical Engineering and Computer Science.
[c] Dept. of Physics.
[d] Dept. of Mechanical Engineering.

ABSTRACT

Using the technique we have developed to grow porous anodic alumina (PAA) templates on the surface of silicon wafers, we have fabricated arrays of nanowires of thermoelectric materials. By this method we can control both (1) the in-plane geometry by the design of the template and the substrate, and (2) the out-of-plane dimension by control over the electrochemical nanowire growth process. We use several straightforward methods to make electrical contacts to the nanowires. Our transport studies show that both the structure of the nanowire and the contact region have a strong influence on the observed properties of the arrays.

INTRODUCTION

Nanoscience has seen significant progress in the last decade, in developing techniques that are increasingly precise in their ability to build nanostructures, such as quantum wells, quantum wires and quantum dots. Simultaneously, analytical tools were adapted to investigate this fascinating regime and characterize the unusual properties of these structures. Theory has also played an important role in guiding the experimental efforts, and in the prediction and understanding of the new phenomena that come to light in the quantum limit.

One example of the impact that such new advances have made is the recent developments in the field of thermoelectrics. Traditionally, material science was the tool used to discover new and improved thermoelectric materials. Today it is accepted that size effects are important, and low-dimensional systems are being explored for their potential to exceed the thermoelectric (TE) performance of their constituent materials in bulk form. According to theoretical studies, the enhancement of the thermoelectric figure of merit, Z, in nanostructures is related to the increase in the electronic density-of-states, the removal of the minority carriers, and the selective scattering of phonons over charge carriers. [1,2] Recently, an increase in Z values was reported for superlattices [3], and quantum-dot superlattices [4], and increased Seebeck coefficient values were measured in nanowire arrays. [5]

$$Z = \frac{\sigma \cdot S^2}{\kappa} \qquad \text{(Equation 1)}$$

Thermoelectric devices make use of the coupling of the electrical current to the thermal current in the body of the material for power generation or for cooling purposes. [6] Such a device is composed of junctions of thermoelectric materials, which are characterized by the thermoelectric figure of merit, Z, a function of the electrical conductivity (σ), the Seebeck coefficient (S), and the thermal conductivity (κ) of the materials (Equation 1). The development of materials of high Z is a focus of on-going research. Theoretical studies predict that as the dimensionality is lowered from three-dimensions to two-dimensions to one-dimension, the

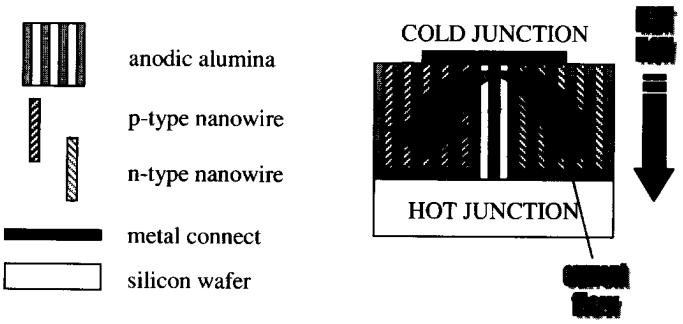

Figure 1. Schematic structure of a nanowire-based thermoelectric device.

phenomena that increase the value of Z become more pronounced. [2] Thus, one-dimensional structures (*i.e.* nanowires) are very interesting structures with respect to low-dimensional thermoelectrics, and will be the focus of this paper.

Figure 1 depicts our proposed structure for a nanowire-based thermoelectric device, consisting of a junction between p-type nanowires and n-type nanowires, which is equivalent to a conventional thermoelectric junction except that the n-type and p-type thermoelectric materials are in the shape of a nanowire, or many nanowires in parallel. For the proper operation of the device, the p-type and n-type regions need to be electrically connected in series, while the thermal current flows in parallel in both regions. Since the synthesis and assembly of nanowires is a challenging task, we proposed a template-based method for the preparation of the nanowires and the thermoelectric device. [7] We have adopted porous anodic alumina [8-10] as a template for the growth of nanowires, for its ability to form ordered parallel channels of uniform diameters of several nanometers, and for its amorphous ceramic composition which makes it a poor electric and thermal conductor. We have demonstrated a fabrication technique that produces porous alumina templates on the surface of a silicon wafer. [7] Such templates were patterned by lithography, their channels were filled to generate nanowires of thermoelectric materials, and contacts were made to both ends of the nanowires while they were still embedded in the template. While the highest quality of thermoelectric nanowires has been achieved by the pressure injection of molten bismuth [11], which results in highly oriented single crystal nanowires, there is no apparent way to implement the pressure injection method in the fabrication of a thermoelectric device. The most convenient alternative is the template synthesis of nanowires by electrochemical deposition. This method can be applied to a wide range of materials (metals, semiconductors, and organic polymers) and it is relatively cheap and simple to carry out. The deposition of different materials in the same template can then be achieved by patterning the working electrode attached to the template.

In this paper we consider some materials-related issues involved in the production of thermoelectric nanowires by electrodeposition in a silicon-supported PAA template. We also give details on the methods employed to make contacts to the embedded nanowires. Measurements of the resistance of the sample and its temperature dependence were employed in order to qualitatively characterize the durability of the contacts and the effect of annealing on the electrical properties of the nanowires.

EXPERIMENTAL

PAA templates were fabricated on silicon wafers in a variation of the procedure described previously [7]. Briefly, n-type silicon substrates were coated with thermal oxide, and 20nm titanium and 100nm platinum were deposited on its front side by e-beam evaporation. A thick aluminum film (6-12μm) was thermally evaporated on the pretreated wafer. The aluminum film was anodized at constant voltage (45V or 50V) in an oxalic acid electrolyte at 15-18ºC. After this anodization, the porous film was etched overnight in a CrO_3 : H_3PO_4 solution and a second anodization was carried out. Once the aluminum has been completely anodized along the thickness of the film, the appearance of the film changes and gas bubbles are formed as the electrolyte reaches the platinum film. The current was limited to 150% of its steady state value, to prevent damage to the PAA film from gas evolution, and the current was stopped as soon as a surge in current was observed. Pore widening was carried out in 5vol% H_3PO_4. A Cr/Au bilayer 120 nm thick was deposited on top of the PAA. Bismuth (Bi) was electrodeposited from a solution of bismuth nitrate (40 mM) and ethylenediaminetetraacetic acid (EDTA, 75 mM) in distilled water using a home-built potentiostat at –650 mV vs. saturated calomel electrode (SCE). Annealing was performed in a tube furnace at temperatures up to 325ºC in a vacuum of 40 mtorr.

Scanning electron microscopy was performed with a JEOL 6320FV microscope. Magnetoresistance measurements were carried out with a Quantum Design DC Magnetic Property Measurement System.

RESULTS AND DISCUSSION

The fabrication of PAA templates on silicon wafers results in high quality alumina films, with the desired pore structure, large area coverage and good mechanical properties. In this example, a Ti/Pt bilayer was placed between the oxidized silicon wafer and the PAA template. The titanium film serves for the adhesion of the layers to the wafer. The platinum film serves as a working electrode during the electrochemical deposition step. In contrast to the case in which titanium alone is used [7], no special measures were taken here to remove the barrier layer. It is believed that the barrier layer gets ruptured during the gas evolution at the end of the anodization. A drawback, however, of using a noble metal as the back electrode is that the current needs to be shut off to preserve the integrity of the PAA film once bubbles are generated, even though the anodization may not have reached completion in all areas of the sample.

Bi nanowires were prepared in the PAA-on-silicon templates by electrochemical deposition from a $Bi(NO_3)_3$/EDTA solution. The platinum layer under the porous film served as the working electrode from which the nanowires began to grow. Fig. 2a shows a cross section of a bismuth-filled template. The composition contrast imaging shows from right-bottom to left-top five layers in the following order: silicon, silicon oxide, Ti/Pt, a dark porous alumina background around bright bismuth nanowires of varying lengths, and the vacuum of the microscope chamber. As seen in the figure, there is nucleation of bismuth deposits only in part of the imaged area. This is because when Pt is used, the anodization is stopped before all the aluminum is oxidized, and some areas still contain the barrier layer and possibly aluminum at the bottom of the pores. The areas of high density of nanowires correlate with the areas where the aluminum was consumed first.

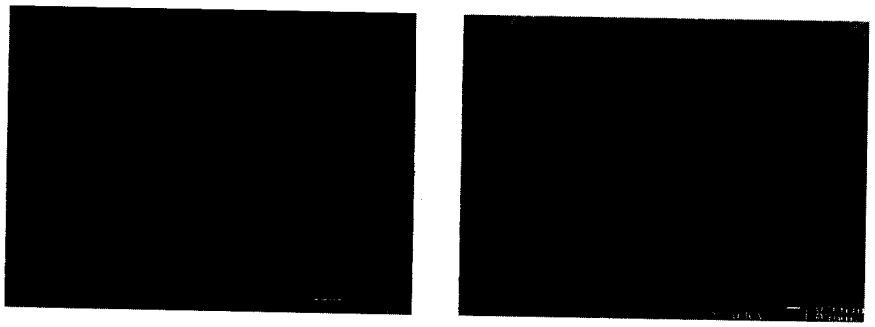

Figure 2. a) Cross section of the silicon-supported membrane with bismuth nanowires grown in it (SEM composition contrast image) **b)** Top surface of the gold coated PAA showing the openings of the pores.

In order to reduce the inhomogeneity in the properties measured from the nanowire array, we attempted to make electrical contacts to only one, or very few nanowires. This was achieved by a variation of a method described before [12], in which a metal film on top of the porous film is used to monitor the emergence of the tips of the nanowires from the channels. Two possible setups for the electrochemical deposition in the PAA-on-silicon template and the detection of contact formation are shown schematically in Fig. 3. Thin layers of gold (<200 nm) can be deposited on the surface of the PAA template without blocking the pore openings (Fig 2b). Thus, the electrolyte can penetrate into the pores of the coated template, nanowires can be deposited, and once they emerge through the coated side of the template, the metal films on both surfaces of the PAA film are electrically shorted. The non-uniform growth of nanowires in PAA-on-Pt-on-silicon templates, as discussed with respect to Fig. 2a, increases the chances that only a few nanowires emerge from the pores at a given time, enabling us to make contact to very few wires, possibly only one.

When nanowires were grown in this arrangement, a sample with a resistance of approximately 200 Ω was obtained. We were not able to image the top ends of the nanowires to find out how many of them are in contact with the electrode. However, when the sample was

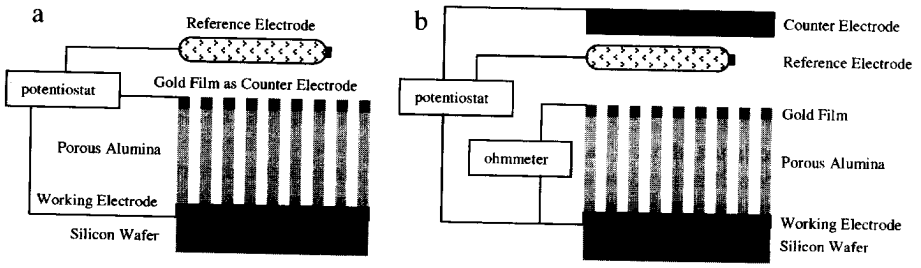

Figure 3. Two setups for the electrodeposition in alumina templates with detection of the establishment of contacts across the membrane.

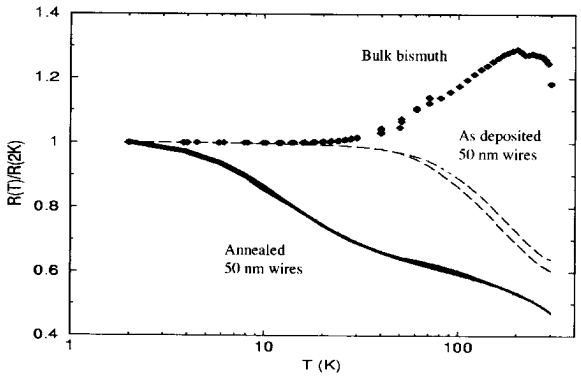

Figure 4. Temperature dependence of electrodeposited 50nm bismuth nanowires and bulk bismuth.

divided into small pieces of about 3 mm^2 (~10^8 pores in each), only one piece showed conductance across the membrane. Assuming a wire diameter of 50 nm and a length of 6 microns, we obtain a resistivity of $8 \cdot 10^{-6}$ Ω·cm. This is one order of magnitude lower than the resistivity of single crystal bulk bismuth [13], meaning that either we were making contact with more than 20 nanowires at a time, or that we are making contact with a nanowire of larger diameter than the nominal pore size.

The resistance of the sample was found to increase significantly with time. Within a few hours, the resistance reached 14 kΩ, and after several weeks the resistance was measured approximately 52 kΩ. The temperature dependence coefficient of the resistance $\partial R(T)/\partial T$ was negative for T=77-300K. Sample manipulation and temperature changes seemed to cause abrupt non-reversible increases in the sample resistance, and eventually the conductivity is lost except for non-linear effects at high-fields (V > 1 Volt).

The above observations seem to indicate that changes occur in the structure of the sample. Since the top tip of the nanowire is the only region in contact with the gold film and the primary region in contact with air, and since an oxide layer is formed on bismuth under ambient conditions [14], it is logical that the behavior of the resistance of the sample is controlled by the nature of the interface between the bismuth and the gold. This was corroborated by measurements on samples where the bismuth nanowires were allowed to grow for several minutes after the establishment of contact with the gold film. The resistance of these samples was approximately 2 Ω, was not irreversibly sensitive to temperature changes, and increased with time in a much-reduced rate. In these samples, the contact of each nanowire with the gold film seems to be significantly more resilient, an indication of a larger contact area.

Alternatively, the bulk properties of the nanowire can be manipulated by thermal treatment of samples with stable resistance followed by the repair of possible damage to the contact area. The repair consists of the deposition of another gold film on the top of the sample, to compensate for gold displaced by liquid bismuth or during bismuth deformation. Fig. 4 shows the temperature dependence of the electrochemically-deposited nanowire sample before and after annealing and recrystallization at 325ºC in vacuum, and compared to a bulk sample of electrodeposited bismuth. Both the as-deposited and the annealed nanowire samples show a

negative temperature dependence of the resistance, unlike the bulk sample. That is explained by the reduction of the importance of phonon scattering in the polycrystalline material confined by the pore walls. Annealing causes the saturation of the resistance at low temperature to disappear, indicative of the lowering of the number of chemical impurities and/or structural defects by the thermal process.

CONCLUSIONS

Nanowires of bismuth were grown on silicon supported PAA templates. The templates were obtained missing the barrier layer due to the action of a Pt layer at the interface. Contacts to few nanowires were made in a straightforward manner; however, the contacts were severely affected by aging and by electrical current transport. More robust contacts were obtained when the deposition was prolonged beyond the point of establishment of contact. Through 2-point electrical transport measurements, we observed the reduction of extrinsic carriers in the as-deposited nanowires by a thermal treatment. We plan to improve the contact without increasing the number of connected nanowires by depositing a noble metal within the pores on top of the nanowires.

ACKNOWLEDGEMENTS

We thank Dr. G. Dresselhaus, Prof. G. Chen, and M. R. Black for valuable discussions, and S. Rabin for providing the potentiostat. The support from MURI subcontract 0205-G-BB853, NSF grant DMR-01-16042, US Navy contracts N00167-98-K0024 and N66001-00-1-8603, and ONR grant N00014-02-1-0865 is gratefully acknowledged.

REFERENCES

1. F.J. DiSalvo, Science **285**, 703 (1999).
2. M.S. Dresselhaus et al., in *Recent Trends in Thermoelectric Materials Research III*, edited by T.M. Tritt (Academic Press, San Diego, 2001), p. 1.
3. R. Venkatasubramanian et al., Nature **413**, 597 (2001).
4. T.C. Harman et al., Science **297**, 2229 (2002).
5. Y.-M. Lin et al., Appl. Phys. Lett. **81**, 2403 (2002).
6. G.S. Nolas, J. Sharp, H.J. Goldsmid, *Thermoelectrics: basic principles and new materials developments*, edited by R. Hull et al., (Springer-Verlag, Berlin, 2001) p. 2.
7. O. Rabin et al., in *Nonlithographic and Lithographic Methods for Nanofabrication*, edited by J. A. Rogers et al. (Mater. Res. Soc. Proc. **636**, Pittsburgh, PA, 2001) p. D4.7.
8. D. Routkevitch et al., IEEE Trans. Elect. Devices **43**, 1646 (1996), and references therein.
9. C.R. Martin, Science **266**, 1961 (1994).
10. J.P. O'Sullivan and G.C. Wood, Proc. Roy. Soc. Lond. A. **317**, 511 (1970).
11. Z. Zhang, D. Gekhtman, M.S. Dresselhaus, and J.Y. Ying, Chem. Mater. **11**, 1659 (1999).
12. J-E. Wegrowe et al., IEEE Trans. Magn. **34**, 903 (1998).
13. Landolt-Börnstein, *Numerical Data and Functional Relationships in Science and Technology*, edited by K.-H. Hellwege and J.L. Olsen, (Springer-Verlag, Berlin, 1983) vol. 17e, p.54.
14. S.B. Cronin et al., Nanotechnology **13**, 653 (2002).

Fabrication and Properties of 3D Nanostructures

Mat. Res. Soc. Symp. Proc. Vol. 739 © 2003 Materials Research Society H1.6

New Processing Techniques for the Creation of Micro-Opto-Mechanical Machines and Photonic Devices Embedded in Glass

Meg Abraham, Peter Fuqua, David P. Taylor, William W. Hansen, Henry Helvajian, Nathan Presser, Frank Livingston, and Stephen La Lumondiere
The Aerospace Corporation, El Segundo, CA 90245

ABSTRACT

The use of lasers to create intricate three-dimensional and buried structures [1] in photo-structural glass has been well demonstrated at The Aerospace Corporation over the past four years. In these instances the glass used (Foturan™, made by the Schott Group) forms a silver nucleation sites on exposure to intense UV laser light via a two-photon process. Subsequent annealing causes a localized crystal growth to form a meta-silicate phase which can be etched in dilute hydrofluoric acid at rates of 20 to 50 times that of the unprocessed glass. We are now in the process of experimenting with another formulation of photosensitive glass, also pioneered by Corning Glass Works, that behaves differently during the bake process. In the second case, a photoexposure and bake process creates a silver-halide crystal and forms an adjacent void in the glass. A second photoexposure and bake allows for the migration of more silver into the void creating patterned formations of silver nano-wires [2]. Recent experiments with this type of glass have shown that the manipulation of the size and density of the embedded nano-wires as well as the overall pattern of the clusters can be controlled using direct-write exposure to laser processing.

INTRODUCTION

New materials processing methods are leading to a revolution in the types of micro-machines that are currently being developed. The size and dimensionality as well as the types of materials are expanding every year greatly enhancing the number of device types that can be made. We have shown that one of the more interesting approaches to these types of new three-dimensional (3D) processes is the combination of photo-structurable glass, which was investigated extensively in the past at Corning Glass Works, with laser direct write patterning to create truly 3D micro-machines in glass. In this instance UV photons initiate a sequence where silver ions are reduced, crystals are formed and a meta-silicate crystalline phase nucleates. In this phase, the silicate etches much faster rates than the glass and it is possible to create very high aspect ratios. Due to the interesting nonlinear properties involved in the initial exposure step, it has been demonstrated that it is possible to create embedded structures in the glass [3] as well as structures with very high aspect ratios by simply varying the laser power, wavelength or focus.[4]

More recently, we have begun to work with a glass which has a different photo structurable characteristics. The second form of the glass generates a cluster of silver complex nano-wires when exposed and baked using several steps. The patterns that are generated are not made by the removal of material, but instead by the creation of precisely patterned nano-scale inclusions. The inclusions can be expected to generate a number of interesting physical and electro-optical changes in the glass. Generally, these processes are due to surface plasmon effects of the embedded nanowires and their optical properties can be described using Mie theory. The most obvious change is to the color of the glass (Fig. 1). The nano-inclusions create a photon

absorption which is dependent on the size of the nano inclusion (Fig. 2). The density of the nano-inclusions dictates the degree of absorption by the inclusions. We believe that by manipulating both the size and density of the particles, it will be possible to change some of the electro-optical properties as well.

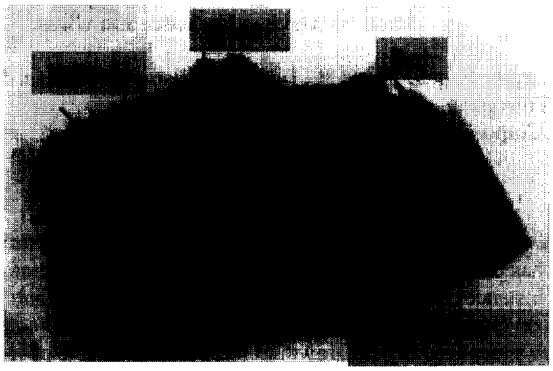

Figure 1. Processed glass with a silver complex gradient "rainbow" exposed using a UV lamp. The round spot represents laser bleaching of the silver using 532 nm laser light.

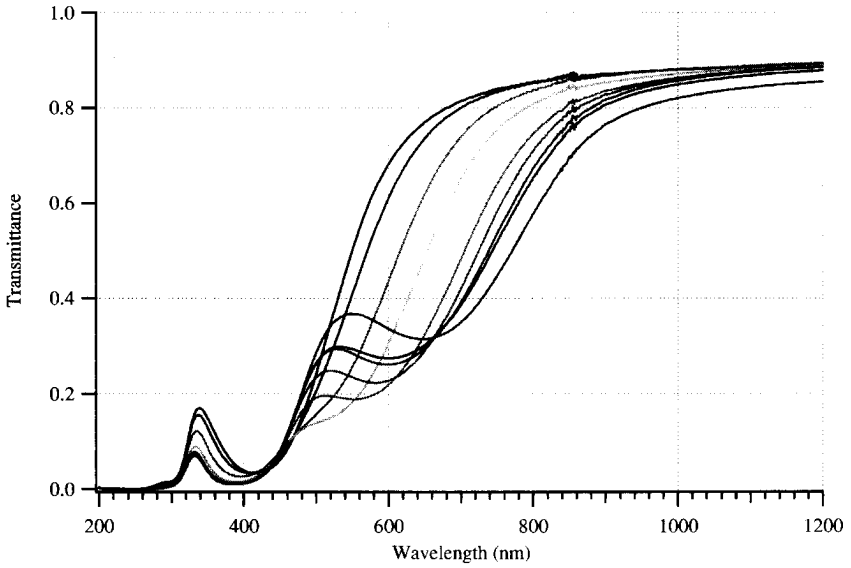

Figure 2. Absorption spectra of the above glass across rainbow of colors.

The rainbow pattern is formed by a series of steps where the areas are first exposed to UV light for a sequentially increasing duration of times, and then baked to form the silver halide inclusion

and adjacent void. A second exposure and bake cycle allows for the mobilization of more silver and redeposition into the voids. While we have been able to generate colors by exposure of this glass using standard lamp techniques to form silver nano-particles, this is of limited use for making micro devices for electro-optics without better control of the size and placement and density of the particles. In short, in order for the glass to be of use to the micro/nano community there is a requirement for increased control over the formation of the nano-clusters. In an effort to achieve this control, we have demonstrated the feasibility of both laser exposure and focused ion beam direct write patterning as a first step to making functioning patterned filters, conducting lines, and potentially nano-particle based devices.

PROCESSES INVESTIGATED

A number of simple experiments were carried out for the purpose of evaluating the conditions that govern the processing of the glass in question. The first was to take the colored glass, in the green region of the rainbow, and expose it to an Nd:YAG operating at 532nm with 3 nanosecond pulses at 10 Hz and with a 6 mm spot. As the power was increased to 200 mJ the colored glass was seen to bleach. This is an indication that the glass is annealing, and so the process is locally reversible, or erasable (fig. 1). Past studies indicate that silver nano-spheres will dissolve into silica at temperatures around 900-1000 degrees C [4]. By simply touching the glass (which was only very slightly above room temperature) it became clear that the glass was not achieving these significant temperatures over all. Rather, the embedded metal nano-clusters are absorbing locally and migrating back into the glass. While deformation [5] and photobleaching [6] of nano spheres in glass has been seen in the past, we believe that the fact that it can be achieved in this distinct type of photostructurable glass, where nano-wires are the end result, is a valuable development. This experiment was repeated using the Nd:YAG operating in the fundamental mode (1064 nm) and third harmonic (355 nm). In these cases, we saw significant bleaching with the 355 nm laser light but reduced bleaching with the 1064 nm laser light at the same power level as with the "green" glass. We also noted that further control of the laser power allows for partial reduction in the intensity of the color of the glass and/or changes to the color of the glass depending on the laser conditions. By further refining the process, we believe that it will be possible to locally change the density or size of the particles by changing the laser wavelength and power. It is noteworthy that we did not see the same effect with CW or long pulsed lasers. In the case of the CW laser, the glass was locally heated under the laser until it shattered with no discernable change in the intensity or hue of the glass. Finally, with a controlled bake cycle we are able to restore the color to areas that were previously erased. The length of time and the temperature of the bake effect the color and intensity of the changes to the glass.

In a second experiment, the glass was exposed using a pico-second UV laser exposure. The laser is a synchronously-pumped, cavity-dumped, rhodamine 6G dye laser. The laser pulse repetition rate is 1 MHz. We frequency doubled the dye laser for operation between 300 and 310 nm, and the temporal duration of the optical pulse was 10 picoseconds at the FWHM of intensity. The incident optical power on the sample was 2.9 microwatts and the spot size was approximately 3 microns. A simple embedded line was drawn in the glass by focusing the laser in the piece and scanning the part under the beam at 45 microns/second (fig. 3). This was followed by the standard bake step to create a line of nano-clusters.

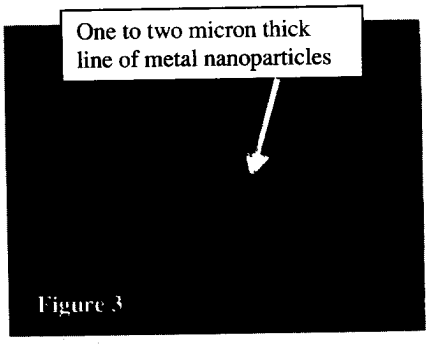

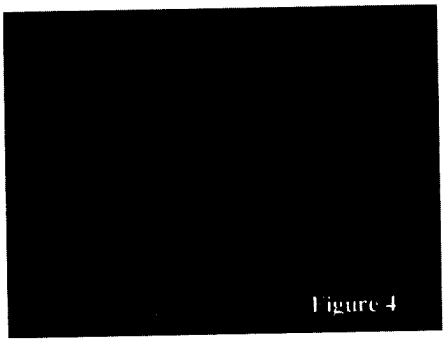

Figure 3. Single line of silver nano-particles embedded in glass after exposure and bake.
Figure 4. Top view of glass surface with lines of nano-particles crossing inside the glass.

Figure 5. Cartoon of glass and laser written crossing lines of nano-wires in side view.

The potential for rapidly creating more complex structures was demonstrated using the same laser but with increased power (96 micro-watts/ pulse) and a faster scan speed (75 microns/sec.). The laser beam was incident at a 45-degree angle to the glass surface. An array of one-second exposures was made before the glass part was rotated through 180 degrees. The same set of exposures was made in the glass, but now normal to the initial lines. This created an array of crosshatches in the glass, which we believe might be the first step to demonstrating devices such as photonic band gap filter in the glass (fig. 4 and 5).

A further refinement of control over the placement of the nano-clusters can be obtained by using a wavelength of light that is absorbed by the glass. In this instance, the strong absorption stops photons from reaching the backside of the glass. Therefore, only the top surface contains the patterned nano-clusters. This was demonstrated using a Lambda Physik Excimer laser model LPX 300. The laser was operating at 248 nm and 5 Hz with power on the order of 800mj in a $5cm^2$ spot. The glass, which previously had some vertical lines exposed using the 300 nm dye laser was exposed a second time with the Excimer for 50 pulses (fig. 6). The 248 nm light is strongly absorbed at the surface of the glass and so the cluster formation is limited to the first half millimeter of the one millimeter thick glass (fig. 6). After baking, the areas exposed to the 300 nm laser develop nano-cluster lines that pass through the entire thickness of the glass, while the areas exposed only to the Excimer laser had a surface layer of nano-clusters.

As a final attempt to manipulate the new glass structure, a FEI Focused Ion Beam (FIB) was used to mill micron-scale arrays and features into the surface of the glass (Fig. 7). The FIB is able to mechanically structure the glass into three-dimensional forms using a Gallium beam to mill the surface with nanometer scale dimensions. This process can be used to further pattern optical devices such as wave-guides and mirrors.

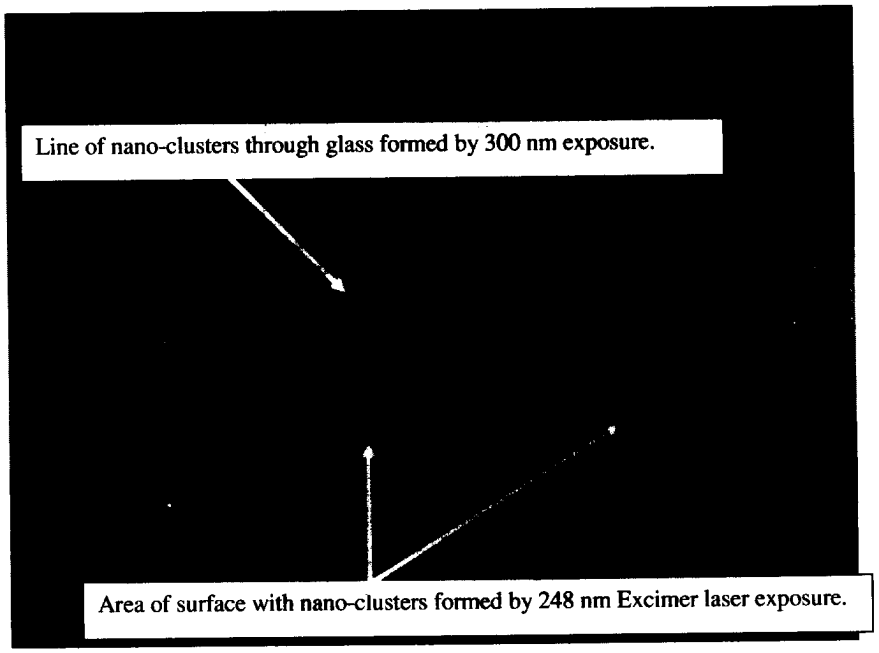

Figure 6. Edge view of glass with exposures at 300 nm and 248 nm.

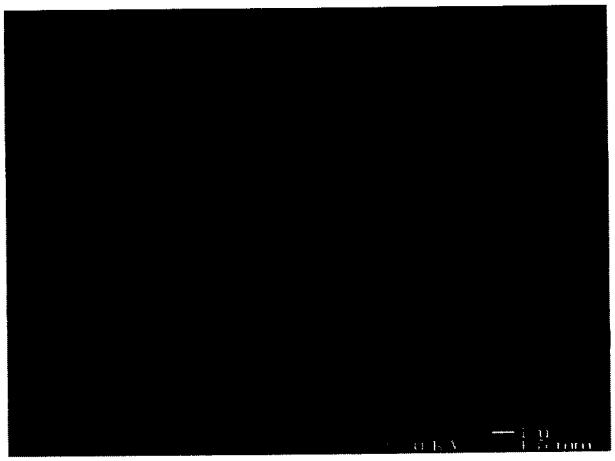

Figure 7. SEM of FIB cut photo-structurable glass

CONCLUSION

We have demonstrated a number of laser direct write techniques for making patterned and embedded clusters of silver complex nano-particles. The size of the particles and density of the clusters depend on the laser exposure and the bake protocols. By focusing the laser on the material during exposure or choosing a wavelength that is absorbed by the glass it is possible to further control the placement and size of the nano-particle clusters. By using lasers in the visible range it is possible to erase structures previously made or modify their density and size. Finally, it is possible to physically structure the glass using direct write with a focused ion beam.

We believe that these direct write techniques will all be useful as methods for developing devices based on nano-particle technology in glass.

ACKNOWLEDGMENTS

The authors would like to thank Lee Steffeny, Dr. Steve Moss, Dr. S. Feuerstein, Adam Wang, Dr. Siegfried Jansen, Dan Harps and Dr Paul Fleischauer for their various contributions to this work.

REFERENCES

1. W. W. Hansen, P. Fuqua, F. Livingston, A. Huang, M. H. Abraham, D. P. Taylor, S. Janson, and H. Helvajian, *The Industrial physicist*, **June/July**, 18, (2002).
2. S. D. Stookey, G. H. Beall, and J. E. Pierson. *Journal of Applied Physics*, **49,** 5114, (1978).
3. P. D. Fuqua, D. P. Taylor, H. Helvajian; W. W. Hansen, M. H. Abraham in *Materials Development for Direct Write Technologies,* edited by D. Christy, D. Ginley, H. Helvajian and D. P. Taylor (*Mater. Res. Soc. Proc.* **624**, Warrendale, PA, 2000) pp 79-87.
4. J. C. Cheang-Wong, A Oliver, J. Roiz, L. Rodriguez-Fernandez, J. M. Hernandez, and A. Crespo-Sosa, *J. Phys.: Cond. Mat.*, **13**, 10207, (2001).
5. M. Kaempfe, T. Rainer, K.-J. Berg, G. Seifert, and H. Graener, *Appl. Phys. Lett.*, **74**, 1200 (1999).
6. Y. Watanabe, M. Inoue and T. Tsuchiya, *J. Appl. Phys.*, **84,** 6457, (1998).

Mat. Res. Soc. Symp. Proc. Vol. 739 © 2003 Materials Research Society

Nanometer-scale Pattern Transfer Using Ion Implantation

Naomi Matsuura, Todd W. Simpson[1], Chris P. McNorgan[1], Ian V. Mitchell[1], Xiang-Yang Mei, Patrick Morales and Harry E. Ruda
Center for Advanced Nanotechnology, Department of Materials Science and Engineering, University of Toronto, 170 College St., Toronto, Ontario, M5S 3E3, Canada.
[1]Department of Physics and Astronomy, University of Western Ontario, London, Ontario, N6A 3K7, Canada.

ABSTRACT

Conventional, broad-area, ion implantation has been combined with unconventional masking to create 2-D geometrical patterns of amorphization in single crystals, with selectable motifs. The patterns are fully developed by use of selective etching. Two examples are discussed. In the first example, a self-assembled array (with lattice spacing ~1 μm) of silica spheres is used as an implant mask over InP. The variation of the mask thickness created by the sphere geometry modulates the implantation depth in a periodic fashion, which is subsequently revealed after selective etching of the associated amorphized volumes. In the second example, nanochannel arrays in an alumina film are used as an implant mask to produce a hexagonal closed packed array of amorphized cylinders in InP and $SrTiO_3$ substrates. The ion beam-amorphized regions of the substrate are then removed by selective chemical etching to achieve the full 3-D patterning of 55 nm diameter holes on a 100 nm lattice spacing.

INTRODUCTION

One of the continuing challenges of nanometer-scale pattern production is the fabrication of large-area patterns with high flexibility and yield, and at a low cost. Patterning methods using self-assembly phenomena provide efficient and low-cost alternative approaches to conventional lithographic techniques for realizing ordered nanostructures. However, the self-assembly approach is typically material dependent, and as such, cannot be easily transferred to other material systems. In contrast, conventional ion implantation allows direct patterning in a wide range of ion-substrate systems, but requires specialized masks for nanoscale patterning. Broad-area ion implantation through self-assembled masks appears to offer a route that overcomes both the material dependence of self-assembly and the difficulty and expense of fabricating nanoscale masks.

In this work, two different types of self-assembled, hexagonal masks are used: a self-assembled close-packed SiO_2 microsphere array (lattice spacing ~1 μm) and a self-assembled nano-channel alumina (NCA) array (lattice spacing ~100 nm). Heavy ions are implanted through the masks to selectively introduce damage into the substrate. The damaged areas are then removed through the use of a wet etchant selective to the amorphized volumes, and the resultant profiles are imaged by field emission scanning electron microscopy (SEM) to determine the fidelity of the nanoscale pattern transfer. Selective etching provides both a method to pattern the substrate and a method to study the 3-D damage distribution produced by the implant. This nano-scale patterning technique is successfully demonstrated on both InP (100) and $SrTiO_3$ (100) substrates.

EXPERIMENTAL DETAILS

Two different configurations were investigated in this work. In the first pattern, aqueous dispersions of 1 μm diameter SiO_2 microspheres were spin-coated onto the InP (100) substrates, using a surfactant-mediated process [1]. This process resulted in monolayer coverage of the substrate in a hexagonal-close-packed lattice. In the second type of pattern, through-hole, self-supported NCA templates were fabricated using a two-step anodic oxidization process [2], and the resultant NCA templates (~150 to 500 nm thick, ~10 mm^2 area) were bonded onto highly polished InP (100) and $SrTiO_3$ (100) wafers.

Ion implantation was performed at the University of Western Ontario Tandetron accelerator. The implant conditions required for amorphization were established in separate experiments, and the implanted ions were selected based on the expected implant depth for the given substrates. In the SiO_2 microsphere array masking process, In ions were implanted through the microsphere array into the substrate at an energy of 1.2 MeV, to a fluence of 5×10^{14} cm^{-2}, sufficient to amorphize the substrate. For the NCA array masked samples, Pt ions were implanted at multiple energies up to 1 MeV, and at fluences sufficient to amorphize the substrate. Here, the Pt ion implantations were performed at normal incidence to the substrate, with the beam aligned parallel to the direction of the pore axis.

In the case of the InP substrates, the amorphized areas were selectively removed using a chemical etch in $HF:HNO_3$ (etch rate 1.7 μm/min) [3], while for $SrTiO_3$, a $HNO_3:H_2O$ solution was used (etch rate 16 nm/min) [4]. Both etchants have selectivities of at least 1000:1. The resultant samples were imaged using a Hitachi S-4500 field emission SEM.

RESULTS AND DISCUSSION

In the first example, a monolayer of monodispersed silica microspheres with a periodicity of ~1 μm was assembled in a hexagonal-close-packed array on an InP (100) substrate (figure 1c). The 2-D array of spheres is used as a physical mask for implantation of the underlying substrate (figure 1a). This mask is unusual because it provides "grayscale" contrast due to the periodic variation in the mask thickness which results in a periodic variation in penetration depth of the ions into the substrate. Following implantation, the damaged regions were removed in $HF:HNO_3$, producing a periodic array of 3-D features on the single crystal substrate (figures 1b, 1d). Good fidelity is observed between the geometry of the mask and the resultant pattern.

In the second example, NCA templates, with periodicities ~100 nm and hole diameters of ~40 nm, were used as masks for ion implantation. The NCA templates, unlike the SiO_2 template mask, have vertical walls (i.e., mask edges). Results from these masks may identify where the physical limitations arise, hence the minimum feature sizes achievable using this technique.

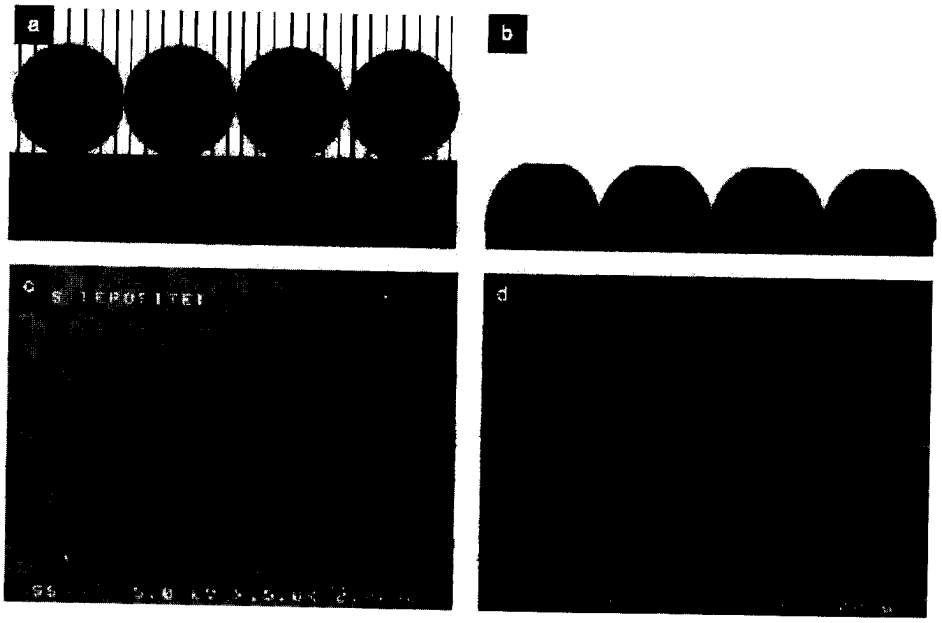

Figure 1. Microsphere array on InP: (a) Schematic representation of the lateral distribution in the ion range produced by the microsphere mask; (b) Schematic representation of the crystalline substrate remaining after the selective etch; (c) Plan view SEM image of the silica sphere array prior to implantation; (d) Tilt view SEM image of the InP substrate following implantation of 1.2 MeV In ions and etching in HF:HNO_3.

Figure 2a shows a plan view SEM image of an as-implanted InP (100), with the NCA template partially removed after implantation. A remaining piece of the NCA template can be seen at the right hand side of the figure, along with the uniformly implanted substrate on the left. In the area where the NCA template has been removed, the pattern of implanted areas is clearly shown, demonstrating the transfer of the NCA nano-hole array pattern to the substrate. Figure 2b shows a side view of the as-implanted InP (100) substrate, along with the overlying NCA mask. The swelling of the implanted areas can be clearly seen in this image, as can the smooth-walled, vertical character of the high-aspect ratio NCA template. Finally, the nanometer-scale pattern transfer due to Pt implantation through the NCA mask into the InP substrate can be clearly seen after selective chemical etching (figures 2c and 2d). The pattern replicates the structure and individual features of the NCA template, with the pore diameters corresponding well to those of the original NCA template. Sub-100 nm feature sizes are achievable using this technique.

One of the benefits of this technique is the material flexibility of this process. This nano-scale patterning process was repeated in $SrTiO_3$ (100), which has excellent selective etching characteristics [4]. Figures 3a and 3b show successful pattern transfer after implantation. After selective removal of the irradiated volumes by chemical etching, the unirradiated crystal was exposed (figures 3c, 3d). The rounded amorphization profile as seen in figure 3d appears to

move slightly underneath the masked area which is consistent with ion stopping theory, which predicts lateral and longitudinal straggle that increase with energy. Interestingly, the etch profiles are well delineated even at the end of the implantation range for deep, high energy implants, suggesting that the lateral scattering is small enough to retain the nanoscale features. It may be noted that the radial straggle of the implanted ions associated with individual Pt ions, derived from the SRIM-2000 simulation is 20 nm [5], which is the order of half the pore-pore separation, indicating that there should be overlap between the implant damage volumes of the adjacent pores, and the nanometer size holes should no longer be delineated from each other at the end of the implantation range. The preservation of individual etch pores suggests that etch rate is a strong function of the degree of disorder in the $SrTiO_3$ lattice. This matter needs to be explored further.

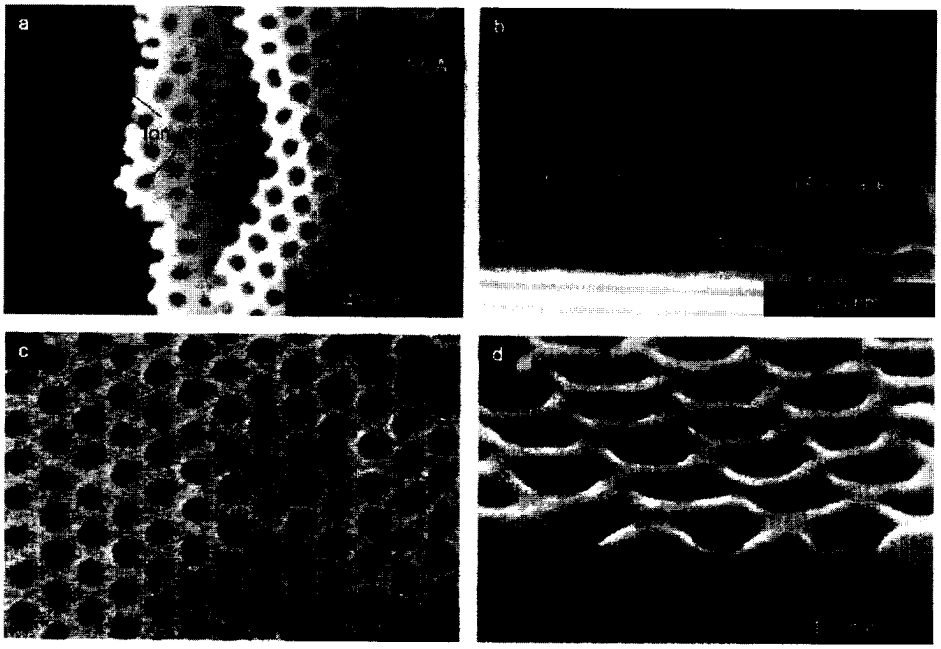

Figure 2. SEM images of an InP (100) substrate, following implantation through a NCA mask: (a) plan view; (b) side view. SEM images after selective etching to remove the amorphized areas: (c) plan view; and (d) tilt view.

In figure 4, the excellent selectivity of amorphous $SrTiO_3$ in the etching solution allows us to observe the lateral spread of damage extending under the region masked by the NCA template at high ion energies (200 keV, 500 keV, and 1 MeV Pt ions at doses of 1×10^{14}, 2×10^{14}, and 2×10^{14} ions/cm^2, respectively). It is clear that when the alumina wall thickness becomes comparable to the lateral spread of damage at such high energies, the individual implanted nanoscale volumes no longer remain separated from each other at the end of the implant range. This feature has very

interesting implications as it suggests that this technique may be used to lift off porous membrane layers, or to nano-machine complex topological features.

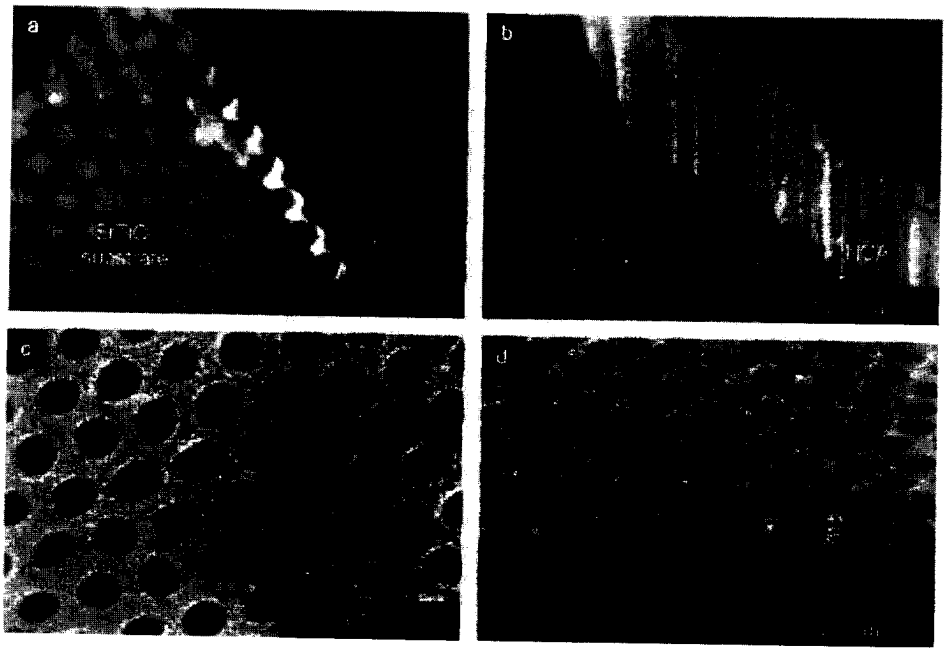

Figure 3. SEM images of a $SrTiO_3$ (100) substrate, implanted with 200 and 500 keV Pt ions at doses of 1×10^{14} and 2×10^{14} ions/cm^2, respectively: (a) plan view; (b) tilted view; and after selective etching to remove the amorphized areas: (c) plan view; and (d) tilt view [4].

Figure 4. Tilted view SEM image of etched, $SrTiO_3$ (100) substrate, amorphized using 200 keV, 500 keV, and 1 MeV Pt ions at doses of 1×10^{14}, 2×10^{14}, and 2×10^{14} ions/cm^2, respectively [4].

The developmental key for this technique is the recent widespread availability of large-area, self-assembled arrays that can be used as masks for conventional ion implantation. The use of such self-assembled structures as masks significantly simplifies the nano-scale array patterning process, as the time-intensive, resolution-limited mask fabrication techniques are no longer required to obtain nano-scale features using conventional ion implantation. Also, the ideal "stencil-type" masks that may be fabricated through self-assembly allows for the direct nanostructure array pattern transfer into the substrate with a selected ion.

CONCLUSIONS

Direct ion implantation of high-density, sub-100 nm nanostructures using conventional ion implantation and self-assembled masks was studied. This work shows there is an alternative means of patterning at sub-100 nm scales, with the distinct advantage of being able to directly pattern extremely high-density features in a massively parallel, single step technique without the use of a resist. This process was successful for patterning both InP and $SrTiO_3$, suggesting that this process may be flexible for a number of species-target configurations. We anticipate that any material that exhibits sufficiently different etch rates in amorphous and single crystal forms may be patterned by this process. Beyond the issue of technology, it is of interest to use the etch behavior to study the limitations of ion lithography. By standard techniques, it is not possible to directly ascertain the three-dimensional profile of the implanted ions in high-density nanoscale patterns [6]. Here, however, we demonstrate the use of a highly selective etch to demarcate the boundaries of the implanted regions. Using this method, we can determine the density and resolution limits of our implant through the removal of the damaged areas, show that we can selectively implant ions in nanometer-scale areas, and can nano-machine structured arrays by selective etching of difficult materials.

ACKNOWLEDGEMENTS

The authors would like to thank Dr. Selva Nair for discussions, and would like to gratefully acknowledge the Canadian Institute for Photonic Innovations and NSERC for their support of this work.

REFERENCES

1. Chris McNorgan, Todd W. Simpson and Ian V. Mitchell, to be published.
2. H. Masuda and K. Fukuda, *Science* **268**, 1466 (1995).
3. Todd W. Simpson, Paul A. Gallivan, and Ian V. Mitchell, *Electrochemical and Solid-State Letters* **4** (3) G26-G27 (2001).
4. Naomi Matsuura, Todd W. Simpson, Ian V. Mitchell, Xiang-Yang Mei, Patrick Morales and Harry E. Ruda, *Appl. Phys. Lett.* **81** (24), (2002) in press.
5. J.F. Ziegler, J.P. Biersack, and U. Littmark, *The Stopping and Range of Ions in Solids* (Pergamon, New York, 1985).
6. N. Peng, C. Jeynes, R.P. Webb, I.R. Chakarov, and M.G. Blamire, *Nucl. Instrum. Methods Phys. Res. B* **178**, 242 (2001).

Mat. Res. Soc. Symp. Proc. Vol. 739 © 2003 Materials Research Society

Fabrication of Perforated Film Nanostructures

A. L. Elias, K. D. Harris and M. J. Brett
Department of Electrical and Computer Engineering,
University of Alberta, Edmonton, AB, Canada T6G 2V4, aelias@ualberta.ca

ABSTRACT

We have demonstrated the fabrication of perforated thin films (PTFs), comprised of thin coatings perforated with unusual pore shapes such as helices or chevrons. PTFs are fabricated using a template of nanohelices or nanochevrons produced using the Glancing Angle Deposition (GLAD) technique. PTFs can be produced by filling GLAD films with a variety of substances, etching back the coating to reveal the tips of the helices or chevrons, and etching out the template film. A process for fabricating nickel PTFs has been developed, and a nickel PTF of helical pores with nominal diameters of 100nm has been produced.

INTRODUCTION

There are a number of techniques that may be used to produce thin films perforated by ordered and randomly arranged pores. A two-step anodization process can be used to produce straight pores 100μm deep in alumina with aspect ratios of around 500 [1]. These pores may be randomly organized, self-organized or grown from a lithographically produced pre-pattern. Similarly, ordered arrangements of pores may be produced in silicon by electrochemically etching an illuminated, pre-patterned wafer in hydrofluoric acid [2]. Etching occurs along the [100] direction of the silicon, resulting in the formation of straight pores. Electrochemically etched pores are typically cylindrically symmetric and extend straight through the film in a direction perpendicular to the surface.

We have previously demonstrated the fabrication of photoresist and spin-on-glass films consisting of thin (1μm – 2μm) films perforated by unusually shaped pores such as helices and chevrons [3]. These films have been produced in a four-step process using SiO and SiO_2 GLAD films as templates. Periodic arrays of helices have been demonstrated by using a template film deposited on a lithographically pre-patterned substrate.

These films have a variety of potential applications. Both helical template and perforated films exhibit circular birefringence – linearly polarized light incident on these films experiences strong rotation. The optical rotatory power of photoresist PTFs has been shown to be two to three times as high as the SiO_2 template films from which they were cast [4]. The large surface area of template and perforated thin films also makes them useful for applications such as sensors. SiO template films and photoresist perforated films have been demonstrated as high speed humidity sensors [5]. Other potential applications for perforated thin films include photonic bandgap crystals [6] or chirally selective filters.

FABRICATION

We will now discuss the 4-step fabrication process used to produce nickel films perforated with helical pores. Each of the four steps is illustrated by scanning electron micrograph (SEM) images of side and top views. These images were taken at every step in the processing of a single film.

Step 1: Template Deposition

The templates from which PTFs are cast are fabricated using GLAD, which is a physical vapour deposition (PVD) process [7-9]. In traditional PVD the substrate is perpendicularly oriented with respect to the source, and growth occurs in the direction from which the sputtered or evaporated material arrives. In glancing angle deposition the substrate is obliquely oriented with respect to the source at an angle α greater than 80°, as shown in Figure 1. Parts of the substrate are shadowed by material that has already been deposited. This results in the growth of porous films with independent, isolated nanostructures. The porosity of the film is determined by the angle α at which it is deposited, with greater α leading to greater porosity. The template film must be sufficiently porous so that the material with which it will be filled can penetrate to the substrate.

Substrate motion can be incorporated into the deposition process in order to produce films with a specific structure. The films will always grow towards the source at an angle β, which is less than α, as shown in Figure 1. This figure illustrates the growth of slanted posts, which can be deposited by holding the substrate stationary. Chevrons, helices and square spirals can all be grown by introducing the appropriate motion. Examples of these structures are shown in Figure 2. The diameter of the resulting nanostructures is determined by a number of factors including the material being deposited and the rate of deposition. Typical dimensions are on the order of tens to hundreds of nanometers.

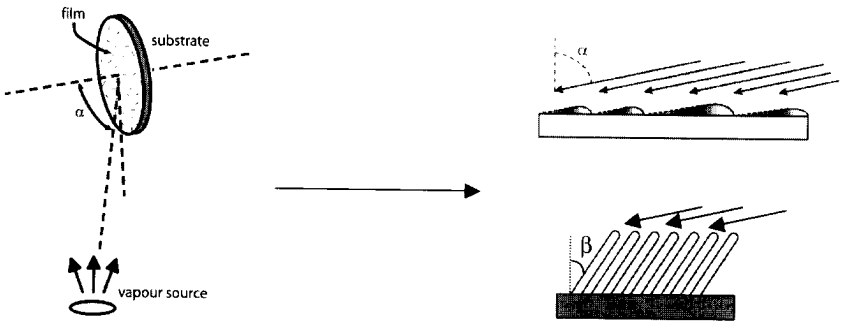

Figure 1: Glancing Angle Deposition: Set-up (left) and film growth for stationary substrate and source (right).

Figure 2: Examples of GLAD Films: Left: Chevrons can be fabricated by abruptly and repeatedly rotating the substrate through 180°. Center: Square spirals can be made by abruptly and repeatedly rotating the substrate through 90° [6]. Right: Vertical posts are grown by continuously rotating the substrate during the deposition process.

The template for the nickel PTF that we are discussing is shown in Figure 3. This template is comprised of SiO helices, which were deposited by e-beam evaporation at an angle of $\alpha = 85°$. The diameter of each helix is approximately 100nm. The substrate is a silicon wafer coated with approximately 75nm of chromium, which acts as an electrical contact for the electroplating process.

Step 2: Filling

A sample of the template film with a surface area of approximately $2cm^2$ is electroplated in a nickel sulfamate bath for 16 minutes. This solution is commercially available from Transene, under the product name Nickel SN10. This bath contains both nickel chloride and boric acid. The bath is heated during the plating process to 35-50°C. The nominal applied voltage and current are 2V and 1.7mA. The electroplated sample is shown in Figure 4. Note that the electroplated material extends beyond the tips of the SiO helices.

Step 3: Etch-Back

The deposited nickel is next stripped back in order to expose the top of the template film. To accomplish this, the sample is immersed in a dilute solution of nitric acid (35%), immediately removed and rinsed with water to stop the etching. The tips of the exposed helices are shown in Figure 5.

Step 4: Etch-Removal

In the final step of this process the template helices are removed by immersing the sample in a solution of buffered oxide etch (BOE) for 10 minutes. BOE is a 10:1 mixture of ammonium bifluoride and hydrofluoric acid (49%). The final perforated thin film is shown in Figure 6.

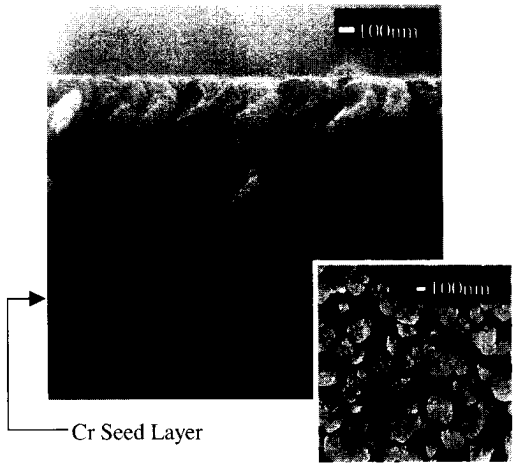

Figure 3: Template Film: SEM images of the side and top view of the original SiO helices, which were deposited on a Cr coated silicon wafer.

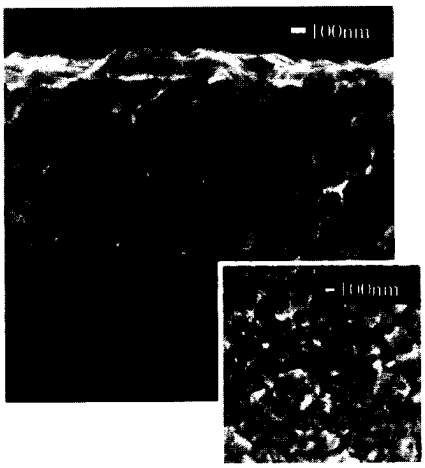

Figure 4: Plated Film: The nickel filling extends from the substrate to above the helices.

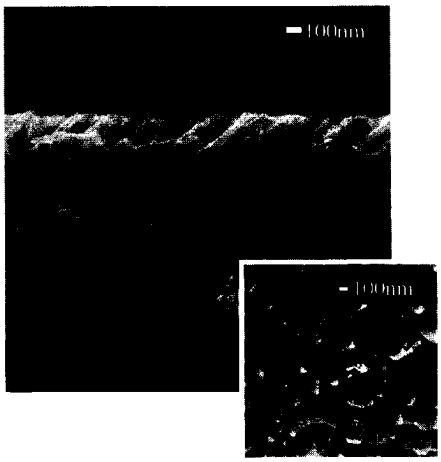

Figure 5: Etched-Back Sample: The tips of the helices now protrude above the top of the nickel deposit.

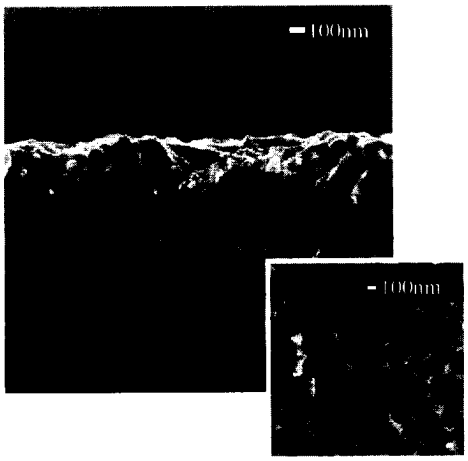

Figure 6: Nickel PTF: The template film has been removed, leaving a nickel film perforated with helical pores.

CONCLUSIONS

GLAD films can be used as templates from which thin films perforated with a variety of nanostructures can be cast. In this report we have demonstrated the fabrication of the first metal thin films perforated with helical pores. We are currently investigating the fabrication of PTFs from other materials, and their potential applications as optically active devices, sensors and photonic bandgap devices.

ACKNOWLEDGEMENTS

The authors would like to thank George Braybrook of the Department of Earth and Atmospheric Sciences at the University of Alberta for the excellent SEM work found within this paper, as well as Scott Kennedy and Mike Colgan for providing images of square spirals and vertical posts. This work was supported by the Alberta Ingenuity Fund, the Natural Sciences and Engineering Research Council of Canada (NSERC), the Alberta Informatics Circle of Research Excellence (iCORE), and Micralyne, Inc.

REFERENCES

1. A.P Li, F. Müller and U. Gösele, *Electrochem. Solid-State Lett.* **3** (3), 131-134 (2000).
2. R.B. Wehrspohn and J. Schilling, *MRS Bull.* **8** (26), 623-625 (2001).
3. K.D. Harris, K.L. Westra, and M.J. Brett in *Nonlithoghraphic and Lithographic Methods of Nanofabrication - From Ultralarge-Scale Integration to Photonics to Molecular Electronics*, edited by L. Merhari, J.A. Rogers, A. Karim, D.J. Norris, and Y. Xia, (Mater. Res. Soc. Proc. **636**, Boston, MA, 2001) D9.37.1-D9.37.6.
4. K.D. Harris, J. Sit and M.J. Brett, *IEEE Trans. Nanotech.* **1** (3), 122-128, (2002).
5. K.D. Harris, A. Huizinga and M.J. Brett, *Electrochem. Solid-State Lett.* **5** (11), H27-H29 (2002).
6. S.R. Kennedy, M.J. Brett, O. Toader, and S. John, *Nano Lett.* **2** (1), 59-62 (2002).
7. K. Robbie and M.J. Brett, *J. Vac. Sci. Technol. A*, **15** (3), 1460-1465 (1997).
8. K. Robbie and M.J. Brett, U.S. Patent No. 5,866,204, (2 February 1999).
9. K. Robbie, M.J. Brett, and A. Lakhtakia, *Nature* **384**, 616 (1996).

Mat. Res. Soc. Symp. Proc. Vol. 739 © 2003 Materials Research Society H8.10

3-D Nanoengineering of Metal Oxides and Oxyhydroxides by Aqueous Chemical Growth

Lionel Vayssieres and Arumugam Manthiram
Texas Materials Institute, University of Texas at Austin, Austin, TX 78712

ABSTRACT

Advanced nanoparticulate thin films of transition metal oxides consisting of nanorods with different orientations onto various substrates have been successfully grown by aqueous chemical growth without template, surfactant, or applied electric/magnetic field. The synthesis involves the aqueous condensation of metal ions from solutions of metal salts or metal complexes. Such low-cost fabrication of nanoengineered 3-D arrays consisting of 1-D nanorods of iron oxide (hematite), zinc oxide (zincite), and manganese oxyhydroxide (manganite) with parallel and perpendicular orientations onto various substrates are presented.

INTRODUCTION

Low-cost fabrication of particulate thin films, coatings, and large three-dimensional (3-D) arrays of anisotropic one-dimensional (1-D) nanomaterials such as nanorods, nanowires, and nanotubes is of importance for the development of future nanodevices. In this regard, our strategy to generate large area of advanced nano and micro-particulate thin films at low cost is a bottom-up chemical approach [1] that is well-sustained by a thermodynamic model for the monitoring of the nucleation, growth, and aging processes and the experimental control of the interfacial free energy of the system [2]. Such a strategy has been well-illustrated on the size control of magnetite nanoparticles over an order of magnitude [3]. This concept and synthetic method allows design and creation of metal oxide nanomaterials with novel morphology, texture, and orientation to probe, tune, and optimize their physical properties. Particulate thin films and 3-D arrays are obtained by direct growth onto various substrates from the condensation of aqueous precursors at low temperatures. Such an approach to material synthesis offers the ability to generate anisotropic nanoparticles and to control their orientation onto substrates. Growing and aligning anisotropic nanoparticles into large arrays on a substrate require consideration of the homogeneous and heterogeneous nucleation phenomena. In most cases, homogeneous nucleation of solid phases from solution requires a higher activation energy barrier, and therefore, heteronucleation will be promoted and energetically more favorable. Indeed, the interfacial energy between the crystal and the substrate is smaller than the interfacial energy between the crystal and the solution, and therefore, nucleation may take place at a lower saturation ratio onto a substrate than in solution. Nuclei will randomly appear onto the entire substrate and if their nucleation is controlled and maintained at a limited rate by the precipitation conditions, epitaxial crystal growth will take place from these nuclei along the easy direction of crystallization and a condensed phase of single-crystalline nanorods perpendicular to the substrate will be generated. Alternatively, by enhancing the number of nuclei, a condensed phase of single-crystalline nanorods parallel to the substrate will be generated [1].

Such an approach has been successfully applied for the growth of advanced nano- and micro- particulate metal oxide materials such as three-dimensional arrays of ferric oxide nanorods [4, 5], nanocomposite arrays of iron and chromium sesquioxides [6], nanorod [7], microrod [8], and microtube [9] oriented arrays of zinc oxide. Porous nanocomposites of metal

oxide/bio-materials [10] for bio-sensing applications and ferromagnetic 3-D array of metallic iron nanorods [11] for magnetic devices have also been fabricated by such a method. In addition to developing functional materials for various applications, growing such large nanostructured arrays with well-controlled orientation and morphology allows experimental probing of well-defined nano- to micro-structures. Consequently, a direct feedback between theoretical calculations and experimental data could contribute to the improvement and optimization of existing devices as well as to a better fundamental knowledge of their physical/chemical properties.

MATERIALS AND METHODS

The materials synthesis was performed according to the concept and general template-free thin film processing technique developed by Vayssieres et al [1]. The general steps involved in this synthetic technique are presented in figure 1.

- 3-D nanorod arrays of α-Fe_2O_3 (hematite) have been created by thermodynamic stabilization and heteronucleation of the metastable β–$FeOOH$ (akaganeite) onto various substrates from iron salts at low pH and high ionic strength. Subsequent heat treatment in air at 450°C for an hour was performed to obtain α-Fe_2O_3 [4].
- 3-D nanorod arrays of ZnO (zincite) have been obtained by thermal decomposition and subsequent hydrolysis-condensation of aqueous solutions of methenamine complexes of Zn(II) [7, 8] at mild temperatures (below 100 °C).
- 3-D nanorod arrays of γ-$MnOOH$ (manganite) have been obtained at 70 °C by aging Mn(III) salts in basic solutions.

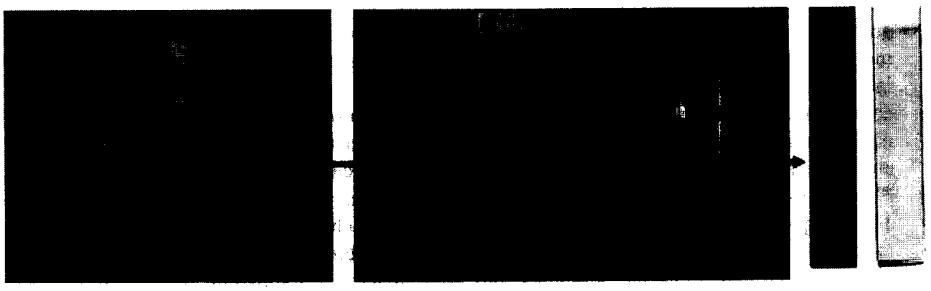

Figure 1. The aqueous chemical growth (ACG) thin film processing technique: immersion of substrates in aqueous solutions of metal salt precursors at room temperature (left), heat treatment in laboratory oven below 100 °C (center), and generation of nano-, meso- and micro-particulate thin films of large (several tens of cm^2) physical surface area on various substrates (right).

RESULTS AND DISCUSSION

Figure 2 shows the SEM pictures of 3-D arrays of metal oxides obtained by aqueous chemical growth. It consists of aligned nanorods with two different orientations: parallel and perpendicular to the substrate. The α-Fe_2O_3 arrays (figure 2, top) consist of 50 nm nanorod bundles, made of nanowires of 3-4 nm in diameter and about 0.7 to 1 μm in length regardless of their orientation. Such advanced particulate thin films have been designed to develop electrodes

for wet photovoltaic cells. Indeed, the diameter of such nanorods is an excellent match of the minority carrier diffusion length of hematite [12]. Therefore, the photogenerated holes have a very short distance to travel and do not recombine easily with photogenerated electrons. Accordingly, a very efficient charge separation occurred along with a high incident photon-to-electron conversion efficiency (IPCE), which led to the creation of a 2-electrode hematite photovoltaic cells [13] and photocatalytic cells for the photo-oxidation of water [14]. In addition to applied knowledge and device optimization, a general fundamental understanding has been developed by probing and demonstrating the influence of the orientation of nanoparticles on the photoelectrochemical properties of metal oxide photo-anodes. Besides the designed grain boundary-free direct electron pathway and the structural match for the hole diffusion length, a quantum confinement has also been suggested which is currently being investigated by resonant inelastic x-ray scattering (RIXS) at synchrotron radiation source facility.

Such theoretical approach and synthetic method is also suitable for other metal oxide particulate thin films and have been demonstrated, for instance, by the creation of 3-D array of ZnO consisting of crystalline hexagonal nanorods (figure 2, center). Such materials have been designed to study their electronic structure and optical properties as well as to probe such low cost and well-designed materials for nanolaser applications due to the large exciton binding energy of ZnO [15, 16].

Manganese oxides and oxyhydroxides have also been investigated and nanorod arrays of γ-*MnOOH* on polypropylene and silicon wafers as well as on Mn_3O_4 (hausmannite) have been obtained (figure 2, bottom). Such materials are under investigation for energy storage and conversion [17-21] as well as for developing a better fundamental understanding of their crystallographic relationships [22].

In addition to nanoparticulate thin films, aqueous chemical growth synthesis can produce highly ordered microparticulate thin films. For instance, zincite ZnO consisting of three-dimensional arrays of perpendicular hexagonal microrods have also been produced [8]. The rods are crystalline and elongated along the c-axis of the wurtzite crystal structure. Such purpose-built material has been designed to study the influence of the rod length on the photoelectrochemical properties and electron transport of ZnO electrodes in the UV region as well as to develop ZnO and dye-sensitized ZnO photovoltaic cells [23-25]. Given that such microparticulate thin films are highly oriented both physically and crystallographically, studies of their electronic structure by polarization dependent soft X-ray absorption spectroscopy (XAS) has been investigated along with first-principle calculations to successfully resolve the oxygen orbital symmetry and its contribution to the conduction band of ZnO [26].

Patterning, assembly, and integration of 1-D nanomaterials as functional 3-D network is an important challenge scientists have to face to develop practical nanodevices. Fabrication of patterned 3-D arrays is possible with the aqueous chemical growth technique and figure 3 shows various examples of such an ability with ZnO materials. Well-defined stars and stripes of ZnO nanorods of various patterns are obtained by chemical and/or physical activation and modification of the silicon wafer substrates [27]. Such fabrications of patterned arrays are currently being investigated with various substrates (amorphous, single crystals and polycrystalline). With this approach, promising results are foreseen for the low-cost fabrication of large patterned array of transition metal oxides as well as for the creation of novel optoelectronic and magnetic nanodevices.

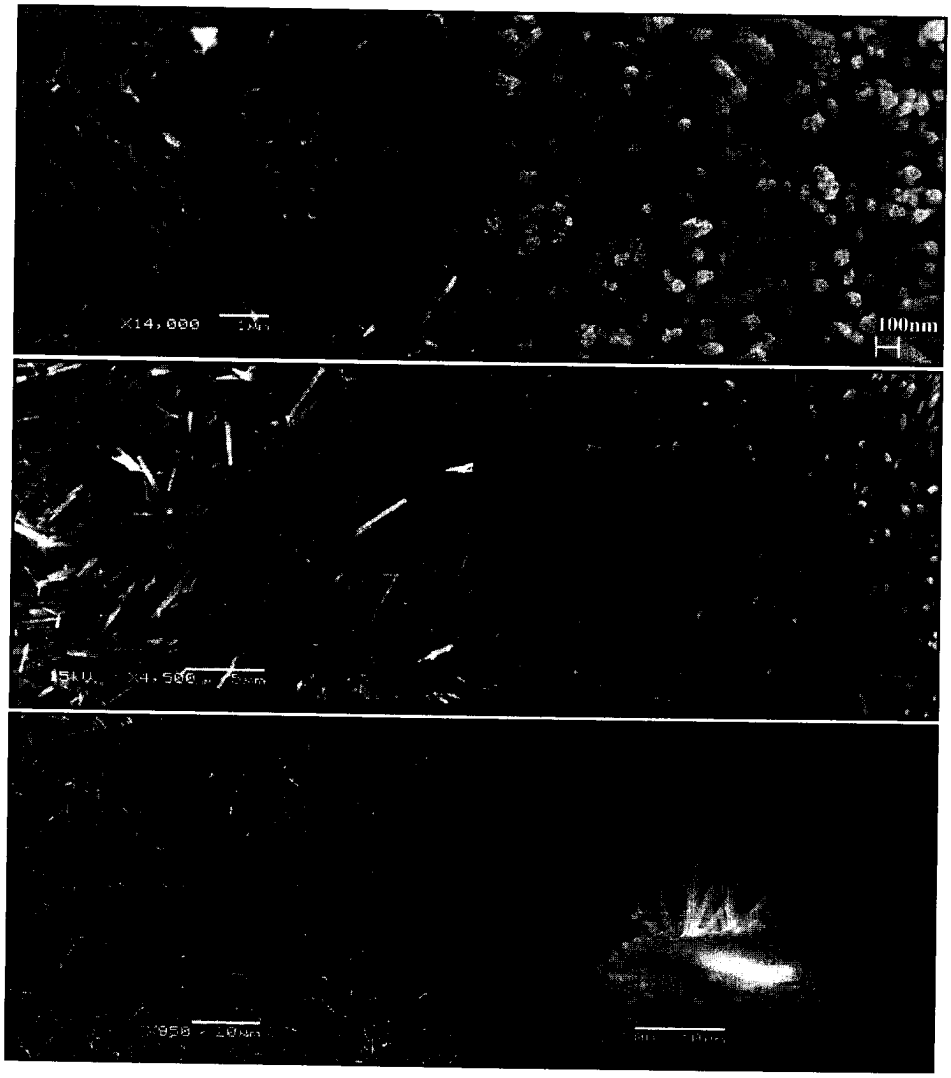

Figure 2. SEM pictures of 3-D arrays of α-Fe_2O_3 (top), ZnO (center), and γ–MnOOH (bottom) grown by aqueous chemical growth. The arrays consist of 1-D nanorods oriented parallel (left) and perpendicular (right) onto the substrates.

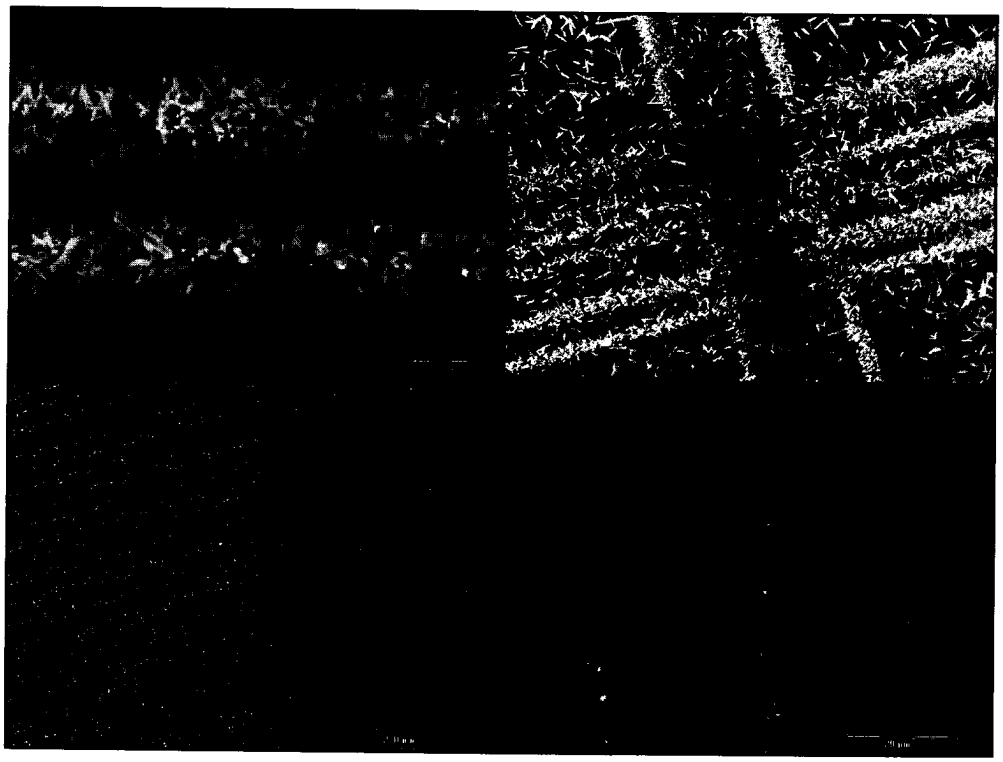

Figure 3. SEM pictures of various 3-D patterned arrays of ZnO (zincite) grown by aqueous chemical growth onto commercial silicon and silicon oxide wafers.

CONCLUSIONS

The ability to produce at low cost large three-dimensional patterned arrays of transition metal oxides consisting of anisotropic nanoparticles with controlled orientations onto various substrates without the use of templates, surfactants, or applied external fields has been presented. This approach to nanoparticulate thin films is anticipated to contribute not only to the development of smart and functional nanomaterials for optoelectronic, photoelectrochemical, and magnetic devices, but also to a better fundamental understanding of the physical and chemical properties of anisotropic nanostructures.

ACKNOWLEDGEMENTS

This work was supported by the Welch Foundation Grant F-1254.

REFERENCES

1. L.Vayssieres, *Int. J. Mater. Prod. Technol.* **18(1-3)**, 1-25 (2003); *Pure Appl. Chem.* **72(1-2)**, 47-52 (2000)
2. L.Vayssieres, *Int. J. Nanotechnol.* **1(1)**, 1 (2003); Ph.D. Dissertation, Université Pierre et Marie Curie (Paris), 1995.
3. L.Vayssieres, C. Chaneac, E. Tronc and J.-P. Jolivet, *J. Colloid Interface Sci.* **205(2)**, 205-212 (1998)
4. L.Vayssieres, N. Beermann, S.-E. Lindquist and A. Hagfeldt, *Chem. Mater.* **13(2)**, 233-235 (2001)
5. L.Vayssieres, J.-H. Guo and J. Nordgren, in *Anisotropic Nanoparticles: Synthesis, Characterization and Applications*, edited by L. A. Lyon, S. J. Stranick, C. D. Keating, P. C. Searson, (*Mater. Res. Soc. Symp. Proc.* **635**, Warrendale, PA, 2001), pp. 781-786
6. L.Vayssieres, J.-H. Guo and J. Nordgren, *J. Nanosci. Nanotech.* **1(4)**, 385-388 (2001)
7. L.Vayssieres, *Adv. Mater.* **15**, (2003) in press.
8. L.Vayssieres, K. Keis, S.-E. Lindquist and A. Hagfeldt, *J. Phys. Chem. B* **105(17)**, 3350-3352 (2001)
9. L.Vayssieres, K. Keis, A. Hagfeldt and S.-E. Lindquist, *Chem. Mater.* **13(12)**, 4395-4398 (2001)
10. L.Vayssieres, in *Surface Engineering: Science and Technology II,* edited by A. Kumar, Y.-W. Chung, J. J. Moore, G. L. Doll, K. Yatsui, and D. S. Misra (The Minerals, Metals and Materials Society, Warrendale, PA, 2002), pp. 51-59
11. L.Vayssieres, L. Rabenberg and A. Manthiram, *Nano Lett.* **2(12)**, 1393-1395 (2002)
12. J. H. Kennedy and K. W. Frese, *J. Electrochem. Soc.* **125(5)**, 709-714 (1978)
13. N. Beermann, L.Vayssieres, S.-E. Lindquist and A. Hagfeldt, *J. Electrochem. Soc.* **147(7)**, 2456-2461 (2000)
14. T. Lindgren, H. Wang, N. Beermann, L.Vayssieres, A. Hagfeldt and S.-E. Lindquist, *Sol. Energy Mater. Sol. Cells* **71(2)**, 231-243 (2002)
15. M. H. Huang, S. Mao, H.Feick, H.Yan, Y.Wu, H. Kind, E. Weber, R. Russo, P. Yang, *Science* **292**, 1897-1899 (2001); *Adv. Mater.* **13(2)**, 113-116 (2001)
16. Y.C. Kong, D.P. Yu, B. Zhang, W. Fang, S.Q. Feng, *Appl. Phys. Lett.* **78**, 407-409 (2001)
17. A. Manthiram and J. Kim, *Trans. Soc. Adv. Electrochem. Sci. Technol.* **34**, 1-5 (1999)
18. A. M. Kannan and A. Manthiram, *Electrochem. Solid State Lett.* **5**, A167-A169 (2002)
19. A. M. Kannan, S. Bhavaraju, F. Prado, M. Manivel Raja, and A. Manthiram, *J. Electrochem. Soc.* **149**, A483-A492 (2002)
20. Y. U. Jeong and A. Manthiram, *J. Electrochem. Soc.* **149(11)**, A1419-1422 (2002)
21. D. Im and A. Manthiram, *J. Electrochem. Soc.* **150**, A68-A73 (2003)
22. L.Vayssieres, L. Rabenberg, and A. Manthiram, to be published
23. J. Zhong, A.H. Kitai, P. Mascher and W. Puff, *J. Electrochem Soc.* **140(12)**, 3644-3649 (1993)
24. K. Keis, L. Vayssieres, S.-E. Lindquist and A. Hagfeldt, *J. Electrochem. Soc.* **148(2)**, A149-155 (2001); *Nanostruct. Mater.* **12(1-4)**, 487-490 (1999)
25. K. Keis, E. Magnusson, H. Lindstrom, S.-E. Lindquist and A. Hagfeldt, *Sol. Energy Mater. Sol. Cells* **73(1)**, 51-58 (2002)
26. J.-H. Guo, L. Vayssieres, C. Persson, R. Ahuja, B. Johansson and J. Nordgren, *J. Phys.: Condens. Matter* **14(28)**, 6969-6974 (2002)
27. L.Vayssieres and A. Manthiram, to be published.

Applications of Nanostructures and Devices

Mat. Res. Soc. Symp. Proc. Vol. 739 © 2003 Materials Research Society

Bio-inspired Self-Assembly of Micro and Nano-Structures for Sensing and Electronic Applications

H. McNally[1], S.W.Lee[1], D.Guo[1], M.Pingle[2], D.Bergstrom[2], R.Bashir[1,3]
School of Electrical and Computer Engineering[1], Department of Medicinal Chemistry[2], Department of Biomedical Engineering[3], Purdue University, W. Lafayette, IN 47907

ABSTRACT

Bio-inspired assembly, through the use of bio-molecules such as DNA and proteins, will play a critical role in the advancement of novel sensing techniques and for the realization of heterogeneous integration of materials. For many of these applications, such as antibody-based biosensor and the study of controlled cell growth, DNA and protein patterning techniques are crucial. We will present an update of our work on protein patterning techniques using microelectronic fabrication, DNA hybridization and biotin-streptavidin pairing. To show its application in biological inspired self-assembly, this technique was used successfully in the self-assembly of 20 nm streptavidin conjugated gold particles. In addition, the integration of nano- and micro-scale heterogeneous materials is very important for novel material synthesis and electro-optic applications. We will present an update on our work to assemble silicon electronic devices using DNA/charged molecules and electric fields. Devices are fabricated, released, charged with molecules, and subsequently manipulated in electric fields. The techniques described can be used to integrate the hybrid devices such as nano- or micro-scale resistors, PN diodes, and MOSFETs on silicon or other substrates such as glass, plastic, etc.

INTRODUCTION

Self-Assembly techniques have experienced a tremendous increase in research activity over the recent years. Applications such as the integration of heterogeneous materials for electronic application, development of nano-scale electronic devices, biological and chemical sensing, and medical diagnostics may all benefit from the understanding of self-assembly processes. Self-assembly of useful devices may come in the form of biological [1,2], chemical [3], electrostatics [4], or fluidics [5] as well as any combination of these techniques. To controllably manipulate structures at the micro and nano-meter scale is a challenge, once accomplished, will lead to a new generation of materials and detection schemes.

Nature assembles nano-scale components using molecular recognition. In the case of DNA, hydrogen bonding is the driving force behind the matching of complementary pairs of single-stranded (ss) DNA to hybridize into a double strand (ds) of helical DNA. It has been estimated that each base pair binds with 0.5kCal/mol of energy [6]. For the use of a 18mer oligonucleotide, the binding energy can be estimated at around 9kCal/mol. However, the actual binding energy of a dsDNA is dependent on the base-pair sequence, salt concentration of surrounding media, temperature, among others. In the case of antibodies/antigens and ligands/receptors, binding takes places by a combination of electrostatic forces, chemical bonding, and shape-mediated effects. As an example, avidin is a large protein that has binding

sites for four biotin molecules. The affinity of the biotin-avidin complex is equivalent to 21kCal/mol [7]. Molecules may be covalently attached to the gold surface of a patterned substrate using the Au-S thiolate bond, which has energy of 44kCal/mol [8]. Hence, DNA and biotin/avidin complexes are useful candidates for self-assembly applications since their binding, even though non-covalent, can be as strong as many covalent interactions.

Assembly of particles in fluids and electric fields can be described by dielectrophoresis (DEP) and electrohydrodynamic forces. The effects of DEP force [9] is understood by knowing the size of the particle, the complex permitivities of the particle and the surrounding media, and the electric field applied. If the DEP force is positive the particle will move toward the maximum electric field gradient. Alternatively, if the DEP force is negative the particle will move toward the minimum electric field gradient. Electrothermal forces [10] in solution are generated by the applied electric field and its associated power density resulting in localized temperature gradients. These temperature gradients produce spatial variation in the electrical conductivity and permitivity leading to electrothermal forces. However, using low frequency AC fields, AC electroosmosic forces (analogous to DC electroosmosis), can be observed [11]. These forces are dependent on the frequency and the square of the magnitude of the applied electric field.

In this paper we present an update of our work to assemble particles, including silicon islands using biological, chemical and electric field techniques. Biological events such as DNA hybridization and ligand/receptor are being investigated for the selective assembly of micron and nano-scale particles. As biological bonds are considered to be short range in nature [12], long range techniques such as electric field assembly is being investigated to bring the particles close to the desired bonding sites.

EXPERIMENTS

The experiments below build upon our experience and success with the attachment and hybridization of DNA to surfaces [13]. In that report we described procedures for oligonucleotide functionalization of surfaces which included a biotin tag for the subsequent capture of avidin coated particles. The procedures were developed and optimized using polystyrene beads due to their lightweight, high concentrations and availability. Recently we have extended these techniques to the patterned assembly of gold nanoparticles and then to the assembly of silicon islands/devices for functional electronics. Figure 1 provides a schematic of the approaches, which may be taken. For all three cases, the particles could be beads, devices, or other nano and micro-scale objects. Figure 1a presents an approach that uses DNA only and relies on hybridization for attachment of the islands to the surface [14]. The substrate surface is functionalized with ssDNA while the complementary strand is attached to the gold surface of the particle. Direct hybridization into a dsDNA would result in capture of the islands onto the patterned gold surface. Indirect hybridization has also been demonstrated, in which a third DNA strand is used to hybridize with the strands attached to the surface and to the particles. We have begun with the approach shown in Figure 1b, which utilizes DNA and ligand-receptors for the capture of avidin-coated particles. A dsDNA is attached to a surface presenting a biotin. The strong affinity between avidin and biotin is relied upon to ultimately capture the particle. This design allows for the verification of ssDNA attachment to the surface, hybridization into the dsDNA and the availability of biotin for particle capture. Figure 1c also shows the capture of

particles with a thin layer of gold so the particles may also be functionalized with DNA via the Au-S bond. The ssDNA is attached to the gold surface and subsequently hybridized. Again, the dsDNA present biotin molecules for attachment to the avidin molecule. Avidin is first absorbed on the substrate surface and then the particles are captured using one of the other three sites of the immobilized avidin. We have used the approach depicted in figure 1c for the attachment of devices to each other in a fluid.

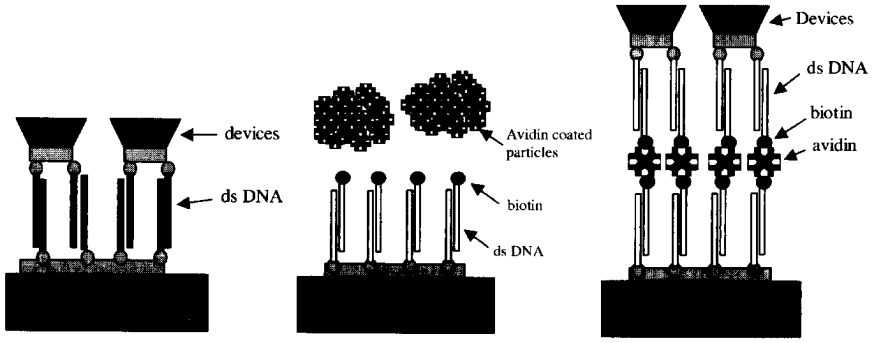

Figure 1 Various strategies for bio-inspired assembly of particles (not drawn to scale). (a) DNA on both devices and substrates, (b) Use of biotinylated-DNA on substrate and avidin on particles, (c) Use of biotinylated-dsDNA on both substrate and devices and avidin as linking element.

Gold Nanoparticle Capture

Reduction of particle size and increase in density are important for detection with high sensitivity and high spatial resolution. Attachment of nanoparticles to surfaces is of significant interest and has previously been accomplished [1,2]. In our work, biological events such as DNA hybridization and protein interactions were used for the assembly of 20nm gold nanoparticles using the strategy presented in Fig1b. 18mer oligonucleotides were obtained through the Laboratory for Macromolecular Structure at Purdue University. These are presented in Table I, along with the function of each sequence. The thiolated oligonucleotides were used for attachment to gold surfaces on patterned silicon substrates. The same oligonucleotides without thiol molecules were used as control for attachment experiments. Non-complementary hybridization sequences were used as control for hybridization. Biotin (Glen Research, Cat No. 10-5950-95) was attached to the 5' end during the DNA synthesis. Our procedure for ssDNA surface attachment and hybridization was adapted from the process to attach DNA strands to gold nanoparticles [15]. Briefly, attachment begins by placing 300μL of15μM thiolated ssDNA in water on the cleaned samples surface. The solution and sample is allowed to incubate on a shaker for 12 hrs. Then 75μL of a 5X phosphate buffer is added to the vials and the solution is again allowed to incubate on a shaker for 24hrs. The sample is then carefully rinsed in 0.3M phosphate-saline buffer. Hybridization is also performed on the same substrate. The substrate is placed into a cleaned vial with 15μM solution of the complementary ssDNA sequence in a

phosphate and NaCl buffer. The vial is then placed in a waterbath at 78°C for 10min. The water bath with vials is allowed to cool slowly to room temperature and the samples are again rinsed in 0.3M phosphate-saline buffer. Now the samples are ready for exposure to the protein coated nanoparticles for capture. We have used streptavidin coated gold nanoparticles (SPI Supplies, Cat# EMSTP20). The patterned substrate surface is exposed to streptavidin-coated gold nanoparticles at a concentration of 10^{x}/ml in PBS. The reaction was performed for 45 minutes at 37°C while swirling the vial contents. Removal of nonspecifically bound nanoparticles was accomplished by placing the assembly substrate into PBS and sonication for 30sec. The samples were then rinsed with DI water and dried with N_2 prior to analysis. A Digital Instruments Dimension 3100 atomic force microscope (AFM) was used to obtain images of the surface in the tapping mode using an etched silicon tip (OTESPA).

Table I Oligonucleotides Used for Assembly

Attachment	5'- (X)-C-A-G-T-C-A-G-G-C-A-G-T-C-A-G-T-C-A- 3'
Control attachment no thiol	5' C-A-G-T-C-A-G-G-C-A-G-T-C-A-G-T-C-A- 3'
Hybridization w/ biotin	5'- (B)-T-G-A-C-T-G-A-C-T-G-C-C-T-G-A-C-T-G-3'
Non-complementary Hyb w/ biotin	5'- (B)-G-C-A-A-T-C-C-C-G-T-A-G-G-A-C-A-T-C-3'

X = thiol (SH), B = biotin

Silicon Island Assembly

The assembly of functional silicon devices is of extreme interest for use in the integration of heterogeneous materials. We have begun by assembling silicon islands of no active electronic characteristics. However the next step would be to fabricate devices with similar dimensions and interesting electronic capabilities. Two types of islands have been fabricated. The first have previously been reported [16]. The silicon islands shown in Figure 2 have a gold layer on one side to allow for molecular functionalization, which was performed prior to and following release from the handle substrate. Oligonucleotide attachment and hybridization of the particles attached to the handle substrate was performed as described earlier. The particles were released into PBS using sonication and the handle substrate removed. The particles were collected using small centripetal forces to gently concentrate the particles, which could then be collected by pipetting.

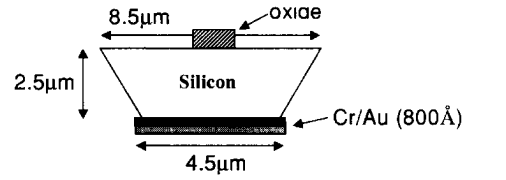

(a)

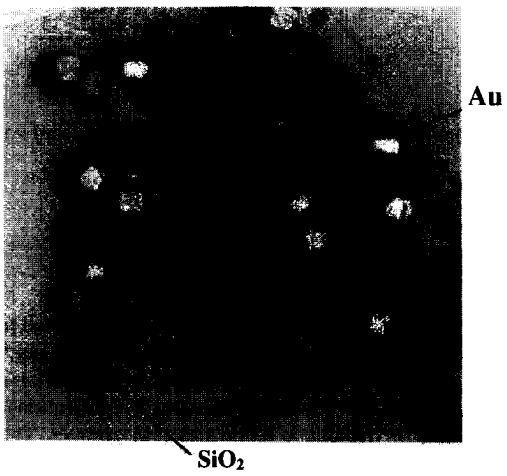

(b)

Figure 2 (a) Drawn cross-section of a silicon particle fabricated and released using process described in reference 16. (b) Scanning Electron Micrograph of particles following release from the handle substrate.

Assembly of these silicon particles has been performed using a variety of methods. For island-to-island assembly, the particles were resuspended in a 1mg/ml solution of avidin in PBS and heated to37°C for 45min. The particles were then rinsed thoroughly and resuspended in water. For particle to surface assembly, gold patterned silicon substrates were functionalized with the dsDNA presenting a biotin molecule for attachment. The substrates were then exposed to 1mg/ml of avidin at 37°C for 45min and rinsed thoroughly in PBS. The silicon islands, also functionalized with dsDNA presenting a biotin were then applied and the reaction was allowed to proceed again at 37°C for 45min. Both swirling and rotating techniques were employed during this process of attachment. Finally, electric field assembly was employed to assist in the assembly of these gold-coated islands. Nonfunctionalized islands were suspended in a buffer of DI water with 0.05% Tween-20 ($1X10^{-4}$ S/m) over a silicon substrate with gold electrodes exposed through a PECVD silicon oxide layer. High and low frequencies were applied to view the DEP and electrohydrodynamic interactions along with voltages ranging 0.1-10volts.

The results of these experiments determined the need for homogeneous silicon islands. This second version of silicon islands were made using commercially available SOI wafers, lithography and RIE etching [17]. The islands, shown in Figure 3, are 4μmx4μmx1.4μm in

dimension with a conductivity of 0.25-1X10^{-2} S/m. They were released from the handle substrate into DI solution with 0.05% Tween-20 using an ultrasonic agitator and collected as previously described to a concentration of 10^{6}/ml. The conductivity of the solution was 1X10^{-6} S/m. The islands were then suspended over the electrode substrate and voltage applied at low and high frequencies. The DEP and electrohydrodynamic effects are reported here.

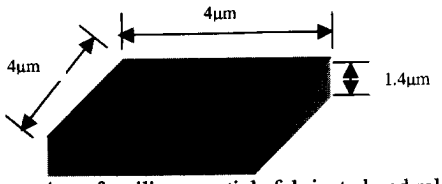

Figure 3 Drawn cross-section of a silicon particle fabricated and released using process described in reference 17.

RESULTS

Gold Nanoparticles

Assembly of gold nanoparticles using the strategy depicted in Figure 1b was successful. Figure 4 shows an AFM image of the nanoparticle assembly on gold (a) compared to the surrounding silicon oxide area (b). Figure 5 provides quantification of the results. Control samples (no thiol attachment and non complimentary hybridization) provided minimal nanoparticle capture both on the silicon oxide and gold surfaces. The assembled samples show minimal attachment on silicon oxide surface and increased attachment on the gold surface. Increased packing densities may be accomplished by further optimizing experimental conditions and by increasing the number of DNA molecules on the surface.

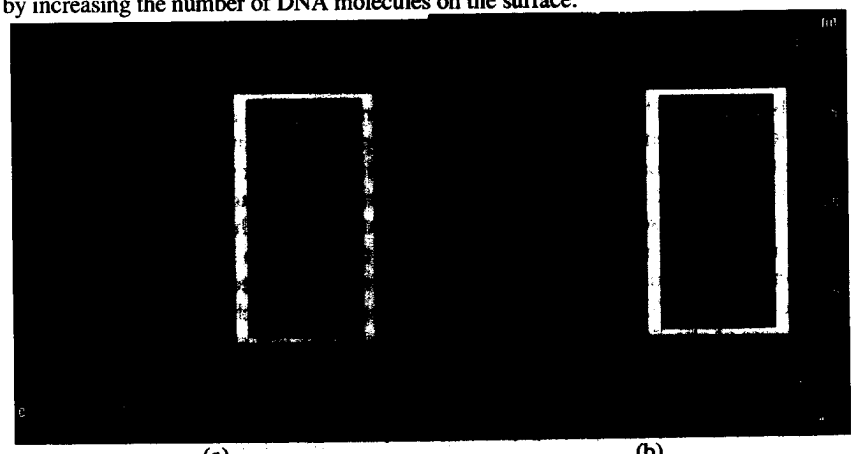

(a) (b)

Figure 4 Atomic Force Microscope scans of gold nanoparticle assembly on gold surface, (a) nanoparticles captured on gold when DNA was attach to the substrate, (b) surrounding silicon oxide area.

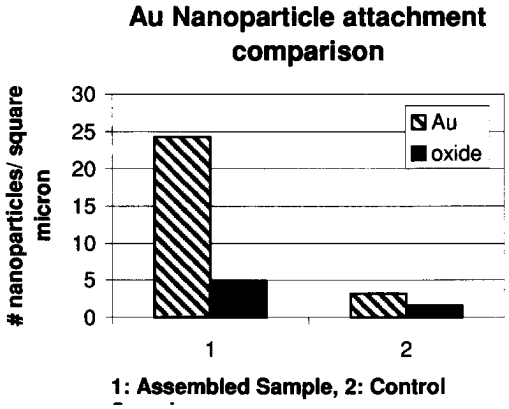

Figure 5 Quantification of the capture of the gold nanoparticles on patterned gold and the oxide surface.

Silicon Islands (and Polystyrene Beads)

The assembly of silicon particles, which may be active electronic device, promises significant progress toward the integration of heterogeneous materials. We have been working with silicon islands which may be replaced with electronically active silicon devices of the same size. Initially, island-to-island assembly was accomplished using the strategy depicted in Figure.1c. The particles were functionalized with the dsDNA presenting a biotin molecule and suspended in an avidin solution. The avidin bound to the biotin from two different particles and duplexes were formed with the gold sides facing each other as shown in Figure 6. This was expected since the avidin molecule, which has four binding sites for biotin, would link biotins from two different islands, hence forming duplets. In a given experiment, 82% of the islands were found to be part of a duplex, whereas without the avidin in the solution, only 1.9% of the islands were found to be part of a duplex, most likely due to random non-specific interactions. This experiment confirmed the functionalization of the silicon islands and the subsequent bonding between the biotin and avidin molecules.

Island to surface attachment was performed also using the strategy depicted in Figure 1c. The gold pattern of the substrate was functionalized, as were the islands with the dsDNA presenting a biotin. The avidin solution was incubated on the substrate surfaces followed by incubation with the islands. Due to the weight of the silicon islands, the islands would fall from suspension before reaching a binding site with the avidin. Numerous methods were implemented to eliminate this problem with minimal success. These included swirling of the suspension while allowing the biotin/avidin reaction to occur and rotating the suspension with the substrate fixed during this process. A few islands appeared to have attached as directed by the functionalized pattern. However, subsequent rinsing of the substrate to remove nonspecifically bound islands also removed the islands that were captured.

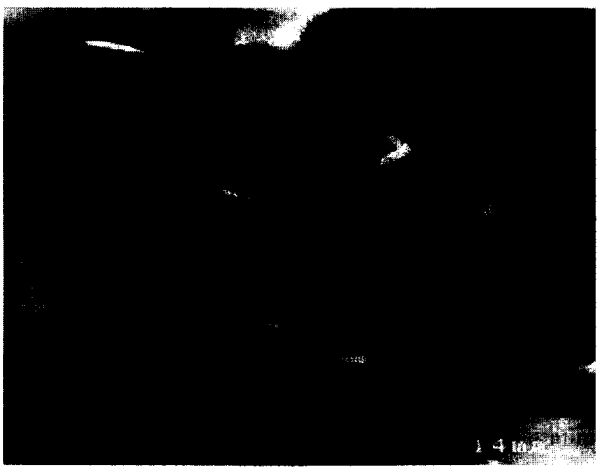

Figure 6 Islands duplexes formed using the DNA and Avidin/Biotin interactions at the Au faces of the two islands.

Forces involved in the assembly included covalent and biological/molecular forces. To complete the particle assembly for useful electronics, the substrates must be rinsed of nonspecifically attached particles and dried. Thus the forces of assembly must be greater than the forces encountered during subsequent processing. The combined biological events (DNA and protein layers) capture the assembled particles with estimated forces on the order of 10kCal/mol. A particle of surface area 16μm^2, as shown in Figure 3, would experience a maximum force of attachment of 10^{-7} N (or10^{-12} N/molecule). This estimate of force includes optimal DNA attachment density of 10^{12} molecules/cm^2 [18] and a hybridization efficiency of 30% [15]. Rinsing the substrates to remove nonspecifically bound particles is critical, specifically when the particle is large and dense as in the case of silicon particles coated with chrome and gold. The mass of the particle is ~10^{-10} g, yielding a force of gravity of 10^{-12} N. The force of drag on the particles was estimated using Stoke's Law for an equivalent volume of a sphere [19]. With a rinse velocity of 1cm/s the force of drag is 10^{-10} N. Actual drag forces on a particle of this shape could be one order of magnitude higher. These estimated forces of particle attachment and release are highly dependent on the DNA attachment and hybridization efficiencies and the procedures used during substrate rinsing. Thus, forces experienced by the silicon particles during the rinsing and drying processes can be of roughly the same orders of magnitude as the binding forces for the current device size used explaining why our captured particles were being released. Critical point drying and freeze-drying processes are being explored to overcome the forces during the drying of the sample.

To initially increase the capture efficiency, long-range forces were employed to attract the particles to their intended binding site. DEP and electrohydrodynamic forces can be used to direct the particle of interest to the proper binding area. The selectivity of the desired binding still depends on the proper biological entity being present for ultimate capture. The movement of the 5.48μm diameter polystyrene beads, charged with carboxyl groups, in an AC electric field is shown in figure 7, as a function of the frequency of the applied AC signal. The beads are

positioned randomly prior to applying the signal. The beads experience a negative dielectrophoresis effect and move towards the center of the electrode at 1MHz, as shown in Figure 2(b), where the gradient of the AC field is the smallest. However, the fact that the beads are located between the open windows cannot be explained if only negative DEP exists in the system. The occurrence can be explained by considering electro-thermal forces. The generated power leads to a local temperature gradient, causing the gradients of conductivity and permittivity of the medium. As a result, the fluidic motion is created which is believed to prevent the beads from positioning at the center of the opening windows.

Silicon islands as shown in Figure 3 were also employed for manipulation in the AC electric field. These silicon islands were suspended above the electrode substrate in a solution and the electric field was applied. Results are shown in Figure 8. Figure 8a shows the silicon blocks randomly distributed with no applied electric field. Figure 8b was taken of the same area 5min after an electric field of 10V and 10MHz was applied. A high percentage (78%) of the silicon islands moved to the expected position, between the electrodes. The position of the islands, standing on edge, can be explained by the fluidic motion generated by the electrohydrodynamic effect.

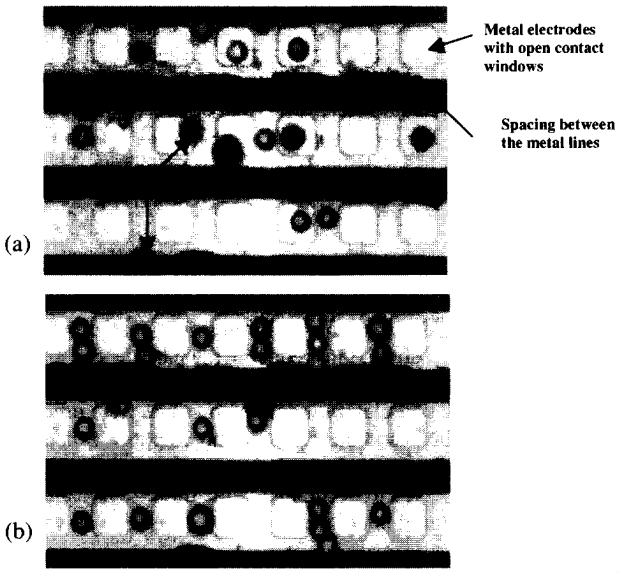

Figure 7 The movements of negatively charged polystyrene beads while the magnitude and the frequency of applied AC signal were changed. (a) No bias, random bead distribution, (b) $10v_{p\text{-}p}$ and 10MHz, beads settle in middle of open windows within one electrode.

(a)

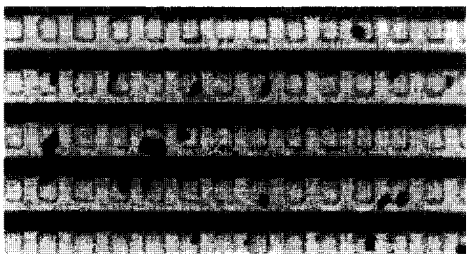

(b)

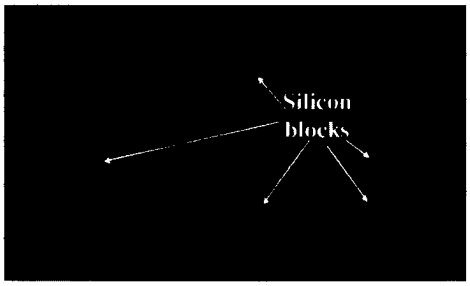

Figure 8 Negative DEP and electro-thermal effects (a) silicon block random distribution (b) 5min after 10V at 10 MHz was applied. Silicon blocks are arranged vertically on the oxide in between the open windows.

CONCLUSIONS

We have reported on our progress toward the assembly of micro and nano-scale particles using biological events and electric fields. Streptavidin coated gold nanoparticles have been captured on a patterned substrate, thus reducing the particle size and increasing the density for high sensitivity and spatial resolution. Our techniques have been extended toward the assembly of silicon islands. Silicon particles with gold on one side were used to form duplexes in solution due to binding of the dsDNA and the avidin-biotin complex. Silicon islands have been manipulated with electric fields to direct these particles toward their intended binding sites. These techniques are expected to be applied to the directed assembly of active silicon devices for use in heterogeneous material integration.

ACKNOWLEDGEMENTS

This work was supported by Center of Nanoscale Devices at Purdue University funded through the State of Indiana, 21st Century Research and Technology Fund and NSF ITR Grant to University of Florida/Purdue University. We would also like to acknowledge Prof. Steve Wereley for helpful discussions and the Micro-fabrication facility and Staff at Purdue University for assistance in device processing.

REFERENCES

1. C.M. Niemeyer , B. Ceyhan, S. Gao, L. Chi, S. Peschel, and U. Simon, Colloid Polymer Science, **279**, 68, (2001).
2. R.L. Edelstein, C.R. Tamanaha, P.E. Sheehan, M.M. Mille, D.R. Baselt, L.J. Whitman and R.L. Colton, Biosensors & Bioelectronics, **14**, 10, (2000).
3. R.P. Andres, S. Datta, D.B. Janes, C.P. Kubiak, and R. Reifenberger, i*nThe Handbook of Nanostructured Materials and Nano-technology*, (Academic Press, 1998) p.10.
4. S.W. Lee, H.A. McNally, D. Guo, M. Pingle, D.E. Bergstrom, and R. Bashir, Langmuir; **18** (8), 3383-3386 (2002).
5. H.J. Yeh, and J.S. Smith, IEEE Photonics Technology Letters, **6** (6), 706 (1994).
6. E. Prohofsky, *Statistical mechanics and stability of macromolecules: application to bond disruption, base pair separation, melting, and drug dissociation of the DNA double helix*, (Cambridge University Press, New York, NY, 1995) p.34.
7. *Methods in Enzymology*, edited by M. Wilcheck and E.A. Bayer, (Academic Press, NewYork, NY, 1990) Vol.184, p.3.
8. A. Ulman, Chem. Rev., **96** (4), 1533 -1554 (1996).
9. H. A. Pohl, *Dielectrophoresis*, (Cambridge University Press, Cambridge, UK, 1978) p52.
10. A. Ramos, H. Morgan, N. G. Green and A. Castellanos, Journal of Physics D, **31**, 2338-2353, (1998).
11. A. Ramos, H. Morgan, N. G. Green, and A. Castellanos, Journal of Electrostatics, **47**, 71-81, 1999.
12. W. H. Nebergall, F. C. Schmidt, H.F. Holtzclaw, *General Chemistry*, 5th Ed., (D.C. Heath and Company, Lexington, MA, 1976) p.143.
13. H. McNally, M. Pingle, S.W. Lee, D. Guo, D. Bergstrom, R. Bashir, in *Nanopatterning: from Ultralarge-scale Integration to Biotechnology*, edited by L. Merhari, K.E. Gonsalves, E.A. Dobisz, M. Angelopoulos, D. Herr, (Mater. Res. Soc. Proc. **705**, Pittsburgh, PA, 2002) pp. 177-185.
14. C.A. Mirkin and T.A. Taton, Nature **405**, 626–627, (2000).
15. L.M. Demers, C.A. Mirkin, R.C. Mucic, R.A. Reynolds, R.L. Letsinger, R. Elghanian, and G. Viswanadham, Analytical Chemistry, **72** (22), 5535-5541 (2000).
16. R. Bashir, S.W. Lee, D. Guo, M. Pingle, D. Bergstrom, H. McNally, and D. Janes, in *Nonlithographic and Lithographic Methods of Nanofabrication: From Ultralarge-Scale Integration to Photonics to Molecular Electronics*, edited by L. Merhari, J.A. Rogers, A. Karim, D.J. Norris, Y. Xia, (Mater. Res. Soc. Proc. **636**, Pittsburgh, PA, 2001).
17. S.W. Lee, H. McNally, R. Bashir, M. Pingle, D. Bergstrom, accepted for publication (Mater. Res. Soc. Proc. **735**, Pittsburgh, PA, 2003).
18. J.K.N. Mbindyo, B.D. Reiss, B.R. Martin, C.D. Keating, M.J. Natan and T.E. Mallouk, Adv. Mater. **13** (4), 249, (2001).
19. Frank M. White, *Viscous Fluid Flow*, 2nd Ed., (McGraw Hill, Boston, MA. 1991) p.67.

Mat. Res. Soc. Symp. Proc. Vol. 739 © 2003 Materials Research Society H9.4

Optically Driven Micromanipulation Tools Fabricated by Two-photon Microstereolithography

Shoji Maruo, Koji Ikuta and Hayato Korogi
Department of Micro System Engineering, Graduate School of Engineering, Nagoya University
Furo-cho, Chikusa-ku, Nagoya 464-8603, Japan

ABSTRACT

Light-driven micromanipulators have been developed by two-photon microstereolithography. The manipulators are driven and controlled by optical trapping. The torque of micromanipulator was successfully controlled on the order of femto-newton by adjusting the focal position of the trapped laser beam. Nanotweezers and a nanoneedle with probe tip of diameter 250 nm were fabricated and driven in a liquid. Such remote-controlled manipulation tools provide a unique and effective handling method of biological samples such as living cell, protein and DNA.

INTRODUCTION

Manipulation techniques at micro and nanometer scale are crucial for progress in biotechnology as well as nanoscale science and technology. Recently several types of nanomanipulators such as carbon nanotube nanotweezers and micromachined nanotweezers have been developed for grabbing or probing nanoscale objects [1-3]. However, since most of these tweezers are based on electrostatic force, they are not ideal for aqueous solution work such as manipulation of cells, microbes and single molecules.

In this paper, we report promising types of nanomanipulators suitable for aqueous solution work. Our manipulators were fabricated by using an assembly-free process based on two-photon microstereolithography that was previously developed by us [4-6]. We have developed several types of microstereolithography [7-9]. The two-photon process is suitable for making nano-manipulators owing to the submicron resolution. The manipulators are driven by optical trapping based on radiation pressure from a tightly focused laser beam. Since optical trapping enables remote manipulation of microobjects in biological fluid environments, the manipulators are especially suited for the application in biotechnology unlike electrostatic types.

TWO-PHOTON MICROSTEREOLITHOGRAPHY

Two-photon microstereolithography uses a pulsed near-infrared (IR) laser as a light source, though conventional methods use an ultraviolet (UV) laser as a light source. The rate of two-photon absorption is proportional to the squared intensity of light, so that near-IR light is strongly absorbed only at the focal point within the photopolymer [10, 11]. The quadratic dependence of two-photon-absorption assists to confine the solidification in submicron volume. This virtue of the two-photon process allows the fabrication of three-dimensional (3D) structures by scanning a focus inside the photopolymer.

Fig. 1 shows our fabrication system. A Ti: sapphire laser is used to generate the two-photon absorption. The beam from the laser is introduced into the galvano-scanner system, and then it is focused with an objective lens (N.A.: 1.3). The beam scans laterally while the stage that supports the photopolymer is scanned vertically, thereby moving the point of focus in three dimensions.

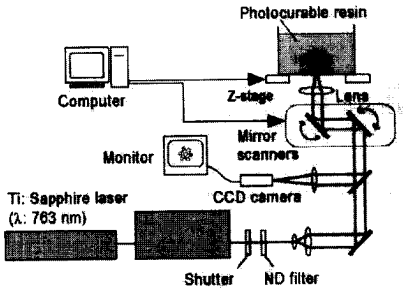

Fig. 1 Fabrication system of two-photon microstereolithography

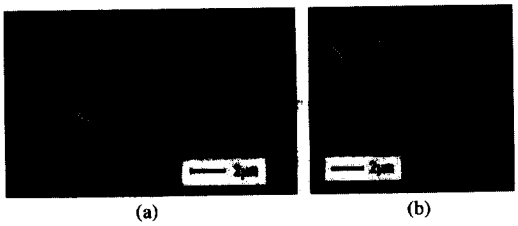

Fig. 2 Three-dimensional microstructures made by two-photon microstereolithography
(a) Micro beetle model (b) Micro locomotive model

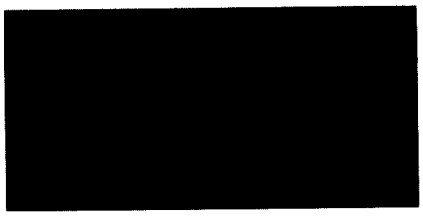

Fig. 3 Laser power dependence of sizes of voxels solidified at a focus

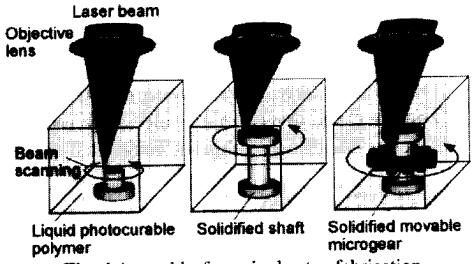

Fig. 4 Assembly-free, single-step fabrication process of movable micromachines

By controlling both the galvano-scanner system and stage with 3D computer-aided design (CAD) data, it is possible to fabricate a 3D microstructure. After the 3D fabrication process, the unsolidified photopolymer is washed out with a rinse.

Fig. 2(a), (b) show SEM images of sophisticated 3D microstructures fabricated by using the fabrication system. A micro beetle model and a micro locomotive model were successfully fabricated in 20 minutes. The resolution of the fabrication system has attained 140 nm. Fig. 3 demonstrates the voxels solidified at a focus in different exposure conditions. At the optimal laser power of 60 mW, the smallest dot of diameter 140 nm is formed.

SINGLE-STEP FABRICATION OF MOVABLE MICROMACHINES

The direct laser writing in the two-photon microstereolithography allows us to make not only sophisticated microstructures but also freely movable micromachines. To fabricate advanced movable micromachines, the scanning pattern of a laser beam should be optimized to reduce the deformation of a solidified object due to the shrinkage of the photopolymer during polymerization. Optimal laser scanning for each movable micromachine makes possible the fabrication of even complicated freestanding micromechanisms without any supporting columns or sacrificial layers.

Fig. 4 illustrates the single-step fabrication process of a movable micromachine, i.e. a microgear. First an attached shaft and a stopper are fabricated by scanning a laser beam circularly, and then a movable component is fabricated only by scanning the laser beam along a proper laser-scanning pattern. Although the movable component is not fixed to other parts while the

laser beam is scanning, the high viscosity of the photopolymer keeps it from moving during the process [12].

OPTICALLY DRIVEN MICROMANIPULATORS

We designed micromanipulators driven by a focused laser beam as shown in Fig. 5 (a). The micromanipulators are driven as follows: The laser beam is initially focused on the arm so that the gradient force of the radiation pressure traps the arm in its equilibrium position. Next, the laser beam is shifted from the equilibrium position, thereby subjecting the trapped arm to an attractive force. As the laser beam scans in an arc, the attractive force induces the manipulator arm to follow the locus of the scanning laser beam at the same speed.

Fig. 5 (b) shows an SEM image of micromanipulators. The movable arm is fabricated as follows: The circular base of the arm is formed by circular scanning, and then the arm is added by scanning the laser beam in arcs with different radii from outside of the previously formed circular base. The optimal scanning removed the drawback owing to the shrinkage of photopolymer.

To drive the manipulators, a laser beam was focused on one of the micromanipulator arms floating in the rinse, and then the arm was turned by scanning the focus in an arc as the other arm floated. Fig. 6 shows sequential optical microscope images of the micromanipulators under the control of the focused laser beam. The trapped arm was successfully opened and closed. In the experiments, a fabrication system shown in Fig. 1 was used for driving micromanipulators.

We attempted to control the torque of the manipulators just by adjusting the position trapped by the laser beam along the length of the arm. This approach makes possible to control the force of a micromachine without changing the laser power. As an experimental verification, we measured the maximum rotation speed of a manipulator arm rotated in the rinse by scanning a laser beam circularly, while the trapped position was shifted along the arm. The torque of the arm

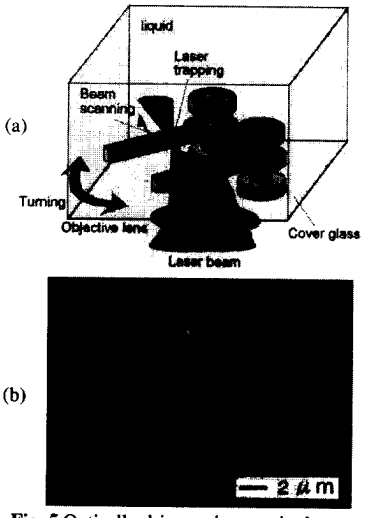

Fig. 5 Optically driven micromanipulators
(a) Driving method of micromanipulators
(b) SEM image of micromanipulators

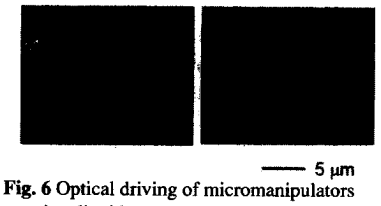

Fig. 6 Optical driving of micromanipulators in a liquid.

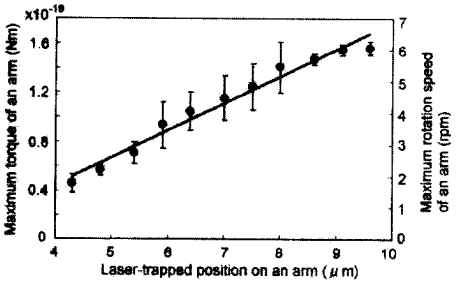

Fig. 7 Force controlling of a manipulator arm by adjusting the position trapped by a laser beam.

can be estimated by the measured rotation speed of the arm. Fig. 7 shows the change in the maximum torque (maximum rotation speed) of the arm as the focal position of the laser beam is shifted under a laser power of 120 mW. The result indicates that the torque of the micromanipulators is proportional to the turning radius of the laser beam. The torque of the arm is approximately 0.4 - 1.5 x 10^{-19} Nm. The force at the tip of the arm can be adjusted between 4 and 15 fN under the laser power. The force range of the arm can be easily changed from fN to pN by controlling the laser power.

OPTICALLY-DRIVEN NANOTWEEZERS

Nanotweezers with submicron probe tips of diameter 250 nm were fabricated by the direct laser writing. Fig. 8 shows SEM images of nanotweezers. The fabrication process of the nanotweezers is follows: Initially, an attached shaft and stopper were fabricated by scanning a laser beam circularly while the focal plane was lowered at regular intervals of 600 nm along the optical axis. Next, the circular parts of the arm were formed by circular scanning, and then the arm was added by scanning the laser beam in arcs with different radii from the outside of the previously formed circular part. Finally, a submicron probe tip was formed at the end of the arm through point-by-point exposure. Optimal laser scanning for each microstructure allows the fabrication of even nanomanipulation tools.

In a preliminary experiment of optical driving, the left-hand arm was fixed to the shaft while the right-hand arm of the nanotweezers was trapped and swung by the scanning of the focused laser beam (Fig. 9 (a)). Fig. 9 (b) shows optical microscope images of nanotweezers opened and shut in the rinse. The probe tips were precisely closed without any gap between them.

The position of the optically driven tweezers can be controlled very precisely and easily, as the position of the probe tip is directly fixed by the focal position with accuracy of nearly 15 nm. In electrostatic-type tweezers, on the other hand, since the separation of the two probe tips is not proportional to applied voltage, the tips close suddenly and adhere to each other when a critical actuating voltage is reached, which makes it much more difficult to precisely control the position of electrostatic tweezers compared with the optically driven type.

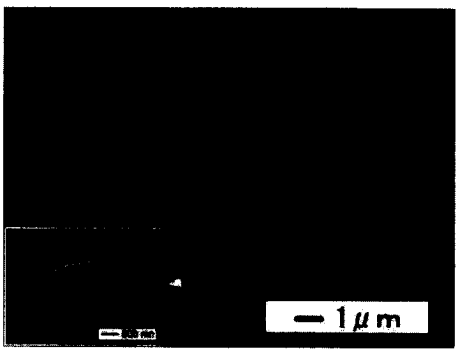

Fig. 8 SEM image of nanotweezers. The diameter of the probes is 250 nm.

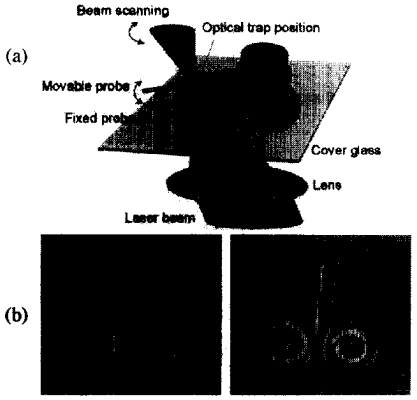

Fig. 9 Optical driving of nanotweezers
(a) Driving method of nanotweezers
(b) Nanotweezers driven by light

OPTICALLY DRIVEN NANONEEDLE WITH TWO DEGREES OF FREEDOM

We propose an effective method of controlling a movable micromachine with great freedom of movement. The movable micromachine is attached to a dot called "Trapping point" to focus a laser beam. By scanning the laser beam focused on the trapping point, we can control the movement of the micromachine in any motion. This method provides a simple way to drive micromanipulators with great freedom of movement only by a single laser beam.

As an example of manipulators with two degrees of freedom, we fabricated a nanoneedle. Fig. 10 (a), (b) show a schematic design and an SEM image of a nanoneedle, respectively. Since the probe tip of the needle is attached to the slotted arm, the nanoneedle can provide translational motion as well as rotational motion. A dot is attached to the end of the slotted arm as the trapping point. Fig. 11 (a) and (b) show the rotational and translational motions of a nanoneedle that has a point of diameter 250 nm. In Fig. 11 (a), the rotation speed was 34 rpm with the laser power of 200 mW. The photos shown in Fig. 11 (b) are sequential images observed at intervals of one second. We could skillfully manipulate the nanoneedle by using the trapping point.

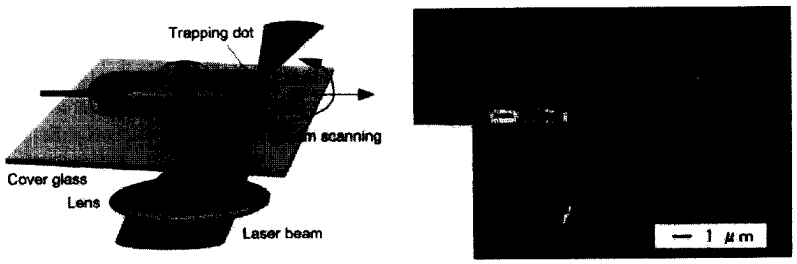

(a) (b)

Fig. 10 Optically driven nanoneedle with 2 D.O.F. (a) Driving method (b) SEM image

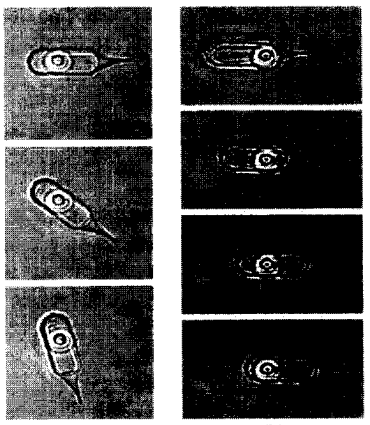

(a) (b)

Fig. 11 Optical driving of nanoneedle. (a) Rotation (b) Translation

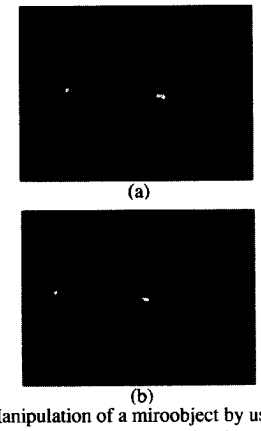

(a) (b)

Fig. 12 Manipulation of a miroobject by using an nanoneedle. (a) Pushing with the arm of nanoneedle (b) Pricking with the probe of nanoneedle

In addition, we demonstrated that the nanoneedle was useful for manipulating a microobject. Fig. 12 (a), (b) illustrate mechanical stimulation of a microobject by the nanoneedle. A tiny particle was pushed with the arm of the nanoneedle or pricked with its probe tip.

ADVANTAGES OF OPTICALLY DRIVEN MICROMANIPULATORS

The main advantages of the optically driven manipulators are as follows: remote drive in an aqueous solution, force control on the order of femto-Newton to pico-Newton, and elimination of the need to use ultrahigh precision 3D stages to move the probe tips. In addition, the flexible, rapid fabrication using the two-photon microstereolithography technique enables tailor-made nanotools for versatile applications. The resolution of the current fabrication system has attained 140 nm. The resolution will exceed 100 nm through the further optimization of the fabrication system and use of higher-order nonlinear effects such as three-photon absorption.

CONCLUSIONS

We have developed novel optically driven micro/nano manipulators by using the assembly-free, rapid fabrication method in two-photon microstereolithography. Such optically driven manipulation tools can be widely applied for biotechnology. In the next stage, we will integrate the manipulators into a 3D polymeric microfluidic circuit by using microstereolithography techniques developed by our group [9-11]. The optically controlled microfluidic devices including various types of manipulation tool are useful for biological applications such as nanosurgery systems for living cells and nanoanalysis systems for single molecules.

ACKNOWLEGEMENTS

This work was partially supported by Grant-in-Aid for Scientific Research from the Ministry of Education, Culture, Science and Technology and a research grant from Foundation Advanced Technology Institute. The authors thank to Mr. M. Ogawa and Mr. S. Ito for their cooperation in fabrication of 3D microstructures from 3D CAD data.

REFERENCES

1. P. Kim and C. M. Lieber, *Science* **286**, p. 2148 (1999).
2. P. Bøggild, et al., *Proc. of the IEEE Conf. on Nanotechnology (IEEE-NANO 2001)*, p. 87.
3. K. Kakushima, et al, *Proc. of IEEE International Conference on Micro Electro Mechanical Systems (MEMS 2001)*, p. 294 (2001).
4. S. Maruo and K. Ikuta, *Proc. of the International Conference on Solid-State Sensors and Actuators (Transducers 99)*, p. 1232 (1999).
5. S. Maruo and K. Ikuta, *Proc. of SPIE* **3937**, p. 106 (2000).
6. S. Maruo, K. Ikuta and H. Korogi, *Proc. of MEMS 2001*, p. 594 (2001).
7. K. Ikuta and K. Hirowatari, *Proc. of MEMS 93*, 42-47 (1993).
8. K. Ikuta, K. Hirowatari and T. Ogata, *Proc. of MEMS 94*, p. 1 (1994).
9. K. Ikuta, T. Ogata, M. Tsuboi, S. Kojima, *Proc. of MEMS 96*, p. 301 (1996).
10. S. Maruo, O. Nakamura, and S. Kawata, *Opt. Lett.* **22**, p. 132 (1997).
11. S. Maruo and S. Kawata, *J. Microelectromech. Sys.* **7**, p. 411 (1998).
12. S. Maruo and K. Ikuta, *Appl. Phys. Lett.* **76**, p. 2656 (2000).

Mat. Res. Soc. Symp. Proc. Vol. 739 © 2003 Materials Research Society H3.7

DFB Structures in Electroactive Conjugated Polymers realized by Soft Lithography

Erik Moderegger[1], Martin Gaal[2], Christoph Gadermaier[2], Harald Plank[2], Emil J.W. List[2], Alexander Pogantsch[3], Roland Güntner[4], Ullrich Scherf[4], Günther Leising[1]
[1]AT&S AG, Science & Technology, Fabriksgasse 13, 8700 Leoben, Austria
[2]Christian Doppler Laboratory for Advanced Functional Materials, Graz University of Technology & Joanneum Research, Petersgasse 16, 8010 Graz, Austria
[3]Institute for Solid-State Physics, Graz University of Technology, Petersgasse 16, 8010 Graz, Austria
[4]Department of Chemistry, BUGH Wuppertal, Gauss-Straße 20, D-42097 Wuppertal, Germany.

ABSTRACT

The realization of a polymeric injection laser diode is an important aim in organic electronics. A crucial step towards this goal lies in the understanding and fabrication of feedback structures for lasers. Such feedback structures may be fabricated either in the substrate or directly in the active polymer layer.
Soft Lithography has proven itself as a useful tool to pattern a wide variety of materials. Typically one uses elastomeric molds (stamps) to pattern materials and structures whereby dimensions as low as 30 nm can be achieved.
Different types of Soft Lithographic processes are applied to produce optical feedback structures for optically pumped laser arrays.

INTRODUCTION

Many of today's technological applications, e.g. in telecommunications, science, medicine, optical data storage, materials processing, and consumer electronics, rely on the use of lasers. At present, a variety of laser sources is available, using very different energies, sizes and wavelengths. For small size applications, inorganic semiconductor diode lasers are the candidates of choice. A large part of the visible spectrum, however, is still not available when employing the most commonly used inorganic III-V semiconductor lasers.
Conjugated polymers are attractive candidates for the realization of solid-state lasers because of various reasons: Conjugated polymers can be easily deposited on any type of substrate and there are conjugated polymers, which emit over broad ranges of the visible spectrum. In a diode configuration, it is also feasible to pump them electrically.

Upon photopumping a conjugated polymer above a threshold value optical gain via stimulated emission is observed. When light travels down a waveguide spontaneously emitted light is amplified by stimulated emission. For this amplified spontaneous emission (ASE) process to happen i) the refractive index of the polymer must be higher than the one of the substrate and ii) the polymer film has to be thick enough to support waveguiding [1].
When an optical feedback is provided for the emitted light in the active medium, the emission becomes coherent and lasing action can be observed.

The first laser-like emission in a solid conjugated polymer was demonstrated in 1996 [2]. Since then, optically pumped polymeric lasers in diverse configurations and using different conjugated polymers have been reported. For a recent overview, see [3]
Resonators can be realized in different geometries: Microcavities [4], dielectric mirrors [5], microdisks, microdroplets, and microrings [6]. A very promising way to achieve the necessary optical feedback is the fabrication of a distributed feedback structure in either the substrate or the polymer material itself. This approach allows rather large-area geometries and is compatible with the standard techniques for the deposition of organic emission layers. DFB structures are realized by a periodic modulation of the refractive index and/or the gain in the material, which leads to Bragg reflection in the polymer. Lasers of this type emit close to the Bragg wavelength λ_{Bragg}, which is related to the grating period Λ by the relation:

$$m\lambda_{Bragg}=2n_{eff}\Lambda \qquad (1)$$

where m is the diffraction order onto the grating and n_{eff} the effective refractive index of the propagating mode.

Soft Lithography [7] is the common name for a set of non-lithographic methods, which can be used to structure materials on the micro- and nanometer scale. Soft Lithographic methods in general can be readily used in the lab from materials that are commercially available. All of these methods have in common that they rely on the contact of an elastomeric stamp with patterned relief structures on its surface with the material to be structured.
Soft Lithography can be used on a wide range of materials, ranging from polymers to inorganic materials and even biological specimen. Both two-dimensional and three-dimensional structures have been realized. The minimum lateral feature sizes that can be produced rely heavily on the elastomeric material employed and can be as low as 30 nm.
In this work we have employed the techniques of Soft Embossing and Liquid Embossing. In Soft Embossing, a thin film of the polymer to be structured is heated above its glass transition temperature T_g. Then a slight pressure is applied to the stamp to produce the patterns in the polymer. After cooling below T_g the stamp is removed from the polymer. In Liquid Embossing the stamp is brought in contact with the polymer, when it is still in its liquid phase and then left to dry.

EXPERIMENTAL DETAILS

For evaluation experiments, typical relief structures from compact discs (without the aluminum and the transparent cover) have been employed as masters.

The masters for the DFB gratings have been fabricated by Interference Lithography. A positive-tone photoresist (X-AR-P 5800, Allresist, Strausberg, Germany) was spin-coated onto a pre-cleaned glass-substrate. A Nd:YAG Laser (1064 nm) with two frequency doublers was used to generate an interference pattern on the photoresist surface. To obtain different grating periods, the angle between the interfering beams was adjusted. The typical spot size for the exposure was 1 cm^2.
After development of the resist film, the resulting grating pattern was transferred onto a stamp for the Soft Lithography procedure.

For the transfer of the grating pattern from the master gratings to the conjugated polymer, a stamp made of PDMS (poly-dimethylsiloxane; Sylgard 184, Dow Corning, Midland, MI) was used.
PDMS was prepared according to standard procedures and cured at 98°C for about one hour.
After cooling the stamp was removed from the master.

The conjugated polymer employed for the laser structures was [2-methoxy, 5-(2'-ethyl-hexyloxy)-p-phenylene-vinylene] (MEH-PPV, Sigma Aldrich), which was dissolved in Toluene at a ratio of 10 g/l.
For the production of a MEH-PPV film with an imprinted DFB structure, a drop of the polymer solution was cast on a glass substrate. Then the PDMS stamp was brought in contact with the polymer solution and left to dry for one hour at ambient conditions.

The third harmonic (355 nm) of Nd:YAG laser (pulse duration < 10 ns) was used to pump the device optically. The DFB emission was collected perpendicular to the sample plane at room temperature with a CCD spectrometer cooled to -20 °C with a spectral resolution below 2 nm.

Atomic Force Microscopy (AFM) micrographs have been taken on a Digital Instruments Nanoscope 3a Instrument.

RESULTS AND DISCUSSION

Initial experiments were taken out with a liquid crystalline poly-fluorene [8]. For these experiments, PDMS stamps made from CDs and CD-ROMs were used. The typical feature sizes in these samples are between 0,7 and 2 µm [9]. As can be seen from Figure 1, the features can be replicated very accurately using the Soft Embossing approach.

Figure 1 Optical micrograph of a PF film on Silicon with Soft Embossing.
Typical feature sizes: 0,7 – 2 µm

For laser resonator structures, the liquid crystalline morphology of the poly-fluorene led to the destruction of the feedback structure on the sample due to the high intensity of the pump beam.

Moreover, the grating depth that could be produced with the Soft Embossing approach was very small (below 10 nm) and thus the feedback efficiency was not good enough for lasing behavior.

Grating masters with periodicities from 370 nm to 400 nm have been fabricated via interference lithography. They exhibit a near-sinusoidal profile with a peak-to-peak height of 40 nm approximately. A similar profile with a reduced peak-to-peak height (roughly 15 nm) is transformed onto the PDMS stamp, as determined from AFM measurements.
Figure 2 displays an AFM micrograph of the MEH-PPV surface.

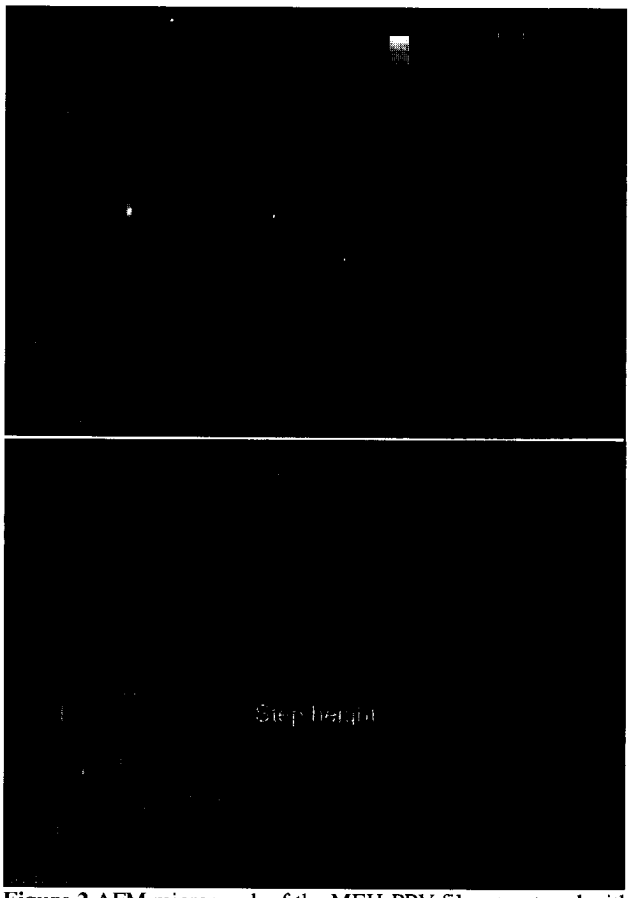

Figure 2 AFM micrograph of the MEH-PPV film structured with Liquid Embossing.

Linear grating masters with periodicities from 370 nm to 400 nm have been fabricated via interference lithography. They exhibit a near-sinusoidal profile with a peak-to-peak height of 40 nm approximately. A similar profile with a reduced peak-to-peak height (roughly 15 nm) is

transformed onto the PDMS stamp. Figure 2 displays an AFM micrograph of an MEH-PPV film. The near-sinusoidal structure with a periodicity of 380 nm has been transferred to the polymer film. The profile depth (peak-to-peak) is approximately 10 nm. The surface is contaminated by fragments of the film, which result from laser ablation due to excessive pumping during the measurement of the ASE and lasing spectra.

The periodic structure embossed into the polymer surface acts as a reflection grating, as can be seen by the gleam on the sample shown in the inset of Figure 3. The lines, which interrupt the gleam are due to laser ablation. The spectra show ASE on top of the fluorescence of MEH-PPV, which appears all over the sample. On some spots the fluorescence and ASE background collapses into a narrow laser line as the feedback produced by the periodic grating becomes efficient. The laser line can be clearly distinguished from the ASE peak since its apparent linewidth is 2nm (thus limited by the resolution of the spectrometer) against 11nm of the ASE peak. Moreover, while ASE peaks at 642 nm, the laser line is determined by the DFB periodicity and appears at 625 nm, where ASE is not efficient. Experiments with different grating periodicities show a shift of the laser line from 625 to 645 nm (figure not shown). The laser emission perpendicular to the film plane results from second-order Bragg reflection. Therefore, using Eq. 1, the effective refractive index of the film can be calculated as $n_{eff} = 1.65$.

The film thickness is very inhomogeneous, which is detrimental for the feedback since n_{eff} depends on the film thickness and hence no single Bragg wavelength is selected. This explains why lasing can be observed only on the most homogeneous spots of the sample.

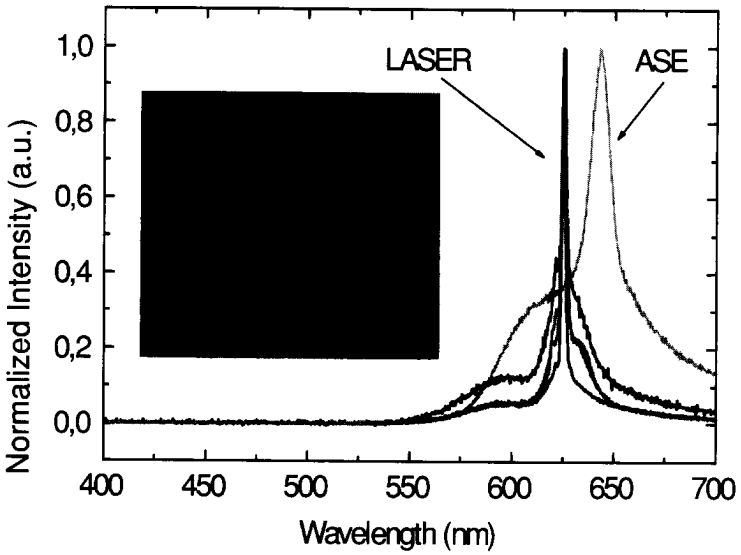

Figure 3 ASE and lasing spectra of MEH-PPV on different spots of the sample shown in inset.

CONCLUSIONS

We have shown a simple way to realize optical structures directly in conjugated polymers. Both Soft Embossing and Liquid Embossing have been used to generate these features in a liquid-crystalline polyfluorene and in commercially available MEH-PPV.
In particular, Liquid Embossing was used to generate a distributed feedback laser in MEH-PPV from master gratings produced using interference lithography.
While a single laser line can be observed on a number of spots on the sample, variations in the film thickness account for spots where laser emission is not seen.

The work presented shows the feasibility of the fabrication of a directly imprinted polymer laser. Determining important parameters like lifetime, stability or efficiency are subject of our ongoing research. Furthermore we focus on the improvement of the Soft Embossing process in connection with the liquid crystalline poly-fluorene and the production of MEH-PPV films with a smoother surface with Liquid Embossing to obtain large-area feedback structures.
Results from this research will be published elsewhere.

ACKNOWLEDGEMENTS

We would like to thank Jürgen Brandt (Sony DADC, Anif, Austria) for providing us with uncovered compact discs and Kurt Iskra (Institute for Experimental Physics, Graz University of Technology) for giving us access to the interference lithography system.

REFERENCES

1. F. Hide, M. Diaz-Garcia, B. Schwartz, M. Andersson, Q. Pei, and A. Heeger, *Science* **273**, 1833 (1996)
2. F. Hide, B. Schwartz, M. Diaz-Garcia, and A. Heeger, *Chem: Phys Letters* **256**, 424 (1996)
3. G. Kranzelbinder, G. Leising, *Rep. Prog. Phys.* **63**, 729 (2000)
4. N. Tessler, G. Denton, R. Friend, *Nature* **382**, 695 (1996)
5. A. Schulzgen, C. Spiegelberg, M. Morrell, S. Mendes, B, Kippelen, N. Peyghambarian et al., *Appl. Phys. Lett.* **72**, 269 (1998); T. Granlund, M. Theander, M. Berggren, M. Andersson, A. Ruzeckas, V. Sundstrom et al., *Chem: Phys Letters* **288**, 879 (1998); S. Burns, G. Denton, N. Tessler, M. Sevens, F. Cacialli, R. Friend, *Opt. Mater.* **9**, 18 (1998)
6. S. Frolov, M. Shkunov, M. Vardeny, K. Yoshino, *Phys. Rev. B* **56**, R4363 (1997); S. Frolov, A. Fujii, D. Chinn, M. Vardeny, K. Yoshino, R. Gregory, *Appl. Phys. Lett.* **72**, 2811 (1998); S. Frolov, M. Vardeny, K. Yoshino, *Appl. Phys. Lett.* **72**, 1802 (1998); S. Frolov, A. Fujii, D. Chinn, M. Hirohata, R. Hidayat, M. Taraguchi et al., *Adv. Mater.* **9**, 869 (1998); Y. Kawabe, C. Spiegelberg, A. Schulzgen, M. Nabor, B. Kippelen, E. Mash et al., *Appl. Phys. Lett.* **72**, 141 (1998); M. Berggren, A. Dodabalapur, Z. Bao, R. Slusher, *Adv, Mater.* **9**, 968 (1997)
7. Y. Xia, G. Whitesides, *Annu. Rev. Mater. Sci.* **28**, 153-184, (1998)
8. E. J. W.List, R. Güntner, P. Scandiucci de Freitas, U. Scherf, Adv. Mater. **14**, 374, (2002)
9. Private communication (Jürgen Brandt)

Mat. Res. Soc. Symp. Proc. Vol. 739 © 2003 Materials Research Society

Synthesis of SiO_2 Nanowires and CdS/SiO_2 Composite Nanowires and Investigation of Their Electron Field Emission Properties

Jun Jiao, Lifeng Dong, David W. Tuggle, Jeremy Petty, Logan Love, and Michael Coulter*
Physics Department, Portland State University, Portland, Oregon 97207
*Oregon Episcopal School, Portland, Oregon 97223

ABSTRACT

A thermal evaporation method was used to obtain SiO_2 and CdS/SiO_2 nanowires by heating Si substrates coated with a gold thin film in a quartz tube furnace. During growth, pure CdS powder was placed at the heating zone in the furnace, serving as the CdS source for the CdS/SiO_2 composite nanowires. It was found that both non-porous and porous Si substrates served as the Si source for the growth of SiO_2 nanowires and the CdS/SiO_2 composite nanowires. It was also found that the effect of the temperature gradient in the reaction chamber plays an important role in the density distribution of different nanowires (SiO_2 or CdS/SiO_2 nanowires). The electron field emission properties of these nanowires were investigated using an electron field emission microscope equipped with a Faraday cup.

INTRODUCTION

Due to quantum confinement effect, nanostructural semiconductors are expected to show optical and electronic properties distinctive from bulk materials. Nanowires, one-dimensional nanostructures, have shown great potential for nanoscaled electronic and optoelectronic devices [1-3]. However, because of the difficulties of fabricating these nanoscale materials with controlled structural configurations, the realization of these technological promises is still a distant goal. In an effort aimed at tailoring nanowires to designed specifications, we have systematically investigated the effects of preparation parameters on the formation of ZnO nanowires [4], SiO_2 nanowires, and CdS nanowires. We also studied the electron field emission properties of these nanowires in relation to their nanostructural morphologies. In this paper, we demonstrate the growth of SiO_2 and CdS/SiO_2 composite nanowires by a thermal evaporation method and the investigation of their electron field emission properties. A comparison of the field emission properties between nanowires and carbon nanotubes is also discussed.

EXPERIMENTAL

(1) Growth of SiO_2 and CdS/SiO_2 Nanowires –Silicon (Si) wafer pieces were used as substrates for the growth of the nanowires. A piece of Si wafer was cut into small rectangles, which were then cleaned ultrasonically in acetone. Some of those pieces were made porous by electrochemical etching. In a 1:1 in volume of HF (48%) and ethanol solution, the Si pieces were etched for approximately 3-4 minutes with a current density of approximately 15 mA/cm^2 and then cleaned thoroughly with distilled water. Both nonporous and porous Si pieces were then sputter coated with a gold thin film approximately 40 nm thick using an SEM sputter coater equipped with a gold target. The thickness of the gold thin film was controlled by the deposition time. Pure CdS powder was put on to a ceramic plate. The plate was then inserted into the center of a quartz tube in a horizontal tube furnace. The Si substrates (nonporous and porous pieces) were laid in a line downstream of the ceramic plate. Prior to heating, the furnace was pumped to a vacuum of 10^{-2} Torr and then Ar gas was supplied to the system to increase the pressure to 150 Torr. The furnace was then heated at a ramp rate of 20° C/min with a continued flow of Ar gas. When the temperature reached 800° C the system was kept at these

conditions for 60 minutes. To end this process, the chamber pressure was then set to 376 Torr of Ar gas. The pump was turned off and the system allowed to cool to room temperature.

*(2) **Electron microscopy characterization of samples*** – An Hitachi 4800 field emission scanning electron microscope (SEM) was used to characterize the surface morphology of the samples. An FEI Tecnai F-20 field emission high-resolution transmission electron microscope (HRTEM) equipped with a high angle annular dark field detector (HAADFD) and an energy-dispersive x-ray (EDX) spectrometer was used to characterize the internal structures of the nanowires and to analyze their elemental composition. To prepare the HRTEM samples, nanowires were scraped from the surface of the porous Si and nonporous Si substrates, and ultrasonically dispersed in acetone solutions. Several drops of solution were then dropped on to holey carbon coated copper TEM grids.

*(3) **Electron Field Emission Measurement*** – The electron field emission of the nanowires was studied using a field emission microscope (FEM) equipped with a moveable Faraday cup. The Faraday cup with a standard SEM aperture (600 μm in diameter at a distance of 70 mm from the tip) was connected to a Keithley 485 picoammeter for the emission current measurement. The nanowire field emitters prepared for these measurements consisted of a tungsten wire mounted on a "V"-shaped tungsten filament attached to pins in a ceramic base. The tip of the tungsten wire was electrochemically etched to a diameter of less than 1μm. A tiny amount of nanowire sample was mounted on the tungsten tip using a small drop of carbon paste (Ted Pella Electrodag-502). The FEM test system had a point-to-plane electrode geometry with a separation of ~120 mm between the phosphor-coated planar anode and the tungsten tip. The field emission microscope base pressure was $\sim 5\times10^{-8}$ Torr. The field emission images and the current-voltage (I-V) behaviors of the nanowire emitters were obtained by applying a negative dc voltage up to 7000 V. Emission current measurements were recorded using digital data acquisition software (Test-Point) in a personal computer. This allowed us to construct both a time-averaged I-V response and current versus time plot at each voltage. The field emission patterns produced on the phosphor screen were imaged using a digital camera and recorded continuously on videotapes.

RESULTS AND DISCUSSION

The samples prepared using the method described in Experimental (1) were found to consist of both SiO_2 nanowires and CdS/ SiO_2 composite nanowires, both of which were grown on the surface of the nonporous and porous Si substrates. However, the density distribution of the specific types of nanowire (SiO_2 or CdS/ SiO_2) was different depending on the location of the Si substrates in the furnace. Our electron microscopy characterization suggests that a high density of SiO_2 nanowires was found on the Si substrates located near the ceramic plate that was originally placed at the center of the heating zone in the furnace. The Si substrates containing SiO_2 nanowires showed a pink-purple color. Figure 1 (a)-(b) demonstrate a set of SEM images of SiO_2 nanowires formed on Si substrates. Note that the surface of each nanowire is very smooth and clean. There are particles attached to the ends of the wires. The diameter of the SiO_2 nanowires ranged from 100 nm to 900 nm. The length of the nanowires ranged from a few μm to more than 30 μm.

Although some CdS nanowires were also found among the high density of the SiO_2 nanowires on the Si substrates placed near the ceramic plate, a high density of CdS/ SiO_2 composite nanowires was found on the Si substrates that were placed near the edge of the heating zone in the furnace, where the temperature was slightly lower than at the center region of the heating zone. These CdS/ SiO_2 composite nanowires were visible on the surface of the substrates in the form of a bright yellow powder. Under the SEM, the yellow powder consisted of numerous tangled nanowires as shown in figure 2 (a)-(b).

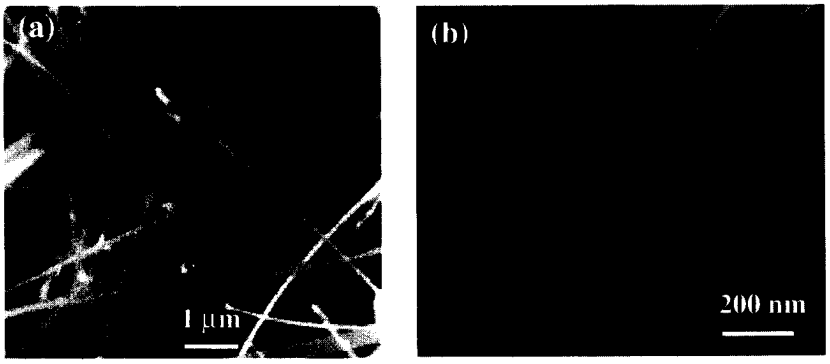

Figure 1. is a set of SEM images of SiO_2 nanowires formed on Si substrates. (a) provides an overview of the SiO_2 nanowire samples. (b) reveals a gold nanoparticle attached to the end of a SiO_2 nanowire.

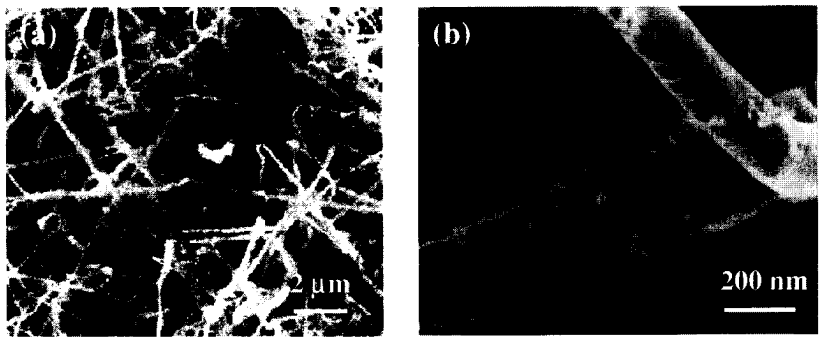

Figure 2. (a) is an SEM overview of CdS/SiO_2 composite nanowires. (b) is a high resolution SEM image of CdS/SiO_2 composite nanowires.

Note in figure 2 that the diameter of the CdS/SiO_2 composite nanowire is about the same as that of SiO_2 nanowires. The surface of the CdS/SiO_2 composite nanowires, however, is not as smooth as that of SiO_2 nanowires. A high resolution SEM image [figure 2 (b)] reveals that the roughness of the surface was caused by the formation of many tiny flakes on the wire surface. To further characterize the chemical composition of the nanowires, a high resolution TEM equipped with an EDX spectrometer was used. Figure 3 (a) shows a TEM image of a SiO_2 nanowire with a nanoparticle at the end. When the nanoprobe of the EDX spectrometer was placed on the nanoparticle, the EDX spectrum indicated that the nanoparticle was elemental gold, while the body of the nanowire was quantitatively characterized to be SiO_2. This result suggests that the growth of the SiO_2 nanowire was led by the gold particle. Figure 3 (b) shows a TEM image of CdS/SiO_2 composite nanowires. It is obvious that the surface of the nanowire is not smooth. When the nanoprobe of the EDX was placed on the areas of small flakes (as indicated by arrows), the EDX spectra showed strong signals of CdS. However, when the nanoprobe was placed near the axis of the wire, the spectra showed strong signals

of SiO_2 mixed with CdS. This analysis suggests that these nanowires are a mixture of CdS and SiO_2. The morphology of these wires was found to be either straight or curved. Nanoparticles were also found on the ends of some of these composite nanowires.

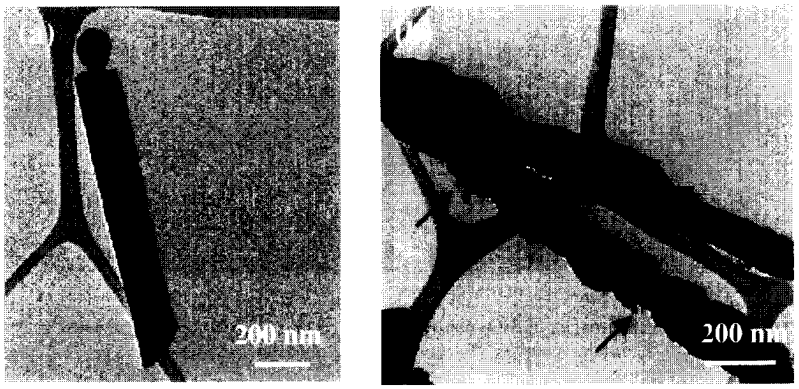

Figure 3. (a) is a TEM image of a SiO_2 nanowire. (b) is a TEM image of CdS/SiO_2 composite nanowires. Arrows indicate the tiny CdS flakes.

To understand the formation mechanism of these nanowires, a series of experiments controlled by different preparation parameters was conducted. The following was found. (1) When no gold thin film was applied to the surface of either porous or nonporous Si substrates, no nanowires were formed. (2) When no CdS powder was placed in the reaction chamber (furnace), no nanowires were formed on the surface of the Si substrates. (3) When gold thin films were applied to the Si substrates and the CdS powder was placed at the heating zone of the furnace, SiO_2 nanowires and CdS/SiO_2 composite nanowires were formed on both nonporous and porous Si substrates. However, most of the SiO_2 nanowires were found on the Si substrates placed near the center of the heating zone of the furnace. The CdS/SiO_2 composite nanowires were found on Si substrates placed near the edge (relatively lower temperature region) of the heating zone. Small CdS flakes were formed on the surface of CdS/SiO_2 composite nanowires. Our experimental results indicate that without the presence of CdS in the reaction chamber, no nanowires were formed on the Si substrates, although it is not clear what the function of the CdS with respect to the formation of the SiO_2 nanowires is. Since gold particles were found at the ends of most nanowires, the catalytic function of the gold is obvious. Temperature gradient also plays an important role in the nucleation of nanowires with different compositions.

Electron field emission of both SiO_2 nanowires and the CdS/SiO_2 composite nanowires was studied using a field emission microscope (FEM) equipped with a Faraday cup. Figure 4 (a) shows an emission pattern (with an applied potential of 2450 V) of a SiO_2 nanowire. The black shadow at the center of the image is the Faraday cup. Since the emission pattern of the SiO_2 nanowire is very similar to those of oriented single crystalline metal field emitters (Au, W, Fe, and Ni) [5], we suspect that this emission pattern results from a gold nanoparticle attached to the tip of the SiO_2 nanowire. The field emission measurement was also performed on a CdS/SiO_2 composite nanowire. It was found that the field emission pattern from the composite nanowire was not stable. Numbers of small emission sites were constantly changing as shown in Figure 4 (b). It was speculated that these emission sites resulted from the tiny CdS flakes.

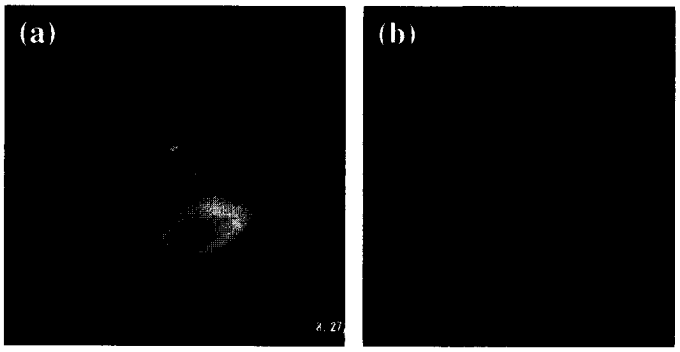

Figure 4. (a) shows a field-emission pattern of a SiO_2 nanowire, (b) shows the emission patterns of the CdS/SiO_2 composite nanowire.

The I-V characteristic for the SiO_2 nanowire is shown in figure 5 (a). The corresponding F-N plot is shown in figure 5 (b), where $\ln(I/V^2)$ was plotted as a function of 1/V. Note that the I-V characteristic of the SiO_2 nanowire followed Fowler-Nordheim (F-N) behavior. A self-consistency

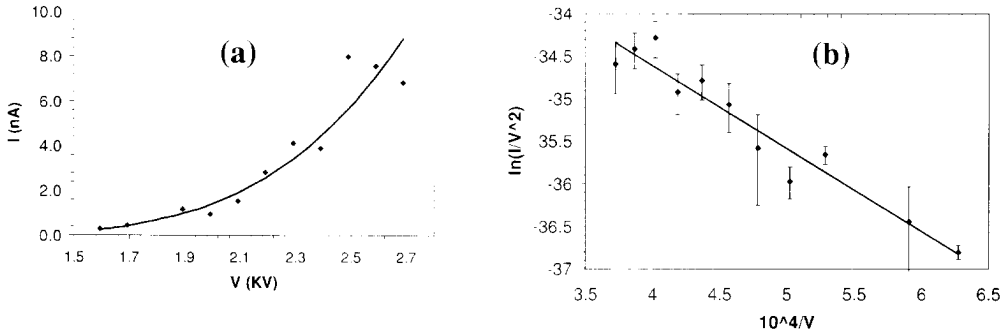

Figure 5. (a) shows the current-voltage behavior of a SiO_2 nanowire, (b) is its corresponding Fowler-Nordheim plot.

calculation using the tip-to-screen distance shows that the pattern size in figure 4 (a) (screen diameter 4 in.) was created by a spherical emitting surface on the order of the size in figure 1 (b). A second self-consistency check using the work function for gold (approximately 4.5 eV) and the slope of the F-N plot in figure 5 (b) shows that the factor k, where $F = V/(kr)$ and r is the radius of the gold particle, is approximately 3. This is between k=1 for an isolated sphere and k=5 for the usual field emitter geometry, which is expected for an emitter shaped like the figure 1 (b) emitter (See ref. 5, page 32). These two calculations suggest that the pattern and the F-N plot come from a gold particle in a configuration and size similar to figure 1 (b). During our experiment, we also noted that a single SiO_2 nanowire produced by the method described in this report was capable of emitting over a fairly large current range. For instance, the emission current from a SiO_2 nanowire measured through a Faraday cup was 50 nA with an applied potential of 2550V. Although pure bulk SiO_2 material is an insulator, this is apparently not the case while

it is in nanometer dimension as was demonstrated in this study. It is possible that impurities in the SiO_2 nanowires cause the nanowires to be semi-conductive and result in the electron field emission through the gold nanoparticle tips. Another possibility is in a report by Ishikawa *et al* that outlined a calculation of a Si – SiO_2 – Metal field emitter showing the possibility of tunneling from the semiconductor to inject charges into the conduction band of the insulator and from there into the metal [6]. In comparison with the angular intensity of electron field emission of single carbon nanotube emitters measured under the same applied field and the same configuration of the SiO_2 emitters, the angular intensity of SiO_2 nanowires is stronger than that of carbon nanotubes [7]. The lifetime of the SiO_2 nanowire emitter is also much longer than that of carbon nanotubes. An in-depth study is under way to further investigate these properties.

CONCLUSIONS

In this report, we demonstrated the preparation and characterization of SiO_2 nanowires and CdS/SiO_2 composite nanowires . It suggests that using the thermal evaporation method, the effects of the substrates have to be taken into consideration during nanowire growth. In our case, the Si substrates served as the Si source for the formation of the SiO_2 nanowires and CdS/SiO_2 composite nanowires. The temperature gradient in the reaction chamber (furnace) has an impact on the nucleation of nanowires of different composition. The higher temperature region favored the formation of SiO_2 nanowires, while the relatively low temperature region resulted in the deposition of CdS/SiO_2 composite nanowires. The electron field emission of the SiO_2 nanowire was dominated by the emission from the gold nanoparticles located at the tip, while the emission patterns of the composite nanowires were unstable due to the emission from the tiny CdS flakes on their surface.

ACKNOWLEDGMENTS

The authors would like to thank Dr. Y.C. Wang at FEI Company for his help with HRTEM/HAADF images and Ms. Sara White at Hitachi High-Technologies Inc. for helping with the S-4800 SEM. Financial support for this work was provided by the National Science Foundation under awards No. ECS-0217061 and DMR-0097575 and the American Chemical Society Petroleum Research Fund under award No. PRF-38108-G5.

REFERENCES

1. T. Ruecks, K. Kim, E. Joselevich, G.Y. Tseng, C. Cheung, C.M. Lieber, *Science* 289, 94 (2000).
2. M.H. Huang, S. Mao, H. Feick, H. Yan, Y. Wu, H. Kind, E. Weber, R. Russo, P. Yang, *Science* 292, 1897 (2001).
3. Y. Wu, H. Yan, M. Huang, B. Messer, J.H. Song, and P. Yang, *Chem. Eur. J.* 8. 1261 (2002).
4. L.F. Dong, J. Jiao, D. W. Tuggle, J. Petty, S. A. Elliff, M. Coulter, to be published in *Appl. Phys. Lett.*, (2002).
5. R. Gomer, *Field Emission and Field Ionization*, p. 103-166, American Institute of Physics, New York (1993).
6. J. Ishikawa, Y. Gotoh, S. Sadakane, K. Inoue, M. Nagao, and H. Tsuji, *J. Vac. Sci. Technol.* B 16(2), 895 (1998)
7. J. Jiao, L. F. Dong, D. W. Tuggle, C. L. Mosher, S. Foxley and J. Tawdekar, *Mat. Res. Soc. Symp. Proc.*, Vol. 706, 113 (Z5.3.1 – Z5.3.6), (2002).

AUTHOR INDEX

SUBJECT INDEX

Three-Dimensional Nanoengineered Assemblies